

ISSN: 2320-8694

Journal of Experimental Biology And Agricultural Sciences



VOLUME 11 || ISSUE V || OCTOBER, 2023

Production and Hosting by Horizon Publisher India[HPI]
(<http://www.horizonpublisherindia.in>)
All rights reserved.

ISSN No. 2320 - 8694

Peer Reviewed - open access journal

Common Creative License - NC 4.0

Volume No - 11

Issue No - V

October, 2023

Journal of Experimental Biology and Agricultural Sciences (JEBAS) is an online platform for the advancement and rapid dissemination of scientific knowledge generated by the highly motivated researchers in the field of biological agricultural, veterinary and animal sciences. JEBAS publishes high-quality original research and critical up-to-date review articles covering all the aspects of biological sciences. Every year, it publishes six issues.

JEBAS has been accepted by SCOPUS UGC CARE, INDEX COPERNICUS INTERNATIONAL (Poland), AGRICOLA (USA), CAS (ACS, USA), CABI - Full Text (UK), International Committee of Medical Journal Editors (ICMJE), SHERPA - ROMEO; J gate and Indian Science Abstracts (ISA, NISCAIR) like well reputed indexing agencies.

[HORIZON PUBLISHER INDIA [HPI]

<http://www.horizonpublisherindia.in/>]

Editorial Board

Editor-in-Chief

Prof Y. Norma-Rashid
(University of Malaya, Kuala Lumpur)
editor.in.chief.jebas@gmail.com

Co-Editor-in-Chief

Dr. Kuldeep Dhama, M.V.Sc., Ph.D.
NAAS Associate, Principal Scientist, IVRI, Izatnagar India - 243 122
co_eic@jebas.org

Managing - Editor

Kamal K Chaudhary, Ph.D. (India)
jebasonline@gmail.com

Technical Editors

Hafiz M. N. Iqbal (Ph.D.)

Research Professor,
Tecnologico de Monterrey, School of Engineering and Sciences,
Campus Monterrey, Ave. Eugenio Garza Sada 2501,
Monterrey, N. L., CP 64849, Mexico
Tel.: +52 (81) 8358-2000Ext.5561-115
E-mail: hafiz.iqbal@my.westminster.ac.uk; hafiz.iqbal@itesm.mx

Prof. Dr. Mirza Barjees Baigis

Professor of Extension (Natural Resource Management),
Department of Agricultural Extension and Rural Society,
College of Food and Agriculture Sciences,
King Saud University, P.O. Box 2460, Riyadh 11451, Kingdom of Saudi Arabia
Email: mbaig@ksu.edu.sa

Dr. Mukesh Kumar Meghvansi

Scientist, Bioprocess Technology Division, Defence R & D Establishment, Gwalior-474002
Email: mk_meghvansi@yahoo.co.in

Dr. B L Yadav

Head – Botany, MLV Govt. College, Bhilwara, India
E mail: drblyadav@yahoo.com

Dr. K L Meena

Associate Professor – Botany, MLV Govt.
College, Bhilwara, India
E mail: kanhaiyameena211@yahoo.com

Dr. Yashpal S. Malik

ICAR – National Fellow Indian Veterinary Research Institute (IVRI)
Izatnagar 243 122, Bareilly, Uttar Pradesh, India

Associate Editors

Dr. Sunil K. Joshi

Laboratory Head, Cellular Immunology
Investigator, Frank Reidy Research Center of Bioelectrics, College of Health Sciences, Old Dominion University,
4211 Monarch Way, IRP-2, Suite # 300, Norfolk, VA 23508 USA
Email: skjoshi@odu.edu

Dr. Vincenzo Tufarelli

Department of Emergency and Organ Transplantation (DETO),
Section of Veterinary Science and Animal Production,
University of Bari 'Aldo Moro', s.p. Casamassima km 3, 70010 Valenzano, Italy
Email: vincenzo.tufarelli@uniba.it

Prof. Sanjay-Swami, Ph.D. (Soil Science & Agril. Chemistry),

School of Natural Resource Management,
College of Post Graduate Studies in Agricultural Sciences,
(Central Agricultural University),
UMIAM (Barapani)-793 103, Meghalaya, INDIA
Email: sanjay.nrm.cpgsas@cau.ac.in

Chiranjib Chakraborty, Ph.D.

Professor, School of Life Science and Biotechnology,
Adamas University, Kolkata, India
Email: drchiranjib@yahoo.com

Jose M. Lorenzo

Centro Tecnológico de la Carne de Galicia
Ourense, Spain
Email: jmlorenzo@ceteca.net

Assistant Editors

Dr Ayman EL Sabagh

Assistant professor, agronomy department, faculty of agriculture
kafresheikh university, Egypt
E-mail: ayman.elsabagh@agr.kfs.edu.eg

Safar Hussein Abdullah Al-Kahtani (Ph.D.)

King Saud University-College of Food and Agriculture Sciences,
Department of the Agricultural Economics
P.O.Box: 2460 Riyadh 11451, KSA
email: safark@ksu.edu.sa

Dr Ruchi Tiwari

Assistant Professor (Sr Scale)
Department of Veterinary Microbiology and Immunology,
College of Veterinary Sciences,
UP Pandit Deen Dayal Upadhyay Pashu Chikitsa Vigyan Vishwavidyalay Evum Go-Anusandhan Sansthan (DUVASU),
Mathura, Uttar Pradesh, 281 001, India
Email: ruchi.vet@gmail.com

Dr. ANIL KUMAR (Ph.D.)

Asstt. Professor (Soil Science)
Farm Science Centre (KVK)
Booh, Tarn Taran, Punjab (India) – 143 412
Email: anilkumarhpkv@gmail.com

Akansha Mishra

Postdoctoral Associate, Ob/Gyn lab
Baylor College of Medicine,
1102 Bates Ave, Houston Tx 77030
Email: akansha.mishra@bcm.edu; aksmisra@gmail.com

Dr. Muhammad Bilal

Associate Professor
School of Life Science and Food Engineering,
Huaiyin Institute of Technology, Huaian 223003, China
Email: bilaluaf@hotmail.com

Dr. Senthilkumar Natesan

Associate Professor

Department of Infectious Diseases, Indian Institute of Public Health

Gandhinagar, Opp to Airforce station HQ, Lekawada, Gandhinagar, Gujarat - 382042, India

Email: snatesan@iiphg.org

Mr. Ram Bahadur Khadka (Microbiologist)

Assistant Professor (Pokhara University)

Crimson College of Technology (CCT)

Butwal-13, Rupandehi, Lumbini Province, Nepal

Email: rambahadurkhadka00@gmail.com

Prof. A. VIJAYA ANAND

Professor

Department of Human Genetics and Molecular Biology

Bharathiar University

Coimbatore – 641 046

Dr. Phetole Mangena

Department of Biodiversity, School of Molecular and Life Sciences,

Faculty of Science and Agriculture, University of Limpopo, Republic of South Africa

Private Bag X1106, Sovenga, 0727

Email: Phetole.Mangena@ul.ac.za ; mangena.phetole@gmail.com

Table of contents

Antimicrobial and anti-biofilm activities of plant extracts against <i>Pseudomonas aeruginosa</i> – a review <i>10.18006/2023.11(5).780.790</i>	780 – 790
Assessment of Heavy Metal Content and Consumption Risks At Selected Paddy Field in Malaysia: A Review <i>10.18006/2023.11(5).791.799</i>	791 – 799
Structure and Reactivity of Halogenated GC PNA Base Pairs – A DFT Approach <i>10.18006/2023.11(5).800.808</i>	800 – 808
Identification and antibiotic susceptibility profiles of anaerobic bacteria isolated from patients with acne vulgaris <i>10.18006/2023.11(5).809.814</i>	809 – 814
Cytotoxic Study of Zinc Oxide Nanoparticles on Cervical Cancer Cell Line <i>10.18006/2023.11(5).815.821</i>	815 – 821
Comparative Evaluation of Masson's Trichrome and Picrosirius Red Staining for Digital Collagen Quantification Using ImageJ in Rabbit Wound Healing Research <i>10.18006/2023.11(5).822.833</i>	822 – 833
Ecological desalination of anchovy residues and their mixture with soybean meal for the production of poultry feed: Optimization of waste through response surface methodology (RSM) <i>10.18006/2023.11(5).834.844</i>	834 – 844
Efficient Solar-Powered IoT Drip Irrigation for Tomato Yield and Quality: An Evaluation of the Effects of Irrigation and Fertilizer Frequency <i>10.18006/2023.11(5).845.853</i>	845 – 853
Application of olive mill waste-based biochar for improving wheat response to salt stress <i>10.18006/2023.11(5).854.865</i>	854 – 865
Work Place Self-Management by Academic Cum Clinical Physiotherapist – A Case Study <i>10.18006/2023.11(5).866.870</i>	866 – 870



Journal of Experimental Biology and Agricultural Sciences

<http://www.jebas.org>

ISSN No. 2320 – 8694

Antimicrobial and anti-biofilm activities of plant extracts against *Pseudomonas aeruginosa* – a review

Subramaniam G.^{1*}, Khan G. Z.¹, Sivasamugham L.A.¹, Wong L.S.¹, Kidd S.², Yap C. K.³

¹Faculty of Health and Life Sciences, INTI International University, Nilai, Negeri Sembilan, Malaysia

²School of Biological Sciences, Australian Centre for Antimicrobial Resistance Ecology (ACARE), The University of Adelaide, Adelaide, South Australia

³Faculty of Science, Universiti Putra Malaysia, Serdang, Selangor

Received – June 05, 2023; Revision – August 01, 2023; Accepted – November 04, 2023

Available Online – November 30, 2023

DOI: [http://dx.doi.org/10.18006/2023.11\(5\).780.790](http://dx.doi.org/10.18006/2023.11(5).780.790)

KEYWORDS

Pseudomonas aeruginosa

Plant extracts

Antimicrobial activity

Anti-biofilm activity

Human health

ABSTRACT

Antimicrobial resistance among bacterial pathogens, including *Pseudomonas aeruginosa*, is a global problem that has led to research on naturally occurring compounds as an alternative source of antibacterial and anti-biofilm agents. This review focuses on determining plant extracts' antimicrobial and anti-biofilm activities against *P. aeruginosa*, an opportunistic pathogen contributing to microbial and biofilm-associated infections in humans. Medicinal plants are being widely researched as they are rich sources of phytochemicals, including flavonoids, alkaloids, tannins and terpenoids. These phytochemicals have been well known for their antibacterial activity, which contributes to the effectiveness of certain plants, including *Punica granatum* and *Triumfetta welwitschia*, against *P. aeruginosa*. *Hypericum perforatum* and *Berginia ciliata* contains phytochemicals that directly inhibit the quorum sensing mechanism, inhibiting the direct cell-to-cell communication, thereby preventing or reducing biofilm formation by *P. aeruginosa*. Plant extracts also inhibit bacterial growth and should be considered an alternative to antibiotics. Furthermore, plant extracts can be used with antibiotics for better efficacy against *P. aeruginosa*. However, more research must be carried out to select plants with a broad spectrum of activity against not only *P. aeruginosa* infections but other gram-negative bacteria in general. It would be economically viable to develop as a therapeutic drug. This would align with the third United Nations sustainable development goals on good health and well-being and is a significant step forward in the battle against antibiotic resistance.

* Corresponding author

E-mail: geetha.subramaniam@newinti.edu.my (Subramaniam G.)

Peer review under responsibility of Journal of Experimental Biology and Agricultural Sciences.

Production and Hosting by Horizon Publisher India [HPI]
(<http://www.horizonpublisherindia.in/>).
All rights reserved.

All the articles published by [Journal of Experimental Biology and Agricultural Sciences](#) are licensed under a [Creative Commons Attribution-NonCommercial 4.0 International License](#) Based on a work at www.jebas.org.



1 Introduction

Pseudomonas aeruginosa is a common species of the genus *Pseudomonas*, which causes human infections. Unfortunately, antipseudomonal drug resistance is increasing, compromising suitable antimicrobial therapy selection. As a result, there is an increase in morbidity and death in patients infected with multi-drug resistant strains of *P. aeruginosa* (Montero et al. 2020). This bacterium has been observed to trigger severe clinical manifestations in humans, such as severe neutropenia and septic shock (Recio et al. 2020). Furthermore, *P. aeruginosa* also causes nosocomial infections such as urinary tract infections (UTI) and ventilator-associated pneumonia (VAP), particularly in immunocompromised patients, which increases the mortality rates of *P. aeruginosa* infections (Ramirez-Estrada et al. 2016).

Further, *P. aeruginosa* can produce biofilms as part of its virulence mechanisms, contributing to its persistence in healthcare (Das et al. 2017; Labovska 2021). These biofilms occur on a variety of abiotic (plastic, metal, minerals, and glass) and biotic (humans, animals, and plants) surfaces and have complex structure and dynamic architecture (Labovska 2021).

A crucial aspect of biofilm-related infections is increased antibiotic resistance among the strains that cause biofilm development, making these infections long-lasting and challenging to eliminate (Dincer et al. 2020). Hence, antimicrobial resistance remains a crucial global health issue for humans and animals, compounded by the problems in developing new antimicrobials.

Plant extracts have significant antimicrobial activity and are a source of effective antimicrobial compounds that can work against planktonic and biofilms of bacterium (Famuyide et al. 2019). Much research is being carried out on the antimicrobial activity of plant extracts, essential oils, and phytochemicals, including secondary metabolites that have been extracted from various parts of the plants, including leaves, roots, and seeds using solvents which are then tested against multiple strains of bacteria including *P. aeruginosa* (Famuyide et al. 2019).

Antibiotics are routinely utilized to control Gram-positive and Gram-negative infections by inhibiting their growth and survival. However, biofilm-forming bacterial isolates have been shown to acquire antibiotic resistance very swiftly (Fair and Tor 2014). Hence, treating infections with microbial biofilms with standard antibiotics is rendered unmanageable. Consequently, new-found antibacterial and anti-biofilm compounds from plant extracts have elicited new attention to counteract microbial growth and biofilm formation (Abdel-Bar et al. 2022). Thus, due to their significant antibacterial and anti-biofilm properties, this study aims to review if plant-derived extracts are potential alternatives to antibiotics to treat infections caused by *P. aeruginosa*.

The methodology used to obtain information for this systematic review utilized keywords such as *P. aeruginosa*, antibacterial activity and antibiofilm activity of medicinal plants. Research articles published between 2012 and 2022 from SCOPUS and Web of Science (WoS) journals were evaluated to extract the information related to this issue.

2 Mechanisms of Resistance in *P. aeruginosa*

Due to the extraordinary ability of this pathogen to withstand antibiotics, treatment of *P. aeruginosa* infections has become increasingly challenging. Most of the commonly used antibiotics, such as imipenem, meropenem, aztreonam, and chloramphenicol, are found to be ineffective in the treatment of some of the *P. aeruginosa* infections due to the high levels of inherent, acquired, and adaptive resistance mechanisms (Meng et al. 2020).

Intrinsic antibiotic resistance is the bacteria's ability to decrease antibiotics' effectiveness because of fundamental structure or functionality features (Blair et al. 2015). *P. aeruginosa* exhibits a high intrinsic resistance to most antibiotics due to reduced outer membrane permeability, efflux pumps which pump out medicines from the cell, and the presence of enzymes such as β -lactamases, which destroy antibiotics (Pachori et al. 2019). By mutational alterations or horizontal transfer of antibiotic resistance genes, bacteria can also develop antibiotic resistance. Acquired resistance helps create multidrug-resistant strains, which, together with the high degree of inherent antibiotic resistance in *P. aeruginosa*, make eradication more challenging and increase the incidence of chronic infections (Munita and Arias 2016). By causing reversible modifications in gene and protein expression in response to stimulation from the environment, this acquired resistance increases a bacterium's capacity to resist antibiotic attack (Papaleo et al. 2022). The formation of biofilms by *P. aeruginosa* is characterized by adaptive resistance mechanisms that cause an infection to last longer and can lead to more severe conditions of existing diseases (Taylor et al. 2014).

3 Quorum Sensing and Biofilm Development in *P. aeruginosa*

Biofilms are microbial communities that are encased in an extracellular matrix (or extracellular polymeric substances, EPS) made up of proteins, extracellular DNA (eDNA), lipids, and exopolysaccharides (Jennings et al. 2015). One of the most essential aspects of microbial biofilms is that bacteria stay within the protected microenvironment of the biofilm while conditions outside the biofilm are harmful. Bacteria typically make up less than 10% of the dry mass of biofilms, while matrix can make up more than 90% (Mishra et al. 2023). The EPS is the matrix formed by microbes comprised of several biopolymers, allowing bacteria to live in proximity and interact and behave differently than their planktonic counterparts (Roy et al. 2018). The EPS offer an extra

layer of protection around the cells, shielding them from numerous pressures, enabling the bacteria within the biofilm to resist antibiotics and environmental challenges and even escape host immunological responses (Gonzalez et al. 2018). Pathogens can, therefore, hide within a biofilm, undetected by the immune system and tolerant of antibiotics. This is the basis for many chronic and relapsing infections. *P. aeruginosa*, an effective biofilm-producing Gram-negative bacteria, habitually forms biofilm throughout virulence exhibition and disease development (Vetrivel et al. 2021). Quorum sensing (QS) is a cell density-based signalling system that aids bacterial cell-to-cell communication and regulates virulence factors, including pigment and biofilm formation, contributing to chronic infection development (Lin and Cheng 2019). Specifically, QS regulates the expression of several genes involved in various biological functions such as virulence determinants, bioluminescence, motility, plasmid transfer, enzyme and toxin secretion, bacteriocin synthesis, efflux pump, and biofilm formation (Sionov and Steinberg 2022). The opportunistic pathogen *P. aeruginosa* has two well-defined QS systems, LasI and RhlI. N-(3-oxododecanoyl) homoserine lactone (3O-C12-HSL) is synthesized by LasI, while N-butyryl homoserine lactone (3O-C12-HSL) is synthesized by RhlIR (C4-HSL) (Lin and Cheng 2019). In *P. aeruginosa*, the las and rhl QS systems regulate various genes and gene products implicated in virulence. Furthermore, it was discovered that the las system controls Rhl at two levels: transcriptional and posttranslational. These two QS systems are vital during the early phases of biofilm formation, particularly when cells adhere to the surface and produce microcolonies (Lin and Cheng 2019).

The resistance mechanisms in *P. aeruginosa* have led to the development of multidrug-resistant strains, which cause difficult-to-treat infections and an increase in the mortality rate due to infections with this bacterium. The currently available antibiotics are losing their therapeutic ability due to the multiple resistance mechanisms employed by *P. aeruginosa*. Hence, there is a need to seek alternative therapeutic options, and one good avenue being explored is using plant extracts.

4 Plants as Potential Sources of Antimicrobial agents

Traditional antibiotic discovery strategies have fallen behind the evolution of resistance. As a result, improved antimicrobial agents are urgently required. Many medicinal plants such as *Punica granatum*, *Zingiber officinales*, *Cuminum cyminum*, *T. impetiginosa*, and *T. welwitschia* are being widely researched for their antimicrobial and anti-biofilm activity against *P. aeruginosa* (Ulloa-Uriza et al. 2015; Mostafa et al. 2018; Mombeshora et al. 2021). The findings from these studies have shown the potential of using plant extracts as antimicrobial agents against *P. aeruginosa* due to the strong inhibitory effects that seem comparable to antibiotics such as ciprofloxacin (Karuppiah and Rajaram 2012). The ability of plant extracts to inhibit microbial growth is based on the presence of plant secondary metabolites (phytochemicals), which are biologically active compounds that are not involved in essential plant processes but play crucial roles in plant defences against pathogens, pests, and environmental stresses (Khare et al. 2021).

Phytochemicals have already been shown to exhibit antibacterial properties when applied alone or synergistically with other antibacterial drugs (Abreu et al. 2012). Using phytochemical products and plant extracts as resistance-modifying agents (RMAs) is becoming a popular issue in science. RMAs slow down the process of resistance development in bacteria against plant phytochemicals. This makes them more suitable for developing antimicrobial agents as an alternative to antibiotics. Table 1 shows a few RMA's from plants (Patel and Patel 2016; Phitaktim et al. 2016; Siriwong et al. 2016; Owusu et al. 2021; Walczak et al. 2021).

Phytochemicals often work through different pathways than traditional antibiotics, making them potentially valuable for treating antibiotic-resistant microorganisms (Abreu et al. 2012). The discovery and development of new active compounds capable of partially or inhibiting bacterial resistance mechanisms is a promising technique for combating the resistance problem (Patel and Patel 2016).

Table 1 Examples of antibiotic resistance modifying compounds from plants

Compound	Plant source	Antibiotics potentiated	Reference
Ferruginol 5-Epispiferol	<i>Chamaecyparis lawsoniana</i>	Oxacillin, Tetracycline, Norfloxacin, Tetracycline,	Patel and Patel 2016
Carnosic acid carnosol	<i>Rosmarinus officinalis</i>	Erythromycin	Patel and Patel 2016
Ethyl gallate	<i>Caesalpinia spinosa</i>	β -lactams	Patel and Patel 2016
Epicatechin gallate	<i>Camellia sinensis</i>	Norfloxacin, Imipenem, Panipenem, β -Lactams	Patel and Patel 2016
Epigallocatechin gallate		Oxacillin	Phitaktim et al. 2016
a-mangostin	<i>Garcinia mangostana</i> L	Amoxicillin	Siriwong et al. 2016
Quercetin	<i>Allium cepa</i> L; <i>Solanaceae lycopersicum</i>	Gentamicin	Walczak et al. 2021
Carvacrol/thymol	<i>Thymus maroccanus</i>		

5 Antibacterial Activity of Plant Extracts Against *Pseudomonas aeruginosa*

Table 2 is a compilation of the antibacterial activity of ethanolic extracts from various plants against common bacterial pathogens, including *P. aeruginosa*, obtained from studies that tested various plant extracts against *P. aeruginosa*, *E. coli* and *S. aureus*. Based on the data summarized in Table 2, the plant that exhibited the most significant antibacterial activity against *P. aeruginosa* was *Triumfetta welwitschii*, followed by *Punica granatum* and *Thymus vulgaris* (Phitakin et al. 2016; Lin and Cheng 2019; Mombeshora et al. 2021).

Of the three bacterial strains tested, *P. aeruginosa* was more susceptible to most plant extracts than *Staphylococcus aureus* and *Escherichia coli*. These findings were interesting as Gram-positive bacteria, including *S. aureus*, are generally more susceptible to antibacterial agents, including plant extracts (Sakha et al. 2018).

Mombeshora and Mukanganyama (2019) demonstrated the antibacterial activity of *T. welwitschii* leaf extracts against *P. aeruginosa* and other bacteria; most of the extracts inhibited *P. aeruginosa* compared to other bacterial species tested. It is interesting to note that *E. coli* remained resistant to the plant extracts, which is expected as Gram-negative bacteria have two cellular membranes, one of which consists of lipopolysaccharides (LPS), which serves as a protective barrier to external molecules (Onivogui et al. 2016). However, the results indicated that the LPS layer did not confer the expected protection to *P. aeruginosa* against these plant extracts.

T. welwitschii was found to be capable of significantly increasing membrane permeability and causing nucleic acid leaking from *P. aeruginosa* cells. The loss of membrane integrity (membrane disruption) was found to be the mechanism of action of the plant

extracts against the bacteria tested in this study, which could have been contributed by the common phytochemicals, phenols, flavonoids and coumarins (Onivogui et al. 2016).

In a study by Rahman et al. (2017), *Punica granatum* was also shown to have significant antibacterial activity against *P. aeruginosa*. Some researchers suggested that phytochemical components of *P. granatum*, such as ellagitannins, phenols, tannins, punicic acid, flavonoids and flavones, exhibit antibacterial activity. *P. granatum* has tannin-rich ellagitannins that may have antimicrobial properties. It has also been proposed that phenolic compounds are important and are active antibacterial substances whereby they interact with enzymes and other proteins, causing cell membrane disruption and inducing a flow of protons out of the cell, resulting in cell death or blocking the amino acid biosynthesis-related enzymes (Mostafa et al. 2018).

As per data in several published studies, different plant extracts vary in phytochemical compositions, which subsequently can contribute to these plants' antibacterial and anti-biofilm activities. Due to the additional outer layer membrane of LPS in the cell membrane and periplasmic space of Gram-negative bacteria, they are often more resistant to antibacterial agents compared to Gram-positive bacteria. However, from the data in the literature, with *P. aeruginosa*, there seems to be significantly more susceptibility against plant extracts than other Gram-negative bacteria (Ahmed et al. 2021; Mombeshora et al. 2021). Some studies have been conducted to elucidate the mechanisms of action of plant extracts against *P. aeruginosa* and have generalized the action of phytochemicals and their effectiveness against bacterial species. There are resistant mechanisms unique to multi-drug resistant *P. aeruginosa*, for example, the synergism between the efflux system or the AmpC β -lactamase and low outer membrane permeability (Zeb et al. 2017). Antibiotic efflux is one of the most common mechanisms in this opportunistic pathogen, where the antibacterial

Table 2 Antimicrobial activity of selected plants against *S. aureus*, *E. coli* and *P. aeruginosa*

Name of plant	Inhibition zones (mm)*			Reference
	<i>S. aureus</i>	<i>E. coli</i>	<i>P. aeruginosa</i>	
<i>Thymus vulgaris</i>	17.6 ± 0.31	0.0 ± 0.0	14.7 ± 0.25	Mostafa et al. 2018
<i>Zingiber officinales</i>	15.4±0.23	0.0±0.0	11.2±0.17	Mostafa et al. 2018
<i>Punica granatum</i>	16.3 ± 0.57	14.2 ± 0.61	16.1 ± 0.46	Phitaktim et al. 2016
<i>Triumfetta welwitschia</i>	20.0 ± 1.00	-	46 ± 1.00	Mombeshora et al. 2021
<i>Olea Europaea</i>	8.0±1.00	8.00±1.00	10.00±1.00	Siriwong et al. 2016
<i>Artemisia vulgaris</i>	8±1.00	9±1.00	11±1.00	Walczak et al. 2021
<i>Azadirachta indica</i>	7±1.00	10±1.00	11±1.00	Walczak et al. 2021
<i>Momordica charantia</i>	13±1.00	0±0.0	10±1.00	Rahman et al. 2017
<i>Thymus algeriensis</i>	15.5±1.00	10±1.00	14±1.00	Shah et al. 2017

agent is expelled through the cell wall (Issa et al. 2018). Efflux pump expression from the resistance-nodulation-cell division (RND) family, which is tightly controlled by regulator genes, is closely linked with this resistance mechanism. In response to an extracellular signal, such as the presence of antibiotics or other environmental variables, gene activators and repressors that control the expression of these pumps have been discovered (Issa et al. 2018). Inhibition of these pumps by efficient EPIs (efflux pump inhibitors) would almost certainly reverse MDR's growth. As a result, the efflux pump regulators of *P. aeruginosa* are also a potential therapeutic target of plant phytochemicals. Plants are a rich source of bioactive compounds, including potential EPIs such as alkaloids, and hence play an important role in developing new antimicrobial agents (Shriram et al. 2018; Seukep et al. 2020).

6 Anti-biofilm Activity of Plant Extracts Against *P. aeruginosa*

Several plant extracts can prevent the implantation of sessile groups of microbial cells on the surface, resulting in biofilm formation, inhibiting and preventing biofilm-associated infection (Table 3). In previous studies, plant extracts such as *Berginia ciliata*, *Clematis grata*, *Eucalyptus globulus* and *Triumfetta welwitschia* have demonstrated significant antibiofilm activities against *P. aeruginosa* (Sambyal et al. 2017; Alam et al. 2020; Mombeshora et al. 2021).

Plant-derived anti-biofilm extracts identified against *P. aeruginosa* consist of phytochemicals alkaloids, organosulfur compounds, flavonoids, phenolic compounds, and terpenoids (Guzzo et al. 2020). These are plant secondary metabolites, which are extra nutritional constituents found in meagre amounts in plants that can affect the physiological and cellular activity of patients who consume them.

Alam et al. (2020) studied three plant extracts, of which *B. ciliata* and *C. grata* were found to efficiently inhibit biofilm formation by *P. aeruginosa* at 81% and 80% inhibition, respectively (Alam et al. 2020). Consequently, phytochemical analysis was conducted to provide a basic understanding of the active compounds in these

extracts involved in biofilm inhibition. The correlation studies showed that flavonoids, particularly catechin, can potentially inhibit quorum sensing-controlled virulence factors in *P. aeruginosa*, including biofilm production (Aliyu et al. 2016; Gorniak et al. 2019). In similar findings, several types of flavonoids have also been found to have the ability to suppress virulence factors such as pyocyanin and elastase synthesis, as well as biofilm inhibition, without affecting the growth of *P. aeruginosa* (Vandeputte et al. 2011; Kalia et al. 2015).

In another study by Sambyal et al. (2017), the essential oils from plant extracts of *M. alternifolia*, *S. aromatic*, *C. zeylanicum* and *E. globulus* oil were investigated to explore their potential as anti-biofilm agents against *P. aeruginosa* and *S. aureus*. In the study, *P. aeruginosa*, producing biofilm, showed 65.43% sensitivity to eucalyptus oil, which was the highest among all the plant oils used, compared to *S. aureus*, which showed 54.16% sensitivity (Sambyal et al. 2017). The findings indicate that certain plant essential oils have anti-biofilm properties against human pathogenic bacteria *P. aeruginosa*. The presence of essential oils is reported in most plant parts; along with this, extracts prepared using ethanol are composed of a variety of chemical components, and their antibacterial activity can be attributed to several distinct mechanisms. The interaction of major essential oils with the cell wall and membrane is the most elucidated action of their function. Compounds such as carvacrol, thymol, and others can disrupt the membrane integrity of the Gram-negative bacteria's envelope and prevent them from growing (Nazzaro et al. 2013).

Furthermore, Mombeshora et al. (2021) investigated the properties of *Triumfetta welwitschia*. They found that this plant is a rich source of phytochemicals that have anti-biofilm and antibacterial properties, including catechin, umbelliferone, and a luteolin derivative, which were shown to reduce the content of capsular polysaccharide in *P. aeruginosa* biofilms by 65% and biofilms' extracellular DNA content by 72%. The eDNA is a structural component of biofilm that binds to the biofilm during formation, protects it against antimicrobials, and is part of *P. aeruginosa* resistance mechanisms. Hence, the release of eDNA is

Table 3 Examples of plants exhibiting antibiofilm activity against *P. aeruginosa*

Plant extract	Main phytochemicals involved	Reference
<i>Berginia ciliata</i>	Flavonoids (catechin)	Alam et al. 2020
<i>Clematis grata</i>	Flavonoids (catechin)	
<i>Eucalyptus globulus</i>	Carvacrol, thymol	Sambyal et al. 2017
<i>Triumfetta welwitschia</i>	Catechin, umbelliferone, luteolin derivative	Mombeshora et al. 2021
<i>Hypericum perforatum</i>	Naphthodianthrones, phloroglucinols	Dogan et al. 2019
<i>Terminalia chebula</i>	Ellagic acid derivatives	Munir et al. 2020
<i>Lavandula coronopifolia</i>	Flavones (glucuronides), to triterpenes	Emam et al. 2021

an important part of anti-biofilm agents' mode of action (Tahrioui et al. 2019). Recent studies have shown that coumarins exhibit potent antioxidant, antibacterial, and anti-biofilm activities on Gram-positive and Gram-negative bacteria, particularly Gram-negative bacteria, because of their strong bioactive properties. Although the exact mechanism of coumarins' antibacterial effect is unknown, studies have revealed that they can destroy bacteria's cellular membranes (Yang et al. 2016). Hence, coumarins might be one of the phytochemicals that decrease the amount of eDNA, which may reduce biofilm formation. In addition, a study by Emam et al. (2021) demonstrated that the extracts from *Lavandula coronopifolia* inhibited the biofilm formation in *P. aeruginosa*, which was attributed to the flavons and triterpenes contained in this plant.

Microbial pathogens have developed biofilms, which have enhanced antibiotic resistance. As a result, finding new techniques to reduce biofilms is critical. Plant extracts (leaves, barks, flowers, and roots) include anti-adherence present in flavonoids and anti-QS chemicals present in phenolic compounds aid in increasing bacteria susceptibility and, therefore, eliminating biofilms (Sikic Pogakar et al. 2016; Husain et al. 2017).

Besides, another plant extract from *Hypericum perforatum* L. (HP), a well-known wound healer, was evaluated to determine its anti-biofilm activity against *P. aeruginosa*. Doğan et al. (2019) extracted aerial parts of HP in ethanol solvents, which were found to inhibit the QS systems of *P. aeruginosa*, specifically the LasIR and RhIR signalling pathways up to 65.43% and 28.80%, respectively (Dogan et al. 2019). QS regulatory system proteins regulate virulence factor transcription and biofilm formation (Alonso et al., 2020). Quorum inhibitory action has already been discovered in several plant-derived phytochemicals. When employed in high concentrations, phenolic compounds derived from plants have been shown to suppress biofilm production in the PAO1 strain of *P. aeruginosa*. In addition, ellagic acid derivatives from *Terminalia chebula*, as well as aqueous extracts from *Callistemon viminalis*, *Bucida buceras*, and *Conocarpus erectus*, have been shown to inhibit QS of *P. aeruginosa* QS via RhIR and LasR, while also reducing virulence factors production and enhancing biofilm sensitivity in the PAO1 strain of *P. aeruginosa* (Munir et al. 2020).

Multiple flavonoids in the plant extracts have recently been shown to prevent *P. aeruginosa* biofilm formation, suggesting that they work by disrupting QS signalling (Paczkowski et al. 2017). Their mechanisms of action, however, were not studied. It is recently discovered that novel flavonoids with dihydroxyl moieties in the flavone A-ring backbone, as well as the previously described flavonoids baicalein and quercetin, bind to the QS receptors LasR and RhIR, reducing their ability to bind to DNA encoding QS-regulated promoters. The presence of two hydroxyl groups in the

flavone A-ring is required for LasR and RhIR inhibition, according to structure-activity relationship (SAR) analysis (Paczkowski et al. 2017). The flavonoids work via an allosteric mechanism, according to LasR, the representative receptor. In a LasR/RhIR-dependent mechanism, the flavonoids decrease virulence factor synthesis and swarming. These are the first noncompetitive QS inhibitors to target LasR/RhIR and impede DNA binding. They antagonize the autoinducer-binding receptors, LasR and RhIR, which impair quorum sensing. According to the structure-activity relationship analysis, including two hydroxyl moieties in the flavone A-ring backbone is necessary to inhibit LasR/RhIR strongly. According to biochemical analysis, the flavonoids block LasR/RhIR DNA binding non-competitively. The flavonoids decrease virulence factor synthesis and modify the transcription of quorum sensing-controlled target promoters (Paczkowski et al. 2017).

To date, most of the research has been focused on the action of phytochemicals on the down-regulation of certain quorum-sensing genes, which impact the QS ability of *P. aeruginosa*. This has significantly contributed to the antibiofilm activity of plant extracts against the bacterium. However, there could be more mechanisms of action, but they have not been elucidated yet.

Another significant contribution of plant extracts towards effective antimicrobial and anti-biofilm activity against *P. aeruginosa* infections could be in combination with currently used antibiotics. When combined with antibiotics, the plant extracts may boost its effectiveness against harmful microorganisms.

7 Combination of Plant Extracts with Antibiotics as an Optional Treatment Against *P. aeruginosa*

Using plant extracts as RMAs is an increasingly researched topic to combat bacterial drug resistance. In the case of RMAs, multiple studies have demonstrated that plant-derived compounds can be employed to boost antibiotic treatment efficacy (Patel and Patel 2016). Self-medication with various plant items from herbal suppliers and natural food stores is becoming increasingly popular as people become more aware of antibiotic resistance issues (Patel and Patel 2016).

Hence, another focus could be on combining these plants with antibiotics. From the data reviewed on the antimicrobial and antibiofilm activity of plant extracts (Table 4), plants such as *E. globulus*, *E. camaldulensis*, *T. maroccanus*, and *R. officinalis* exhibit antibiofilm and antimicrobial activities against *P. aeruginosa* (Reda et al. 2017; Cheesman et al. 2017; Sagar et al. 2020; Abu El-Wafa et al., 2020). Therefore, it would be interesting to see if, when combined with antibiotics, these plant extracts can enhance the activity of antibiotics against *P. aeruginosa* while reducing the possibility of resistance development against antibiotics. Several studies have already been conducted

Table 4 Examples of plant-based antimicrobials used in combination with antibiotics demonstrate successful antimicrobial activity

Plant extract	Antibiotic	Comments	Reference
<i>Eucalyptus globulus</i>	Hyperoside + ceftazidime	Inhibition of quorum sensing-dependent factors and biofilm formation	Sagar et al. 2020
<i>Eucalyptus camaldulensis</i>	Proanthocyanidine/ ellagitannin + ceftriaxone	Cytoplasmic membrane rupture observed in <i>P. aeruginosa</i>	Reda et al. 2017
<i>Thymus maroccanus</i>	Caravacrol/thymol + ciprofloxacin	Synergy up to 98% demonstrated against <i>P. aeruginosa</i> .	Cheeseman et al. 2017
<i>Rosmarinus officinalis</i>	Rosmaridiphenol + piperacillin	Decrease in biofilm formation	Abu El-Wafa et al. 2020

combining different plants with antibiotics to treat *P. aeruginosa* infections. A study was conducted by Dzotam and Kuete (2017) to determine the antimicrobial activity of several Cameroonian plant extracts in combination with antibiotics against *P. aeruginosa*. The research findings indicated that the tested plants could be used alone or with antibiotics to treat bacterial infections, including the multidrug-resistant bacteria *P. aeruginosa*, as they showed 75% antibacterial activity against the bacterium (Dzotam and Kuete 2017). This suggests that the combination of the two substances may then aid in preventing resistant mutants and restoring antibiotic action. In another study, a combination of antibiotics and extracts of clove, jambolan, pomegranate, and thyme demonstrated significant synergistic activity against a multidrug-resistant isolate of *P. aeruginosa* (Cheesman et al. 2017).

Certain plants have significant antibacterial activity against *P. aeruginosa*, and it is interesting to know that there are natural solutions for developing a drug which could be an alternative to antibiotics against *P. aeruginosa* using plant extracts. Plant-based antimicrobials have powerful antimicrobial properties and can be used alone or in combination with antibiotics to combat the current antibiotic resistance challenge, which aligns with the third United Nations sustainable development goal on good health and well-being.

Detailed research on plant extracts is required as not all show significant activity against *P. aeruginosa*. Some studies show *Justicia flava* and *Myrianthus arboreu* are the plants to which *P. aeruginosa* was not susceptible compared to *S. aureus* or other bacterial species (Rahman et al. 2017). Plant extracts with significant antimicrobial activity against Gram-positive bacteria do not appear to have the same antimicrobial activity against other Gram negative bacteria (Elisha et al. 2017). This might challenge drug development companies as the plants to develop antimicrobial agents against this need to be carefully sourced. Furthermore, finding plants effective against *P. aeruginosa* alone might be economically unviable as drug companies look to produce effective antimicrobial agents against various bacteria. In addition, the quantity of extracted phytochemicals used should be considered to ensure that drug development companies determine the toxicity levels for these compounds before developing them into consumable therapeutic agents. Hence, although plants hold

considerable promise as the future of antimicrobial and anti-biofilm agents, much research must be carried out before they can become a commercially viable entity.

Conclusion and Future Prospects

This review showed that plant extracts have significant antimicrobial and anti-biofilm activity and thus have the potential to become alternatives to antibacterial agents. Another advantage of plant extracts over antibiotics is resistance modifying agents that slow the development of bacterial resistance to plant phytochemicals. However, from the drug development perspective, there are certain limitations because all the research that has been done has pointed out a few things. Firstly, plant extracts that are effective against *P. aeruginosa* are not as effective against other gram-negative bacteria. This would make drug development very challenging economically because antibiotics cannot just be developed for *P. aeruginosa* only. The antibacterial is needed to be set against gram-negative pathogens in general. Secondly, not all plants are effective against *P. aeruginosa*; hence, finding the correct plant extract can be challenging. Another reason is that most gram-negative bacteria are not susceptible to the plant extracts. However, *P. aeruginosa* seems unusual in that specific plant extracts that can be used against a broad range of clinically critical gram-negative bacteria must be identified. Also, drug-developing companies take up to ten years to develop a new antibiotic. But it only takes two years for a bacterium to become resistant to that antibiotic. So, there are less new antimicrobials available against resistance pathogens. Thus, alternatives must be sourced. Phytochemicals can be made into therapeutic agents or along with currently used antibiotics. However, to do this, the drug companies need to test toxicity and determine the dosage patients could consume. Plant extracts seem to be the best alternative if scientists can do more research and overcome the issues involved in plant extracts. If suitable plant extracts are extracted, they can be developed as potential drug targets with a broad spectrum of antimicrobial and anti-biofilm activities against gram-negative bacteria, including *P. aeruginosa*. Given the global dimension of this epidemic and its significant health and economic costs, we urgently need to find new solutions and implement new policies to prevent antibiotic resistance. Plants are the safest and most effective solution to these concerns due to the presence of natural

compounds, which have shown phenomenal antimicrobial and anti-biofilm activity on *P. aeruginosa*.

Acknowledgements

We are grateful for the funding provided by INTI Research Grant 2021: Seed Grant INTI-FHLS-11-02-2021 to carry out this study.

Conflict of Interest

None of the authors have a conflict of interest to report. This paper has not been submitted for publication in any other journal.

References

- Abdel Bar, F. M., Alossaimi, M. A., Elekhawy, E., Alzeer, M. A. A., Abo Kamer, A., Moglad, E., & ElNaggar, M. H. (2022). Anti-Quorum Sensing and Anti-Biofilm Activity of Pelargonium × hortorum Root Extract against *Pseudomonas aeruginosa*: Combinatorial Effect of Catechin and Gallic Acid. *Molecules*, 27(22), 7841.
- Abreu, A.C., McBain, A.J., & Simoes, M. (2012). Plants as sources of new antimicrobials and resistance-modifying agents. *Natural Product Reports*, 29(9), 1007-1021.
- Abu El-Wafa, W. M., Ahmed, R. H., & Ramadan, M.A. (2020). Synergistic effects of pomegranate and rosemary extracts in combination with antibiotics against antibiotic resistance and biofilm formation of *Pseudomonas aeruginosa*. *Brazilian Journal of Microbiology*, 51(3), 1079-1092.
- Ahmed, O.M., Mohamed, H., Salem, W., Afifi, M.M., & Song, Y. (2021). Efficacy of Ethanolic Extract of *Syzygium aromaticum* in the Treatment of Multidrug-Resistant *Pseudomonas aeruginosa* Clinical Isolates Associated with Urinary Tract Infections. *Evidence-based Complementary and Alternative Medicine : eCAM*, 2021.. doi: 10.1155/2021/6612058.
- Alam, K., Farraj, D. A. A., Mah-E-Fatima, S., Yameen, M. A., Elshikh, M. S., et al. (2020). Anti-biofilm activity of plant derived extracts against infectious pathogen- *Pseudomonas aeruginosa* PAO1. *Journal of infection and public health*, 13(11), 1734–1741. <https://doi.org/10.1016/j.jiph.2020.07.007>.
- Aliyu, A.B., Koorbanally, N.A., Moodley, B., Singh, P., & Chenia, H.Y. (2016). Quorum sensing inhibitory potential and molecular docking studies of sesquiterpene lactones from *Vernonia blumeoides*. *Phytochemistry*, 126, 23-33
- Alonso, B., Fernández-Barat, L., Di Domenico, E. G., Marín, M., Cercenado, E., Merino, I., de Pablos, M., Muñoz, P., & Guembe, M. (2020). Characterization of the virulence of *Pseudomonas aeruginosa* strains causing ventilator-associated pneumonia. *BMC infectious diseases*, 20(1), 909. <https://doi.org/10.1186/s12879-020-05534-1>
- Blair, J. M., Webber, M. A., Baylay, A. J., Ogbolu, D. O., & Piddock, L. J. (2015). Molecular mechanisms of antibiotic resistance. *Nature reviews. Microbiology*, 13(1), 42–51. <https://doi.org/10.1038/nrmicro3380>.
- Cheesman, M. J., Ilanko, A., Blonk, B., & Cock, I. E. (2017). Developing New Antimicrobial Therapies: Are Synergistic Combinations of Plant Extracts/Compounds with Conventional Antibiotics the Solution?. *Pharmacognosy reviews*, 11(22), 57–72. https://doi.org/10.4103/phrev.phrev_21_17.
- Das, A., Das, M.C., Sandhu, P., Tribedi, P., De, U.C., et al. (2017). Antibiofilm activity of *Parkia javanica* against *Pseudomonas aeruginosa*: a study with fruit extract. *RSC advances*, 7(9), 5497-5513.
- Dincer, S., Uslu, F.M., & Delik, A. (2020). Antibiotic resistance in biofilm. In *Bacterial biofilms. IntechOpen*. 2020. <https://doi:10.5772/intechopen.92388>
- Doğan, Ş., Gökalsın, B., Şenkardeş, İ., Doğan, A., & Sesal, N. C. (2019). Anti-quorum sensing and anti-biofilm activities of *Hypericum perforatum* extracts against *Pseudomonas aeruginosa*. *Journal of ethnopharmacology*, 235, 293–300. <https://doi.org/10.1016/j.jep.2019.02.020>.
- Dzotam, J. K., & Kuete, V. (2017). Antibacterial and antibiotic-modifying activity of methanol extracts from six Cameroonian food plants against multidrug-resistant enteric bacteria. *BioMed Research International*. 1583510. doi: 10.1155/2017/1583510. Epub 2017 Aug 20.
- Elisha, I.L., Botha, F.S., McGaw, L.J., & Eloff, J.N. (2017). The antibacterial activity of extracts of nine plant species with good activity against *Escherichia coli* against five other bacteria and cytotoxicity of extracts. *BMC Complementary and Alternative Medicine*, 17(1), 1-10.
- Emam, M., Abdel-Haleem, D.R., Salem, M.M., Abdel-Hafez, L.J.M., Latif, R.R.A., et al. (2021). Phytochemical Profiling of *Lavandula coronopifolia* Poir. Aerial Parts Extract and Its Larvicidal, Antibacterial, and Antibiofilm Activity Against *Pseudomonas aeruginosa*. *Molecules*, 26, 1710. <https://doi.org/10.3390/molecules26061710>
- Fair, R. J., & Tor, Y. (2014). Antibiotics and bacterial resistance in the 21st century. *Perspectives in medicinal chemistry*, 6, 25–64. <https://doi.org/10.4137/PMC.S14459>.

- Famuyide, I.M., Aro, A.O., Fasina, F.O., Eloff, J.N., & McGaw, L.J. (2019). Antibacterial and antibiofilm activity of acetone leaf extracts of nine under-investigated south African *Eugenia* and *Syzygium* (Myrtaceae) species and their selectivity indices. *BMC Complementary and Alternative Medicine*, *19*(1), 1-13.
- González, J.F., Hahn, M.M., & Gunn, J.S. (2018). Chronic biofilm-based infections: skewing of the immune response. *Pathogens and Disease*, *76*(3):fty023. doi: 10.1093/femspd/fty023.
- Górniak, I., Bartoszewski, R., & Króliczewski, J. (2019). Comprehensive review of antimicrobial activities of plant flavonoids. *Phytochemistry Reviews*, *18*(1), 241-272.
- Guzzo, F., Scognamiglio, M., Fiorentino, A., Buommino, E., & D'Abrosca, B. (2020). Plant Derived Natural Products against *Pseudomonas aeruginosa* and *Staphylococcus aureus*: Antibiofilm Activity and Molecular Mechanisms. *Molecules (Basel, Switzerland)*, *25*(21), 5024. <https://doi.org/10.3390/molecules25215024>.
- Husain, F. M., Ahmad, I., Al-Thubiani, A. S., Abulreesh, H. H., AlHazza, I. M., & Aqil, F. (2017). Leaf Extracts of *Mangifera indica* L. Inhibit Quorum Sensing - Regulated Production of Virulence Factors and Biofilm in Test Bacteria. *Frontiers in microbiology*, *8*, 727. <https://doi.org/10.3389/fmicb.2017.00727>
- Issa, H.B., Phan, G., & Broutin, I. (2018). Functional mechanism of the efflux pumps transcription regulators from *Pseudomonas aeruginosa* based on 3D structures. *Frontiers in Molecular Biosciences*, *5*, 57.
- Jennings, L. K., Storek, K. M., Ledvina, H. E., Coulon, C., Marmont, L. S., et al. (2015). Pel is a cationic exopolysaccharide that cross-links extracellular DNA in the *Pseudomonas aeruginosa* biofilm matrix. *Proceedings of the National Academy of Sciences of the United States of America*, *112*(36), 11353-11358. <https://doi.org/10.1073/pnas.1503058112>.
- Kalia, M., Yadav, V. K., Singh, P. K., Sharma, D., Pandey, H., Narvi, S. S., & Agarwal, V. (2015). Effect of Cinnamon Oil on Quorum Sensing-Controlled Virulence Factors and Biofilm Formation in *Pseudomonas aeruginosa*. *PLoS one*, *10*(8), e0135495. <https://doi.org/10.1371/journal.pone.0135495>.
- Karuppiyah, P., & Rajaram, S. (2012). Antibacterial effect of *Allium sativum* cloves and *Zingiber officinale* rhizomes against multiple-drug resistant clinical pathogens. *Asian Pacific Journal of Tropical Biomedicine*, *2*(8), 597-601.
- Khare, T., Anand, U., Dey, A., Assaraf, Y. G., Chen, Z. S., Liu, Z., & Kumar, V. (2021). Exploring Phytochemicals for Combating Antibiotic Resistance in Microbial Pathogens. *Frontiers in pharmacology*, *12*, 720726. <https://doi.org/10.3389/fphar.2021.720726>.
- Labovska, S. (2021). *Pseudomonas aeruginosa* as a cause of nosocomial infections. In Das, T. (Ed.), *Pseudomonas aeruginosa - Biofilm Formation, Infections and Treatments*. *IntechOpen*. <https://doi.org/10.5772/intechopen.95908>
- Lin, J., & Cheng, J. (2019). Quorum sensing in *Pseudomonas aeruginosa* and its relationship to biofilm development. In *Introduction to Biofilm Engineering, ACS Symposium Series, Vol. 1323* (pp. 1-16). American Chemical Society, DOI: 10.1021/bk-2019-1323.ch001.
- Meng, L., Liu, H., Lan, T., Dong, L., Hu, H., Zhao, S., Zhang, Y., Zheng, N., & Wang, J. (2020). Antibiotic Resistance Patterns of *Pseudomonas* spp. Isolated From Raw Milk Revealed by Whole Genome Sequencing. *Frontiers in microbiology*, *11*, 1005. <https://doi.org/10.3389/fmicb.2020.01005>.
- Mishra, S., Gupta, A., Upadhye, V., Singh, S. C., Sinha, R. P., & Häder, D. P. (2023). Therapeutic Strategies against Biofilm Infections. *Life (Basel)*, *13*(1):172, doi: 10.3390/life13010172.
- Mombeshora, M., Chi, G.F., & Mukanganyama, S. (2021). Antibiofilm activity of extract and a compound isolated from *Triumfetta welwitschii* against *Pseudomonas aeruginosa*. *Biochemistry Research International*, *2021*. <https://doi.org/10.1155/2021/9946183>
- Mombeshora, M., & Mukanganyama, S. (2019). Antibacterial activities, proposed mode of action and cytotoxicity of leaf extracts from *Triumfetta welwitschii* against *Pseudomonas aeruginosa*. *BMC complementary and alternative medicine*, *19*(1), 315. <https://doi.org/10.1186/s12906-019-2713-3>
- Montero, M.M., Lopez Montesinos, I., Knobel, H. et al. (2020). Risk factors for mortality among patients with *Pseudomonas aeruginosa* bloodstream infections, *Journal of Clinical Medicine*, *9*(2), 514.
- Mostafa, A. A., Al-Askar, A. A., Almaary, K. S., Dawoud, T. M., Sholkamy, E. N., & Bakri, M. M. (2018). Antimicrobial activity of some plant extracts against bacterial strains causing food poisoning diseases. *Saudi journal of biological sciences*, *25*(2), 361-366. <https://doi.org/10.1016/j.sjbs.2017.02.004>.
- Munir, S., Shah, A. A., Shahid, M., & Manzoor, I. (2020). Quorum sensing interfering strategies and their implications in the management of biofilm-associated bacterial infections. *Brazilian Archives of Biology and Technology*, *63*, e20190555.

- Munita, J.M., & Arias, C.A. (2016). Mechanisms of antibiotic resistance. Virulence mechanisms of bacterial pathogens. *Microbiology Spectrum*, 4(2), 10.1128/microbiolspec.VMBF-0016-2015 481-511.
- Nazzaro, F., Fratianni, F., De Martino, L., Coppola, R., & De Feo, V. (2013). Effect of essential oils on pathogenic bacteria. *Pharmaceuticals (Basel, Switzerland)*, 6(12), 1451–1474. <https://doi.org/10.3390/ph6121451>
- Onivogui, G., Letsididi, R., Diaby, M., Wang, L., & Song, Y. (2016). Influence of extraction solvents on antioxidant and antimicrobial activities of the pulp and seed of *Anisophyllea laurina* R. Br. ex Sabine fruits. *Asian Pacific Journal of Tropical Biomedicine*, 6(1), 20-25.
- Owusu, E., Ahorlu, M. M., Afutu, E., Akumwena, A., & Asare, G. A. (2021). Antimicrobial Activity of Selected Medicinal Plants from a Sub-Saharan African Country against Bacterial Pathogens from Post-Operative Wound Infections. *Medical sciences (Basel, Switzerland)*, 9(2), 23. <https://doi.org/10.3390/medsci9020023>.
- Pachori, P., Gothwal, R., & Gandhi, P. (2019). Emergence of antibiotic resistance *Pseudomonas aeruginosa* in intensive care unit; a critical review. *Genes and Diseases*, 6(2), 109-119. doi: 10.1016/j.gendis.2019.04.001.
- Paczkowski, J. E., Mukherjee, S., McCready, A. R., Cong, J. P., Aquino, C. J., et al. (2017). Flavonoids Suppress *Pseudomonas aeruginosa* Virulence through Allosteric Inhibition of Quorum-sensing Receptors. *The Journal of biological chemistry*, 292(10), 4064–4076. <https://doi.org/10.1074/jbc.M116.770552>.
- Papaleo, S., Alvaro, A., Nodari, R., Panelli, S., Bitar, I., & Comandatore, F. (2022). The red thread between methylation and mutation in bacterial antibiotic resistance: How third-generation sequencing can help to unravel this relationship. *Frontiers in microbiology*, 13, 957901. <https://doi.org/10.3389/fmicb.2022.957901>
- Patel, V., & Patel, R. (2016). Plants as latent sources of new antimicrobials and resistance modifying agents against multi drug resistant (MDR) strains. *International Journal of Biochemistry and Molecular Biology*, 4, 27-42.
- Phitaktim, S., Chomnawang, M., Sirichaiwetchakoon, K., Dunkhunthod, B., Hobbs, G., & Eumkeb, G. (2016). Synergism and the mechanism of action of the combination of α -mangostin isolated from *Garcinia mangostana* L. and oxacillin against an oxacillin-resistant *Staphylococcus saprophyticus*. *BMC microbiology*, 16(1), 195. <https://doi.org/10.1186/s12866-016-0814-4>
- Rahman, M.M., Shahriar, M.R., Sultana, N., & Ishika, T. (2017). Antimicrobial activity of some medicinal plant extracts against Gram positive and 38 Gram negative bacteria in Bangladesh. *Asian Journal of Medical and Biological Research*, 3(4), 405-411.
- Ramírez-Estrada, S., Borgatta, B., & Rello, J. (2016). *Pseudomonas aeruginosa* ventilator-associated pneumonia management. *Infection and drug resistance*, 9, 7–18.
- Recio, R., Mancheño, M., Viedma, E., Villa, J., Orellana, M. Á., Lora-Tamayo, J., & Chaves, F. (2020). Predictors of Mortality in Bloodstream Infections Caused by *Pseudomonas aeruginosa* and Impact of Antimicrobial Resistance and Bacterial Virulence. *Antimicrobial agents and chemotherapy*, 64(2), e01759-19. <https://doi.org/10.1128/AAC.01759-19>.
- Reda, F.M., El-Zawahry, Y.A., & Omar, A.R. (2017). Synergistic effect of combined antibiotic and methanol extract of *Eucalyptus camaldulensis* leaf against *Staphylococcus aureus* and *Pseudomonas aeruginosa*. *International Journal of Applied Sciences and Biotechnology*, 5(4), 486-497.
- Roy, R., Tiwari, M., Donelli, G., & Tiwari, V. (2018). Strategies for combating bacterial biofilms: A focus on anti-biofilm agents and their mechanisms of action. *Virulence*, 9(1), 522–554. <https://doi.org/10.1080/21505594.2017.1313372>.
- Sagar, P. K., Sharma, P., & Singh, R. (2020). Antibacterial efficacy of different combinations of clove, eucalyptus, ginger, and selected antibiotics against clinical isolates of *Pseudomonas aeruginosa*. *Ayu*, 41(2), 123–129. https://doi.org/10.4103/ayu.AYU_101_19.
- Sakha, H., Hora, R., Shrestha, S., Acharya, S., Dhakal, D., Thapaliya, S., & Prajapati, K. (2018). Antimicrobial Activity of Ethanolic Extract of Medicinal Plants against Human Pathogenic Bacteria. *Tribhuvan University Journal of Microbiology*, 5, 1–6. <https://doi.org/10.3126/tujm.v5i0.22292>.
- Sambyal, S. S., Sharma, P., & Shrivastava, D. (2017). Anti-biofilm activity of selected plant essential oils against *Pseudomonas aeruginosa* and *Staphylococcus aureus*. *International Journal of Current Microbiology and Applied Sciences*, 6(3), 444-450.
- Seukep, A. J., Kuete, V., Nahar, L., Sarker, S. D., & Guo, M. (2020). Plant-derived secondary metabolites as the main source of efflux pump inhibitors and methods for identification. *Journal of pharmaceutical analysis*, 10(4), 277–290. <https://doi.org/10.1016/j.jppha.2019.11.002>.
- Shah, F., Hasan, Z., & Zaidi, K.U. (2017). Phytochemical constituents and synergistic activity of *Olea europaea* plant

- extracts against some human disease-causing species. *Journal of Microbiology and Experimentation*, 4(5), 00127.
- Shriram, V., Khare, T., Bhagwat, R., Shukla, R., & Kumar, V. (2018). Inhibiting Bacterial Drug Efflux Pumps via Phyto-Therapeutics to Combat Threatening Antimicrobial Resistance. *Frontiers in microbiology*, 9, 2990. <https://doi.org/10.3389/fmicb.2018.02990>
- Šikić Pogačar, M., Klančnik, A., Bucar, F., Langerholc, T., & Smole Možina, S. (2016). Anti-adhesion activity of thyme (*Thymus vulgaris* L.) extract, thyme post-distillation waste, and olive (*Olea europea* L.) leaf extract against *Campylobacter jejuni* on polystyrene and intestine epithelial cells. *Journal of the science of food and agriculture*, 96(8), 2723–2730. <https://doi.org/10.1002/jsfa.7391>.
- Sionov, R.V., & Steinberg, D. (2022). Targeting the Holy Triangle of Quorum Sensing, Biofilm Formation, and Antibiotic Resistance in Pathogenic Bacteria. *Microorganisms*, 10, 1239. <https://doi.org/10.3390/microorganisms10061239>
- Siriwong, S., Teethaisong, Y., Thumanu, K., Dunkhunthod, B., & Eumkeb, G. (2016). The synergy and mode of action of quercetin plus amoxicillin against amoxicillin-resistant *Staphylococcus epidermidis*. *BMC pharmacology & toxicology*, 17(1), 39. <https://doi.org/10.1186/s40360-016-0083-8>.
- Tahrioui, A., Duchesne, R., Bouffartigues, E., Rodrigues, S., Maillot, O., Tortuel, D., et al. (2019). Extracellular DNA release, quorum sensing, and PrrF1/F2 small RNAs are key players in *Pseudomonas aeruginosa* tobramycin-enhanced biofilm formation. *NPJ biofilms and microbiomes*, 5(1), 15. <https://doi.org/10.1038/s41522-019-0088-3>
- Taylor, P.K., Yeung, A.T., & Hancock, R. E. (2014). Antibiotic resistance in *Pseudomonas aeruginosa* biofilms: towards the development of novel anti-biofilm therapies. *Journal of Biotechnology*, 191, 121-130
- Ulloa-Urizar, G., Aguilar-Luis, M. A., De Lama-Odrýa, M.D.C., Camarena-Lizarzaburu, J., & del Valle Mendoza, J. (2015). Antibacterial activity of five Peruvian medicinal plants against *Pseudomonas aeruginosa*. *Asian Pacific Journal of Tropical Biomedicine*, 5(11), 928-931.
- Vandeputte, O. M., Kiendrebeogo, M., Rasamiravaka, T., Stévigny, C., Duez, P., et al. (2011). The flavanone naringenin reduces the production of quorum sensing-controlled virulence factors in *Pseudomonas aeruginosa* PAO1. *Microbiology (Reading, England)*, 157(Pt 7), 2120–2132. <https://doi.org/10.1099/mic.0.049338-0>.
- Vetrivel, A., Ramasamy, M., Vetrivel, P., Natchimuthu, S., Arunachalam, S., Kim, G.S., & Murugesan, R. (2021). *Pseudomonas aeruginosa* Biofilm Formation and Its Control. *Biologics*, 1(3), 312–336. <http://dx.doi.org/10.3390/biologics1030019>
- Walczak, M., Michalska-Sionkowska, M., Olkiewicz, D., Tarnawska, P., & Warzyńska, O. (2021). Potential of Carvacrol and Thymol in Reducing Biofilm Formation on Technical Surfaces. *Molecules (Basel, Switzerland)*, 26(9), 2723. <https://doi.org/10.3390/molecules26092723>.
- Yang, L., Ding, W., Xu, Y., Wu, D., Li, S., Chen, J., & Guo, B. (2016). New Insights into the Antibacterial Activity of Hydroxycoumarins against *Ralstonia solanacearum*. *Molecules (Basel, Switzerland)*, 21(4), 468. <https://doi.org/10.3390/molecules21040468>.
- Zeb, A., Ullah, I., Rehman, H.U., et al. (2017). Antibiotic susceptibility patterns of *Pseudomonas aeruginosa* in tertiary care hospital. *Journal of Entomology and Zoology Studies*, 20, 50.



Journal of Experimental Biology and Agricultural Sciences

<http://www.jebas.org>

ISSN No. 2320 – 8694

Assessment of Heavy Metal Content and Consumption Risks At Selected Paddy Field in Malaysia: A Review

Chew Jia Yin, Cheng Wan Hee*, Wong Ling Shing, Ong Ghim Hock, Geetha Subramaniam, Jayanthi Barasarathi

Faculty of Health and Life Sciences, INTI International University, Persiaran Perdana BBN, Putra Nilai, 71800 Nilai, Negeri Sembilan, Malaysia.

Received – June 05, 2023; Revision – August 03, 2023; Accepted – November 04, 2023

Available Online – November 30, 2023

DOI: [http://dx.doi.org/10.18006/2023.11\(5\).791.799](http://dx.doi.org/10.18006/2023.11(5).791.799)

KEYWORDS

Paddy

Copper

Cadmium

Lead

Health risk assessment

ABSTRACT

As the Malaysian population grows, there is a high demand for rice, the main staple food in this region. This has caused the overuse of agrochemicals that contain heavy metals and the utilization of contaminated groundwater to increase paddy yield, posing a risk to humans. This study reviewed the accumulated heavy metals in paddy fields of Malaysia's Selangor, Kedah and Sabah states and further calculated the consumption risks of rice grains from the selected areas. The study revealed that paddy soil in Ranau Valley (Sabah), Kota Marudu (Sabah) and Tanjung Karang (Selangor) showed presences of Cu and Cd in high concentration, respectively, creating higher potential to be uptake by paddy roots. These findings also revealed that Ranau Valley (Sabah) paddy grains contained high Cu and Cd concentrations, while Sabak Bernam (Selangor) contained high Pb concentrations. Further, a higher Cd concentration was reported from the Ranau Valley (Sabah), while the higher Pb concentrations were reported from the samples collected from Sabak Bernam (Selangor), Tanjung Karang (Selangor) and Kubang Pasu (Kedah). Based on the health risk indices calculation in this study, carcinogenic and non-carcinogenic health risks in all study areas except in Kubang Pasu (Kedah) and Langkawi (Kedah) are likely to occur due to Cu mining activities, ultrabasic soil contamination, utilization of contaminated groundwater and rock phosphate fertilizer and vehicular emission. Regular assessment of heavy metal content and consumption risks of paddy is essential to ensure the paddy field is free from contamination and will help protect the ecosystem and human health.

* Corresponding author

E-mail: wanhee.cheng@newinti.edu.my (Cheng Wan Hee)

Peer review under responsibility of Journal of Experimental Biology and Agricultural Sciences.

Production and Hosting by Horizon Publisher India [HPI]
(<http://www.horizonpublisherindia.in/>).
All rights reserved.

All the articles published by [Journal of Experimental Biology and Agricultural Sciences](#) are licensed under a [Creative Commons Attribution-NonCommercial 4.0 International License](#) Based on a work at www.jebas.org.



1 Introduction

Apart from being the staple food for Malaysians, paddy serves as a primary income source for farmers and agricultural workers in Malaysia (Omar et al. 2019; Firdaus et al. 2020). An estimated agricultural land in Malaysia was 645,000 ha, used to cultivate the paddy (Akinbile et al. 2011). Since 2018, more and more lands have been developed for paddy farming in Malaysia to meet the country's high rice consumption demand (Malaysia Population 1950-2021 2021). This has led to farmers using excessive agrochemicals such as fertilizers, insecticides, and herbicides to manage weeds and pests while also ensuring higher yield of paddy cultivation (Rudzi et al. 2018; Engwa et al. 2019; Alengebawy et al. 2021).

Agrochemicals contain toxic heavy metals that bioaccumulate to concentrations higher than permissible (Ali et al. 2018). According to Rudzi et al. (2018), overuse of agrochemicals is one of the primary causes of limiting high rice production as it makes paddy unsafe for human consumption. Due to the heavy metals' non-biodegradable characteristics, excessive use of agrochemicals, including lead (Pb), cadmium (Cd), and copper (Cu), causes environmental pollution and, more seriously, contamination of the paddy soil and grains themselves (Rudzi et al. 2018; Irshad et al. 2023). Using tainted irrigation water and soil for rice production is a problem since they contain heavy metals that can be transferred from the roots of the paddy into the grains (Akinbile et al. 2011).

Despite the grave consequences of heavy metals released from agrochemicals to humans and the environment, the health risk assessments of paddy in Malaysia are not well documented.

Further studies on the heavy metals contained in paddy are crucial as rice production expands and intensifies. Therefore, this review aims to investigate the accumulation levels of Cu, Cd, and Pb in the soils of paddy fields and the risk of rice grains via ingestion in Selangor, Kedah, and Sabah.

2 Review of heavy metals and risk assessment in paddy fields at the selected states

Data obtained from the Selangor, Kedah, and Sabah state paddy fields were chosen for this study because they are Malaysia's leading rice-producing states. These sites are all situated in different parts of Malaysia: Selangor (central region) and Kedah (northern region) are both situated on Peninsular Malaysia's western coast, while Sabah is located in East Malaysia (Alias et al. 2014; Zulkafflee et al. 2019). This article is based on the compilation of data on the mean concentrations of Cu, Cd and Pb from soil and grains samples collected from Sabak Bernam (Selangor), Tanjung Karang (Selangor), Langkawi (Kedah), Kubang Pasu (Kedah), Kota Marudu (Sabah) and Ranau Valley (Sabah). Furthermore, Hazard Quotients (HQ) and Lifetime Cancer Risk (LCR) of rice grains calculated based on the data taken from reported studies in these areas were performed.

2.1 Concentrations of Cu, Cd, and Pb in Soil Samples

The mean levels of Cu, Cd, and Pb (mg/kg) in paddy soil collected from Sabak Bernam, Tanjung Karang, Langkawi, Kubang Pasu, Kota Marudu, and Ranau Valley are displayed in Table 1. Based on compiled data (Table 1), the highest levels of Cu and Cd (154.83 and 0.776 mg/kg, respectively) were found in paddy soil

Table 1 The mean concentration data of Cu, Cd, and Pb (mg/kg) in paddy soil samples collected from the selected study area

Study Areas	Mean concentration (mg/kg)			References
	Cu	Cd	Pb	
SabakBernam (Selangor)	0.451	0.012	0.984	Zulkafflee et al. 2019
Tanjung Karang (Selangor)	0.538	0.014	1.088	Zulkafflee et al. 2019
	3.87	0.06	6.64	Rudzi et al. 2018
Langkawi (Kedah)	0.178	0.014	0.380	Jusoh et al. 2013; Zakaria et al. 2021
Kubang Pasu (Kedah)	0.331	0.117	0.571	Zulkafflee et al. 2021
	-	0.20	3.72	Looi et al. 2014; Zakaria et al. 2021
Kota Marudu (Sabah)	ND	0.776	ND	Yap et al. 2009; Zakaria et al. 2021
Ranau Valley (Sabah)	154.83	0.45	-	Aziz et al. 2015; Zakaria et al. 2021
Comparison with standard data				
GB15618-2018	50	0.30	80	Soil Environmental Quality Standards (GB 15618-2018), 2018)
European Standards Agriculture Soils	140	3	300	EU Soil Policy 2018

*ND: Not Detected; *GB15618-2018: Soil environmental quality: Risk control standard for soil contamination on agricultural land.

*Significant level for one sample *T*-test at $p < 0.05$.

samples taken from Ranau Valley in Sabah and Kota Marudu in Sabah (Yap et al. 2009; Aziz et al. 2015; Rudzi et al. 2018; Zakaria et al. 2021). Pb was reported to have the highest concentration of 6.64 mg/kg in paddy soil collected from Tanjung Karang, Selangor (Rudzi et al. 2018).

Soil analysis from the paddy field of Ranau Valley in Sabah demonstrates a high concentration of Cu of 154.83 mg/kg, which exceeded the permissible limit, and this can be associated with the ultra-basic soil pollution and absorption by organic matter and clay minerals in the soil (Aziz et al. 2015). It was reported that some metals were enriched through precipitation in ultrabasic soil and positively correlated with Cu (Aziz et al. 2015).

Precipitation immobilizes the Cu in the soil, raising the concentration of Cu present (Yoon et al. 2019). Furthermore, the sampling site is close to the ex-Mamut Cu Mine (MCM), which also releases Cu into the environment during smelting, possibly flowing through neighbouring paddy soil (Lo and Saibeh 2013; Kiprof 2021). MCM mining activities generate large amounts of wastewater contaminating the groundwater in Ranau Valley (Wuana and Okieimen 2011; Masindi and Meudi 2018). Runoff and using contaminated groundwater for paddy cultivation can result in high Cu concentrations in the sediment (Lo and Saibeh 2013). At minute levels, Cu promotes plant growth; therefore, it is necessary to maintain crop yield. On the contrary, excessive Cu buildup and leaching from agricultural soils might lead to groundwater pollution, causing harm to all organisms via the food chain (Stanislawska and Korzeniowska 2018; Aziz et al., 2023). Heavy metals contaminated soils are likely to be directly absorbed by paddy roots and eventually translocated to edible plant parts, endangering rice consumers (Aziz et al. 2015).

The fertilizer utilized in the paddy fields in Kota Marudu and Tanjung Karang is mainly in the form of rock phosphate, which contains Cd and has a solubility of 65% (Yap et al. 2009; Rudzi et al. 2018; Teles 2020; Zakaria et al. 2021). It shows that only 65% of the total rock phosphate is accessible for paddy, while the remaining 35% remains in the soil, resulting in elevated levels of Cd (Teles 2020; Suci et al. 2022). The Cd concentrations in paddy soil were higher in Kota Marudu (Sabah) and Ranau Valley (Sabah), which suggests that the potential for Cd to be absorbed by rice roots in these regions is higher than the suggested one (Payus et al. 2015).

Further, Cd concentrations in Ranau Valley and Kota Marudu, Sabah are 0.45 mg/kg and 0.776 mg/kg, respectively and found to be exceeding the maximum allowable concentration suggested by Soil Environmental Quality Standards and European Standards Agriculture Soils (EU Soil Policy 2018; Soil Environmental Quality Standards (GB 15618-2018) 2018). This suggests that the soil samples from Kota Marudu and Ranau Valley may not be

suited for paddy agriculture since excessive levels of Cd tend to bio-accumulate in paddy plant roots and translocate into paddy grains, thereby reducing the overall paddy yield and detrimental to human health (Satpathy et al. 2014). Various causes could affect Cd concentrations, such as industrial activities, air emissions, and organic sediment deposition (Kahn et al. 1992). It is also evident that, based on in-depth analyses of numerous fertilizer products, some micronutrient and phosphate fertilizers contain elevated Cd compared to others. The public's main concern is the persistent nature of Cd and its bioaccumulation in the food chain (Gao et al. 2022). The effect of Cd on the human body is kidney disease and can potentially affect the pulmonary, cardiovascular, and musculoskeletal systems (Munir et al. 2023). The 'itai-itai' disease is also associated with Cd toxicity in rice grown on industrial waste-contaminated soils (Nishijo 2017; Zulkafflee et al. 2019). Cd uptake and bioaccumulation in crops are influenced by soil factors such as pH, salinity, fertilizers, level of organic matter, and species of crops (Tang et al. 2023). The application of fertilizer, therefore, could increase the risk of Cd being transferred to the food chain (Robert 2014).

2.2 Concentrations of Cu, Cd and Pb in paddy grain samples

The mean concentrations of Cu, Cd and Pb (mg/kg) in the paddy grain from Sabak Bernam, Tanjung Karang, Langkawi, Kubang Pasu, Kota Marudu and Ranau Valley paddy field are tabulated in Table 2.

According to Aziz et al. (2015) and Zakaria et al. (2021), paddy grain samples taken from Ranau Valley (Sabah) has the highest concentrations of Cu (2.61 mg/kg) and Cd (0.54 mg/kg), which surpassed the permissible limit of Malaysian Food Regulations 1985 and FAO/WHO CAC 1984. This is due to a greater tendency for Cu and Cd in the soil to be taken up by the paddy roots and translocated into the grains (Chibuike and Obiora 2014; Yan et al. 2020). It is also evident from Table 1 that the soil samples analysis of Ranau Valley indicated a high concentration of Cu. This shows strong Cu translocation from the paddy soil to the grain sample. The ability of different parts of crop plants to bioaccumulate and translocate heavy metals among plants varies according to the species (Zulkafflee et al. 2021). Genotypic variation and organic soil material are other factors that may affect the metals in the crops (Liu et al. 2015). This is something to be concerned about, whereby the ingestion of metal-contaminated crops could cause detrimental effects to consumers.

According to Zulkafflee et al. (2019), paddy grain samples from Sabak Bernam (Selangor) had the highest Pb concentration (2.245 mg/kg). This might be due to the proximity of sampling sites to Route 5, considered a busy route in Malaysia (InventoriRangkaian Jalan Utama Persekutuan Semanjung Malaysia, 2021). The increased Pb concentration in paddy grains is a result of the

Table 2 Mean concentrations data of the Cu, Cd and Pb (mg/kg) of grains collected from the selected study area

Study Areas	Mean concentration (mg/kg)			References
	Cu	Cd	Pb	
SabakBernam (Selangor)	1.166	0.026	2.245	Zulkafflee et al. 2019
Tanjung Karang (Selangor)	1.477	0.324	0.406	Zulkafflee et al. 2019
Langkawi (Kedah)	0.058	0.029	0.069	Jusoh et al. 2013; Zakaria et al. 2021
Kubang Pasu (Kedah)	0.125	0.003	0.043	Zulkafflee et al. 2021
	-	0.060	1.05	Looi et al. 2014; Zakaria et al. 2021
Kota Marudu (Sabah)	0.312	0.180	ND	Yap et al. 2009; Zakaria et al. 2021
Ranau Valley (Sabah)	2.61	0.54	-	Aziz et al. 2015; Zakaria et al. 2021
Comparison with the standard value				
Malaysian Food Regulations 1985	30	1.0	2.0	Malaysia Food Regulations 1985, 1985
FAO/WHO CAC 1984	10	0.4	0.2	FAO/WHO 2011

*ND: Not Detected; *Significant level for one sample *T*-testat $p < 0.05$.

disclosure to exhaust fumes released by motor vehicles due to numerous inhabitants and visitor's heavy use of Route 5 (França et al. 2017; Rai et al. 2019; Inventori Rangkaian Jalan Utama Persekutuan Semanjung Malaysia 2021).

Looi et al. (2014) and Zakaria et al. (2021) found elevated levels of Cd and Pb (0.01 and 0.21 mg/kg, respectively) in paddy grain samples in Kubang Pasu (Kedah) than the value (0.003 and 0.043 mg/kg, respectively) reported by Zulkafflee et al. (2021), it denoting that high concentrations of Cd and Pb in sediment are more likely to be uptaken by paddy roots and translocated into the grains. This will increase the risk that consumers may experience health concerns like bone malformation, liver damage, and pancreatic cancer (Eske 2020; Guo et al. 2020; TатаhMentan et al. 2020; Rai et al. 2019).

Malaysian Food Regulations 1985 and FAO/WHO CAC 1984 reported that the paddy grains' Cd concentration in Ranau Valley, Sabah (0.54 mg/kg) and Pb concentration in Sabak Bernam, Selangor (2.245 mg/kg), Tanjung Karang, Selangor (0.406 mg/kg) and Kubang Pasu, Kedah (1.05 mg/kg) surpassed the maximum permissible level. Paddy grains containing Cd and Pb concentrations over the acceptable limits are not safe for ingestion by humans since they may cause kidney dysfunction, bone pain, and lung cancer when consumed in large quantities (Eske 2020; Genchi et al. 2020; TатаhMentan et al. 2020; Hasan et al. 2022).

2.3 Hazard Quotient Values of Cu, Cd and Pb in Adults

The paddy grain consumption risks can be accessed through hazard quotients (HQ)(Zheng et al. 2020). Here, the assessment can be divided into different degrees of risk. Table 3 shows the adult's Hazard Quotient (HQ) values for Cu, Cd and Pb calculated based

on reported data in Table 2 by using the formula listed below (Calculating Exposure Doses 2005; IRIS 2011; Fan et al. 2017; Zulkafflee et al. 2019):

$$HQ = D \text{ (mg/kg-day)} / \text{RfD (mg/kg-day)}$$

$$HQ = A \times \frac{I \times E \times D}{W \times T} / \text{RfD}$$

Where

D = Average daily intake

RfD = Reference dose

A = Exposure point concentration

I = Intake rate of contaminated medium, 0.425

E = Exposure factor, 74 days per year

D = Exposure duration, 1 years

W=Body Weight, 70 kg

T=Averaging time, 74 x 1 year

RfD used are Cd = 0.001, Cu = 0.040, and Pb = 0.004(IRIS 2011).

Based on Table 3, all HQ values of Cu exposure for adults were below 1 (HQ <1) and did not show any non-carcinogenic health risk caused by Cu, such as kidney failure, liver damage and hemolysis in all study areas (Eske 2020; Moussiegt et al. 2020). HQ values of Cd exposure for adults were below 1 (HQ <1) except for the HQ values in Tanjung Karang, Selangor (1.967), Kota Marudu, Sabah (1.093) and Ranau Valley, Sabah (3.279). These Cd levels could cause potential non-carcinogenic health risks, for

Table 3 Hazard Quotient (HQ) values of Cu, Cd and Pb in adults calculated based on the data taken from the reported studies and using the formula listed above

Areas of Study	HQ values		
	Cu	Cd	Pb
SabakBernam (Selangor)	0.177	0.158	3.407
Tanjung Karang (Selangor)	0.224	1.967	0.616
Langkawi (Kedah)	0.009	0.176	0.105
Kubang Pasu (Kedah)	0.019	0.018	0.065
Kota Marudu (Sabah)	0.047	1.093	ND
Ranau Valley (Sabah)	0.396	3.279	-

*ND: Not Detected

instance, cardiovascular disease, kidney dysfunction and severe bone pain (Nishijo 2017; Rahimzadeh et al. 2017; Zulkafflee et al. 2019) for inhabitants in these areas. All the HQ values of Pb exposure for adults were below 1 (HQ <1) except for the HQ value for Sabak Bernam, Selangor (3.407). This indicates non-carcinogenic health effects caused by Pb, for instance, bone malformation, nervous system damage and high blood pressure (Chari 2016; Health Problems Caused by Lead 2018), which consumers would likely experience in Sabak Bernam, Selangor.

2.4 Lifetime Cancer Risk Values of Cadmium and Lead in Adults

The adult's Lifetime Cancer Risk (LCR) values for Cd and Pb are calculated based on the data taken from the reported studies in Table 2 by using the formula listed below, and the value is tabulated in Table 4 (Calculating Exposure Doses 2005; RAIS 2011; Fan et al. 2017; Zulkafflee et al. 2019):

$$\text{LCR} = \text{DS (mg/kg-day)} \times \text{CSF (mg/kg-day)}^{-1}$$

$$\text{LCR} = \left(A \times \frac{I \times E \times D}{W \times AT} \right) \times \text{CSF}$$

$$\text{LCR} = \left(0.026 \times \frac{0.425 \times 74 \times 1}{70 \times 74 \times 1} \right) \times 0.38$$

$$\text{LCR} = 6.00 \times 10^{-5}$$

Where

DS = Average Daily Dose (mg/kg/day)

CSF = Cancer Slope Factor

This study did not determine the LCR values of Cu as, according to RAIS (2011), Cu's cancer slope factor (CSF) values were inaccessible, and Cu was regarded as non a cancer-causing element.

Based on Table 4, all LCR values of Cd exposure for adults were less than 1×10^{-4} (LCR < 1×10^{-4}) except for the LCR values of Cd

in Tanjung Karang, Selangor (7.48×10^{-4}), Kota Marudu, Sabah (4.15×10^{-4}) and Ranau Valley, Sabah (1.25×10^{-3}). This indicates that among every 10,000 adult individuals in Tanjung Karang (Selangor), Kota Marudu (Sabah) and Ranau Valley (Sabah), there is a probability of 4 to 13 individuals who may develop carcinogenic-related health risks caused by Cd exposure such as lung, pancreas and breast cancers over a period 74 years (Rahimzadeh et al. 2017; Genchi et al. 2020; Tatah Mentan et al. 2020). Intake of Cd-contaminated rice may pose a risk of contracting the itai-itai disease. During the 1950s, ingesting cadmium-contaminated rice (itai-itai disease) impacted humans' well-being (Nishijo 2017). Itai-itai disease complications are associated with osteomalacia and severe bone pain, as well as renal tubular failure (Shi et al. 2020).

All adult's LCR values of Pb exposure were below 1×10^{-4} (LCR < 1×10^{-4}) except for the LCR value of Pb in Sabak Bernam, Selangor (1.16×10^{-4}). This indicates that among every 10,000 adult individuals in SabakBernam, Selangor, there is a probability of 1 individual who may develop carcinogenic-related health risks caused by Pb exposure, such as brain, stomach and lung cancers over 74 years (Lead Poisoning and Health 2019; Rai et al. 2019).

2.5 Determination of Safety Consumption of Paddy

According to the findings, paddy from Langkawi and Kubang Pasu in Kedah is safe to eat because the HQ values of Cu (0.009 and 0.019), Cd (0.176 and 0.018) and Pb (0.105 and 0.065) are less than 1. The LCR values for Cd (6.69×10^{-5} and 6.92×10^{-6}) and Pb (3.56×10^{-6} and 2.22×10^{-6}) are less than 1×10^{-4} , indicating that serious health risks like cardiac failure, kidneys dysfunction and pancreas cancer would not occur due to exposure to these chemicals or lack thereof (Chari 2016; Genchi et al. 2020; Moussiagt et al. 2020). These data are in line with the studies reported in Iranshahr, Iran (Djahed et al. 2018); Zhejiang Province, China (Huang et al. 2013); Enugu, Nigeria and Omar (Ezeofor et al. 2019); and Yan and Pendang, Kedah (Omar et al., 2015).

Table 4 The Lifetime Cancer Risk (LCR) values of Cd and Pb in adults were calculated based on the data taken from the reported studies by using the formula listed above

Areas of Study	LCR values	
	Cadmium (Cd)	Lead (Pb)
Sabak Bernam (Selangor)	6.00×10^{-5}	1.16×10^{-4}
Tanjung Karang (Selangor)	7.48×10^{-4}	2.10×10^{-5}
Langkawi (Kedah)	6.69×10^{-5}	3.56×10^{-6}
Kubang Pasu (Kedah)	6.92×10^{-6}	2.22×10^{-6}
Kota Marudu (Sabah)	4.15×10^{-4}	ND
Ranau Valley (Sabah)	1.25×10^{-3}	-

*ND: Not Detected

It appears to be unsafe to consume paddy from SabakBernam (Selangor), Tanjung Karang (Selangor), Kota Marudu (Sabah), and Ranau Valley (Sabah) as the HQ values of Cd (1.093 to 3.279) and Pb (3.407) are more than 1. The LCR values of Cd (4.15×10^{-4} to 1.25×10^{-3}) and Pb (1.16×10^{-4}) are more than 1×10^{-4} , indicating that severe health risks such as liver damage, bone malformation and lung cancer might occur (Rai et al. 2019; Eske 2020; TатаhMentan et al. 2020). These data are in line with those reported in Hunan Province, China (Zeng et al. 2015), the Pearl River Delta of China (Zheng et al. 2020), Enugu, Nigeria (Ihedioha et al. 2016; Ezeofor et al. 2019), and Iran (Fakhri et al. 2018).

Conclusion

Based on information from published studies, elevated concentrations of Cu and Cd in the paddy soil in Ranau Valley and Kota Marudu increased the possibility of paddy roots absorbing these metals. Cu and Cd levels in Ranau Valley and Cd levels in Kota Marudu exceeded the maximum allowable concentration suggested by Soil Environmental Quality Standards and European Agricultural Standards Soils. The paddy grains' Cd concentration in Ranau Valley and the Pb concentrations in Sabak Bernam, Tanjung Karang, and Kubang Pasu exceeded the maximum allowable level recommended by the Malaysian Food Regulations of 1985 and the FAO/WHO CAC 1984.

Based on the calculated HQ and LCR values of Cu, Cd and Pb, paddy from Langkawi and Kubang Pasu were safe for consumption. This study also indicated that the paddy grain taken from Sabak Bernam, Tanjung Karang, Kota Marudu and Ranau Valley was not safe for consumption based on the HQ and LCR value analysis. From this review, we found that the paddy is not safe for consumption, and it is important to carry out a monitoring program on the presence of Cu, Cd and Pb in paddy soils and grains. These findings also provide valuable insights for evaluating future impacts of environmental pollution towards rice production and potential health risks from Cu, Cd and Pb. Regular assessment

of paddy consumption risks should be done to protect the ecosystem and human health.

Acknowledgements

The authors would like to acknowledge the funding of this research article provided by the INTI International University Research Grant Scheme (INTI-FHLS-02-01-2021).

References

- Akinbile, C. O., El-Latif, K. M. A., Abdullah, R., & Yusoff, M. S. (2011). Rice Production and Water use Efficiency for Self-Sufficiency in Malaysia: A Review. *Trends in Applied Sciences Research*, 6, 1127-1140.
- Alengebawy, A., Abdelkhalek, S. T., Qureshi, S. R., & Wang, M. (2021). Heavy Metals and Pesticides Toxicity in Agricultural Soil and Plants: Ecological Risks and Human Health Implications. *Toxics*, 9(3), 24.
- Ali, I., Khan, M. J., Khan, M., Deeba, F., Hussain, H., Abbas, M., & Khan, M. D. (2018). Impact of Pollutants on Paddy Soil and Crop Quality. *Environmental Pollution of Paddy Soils*, 53, 125-137. https://doi.org/10.1007/978-3-319-93671-0_8125-137
- Alias, H., Surin, J., Mahmud, R., Shafie, A., Zin, J. M., Mohamad Nor, M., Ibrahim, A. S., & Rundi, C. (2014). Spatial distribution of malaria in Peninsular Malaysia from 2000 to 2009. *Parasites & Vectors*, 7(1), 186.
- Hasan, G. M. M. A., Das, A. K., & Satter, M. A. (2022). Accumulation of Heavy Metals in Rice (*Oryza sativa*. L) Grains Cultivated in Three Major Industrial Areas of Bangladesh. *Journal of environmental and public health*, 2022, 1836597. <https://doi.org/10.1155/2022/1836597>.
- Appendix G: Calculating Exposure Doses. (2005). Retrieved from Agency for Toxic Substances and Disease Registry. Retrieved from <https://www.atsdr.cdc.gov/hac/phamannual/appg.html>

- Aziz, R. A., Rahim, S. A., Sahid, I., Idris, W. M. R., & Bhuiyan, M. A. R. (2015). Determination of Heavy Metals Uptake in Soil and Paddy Plants. *American-Eurasian Journal of Agriculture and Environment Sciences*, *15*(2), 161-164.
- Aziz, R. A., Yiwen, M., Saleh, M., Salleh, M.N., Gopinath, S.C.B., Giap, S.G.E., Chinni, S.V., & Gobinath, R. (2023). Bioaccumulation and Translocation of Heavy Metals in Paddy (*Oryza sativa* L.) and Soil in Different Land Use Practices. *Sustainability*, *15*, 13426. <https://doi.org/10.3390/su151813426>
- Chari, S. (2016). *Lead Poisoning*. Retrieved from MedIndia: <https://www.medindia.net/patients/patientinfo/lead-poisoning.htm>.
- Chibuikwe, G. U., & Obiora, S. C. (2014). Heavy Metal Polluted Soils: Effect on Plants and Bioremediation Methods. *Applied and Environmental Soil Science*, *2014*, Article ID 752708. <https://doi.org/10.1155/2014/752708>.
- Djahed, B., Taghavi, M., Farzadkia, M., Norzaee, S., & Miri, M. (2018). Stochastic exposure and health risk assessment of rice contamination to the heavy metals in the market of Iranshahr, Iran. *Food and Chemical Toxicology*, *115*, 405-412.
- Engwa, G. A., Ferdinand, P. U., Nwalo, F. N., & Unachukwu, M. N. (2019). Mechanism and health effects of heavy metal toxicity in humans. *Poisoning in the modern world-new tricks for an old dog?*. <https://doi.org/10.5772/intechopen.82511>
- Eske, J. (2020). *Copper toxicity: Symptoms and treatment*. Retrieved from Medical News Today: <https://www.medicalnewstoday.com/articles/copper-toxicity>.
- EU Soil Policy (2018). Retrieved from European Commission on Environment: https://ec.europa.eu/environment/soil/index_en.htm
- Ezeofor, C. C., Ihedioha, J. N., Ujam, O. T., Ekere, N. R., & Nwuche, C. O. (2019). Human health risk assessment of potential toxic elements in paddy soil and rice (*Oryza sativa*) from Ugbawka fields, Enugu, Nigeria. *Open Chemistry*, *17*(1), 1050-1060.
- Fakhri, Y., Bjørklund, G., Bandpei, A. M., Chirumbolo, S., Keramati, H., et al. (2018). Concentrations of arsenic and lead in rice (*Oryza sativa* L.) in Iran: A systematic review and carcinogenic risk assessment. *Food and Chemical Toxicology*, *113*, 267-277.
- Fan, Y., Zhu, T., Li, M., He, J., & Huang, R. (2017). Heavy Metal Contamination in Soil and Brown Rice and Human Health Risk Assessment near Three Mining Areas in Central China. *Journal of Healthcare Engineering*, *2017*, 4124302. <https://doi.org/10.1155/2017/4124302>
- FAO/WHO (1984) List of Maximum Levels Recommended for Contaminants by the Joint FAO/ WHO Codex Alimentarius Commission. Second Series. CAC/FAL, Rome, 3, 1-8.
- FAO/WHO. (2011). *Evaluation of Certain Food Additives and Contaminants*. Retrieved from WHO Technical Report Series 960: http://apps.who.int/iris/bitstream/handle/10665/44515/WHO_TRS_960_eng.pdf?sequence=1
- Firdaus, R., Tan, M. L., Rahmat, S. R., & Gunaratne, M. S. (2020). Paddy, rice and food security in Malaysia: A review of climate change impacts. *Cogent Social Sciences*, *6*(1). <https://doi.org/10.1080/23311886.2020.1818373>
- França, F. C. S. S., Albuquerq, A. M. A., Almeida, A. C., Silveira, P. B., Filho, C. A., Hazin, C. A., & Honorato, E. V. (2017). Heavy metals deposited in the culture of lettuce (*Lactuca sativa* L.) by the influence of vehicular traffic in Pernambuco, Brazil. *Food Chemistry*, *215*, 171-176. <https://doi.org/10.1016/j.foodchem.2016.07.168>
- Gao, Y., Duan, Z., Zhang, L., Sun, D., & Li, X. (2022). The Status and Research Progress of Cadmium Pollution in Rice- (*Oryza sativa* L.) and Wheat- (*Triticum aestivum* L.) Cropping Systems in China: A Critical Review. *Toxics*, *10*(12), 794. <https://doi.org/10.3390/toxics10120794>
- Genchi, G., Sinicropi, M. S., Lauria, G., Carocci, A., & Catalano, A. (2020). The Effects of Cadmium Toxicity. *International Journal of Environmental Research and Public Health*, *17*(11), 3782. <https://doi.org/10.3390/ijerph17113782>
- Guo, B., Hong, C., Tong, W., Xu, M., Huang, C., Yin, H., Lin, Y., & Fu, Q. (2020). Health risk assessment of heavy metal pollution in a soil-rice system: a case study in the Jin-Qu Basin of China. *Scientific Reports*, *10*, 11490. <https://doi.org/10.1038/s41598-020-68295-6>
- Health Problems Caused by Lead. (2018). Retrieved from Centers for Disease Control and Prevention: <https://www.cdc.gov/niosh/topics/lead/health.html>
- Huang, Z., Pan, X. D., Wu, P. G., Han, J. L., & Chen, Q. (2013). Health Risk Assessment of Heavy Metals in Rice to the Population in Zhejiang, China. *PLoS One*, *8*(9), e75007. <https://doi.org/10.1371/journal.pone.0075007>
- Ihedioha, J. N., Ujam, O. T., Nwuche, C. O., Ekere, N. R., & Chime, C. C. (2016). Assessment of heavy metal contamination of rice grains (*Oryza sativa*) and soil from Ada field, Enugu, Nigeria: Estimating the human health risk. *Human and Ecological Risk Assessment*, *22*, 1665-1677.

- Integrated Risk Information System (IRIS). (2011). Retrieved from US EPA: <https://www.epa.gov/iris>
- Inventori Rangkaian Jalan Utama Persekutuan Semanjung Malaysia. (2021). Retrieved from Kementerian Kerja Raya: <https://www.kkr.gov.my/ms/node/2431>
- Irshad, M. K., Zhu, S., Javed, W., Lee, J. C., Mahmood, A., Lee, S. S., Shang, J., Albasher, G., Ali, A. (2023). Risk assessment of toxic and hazardous metals in paddy agroecosystem by biochar-for bio-membrane applications. *Chemosphere*, 340, 139719.
- Jusoh, K., Ramlee, A. R., Jamil, H., Ismail, Z., & Ismail, B. S. (2013). Heavy metal content of paddy plants in Langkawi, Kedah, Malaysia school of environmental and natural resource sciences, faculty of science and technology. *Australian Journal of Basic and Applied Sciences*, 7(2), 123–127.
- Kahn, A. H., Nolting, R. F., Van der Gaast, S. J., & Van Raaphorst, W. (1992). Trace element geochemistry at the sediment-water interface in the North Sea and the Western Wadden Sea. *NIOZ-RAPPORT*, 10 (1), 18. Retrieved from <https://www.vliz.be/imisdocs/publications/263202.pdf>.
- Kiprop, J. (2021). *What Are The Sources And Effects Of Copper Pollution In The Environment?* Retrieved from WorldAtlas: <https://www.worldatlas.com/articles/what-are-the-sources-and-effects-of-copper-pollution-in-the-environment.html>
- Lead Poisoning and Health. (2019). Retrieved from World Health Organization: Retrieved from <https://www.who.int/news-room/fact-sheets/detail/lead-poisoning-and-health>
- Liu, M., Yang, Y., Yun, X., Zhang, M., & Wang, J. (2015). Concentrations, distribution, sources, and ecological risk assessment of heavy metals in agricultural topsoil of the Three Gorges Dam region, China. *Environmental Monitoring and Assessment*, 187, 1-11.
- Lo, V. Y., & Saibeh, K. (2013). Phytoremediation using *Typha angustifolia* L. for Mine Water Effluence Treatment: Case Study of Ex-Mamut Copper Mine, Ranau, Sabah. *Borneo Science*, 33, 16-22.
- Looi, L. J., Aris, A. Z., Lim, W. Y., & Haris, H. (2014). Bioconcentration and Translocation Efficiency of Metals in Paddy (*Oryza sativa*): A Case Study from Alor Setar, Kedah, Malaysia. *Sains Malaysiana*, 43(4), 521–528.
- Malaysia Food Regulations 1985. (1985). Retrieved from https://extranet.who.int/nutrition/gina/sites/default/filesstore/MYS%201985%20Food%20Regulations_0.pdf
- Malaysia Population 1950-2021. (2021). Retrieved from Macrotrends: <https://www.macrotrends.net/countries/MYS/malaysia/population>
- Masindi, V., & Meudi, K. L. (2018). Environmental Contamination by Heavy Metals. In Saleh, H.E.M., & Aglan, R.F. (Eds.) *Heavy Metals*. Intechopen publication <https://doi.org/10.5772/intechopen.76082>.
- Moussiegt, A., Ferreira, J., Aboab, J., & Silva, D. (2020). She Has The Blues: An Unusual Case of Copper Sulphate Intoxication. *European Journal of Case Reports in Internal Medicine*,7(2). https://doi.org/10.12890/2020_001394
- Munir, R., Jan, M., Muhammad, S., Afzal, M., Jan, N., Yasin, M. U., Munir, I., et al. (2023). Detrimental effects of Cd and temperature on rice and functions of microbial community in paddy soils. *Environmental Pollution*, 324(121371), 0269-7491. <https://doi.org/10.1016/j.envpol.2023.121371>
- Nishijo, M., Nakagawa, H., Suwazono, Y., Nogawa, K., & Kido, T. (2017). Causes of death in patients with Itai-itai disease suffering from severe chronic cadmium poisoning: a nested case-control analysis of a follow-up study in Japan. *BMJ Open*, 7(7).e015694. <https://doi.org/10.1136/bmjopen-2016-015694>
- Omar, S. C., Shaharudin, A., & Tumin S. A. (2019). *The Status of the Paddy and Rice Industry in Malaysia*. Retrieved from Khazanah Research Institute: http://www.krinstitute.org/assets/contentMS/img/template/editor/Rice%20Report_Ppt%20Slide_Sar ena.pdf
- Omar, N. A., Praveena, S. M., Aris, A. Z., & Hashim, Z. (2015). Health Risk Assessment using in vitro digestion model in assessing bioavailability of heavy metal in rice: A preliminary study. *Food Chemistry*, 188, 46-50. <https://doi.org/10.1016/j.foodchem.2015.04.087>
- Payus, C., Talip, A. F. A., & Tan, W. H. (2015). Heavy Metals Accumulation in Paddy Cultivation Area of Kompipinan, Papar District, Sabah. *Journal of Sustainability Science and Management*, 10(1), 76-86.
- Rahimzadeh, M. R., Rahimzadeh, M. R., Kazemi, S., & Moghadamnia, A. (2017). Cadmium toxicity and treatment: An update. *Caspian Journal of Internal Medicine*,8(3), 135–145. <https://doi.org/10.22088/cjim.8.3.135>
- Rai, P. K., Lee, S. S., Zhang, M., Tsang, Y. F., & Kim, K. H. (2019). Heavy metals in food crops: Health risks, fate, mechanisms, and management. *Environment International*, 125, 365-385. <https://doi.org/10.1016/j.envint.2019.01.067>

- Roberts, T. L. (2014). Cadmium and phosphorous fertilizers: the issues and the science. *Procedia Engineering*, 83, 52-59.
- Rudzi, S. K., Ho, Y. B., & Kharni, I. I. A. (2018). Heavy Metals Contamination in Paddy Soil and Water and Associated Dermal Health Risk Among Farmers. *Malaysian Journal of Medicine and Health Sciences*, 14(2), 2-10. https://medic.upm.edu.my/upload/dokumen/2018120408433001_MJMHS_SP_Nov_2018.pdf
- Satpathy, D., Reddy, M. V., & Dhal, S. P. (2014). Risk Assessment of Heavy Metals Contamination in Paddy Soil, Plants, and Grains (*Oryza sativa L.*) at the East Coast of India. *BioMed Research International*, 2014, 11. <https://doi.org/10.1155/2014/545473>
- Shi, Z., Carey, M., Meharg, C. Williams, P. N., Signes-Pastor, A. J., et al. (2020). Rice Grain Cadmium Concentrations in the Global Supply-Chain. *Exposure and Health*, 12, 869-876. <https://doi.org/10.1007/s12403-020-00349-6>
- Soil Environmental Quality Standards (GB 15618-2018). (2018). Retrieved from Chinese Standard GB/T, GBT, GB: <https://www.chinesestandard.net/PDF/English.aspx/GB15618-2018>
- Stanislawski-Glubiak, E., & Korzeniowska, J. (2018). Fate of Copper in Soils from Different Fertilizer Doses in Relation to Environmental Risk Assessment. *Polish Journal of Environmental Studies*, 27(4), 1735-1741.
- Suciu, N. A., Vivo, R. D., Rizzati, N., & Capri, E. (2022). Cd content in phosphate fertilizer: Which potential risk for the environment and human health? *Current Opinion in Environmental Science & Health*, 30(100392), 2468-5844. <https://doi.org/10.1016/j.coesh.2022.100392>
- Tang, S. T., Lu, Y. M., Xiao, S. B., Cui, H., & Wei, S. Q. (2023). *Huan jing ke xue= Huanjing kexue*, 44(10), 5704-5717. <https://doi.org/10.13227/j.hjxk.202210317>
- TatahMentan, M., Nyachoti, S., Scott, L., Phan, N., Okwori, F. O., Felemban, N., & Godebo, T. R. (2020). Toxic and Essential Elements in Rice and Other Grains from the United States and Other Countries. *International Journal of Environmental Research and Public Health*, 17(21), 8128. <https://doi.org/10.3390/ijerph17218128>
- Teles, A. P. B., Rodrigues, M., & Pavinato, P. S. (2020). Solubility and Efficiency of Rock Phosphate Fertilizers Partially Acidulated with Zeolite and Pillared Clay as Additives. *Agronomy*, 10(7), 918. <https://doi.org/10.3390/agronomy10070918>
- The Risk Assessment Information System (RAIS). (2011). Retrieved from US DOE: <https://rais.ornl.gov/>
- Wuana, R. A., & Okieimen, F. E. (2011). Heavy Metals in Contaminated Soils: A Review of Sources, Chemistry, Risks and Best Available Strategies for Remediation. *International Scholarly Research Notices*, 2011, 1 - 20. <https://doi.org/10.5402/2011/402647>
- Yan, A., Wang, Y., Tan, S. N., Yusof, M. L. M., Ghosh, S., & Chen, Z. (2020). Phytoremediation: A Promising Approach for Revegetation of Heavy Metal-Polluted Land. *Frontiers in Plant Science*, 11(359). <https://doi.org/10.3389/fpls.2020.00359>
- Yap, D. W., Adezrian, J., Jusoh, K., Ismail, B. S., & Mahir, A. (2009). The Uptake of Heavy Metals by Paddy Plants (*Oryza sativa*) in Kota Marudu, Sabah, Malaysia. *American-Eurasian Journal of Agriculture and Environment Sciences*, 6(1), 16-19.
- Yoon, D. H., Choi, W. S., Hong, Y. K., Lee, Y. B., & Kim, S. C. (2019). Effect of chemical amendments on reduction of bioavailable heavy metals and ecotoxicity in soil. *Applied Biological Chemistry*, 62(53). <https://doi.org/10.1186/s13765-019-0460-2>
- Zakaria, Z., Zulkafflee, N. S., Redzuan, N. A. M., Selamat, J., Ismail, M. R., et al. (2021). Understanding Potential Heavy Metal Contamination, Absorption, Translocation and Accumulation in Rice and Human Health Risks. *Plants*, 10, 1070. <https://doi.org/10.3390/plants10061070>
- Zeng, F., Wei, W., Li, M., Huang, R., Yang, F., & Duan, Y. (2015). Heavy Metal Contamination in Rice-Producing Soils of Hunan Province, China and Potential Health Risks. *International Journal of Environmental Research and Public Health*, 12(12), 15584-15593. <https://doi.org/10.3390/ijerph121215005>
- Zheng, S., Wang, Q., Yuan, Y., & Sun, W. (2020). Human health risk assessment of heavy metals in soil and food crops in the Pearl River Delta urban agglomeration of China. *Food Chemistry*, 316, 126213. <https://doi.org/10.1016/j.foodchem.2020.126213>
- Zulkafflee, N. S., Redzuan, N. A. M., Hanafi, Z., Selamat, J., Ismail, M. R., Praveena, S. M., & Razis, A. F. A. (2019). Heavy Metal in Paddy Soil and its Bioavailability in Rice Using In Vitro Digestion Model for Health Risk Assessment. *International Journal of Environmental Research and Public Health*, 16, 4769. <https://doi.org/10.3390/ijerph16234769>
- Zulkafflee, N. S., Redzuan, N. A. M., Selamat, J., Ismail, M. R., Praveena, S. M., & Razis, A. F. A. (2021). Evaluation of Heavy Metal Contamination in Paddy Plants at the Northern Region of Malaysia Using ICPMS and Its Risk Assessment. *Plants*, 10(1), 3. <https://doi.org/10.3390/plants10010003>



Journal of Experimental Biology and Agricultural Sciences

<http://www.jebas.org>

ISSN No. 2320 – 8694

Structure and Reactivity of Halogenated GC PNA Base Pairs – A DFT Approach

Ranjithkumar Rajamani¹, Indumathi K², Srimathi P², Praveena G^{2*},
 Ling Shing Wong³, Sinouvassane Djearamane^{4,5*}

¹Viyen Biotech LLP, Coimbatore, Tamil Nadu 641031, India²Department of Physics, PSGR Krishnammal College for Women, Coimbatore, Tamilnadu, 641004, India³Life Science Division, Faculty of Health and Life Sciences, INTI International University, Nilai, 71800, Malaysia⁴Department of Biomedical Science, Faculty of Science, UniversitiTunku Abdul Rahman, Kampar 31900, Perak, Malaysia⁵Biomedical Research Unit and Lab Animal Research Centre, Saveetha Dental College, Saveetha Institute of Medical and Technical Sciences, Saveetha University, Chennai 602 105, India

Received – June 05, 2023; Revision – August 07, 2023; Accepted – October 07, 2023

Available Online – November 30, 2023

DOI: [http://dx.doi.org/10.18006/2023.11\(5\).800.808](http://dx.doi.org/10.18006/2023.11(5).800.808)

KEYWORDS

PNA

Halogen

DFT

Reactivity

Stability

ABSTRACT

The present study explored the structural and reactivity relationship of halogenated G-C PNA base pairs using density functional theory (DFT) calculations. The halogens such as F, Cl, and Br are substituted by replacing H atoms involved in H-bonds of the base pairs. All structures were optimized using the B3LYP/6-311++G** theory level, and positive frequencies confirmed their equilibrium states. To understand the structural variations of the considered halogenated systems, the bond distances of R–X, R–H, and X/H•••Y and the bond angles of R–X•••Y were analyzed. The obtained structural parameters and interaction energies are comparable with the previous theoretical reports. In addition, the interaction energies (E_{int}) and quantum molecular descriptors (QMD) are also calculated to understand the difference between halogenated PNA systems and their non-halogenated counterparts. In this study, the enhancement in the reactivity properties ω , χ , EA and S of halogenated PNA systems has been demonstrated, which indicates their improved responsive characteristics in various chemical reactions. Based on the available results, the halogenated PNA systems, carefully considering their substitutional position, facilitate better accommodation for the triplex formation of dsDNA/dsRNA. Therefore, it is concluded that the improved reactivity properties of halogenated PNA base pairs would make them potential candidates for various biological applications.

* Corresponding author

E-mail: praveenag@psgrkcw.ac.in (Praveena G);sinouvassane@utar.edu.my (Sinouvassane Djearamane)

Peer review under responsibility of Journal of Experimental Biology and Agricultural Sciences.

Production and Hosting by Horizon Publisher India [HPI]
 (<http://www.horizonpublisherindia.in/>).
 All rights reserved.

All the articles published by [Journal of Experimental Biology and Agricultural Sciences](#) are licensed under a [Creative Commons Attribution-NonCommercial 4.0 International License](#) Based on a work at www.jebas.org.



1 Introduction

Promoting the formation of halogen bonds in biomolecules is an effective method for engineering new artificial proteins and nucleotides (Metrangolo and Resnati 2008). In biomolecules, a halogen bond can be generally defined as $R-X\cdots Y-R'$, where "X" represents a halogen atom in one molecule ($R-X$) and "Y" represents an electron-rich group ($Y-R'$) such as oxygen, nitrogen, and so on (Auffinger et al. 2004). Especially in nucleic acid systems, for example, halogens can strengthen the base stacking interaction, paving the way for enhancing the stability of higher-ordered strands (Kolář and Tabarrini 2017). Furthermore, Auffinger et al. (2004) have demonstrated the effectiveness of a brominated DNA complex $d(\text{CCAGTACbr}^5\text{UGG})$ (br^5U , 5-bromouridine) in ligand binding, molecular recognition events, and molecular folding. The molecular-level insights of halogenated Watson-Crick base pairs have been studied by Parker et al. (2012) and Gomila et al. (2023) using theoretical techniques. They found that brominated structures form more stable complexes due to their size and polarizability. Several halogenated drugs, containing either fluorine or chlorine, or both, have been used commercially to treat various diseases, including migraine, various cancer types, cardiovascular disease, vasculitis and multiple sclerosis. These drugs were sanctioned by the Food and Drug Administration (FDA) (Inoue et al. 2020; Yu et al. 2021). For example, vancomycin, a chlorine-containing antibiotic drug, is used to treat MRSA infections (Álvarez-Martínez et al. 2020). Recently, anticancer halogenated medicines such as tivozanib, melphalan flufenamide, sotorasib, asciminib, umbralisib and infrinatinib were approved in 2021 to limit the growth of cancer cells by controlling various kinds of biological activities (Benedetto Tiz et al. 2022).

Moreover, studies have shown that the incorporation of 5-bromocytosine, 5-halo-2'-deoxyuridines bromodeoxyuridine and iododeoxyuridine as nucleoside into the cellular DNA can potentially act as a photosensitizer to detect the breakages and cross-links in DNA strands (Wang and Lu 2010; Zdrowowicz et al. 2016). Chemically modified nucleic acid structures have received notable attention in scientific investigation since their usage has been found in *in vivo* applications (Ochoa and Milam 2020). In this approach, Peptide nucleic acid (PNA), an artificial oligonucleotide, was modeled by Nielsen et al. (1992) and found interesting biological applications since it is the best compensation for phosphate backbone in DNA. The same group examined the rival biostability of the PNA H-T10-LysNH₂ against proteases using various bodily fluids such as cellular extracts in human serum and bacterial and ascites tumour cell extracts (Demidov et al. 1994). Patil et al. (2018) formed the triplex strand by using double-stranded RNA (dsRNA) with single-stranded PNA (ssPNA), wherein the utilization of halouracil complexes showed a significant impact on strengthening the adjacent

bases via H-bond interactions, enhancing well-ordered triplex strands. On the other hand, studies revealed that the incorporation of halogens into the peptide/protein complexes is capable of conformational stabilization due to the directionality and strength compared to that of an analogous H-bond, proving their implementation in protein engineering (Danelius et al. 2017). Considering the influential role of halo-modified nucleic acid constituents for various biological purposes, we systematically designed a peptidic chain linked 9 halogenated GC base pairs, named $\text{G}_{\text{PNA}}\text{C}_{\text{PNA}}\text{-F}^1$, $\text{G}_{\text{PNA}}\text{C}_{\text{PNA}}\text{-F}^2$, $\text{G}_{\text{PNA}}\text{C}_{\text{PNA}}\text{-F}^3$, $\text{G}_{\text{PNA}}\text{C}_{\text{PNA}}\text{-Cl}^1$, $\text{G}_{\text{PNA}}\text{C}_{\text{PNA}}\text{-Cl}^2$, $\text{G}_{\text{PNA}}\text{C}_{\text{PNA}}\text{-Cl}^3$, $\text{G}_{\text{PNA}}\text{C}_{\text{PNA}}\text{-Br}^1$, $\text{G}_{\text{PNA}}\text{C}_{\text{PNA}}\text{-Br}^2$ and $\text{G}_{\text{PNA}}\text{C}_{\text{PNA}}\text{-Br}^3$ to explore their structure and reactivity relationship properties applying quantum chemical techniques. Thus, the main purpose of this study is to focus on revealing the structure and reactivity properties of halogenated PNA base pairs, emphasizing their substitutional positions.

2 Materials and Methods

2.1 System setup and computational methods

Halogenated PNA base-pair structures were systematically designed by the substitution of halogens ($X=\text{F}$, Cl , and Br , where s in X^s represent the position of the halogen atom in H-bonds, as numbered in Figure 1) at each possible site of the H-bond. In contrast, the peptide linkage N-(2-aminoethyl)-glycine is connected via the N⁹th position of Guanine and the N¹st position of Cytosine. Totally, 9 halogenated GC PNA base pair structures such as $\text{G}_{\text{PNA}}\text{C}_{\text{PNA}}\text{-F}^1$, $\text{G}_{\text{PNA}}\text{C}_{\text{PNA}}\text{-F}^2$, $\text{G}_{\text{PNA}}\text{C}_{\text{PNA}}\text{-F}^3$, $\text{G}_{\text{PNA}}\text{C}_{\text{PNA}}\text{-Cl}^1$, $\text{G}_{\text{PNA}}\text{C}_{\text{PNA}}\text{-Cl}^2$, $\text{G}_{\text{PNA}}\text{C}_{\text{PNA}}\text{-Cl}^3$, $\text{G}_{\text{PNA}}\text{C}_{\text{PNA}}\text{-Br}^1$, $\text{G}_{\text{PNA}}\text{C}_{\text{PNA}}\text{-Br}^2$ and $\text{G}_{\text{PNA}}\text{C}_{\text{PNA}}\text{-Br}^3$ were obtained (Figure 1). As Density functional theory (DFT) being extensively used to study the H-bonded systems and organic molecules (Fonseca Guerra et al. 2000) for providing reliable results, we have chosen B3LYP functional (Lee et al. 1988) for the present work to study the structure and reactivity relationship of halogenated PNA systems. All considered structures were constructed using Chemcraft software (<https://www.chemcraftprog.com>) and are optimized at B3LYP/6-311++G** level of theory with the help of the Gaussian 09W program suite (Gaussian 09, A Revision 2016). Positive frequencies confirmed the equilibrium state of the ground state structures. The following analyses were conducted to examine the structure and reactivity of halogenated PNA base pairs: structural parameters, interaction energies (E_{int}) and quantum molecular descriptors (QMD). In addition, molecular electrostatic potential (MESP) was generated for the optimized structures using the Gaussview 5.0 package (Dennington et al. 2009). The plots of MESP were generated in atomic units (Hartrees), and an isodensity surface value was fixed at 0.004 electrons/bohr³ for all the systems studied (Figure 2). The theoretical description of the present work is provided below.

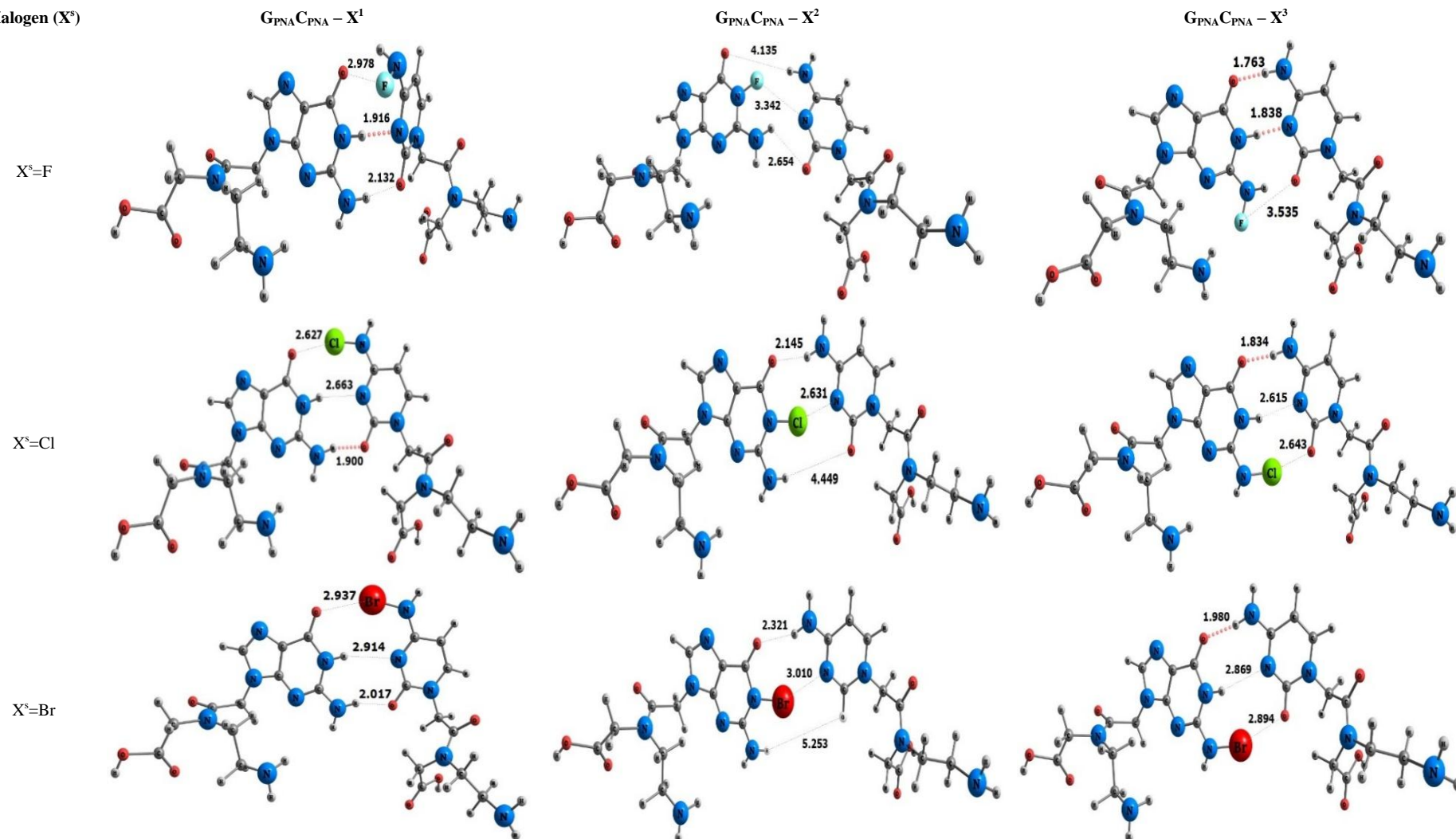
Halogen (X^s)

Figure 1 Optimized structures of $G_{PNA}C_{PNA} - F^1$, $G_{PNA}C_{PNA} - F^2$, $G_{PNA}C_{PNA} - F^3$, $G_{PNA}C_{PNA} - Cl^1$, $G_{PNA}C_{PNA} - Cl^2$, $G_{PNA}C_{PNA} - Cl^3$, $G_{PNA}C_{PNA} - Br^1$, $G_{PNA}C_{PNA} - Br^2$ and $G_{PNA}C_{PNA} - Br^3$ obtained at B3LYP/6-311++G** level of theory.

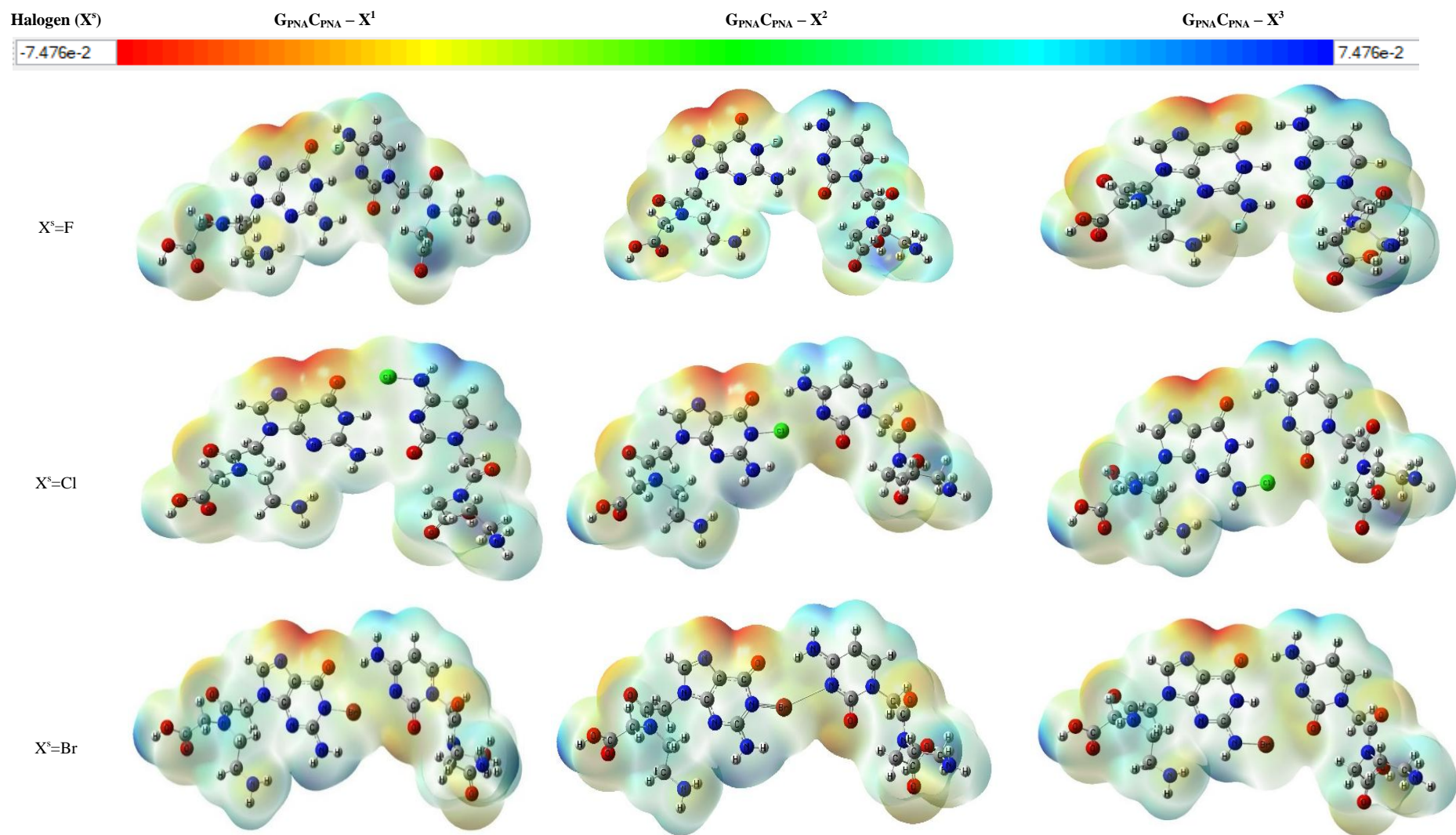


Figure 2 Electrostatic potential maps of $G_{PNA}C_{PNA}-F^1$, $G_{PNA}C_{PNA}-F^2$, $G_{PNA}C_{PNA}-F^3$, $G_{PNA}C_{PNA}-Cl^1$, $G_{PNA}C_{PNA}-Cl^2$, $G_{PNA}C_{PNA}-Cl^3$, $G_{PNA}C_{PNA}-Br^1$, $G_{PNA}C_{PNA}-Br^2$ and $G_{PNA}C_{PNA}-Br^3$ whereas the isodensity surface value was fixed at 0.004 electrons/bohr³ obtained from optimized structures at B3LYP/6-311++G** level of theory.

The interaction energy was calculated for all the considered systems using the counterpoise procedure (ΔE_{int}^{cp}), which was proposed by Boys and Bernardi (1970). It is defined as follows,

$$\Delta E_{int}^{cp} = E_{AB} - (E_A)_{in AB} - (E_B)_{in AB} \quad (1)$$

where E_{AB} is the total energy of the base pair, $(E_A)_{in AB}$ represents the energy of nucleoside1 in the base pair (with the orbitals of nucleoside2 superimposed), and $(E_B)_{in AB}$ represents the energy of nucleoside 2 in the base pair (with the orbitals of nucleoside1 superimposed)

2.1.1 Quantum molecular descriptors (QMD)

Studying the quantum molecular descriptors (QMD), including ionization potential (IP), electron affinity (EA), Chemical potential (μ), Chemical hardness (η), Chemical softness (S), Electrophilicity (ω), and Electronegativity (χ) would provide an insightful understanding of the reactive sites of various molecular systems (Chattaraj et al. 2006; Padmanabhan et al. 2007; Uppuladinne et al. 2013; Jerbi and Springborg 2018). The QMD of all the considered systems were calculated based on Koopmans' theorem, which states that the negative energy of the highest occupied molecular orbital (HOMO) and lowest unoccupied molecular orbital (LUMO) is related to the IP and EA, respectively:

$$IP = -HOMO$$

$$EA = -LUMO$$

Additional descriptors: The formula for Electronegativity (χ), Chemical potential (μ), Chemical hardness (η), Chemical softness (S) and Electrophilicity (ω) by using the IP and EA, as shown below,

$$\text{Electronegativity } (\chi) = \frac{(IP+EA)}{2}$$

$$\text{Chemical potential } (\mu) = -\chi$$

$$\text{Chemical hardness } (\eta) = \frac{(IP-EA)}{2}$$

$$\text{Chemical softness } (S) = \frac{1}{\eta}$$

$$\text{Electrophilicity } (\omega) = \frac{\mu^2}{2\eta}$$

3 Results and discussion

Based on DFT calculations, the structural parameters, interaction energies and quantum molecular descriptors of all halogenated PNA base pair systems such as $G_{PNA}C_{PNA}-F^1$, $G_{PNA}C_{PNA}-F^2$, $G_{PNA}C_{PNA}-F^3$, $G_{PNA}C_{PNA}-Cl^1$, $G_{PNA}C_{PNA}-Cl^2$, $G_{PNA}C_{PNA}-Cl^3$, $G_{PNA}C_{PNA}-Br^1$, $G_{PNA}C_{PNA}-Br^2$ and $G_{PNA}C_{PNA}-Br^3$, were calculated at the B3LYP/6-311++G** level of theory and tabulated in Table 1 and 2.

3.1.1 Structural Parameters

The structural parameters such as bond distance of R-X, R-H and X/H...Y (Å) and bond angle ($^\circ$) (X=F, Cl and Br) for all optimized structures were measured and are shown in Table 1. The bond distances of R-X and R-H for all halogenated structures were found to be between $\sim 1.332\text{\AA}$ to 1.855\AA and $\sim 0.991\text{\AA}$ to 1.040\AA , respectively. The bond distance of X...Y for all considered structures varied from ~ 1.762 to 5.253\AA . Halogenation at position #2 affects the adjacent H-bond, causing N-H...O stretching by about 4.449\AA for Cl and 5.253\AA for Br substitutions. Substituting the halogens at either #1 or #3 position leads to stronger nucleoside interactions than at position #2 in the base pair geometry. The bond distance X...Y of halogenated PNA structures increases by about $\sim 0.1\text{\AA}$ to 0.4\AA when compared to their natural counterparts, as by Parker et al. (2012). The bond angle R-X...Y of $G_{PNA}C_{PNA}-F^2$, $G_{PNA}C_{PNA}-Cl^1$, $G_{PNA}C_{PNA}-Cl^2$, $G_{PNA}C_{PNA}-Cl^3$, $G_{PNA}C_{PNA}-Br^1$, $G_{PNA}C_{PNA}-Br^2$ and $G_{PNA}C_{PNA}-Br^3$ was found to be $\sim 160^\circ$ - 172° , resulting in coplanar structures that are more favourable for the proper orientation of the σ -hole, as given in the ESP plot in Figure 2. The R-X...Y of $G_{PNA}C_{PNA}-F^1$ and $G_{PNA}C_{PNA}-F^3$ were found to be $\sim 70.8^\circ$ and 48.7° , respectively, indicating that their planarity has been distorted due to the unequal charge distribution (Figure 2). The size of the halogen atom significantly affects the bond distances X/H...Y by elongating about $\sim 0.002\text{\AA}$ to 3.294\AA . The exhibited intra/inter-atomic R-X, R-H and also the X/H...Y distances and bond angle R-X...Y of Cl and Br substituted structures are found to be in the probable range for the formation of σ -hole, as per studies shown the stability of the halogen bond depends on proper orientation of the σ -hole which is associated with the covalent bonding region of R-X...Y (Shields et al. 2010; Seidler et al. 2022; Smirnov et al. 2023).

3.1.2 Influence of halogenation on the interaction energy (E_{int})

The interaction energies (E_{int}) of all the halogenated PNA base pairs, including $G_{PNA}C_{PNA}-F^1$, $G_{PNA}C_{PNA}-F^2$, $G_{PNA}C_{PNA}-F^3$, $G_{PNA}C_{PNA}-Cl^1$, $G_{PNA}C_{PNA}-Cl^2$, $G_{PNA}C_{PNA}-Cl^3$, $G_{PNA}C_{PNA}-Br^1$, $G_{PNA}C_{PNA}-Br^2$ and $G_{PNA}C_{PNA}-Br^3$, were calculated at the B3LYP/6-311++G** level of theory and are evaluated with the available results (Table 1). The calculated E_{int} of all the halogenated PNA structures is tabulated concerning their substitutional positions (#1, #2, and #3), along with the results for halogenated DNA base pairs. The range of E_{int} for all halogenated PNA base pairs varies from -30.9kcal/mol to -6.9kcal/mol , whereas their respective H-bonded base pair has -29.53kcal/mol , as reported by Parker et al. (2012). The ascending order E_{int} , according to the position of halogen atom placed in considered systems, is as follows: $G_{PNA}C_{PNA}-F^3 < G_{PNA}C_{PNA}-F^1 < G_{PNA}C_{PNA}-Cl^1 < G_{PNA}C_{PNA}-Br^1 < G_{PNA}C_{PNA}-Cl^3 < G_{PNA}C_{PNA}-Br^3 < G_{PNA}C_{PNA}-Cl^2 < G_{PNA}C_{PNA}-Br^2 < G_{PNA}C_{PNA}-F^2$. It is noted that the E_{int} of $G_{PNA}C_{PNA}-Br^1$ and $G_{PNA}C_{PNA}-Cl^3$ were found to be almost similar at approximately 16.71kcal/mol and 16.31kcal/mol ,

Table 1 Inter/Intra-nucleoside H/X bond distances (Å) R–X and R–H covalent bond length (Å), X/H...Y bond distance (Å), R–X...Y bond angles Θ (degrees) and interaction energies (E_{int}) for optimized halogenated PNA base pair geometries at B3LYP/6-311++G** level of theory

Base pair	bonds	R–X/Å	R–H/Å	X/H...Y/Å	Θ/deg	E_{int} with PNA (in kcal/mol)	E_{int} with DNA (in kcal/mol) ⁵
$G_{\text{PNA}}C_{\text{PNA}}\text{-F}^1$	#1	1.382	-	2.978	70.8	-20.94	-
	#2	-	1.025	1.916	161.8		
	#3	-	1.017	2.132	164.9		
$G_{\text{PNA}}C_{\text{PNA}}\text{-F}^2$	#1	-	0.994	4.135	169.5	-6.69	-
	#2	1.332	-	3.342	122.7		
	#3	-	1.000	2.654	112.0		
$G_{\text{PNA}}C_{\text{PNA}}\text{-F}^3$	#1	-	1.033	1.762	175.7	-30.93	-
	#2	-	1.040	1.838	173.0		
	#3	1.383	-	1.789	48.7		
$G_{\text{PNA}}C_{\text{PNA}}\text{-Cl}^1$	#1	1.723	-	2.627	165.4	-17.68	-18.72
	#2	-	1.017	2.663	164.4		
	#3	-	1.021	1.900	163.9		
$G_{\text{PNA}}C_{\text{PNA}}\text{-Cl}^2$	#1	-	1.016	2.145	161.8	-11.83	-12.09
	#2	1.753	-	2.631	160.6		
	#3	-	1.008	4.449	160.4		
$G_{\text{PNA}}C_{\text{PNA}}\text{-Cl}^3$	#1	-	1.024	1.834	171.9	-16.36	-16.68
	#2	-	1.022	2.615	163.1		
	#3	1.746	-	2.643	164.3		
$G_{\text{PNA}}C_{\text{PNA}}\text{-Br}^1$	#1	1.830	-	2.937	156.6	-16.71	-24.16
	#2	-	1.000	2.914	163.8		
	#3	-	1.000	2.017	162.9		
$G_{\text{PNA}}C_{\text{PNA}}\text{-Br}^2$	#1	-	0.998	2.321	161.3	-10.68	-18.02
	#2	1.855	-	3.010	150.7		
	#3	-	0.991	5.253	151.7		
$G_{\text{PNA}}C_{\text{PNA}}\text{-Br}^3$	#1	-	1.001	1.980	171.8	-15.27	-20.39
	#2	-	1.000	2.869	161.8		
	#3	1.844	-	2.894	156.7		

⁵The interaction energy (E_{int}) values of halogenated GC base pair structures with plain forms obtained at B3LYP/6-31G* level of theory by J Parker et al. (2012).

respectively. The E_{int} of chlorinated structures, such as $G_{\text{PNA}}C_{\text{PNA}}\text{-Cl}^1$, $G_{\text{PNA}}C_{\text{PNA}}\text{-Cl}^2$, and $G_{\text{PNA}}C_{\text{PNA}}\text{-Cl}^3$ varies slightly from their respective natural counterparts, with values of -11.83kcal/mol, -16.36kcal/mol and -16.71kcal/mol showing a difference of approximately -0.24kcal/mol to -1.04kcal/mol. In the case of brominated structures such as $G_{\text{PNA}}C_{\text{PNA}}\text{-Br}^1$, $G_{\text{PNA}}C_{\text{PNA}}\text{-Br}^2$ and $G_{\text{PNA}}C_{\text{PNA}}\text{-Br}^3$, the E_{int} values were found to be -16.36 kcal/mol, -10.68 kcal/mol and -15.27 kcal/mol, while the E_{int} values for their

respective natural counterparts as by Parker et al.(2012) were found to be -24.16 kcal/mol, -18.02kcal/mol and -20.39kcal/mol respectively. Among all the substitutional positions, it is evident from Table 1 that position #2 has the highest E_{int} , approximately -6.9kcal/mol, -11.83 kcal/mol, and -10.68kcal/mol for $G_{\text{PNA}}C_{\text{PNA}}$ with F, Cl and Br. Therefore, position #2 is the most favourable position for stronger interactions while stabilizing the adjacent bases to form higher-order strands.

3.1.3 Quantum molecular descriptors (QMD)

Based on Koopmans' theorem, we have calculated the QMD, including ionization potential (IP) and electron affinity (EA), Electronegativity (X), Chemical potential (μ), Chemical hardness (η), Chemical softness (S), and Electrophilicity (ω) for all the considered systems in the present work using the B3LYP/6-311++G** level of theory. The QMD of halogenated PNA structures are tabulated in Table 2 along with the non-halogenated

PNA base pair results obtained B3LYP/6-31G**/B3LYP/6-311++G** level of theory (Indumathi et al. 2020). The IP of $G_{PNA}C_{PNA}-F^1$, $G_{PNA}C_{PNA}-F^2$, $G_{PNA}C_{PNA}-F^3$, $G_{PNA}C_{PNA}-Cl^1$, $G_{PNA}C_{PNA}-Cl^2$, $G_{PNA}C_{PNA}-Cl^3$, $G_{PNA}C_{PNA}-Br^1$, $G_{PNA}C_{PNA}-Br^2$ and $G_{PNA}C_{PNA}-Br^3$ ranges between ~ 5.66 eV and 6.18eV whereas the non-halogenated $G_{PNA}C_{PNA}$ system is higher about ~ 7.32 eV as by Indumathi et al. (2020). The Bar graph showing the calculated QMDs of all the halogenated PNA systems ($G_{PNA}C_{PNA}-F^1$, $G_{PNA}C_{PNA}-F^2$, $G_{PNA}C_{PNA}-F^3$, $G_{PNA}C_{PNA}-Cl^1$, $G_{PNA}C_{PNA}-Cl^2$,

Table 2 Reactivity descriptors: IP, EA, μ , η , ω , S and χ of halogenated PNA base pairs obtained at B3LYP/6-311++G** level of theory

Base pair	E_{HOMO} (in Hartrees)	E_{LUMO} (in Hartrees)	IP (in eV)	EA (in eV)	μ (in eV)	H (in eV)	ω (in eV)	S (in eV)	X (in eV)
$G_{PNA}C_{PNA}-F^1$	-0.217	-0.085	5.90	2.31	-4.105	1.795	4.708	0.557	4.105
$G_{PNA}C_{PNA}-F^2$	-0.219	-0.060	5.96	1.63	-3.795	2.165	3.347	0.462	3.795
$G_{PNA}C_{PNA}-F^3$	-0.224	-0.070	6.10	1.90	-4.000	2.1	3.810	0.476	4.000
$G_{PNA}C_{PNA}-Cl^1$	-0.208	-0.073	5.66	1.99	-3.825	1.835	3.973	0.545	3.825
$G_{PNA}C_{PNA}-Cl^2$	-0.227	-0.054	6.18	1.47	-3.825	2.355	3.102	0.425	3.825
$G_{PNA}C_{PNA}-Cl^3$	-0.228	-0.053	6.20	1.44	-3.820	2.38	3.075	0.420	3.820
$G_{PNA}C_{PNA}-Br^1$	-0.210	-0.061	5.71	1.66	-3.685	2.025	3.347	0.494	3.685
$G_{PNA}C_{PNA}-Br^2$	-0.227	-0.060	6.18	1.63	-3.905	2.275	3.347	0.440	3.905
$G_{PNA}C_{PNA}-Br^3$	-0.224	-0.059	6.10	1.61	-3.855	2.245	3.293	0.445	3.855
${}^sG_{PNA}C_{PNA}$	-	-	7.32	0.39	-3.849	3.471	2.134	0.288	3.849

^sThe compared reactivity descriptors values of $G_{PNA}C_{PNA}$ obtained at B3LYP/6-31G**/B3LYP/6-311++G** level of theory by Indumathi et al. (2020).

QUANTUM MOLECULAR DESCRIPTORS

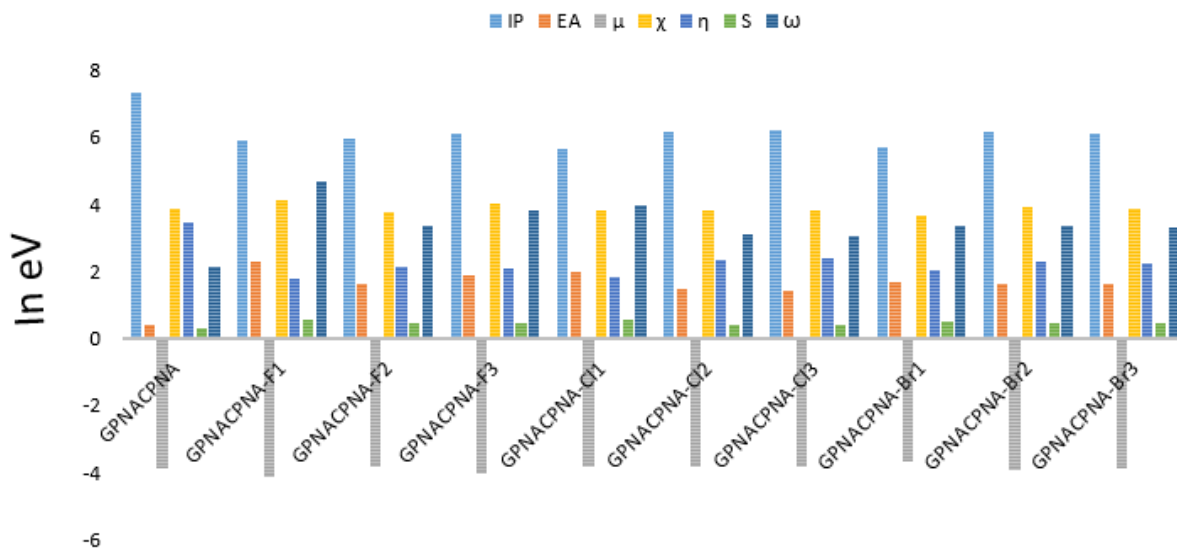


Figure 3 The IP, EA, μ , χ , η , S and ω in eVs plotted for $G_{PNA}C_{PNA}-F^1$, $G_{PNA}C_{PNA}-F^2$, $G_{PNA}C_{PNA}-F^3$, $G_{PNA}C_{PNA}-Cl^1$, $G_{PNA}C_{PNA}-Cl^2$, $G_{PNA}C_{PNA}-Cl^3$, $G_{PNA}C_{PNA}-Br^1$, $G_{PNA}C_{PNA}-Br^2$ and $G_{PNA}C_{PNA}-Br^3$ obtained at B3LYP/6-311++G** level of theory.

$G_{PNA}C_{PNA}-Cl^3$, $G_{PNA}C_{PNA}-Br^1$, $G_{PNA}C_{PNA}-Br^2$ and $G_{PNA}C_{PNA}-Br^3$) along with the non-halogenated $G_{PNA}-C_{PNA}$ system is given in Figure 3. The decrement in IP by about $\sim 1.12\text{eV}$ to 1.66eV , indicating halogenated PNA structures required less energy for removing electrons than non-halogenated PNA systems. The halogenated systems' EA is about $\sim 1.05\text{eV}$ to 1.92eV higher than the $G_{PNA}C_{PNA}$ system. While comparing EA among halogenated PNA systems, $G_{PNA}C_{PNA}-F^1$, $G_{PNA}C_{PNA}-F^3$ and $G_{PNA}C_{PNA}-Cl^1$ have the highest EA, about $\sim 2.31\text{eV}$, 1.90eV and 1.99eV , respectively. The chemical potential (μ) of #1 and #3 of fluorinated $G_{PNA}C_{PNA}$ and #2 and #3 of Brominated $G_{PNA}C_{PNA}$ are higher, about $\sim 0.006\text{eV}$ to -0.256eV , than others. Further, the increment of the ω value from about $\sim 0.941\text{eV}$ to 2.674eV showed the ability of halogenated $G_{PNA}C_{PNA}$ systems reactivity has enhanced compared to the non-halogenated PNA base pair systems. In addition, the highest χ is observed for #1 and #3 of fluorinated $G_{PNA}C_{PNA}$, and #2 and #3 of Brominated $G_{PNA}C_{PNA}$ structures and were found to be $\sim 4.110\text{eV}$, 4eV , 3.864eV , and 3.918eV respectively. The remaining structures, such as $G_{PNA}C_{PNA}-F^2$, $G_{PNA}C_{PNA}-Cl^1$, $G_{PNA}C_{PNA}-Cl^2$, $G_{PNA}C_{PNA}-Cl^3$, and $G_{PNA}C_{PNA}-Br^1$ are found to be slightly lowered by about $\sim 0.012\text{eV}$ to 0.149eV , when compared to the non-halogenated $G_{PNA}C_{PNA}$ systems. Also, the η for halogenated $G_{PNA}C_{PNA}$ base pair is found to be lower, about $\sim 1.016\text{eV}$ to 1.575eV , whereas the S of halogenated $G_{PNA}C_{PNA}$ base-pair structures are found to be higher, about $\sim 0.132\text{eV}$ to 0.269eV than the non-halogenated $G_{PNA}C_{PNA}$ systems. From the results of QMD, a significant effect on $G_{PNA}C_{PNA}$ systems upon halogenations was observed in enhanced reactive properties by the increment of ω , χ , EA and S indicating their readiness towards the immediate chemical reactions.

Conclusion

The present work highlights the halogenation effect on $G_{PNA}C_{PNA}$ base pair systems concerning their positions by employing density functional theory (DFT). We found the size of the halogen atom affects the bond distance and the planarity of the base pairs based on the structural analysis. Additionally, we found that the Cl and Br substituted systems are most favourable for the spatial orientation of the σ -hole and maintaining good stability. However, we found that the quantum molecular descriptors that reveal the halogenated $G_{PNA}C_{PNA}$ systems are more susceptible to chemical reactions than their natural counterparts. Therefore, we concluded that halogenation in peptide nucleic acid systems significantly impacts both the structure and reactivity properties when compared to non-halogenated PNA. This study helps to understand the molecular characteristics of the halogenation effect on PNA base pair systems concerning substitutional position. Also, this study investigated how using various chemically modified PNA structures with halogenation could facilitate the progression of well-ordered triplexes for therapeutic applications. Our report on the structure and reactivity properties of halogenated PNA base

pairs shows that it is worth understanding the physiochemical properties of such systems in therapeutic applications. Hence, our future study will explore the chemical properties, especially in the biological environment, by applying molecular dynamics simulation and experimental studies.

Acknowledgement

The Authors GP and IK would like to thank the "Bioinformatics Resources and Applications Facility (BRAAF), C-DAC, Pune" for offering the computational facilities to carry out this work. Also, Author IK is thankful to the GRG Institutions, Coimbatore, India, for providing a workstation to carry out this work.

References

- Álvarez-Martínez, F. J., Barrajón-Catalán, E., & Micol, V. (2020). Tackling Antibiotic Resistance with Compounds of Natural Origin: A Comprehensive Review. *Biomedicines*, *8*(10), 405. DOI: 10.3390/biomedicines8100405
- Auffinger, P., Hays, F. A., Westhof, E., & Ho, P. S. (2004). Halogen bonds in biological molecules. *Proceedings of the National Academy of Sciences of the United States of America*, *101*(48), 16789–16794. <https://doi.org/10.1073/pnas.0407607101>
- Benedetto Tiz, D., Bagnoli, L., Rosati, O., Marini, F., Sancineto, L., & Santi, C. (2022). New Halogen-Containing Drugs Approved by FDA in 2021: An Overview on Their Syntheses and Pharmaceutical Use. *Molecules*, *27*(5), 1643. DOI: 10.3390/molecules27051643
- Boys, S.F., & Bernardi, F. (1970) The calculation of small molecular interactions by the differences of separate total energies. Some procedures with reduced errors. *Molecular Physics*, *19* (4), 553-566, DOI: 10.1080/00268977000101561
- Chattaraj, P. K., Sarkar, U., & Roy, D. R. (2006). Electrophilicity Index. *Chemical Reviews*, *106*(6), 2065-2091. DOI: 10.1021/cr040109f
- Danielius, E., Andersson, H., Jarvoll, P., Lood, K., Gräfenstein, J., & Erdélyi, M. (2017). Halogen Bonding: A Powerful Tool for Modulation of Peptide Conformation. *Biochemistry*, *56*(25), 3265-3272. DOI: 10.1021/acs.biochem.7b00429
- Demidov, V. V., Potaman, V. N., Frank-Kamenetskii, M. D., Egholm, M., Buchard, O., Sönnichsen, S. H., & Nielsen, P. E. (1994). Stability of peptide nucleic acids in human serum and cellular extracts. *Biochemical Pharmacology*, *48*(6), 1310-1313. [https://doi.org/10.1016/0006-2952\(94\)90171-6](https://doi.org/10.1016/0006-2952(94)90171-6)
- Dennington, R., Keith, T., & Millam, J. (2009). GaussView, Version 5.0.8.: Semichem Inc., Shawnee Mission KS

- Fonseca Guerra, C., Bickelhaupt, F. M., Snijders, J. G., & Baerends, E. J. (2000). Hydrogen Bonding in DNA Base Pairs: Reconciliation of Theory and Experiment. *Journal of the American Chemical Society*, *122*(17), 4117-4128. DOI: 10.1021/ja993262d
- Gaussian 09, Revision A. (2016). Gaussian, Inc., Wallingford, CT
- Gomila, R. M., Frontera, A., & Bauzá, A. (2023). A Comprehensive Ab Initio Study of Halogenated A··U and G··C Base Pair Geometries and Energies. *International Journal of Molecular Sciences*, *24*(6), 5530. DOI: 10.3390/ijms24065530
- Indumathi, K., Abiram, A., & Praveena, G. (2020). Effect of peptidic backbone on the nucleic acid dimeric strands. *Molecular Physics*, *118*(1), e1584682. DOI: 10.1080/00268976.2019.1584682
- Inoue, M., Sumii, Y., & Shibata, N. (2020). Contribution of Organofluorine Compounds to Pharmaceuticals. *ACS Omega*, *5*(19), 10633-10640. DOI: 10.1021/acsomega.0c00830
- Jerbi, J., & Springborg, M. (2018). Reactivity descriptors for DNA bases and the methylation of cytosine. *International Journal of Quantum Chemistry*, *118*(11), e25538. <https://doi.org/10.1002/qua.25538>
- Kolář, M. H., & Tabarrini, O. (2017). Halogen Bonding in Nucleic Acid Complexes. *Journal of Medicinal Chemistry*, *60*(21), 8681-8690. DOI: 10.1021/acs.jmedchem.7b00329
- Lee, C., Yang, W., & Parr, R. G. (1988). Development of the Colle-Salvetti correlation-energy formula into a functional of the electron density. *Physical Review B Condensed Matter*, *37*(2), 785-789. DOI: 10.1103/physrevb.37.785
- Metrangolo, P., & Resnati, G. (2008). Chemistry. Halogen versus hydrogen. *Science*, *321*(5891), 918-919. DOI: 10.1126/science.1162215
- Nielsen, P., Egholm, M., Berg, R., & Buchardt, O. (1992). Sequence-Selective Recognition of DNA by Strand Displacement with a Thymine-Substituted Polyamide. *Science* (New York, N.Y.), *254*, 1497-1500. DOI: 10.1126/science.1962210
- Ochoa, S., & Milam, V. T. (2020). Modified Nucleic Acids: Expanding the Capabilities of Functional Oligonucleotides. *Molecules (Basel, Switzerland)*, *25*(20), 4659. <https://doi.org/10.3390/molecules25204659>
- Padmanabhan, J., Parthasarathi, R., Elango, M., Subramanian, V., Krishnamoorthy, B. S., et al. (2007). Multiphilic Descriptor for Chemical Reactivity and Selectivity. *The Journal of Physical Chemistry A*, *111*(37), 9130-9138. DOI: 10.1021/jp0718909
- Parker, A. J., Stewart, J., Donald, K. J., & Parish, C. A. (2012). Halogen Bonding in DNA Base Pairs. *Journal of the American Chemical Society*, *134*(11), 5165-5172. DOI: 10.1021/ja2105027
- Patil, K. M., Toh, D. K., Yuan, Z., Meng, Z., Shu, Z., et al. (2018). Incorporating uracil and 5-halouracils into short peptide nucleic acids for enhanced recognition of A-U pairs in dsRNAs. *Nucleic Acids Research*, *46*(15), 7506-7521. DOI: 10.1093/nar/gky631
- Seidler, M., Li, N. K., Luo, X., Xuan, S., Zuckermann, R. N., et al. (2022). Importance of the Positively Charged σ -Hole in Crystal Engineering of Halogenated Polypeptoids. *The Journal of Physical Chemistry B*, *126*(22), 4152-4159. DOI: 10.1021/acs.jpcc.2c01843
- Shields, Z. P., Murray, J. S., & Politzer, P. (2010). Directional tendencies of halogen and hydrogen bonds. *International Journal of Quantum Chemistry*, *110*(15), 2823-2832. <https://doi.org/10.1002/qua.22787>
- Smirnov, A. S., Mikherdov, A. S., Rozhkov, A. V., Gomila, R. M., Frontera, A., Kukushkin, V. Y., & Bokach, N. A. (2023). Halogen Bond-Involving Supramolecular Assembly Utilizing Carbon as a Nucleophilic Partner of I··C Non-Covalent Interaction. *Chemistry – An Asian Journal*, *18*(7), e202300037. <https://doi.org/10.1002/asia.202300037>
- Uppuladinne, M. V. N., Jani, V., Sonavane, U. B., & Joshi, R. R. (2013). Quantum chemical studies of novel 2'-4' conformationally restricted antisense monomers. *International Journal of Quantum Chemistry*, *113*(23), 2523-2533. <https://doi.org/10.1002/qua.24492>
- Wang, C.R., & Lu, Q.B. (2010). Molecular Mechanism of the DNA Sequence Selectivity of 5-Halo-2'-Deoxyuridines as Potential Radiosensitizers. *Journal of the American Chemical Society*, *132*(42), 14710-14713. DOI: 10.1021/ja102883a
- Yu, Y., Liu, A., Dhawan, G., Mei, H., Zhang, W., Izawa, K., Soloshonok, V. A., & Han, J. (2021). Fluorine-containing pharmaceuticals approved by the FDA in 2020: Synthesis and biological activity. *Chinese Chemical Letters*, *32*(11), 3342-3354. <https://doi.org/10.1016/j.ccllet.2021.05.042>
- Zdrowowicz, M., Wityk, P., Michalska, B., & Rak, J. (2016). 5-Bromo-2'-deoxycytidine — a Potential DNA Photosensitizer. *Organic and Biomolecular Chemistry*, *14*, 9312-9321. DOI: 10.1039/C6OB01446A



Identification and antibiotic susceptibility profiles of anaerobic bacteria isolated from patients with acne vulgaris

Salma Walid¹, Geetha Subramaniam^{1*}, Lalita Ambigai Sivasamugham¹,
Wong Ling Shing¹, Preamala Gunabalasingam², Nurfara Ain Binti Ramli²,
Nithiya Visayaragawan², Gan Li Lian³, Anshoo Agarwal⁴

¹INTI International University, Persiaran Perdana BBN, Putra Nilai, 71800 Nilai, Negeri Sembilan, Malaysia

²Department of Dermatology, Hospital Tuanku Jaafar Seremban, Ministry of Health Malaysia

³Clinical Research Center, Hospital Tuanku Jaafar Seremban, Ministry of Health Malaysia

⁴Department of Pathology, Northern Border University, 9280 Arar, Saudi Arabia

Received – June 05, 2023; Revision – August 06, 2023; Accepted – November 03, 2023

Available Online – November 30, 2023

DOI: [http://dx.doi.org/10.18006/2023.11\(5\).809.814](http://dx.doi.org/10.18006/2023.11(5).809.814)

KEYWORDS

Acne vulgaris

Antibiotic susceptibility profiles

Anaerobic bacterial isolates

Human Health

ABSTRACT

Commensal bacteria like the Staphylococcal species are part of the skin microbiota, which helps maintain healthy skin. However, certain factors can lead to these commensals becoming opportunistic pathogens capable of causing diseases like acne vulgaris. Topical and systemic antibiotics have been the main treatment for acne. However, long-term antibiotic usage could result in the emergence of resistant bacterial strains and treatment failure. This study evaluated the antibiotic susceptibility patterns of anaerobic bacteria isolated from clinical acne samples. Skin swabs were collected from 50 acne patients and cultured under anaerobic conditions. The resulting bacterial isolates were identified using biochemical tests and 16S rRNA gene sequencing. The antibiotic susceptibility patterns of the confirmed isolates were determined using the disc diffusion assay for eight commonly prescribed antibiotics for acne treatment. Sequencing results revealed that *S. epidermidis* was the most isolated bacterial species (68%, n=34), followed by *S. aureus* (8%, n=4). However, a significant proportion of bacterial isolates were susceptible to all eight tested antibiotics, which is unusual. On the other hand, 26% (n=13) of the tested bacterial species isolates were found to be resistant to clindamycin, while 36% (18) were resistant to erythromycin and 20% (n=10) were to tetracycline. Since there has been limited research regarding the antibiotic resistance patterns of anaerobic acne-associated bacteria in Malaysia, this study can help shed some light on suitable local prescription practices and raise awareness about the cautious use of antibiotics in treating acne vulgaris.

* Corresponding author

E-mail: geetha.subramaniam@newinti.edu.my (Geetha Subramaniam)

Peer review under responsibility of Journal of Experimental Biology and Agricultural Sciences.

Production and Hosting by Horizon Publisher India [HPI]
(<http://www.horizonpublisherindia.in/>).
All rights reserved.

All the articles published by [Journal of Experimental Biology and Agricultural Sciences](#) are licensed under a [Creative Commons Attribution-NonCommercial 4.0 International License](#) Based on a work at www.jebas.org.



1 Introduction

Many of the bacteria found on the skin are not only ubiquitous but are also harmless. These bacteria help to create an environment that suppresses the growth of pathogenic bacteria. The involvement of the microbiome in numerous skin disorders, such as acne vulgaris, has become the focus of research in recent decades, particularly when it comes to anaerobic and facultative anaerobic bacteria since anaerobic bacteria are a common cause of infections, some of which can be serious and life-threatening. This is compounded by the fact that these bacteria are frequently underestimated due to inefficiencies in collecting and transit protocols and a lack of isolation and susceptibility testing in many clinical microbiology laboratories (Pauzenberger et al. 2019). The microbiome offers genetic variation, influences disease symptoms and manifestations, and impacts dynamic metabolic processes and immunomodulatory competence (Mawardi et al. 2021).

However, factors such as genetics, as well as alterations in the chemical and physical environment of the skin, including changes in pH, hormonal imbalance, or abrasion, may result in a disproportionate growth of commensal bacteria such as *Cutibacterium acnes* and *Staphylococcus* spp., which causes an imbalance in the normal skin microflora and can therefore lead to a localized and/or systemic infection and disease.

Infections caused by such opportunistic pathogens have been treated with antibiotics for decades, which has led to the development of antibiotic resistance to routinely used antibiotics, such as erythromycin as well as clindamycin, have been documented in many countries (Walsh et al. 2016; Alkhawaja et al. 2020). Furthermore, via horizontal gene transfer, antibiotic resistance may transfer to other commensal bacteria that colonize the skin, such as *S. aureus*. As a result, indiscriminate antibiotic prescription could lead not only to the emergence of antibiotic resistance in *C. acnes* but also to the transmission of resistance to other species of bacteria (Alkhawaja et al. 2020).

Despite the prevalence of acne vulgaris among the Malaysian population, little work has been done to evaluate antibiotic resistance patterns of skin bacteria, including *Staphylococcus* spp. isolates. While the association between *C. acnes* and acne has been extensively researched, only a few studies have analyzed the overall bacterial composition of acne patients' skin and their susceptibility to antibiotics commonly used to treat acne conditions. Therefore, this study aimed to determine the antibiotic susceptibility patterns of anaerobic bacteria isolated from clinical acne samples from patients treated at the Dermatology Department of Hospital Tuanku Ja'afar Seremban, Malaysia. This information would be valuable in identifying the current trend of antibiotic

resistance among bacterial isolates from acne vulgaris patients and could aid in more definitive and effective treatment of acne vulgaris in Malaysian hospitals.

2 Materials and Methods

2.1 Ethical clearance

Before the commencement of the study, the Research & Ethics Committee of INTI International University (INTI/UEC/2018/001) as well as the Medical Research and Ethics Committee (MREC) (21-1891-61558[2]) under the National Medical Research Register (NMRR-21-1891-61558), granted the ethics approval. Patients who participated in this study were asked to complete an informed consent form using the Patient Information Sheet (PIS) authorized by the MREC before collecting the acne samples.

2.2 Clinical sample collection

Trained dermatologists collected acne samples at the Dermatology Clinic of Hospital Tuanku Jaafar Seremban (HTJS). Patients who were taking antibiotics, undergoing other types of medical treatment, pregnant mothers or below the age of 18 years were excluded from this study. The acne samples were collected from the nodules, papules, and pustules on the patients' jaw, cheeks, and forehead. The external skin area of the acne lesions was swabbed with an alcohol pad before the collection using the Amies transport media with charcoal (Microscience). The acne swabs were delivered to INTI International University's Molecular Biology Laboratory 1 within 24 to 48 hours of collection for processing.

2.3 Isolation and growth of bacterial isolates

The acne swabs were cultured on nutrient agar and incubated under anoxic conditions at 37°C. Colonies with different morphology were sub-cultured to obtain pure cultures for further analysis. Gram staining, catalase test, oxidase test, and subculturing on MSA were performed for preliminary identification of the individual cultures (Shoab et al. 2020).

2.4 16S rRNA analysis of bacterial isolates

DNA of each bacterial isolate from pure, overnight cultures was extracted in a cell lysis buffer (100mM Tris-HCl, pH8.0, 10mM EDTA, pH8.0, 0.5% Tween-20, 1% Triton-X) using the boiling method (Dimitrakopoulou et al. 2020). The 16S rRNA gene was amplified using universal primers pA (5'-AGA GTT TGA TCC TGG CTC AG-3') and pH (5'-ACG GGC GGT GTG TAC AAG-3') with Promega Go-Taq Green Master Mix. PCR amplification was performed in a Biorad thermocycler with the following thermocycling profile: an initial denaturation step at 95°C for 3 mins, followed by 30 cycles consisting of 95°C for 30s, 55°C for

1 min and 72⁰C for 1 min, as well as a final extension step at 72⁰C for 10 mins (Alnabati et al. 2021). Following the PCR amplification of the 16S rRNA gene, the PCR products with a size of 1530 bp were partially sequenced at Apical Scientific Sdn. Bhd. using the universal primers pA and pH. BioEdit version 7.2 was used to evaluate the acquired sequencing results, and the obtained sequences were then matched with those in DNA databases using NCBI Blast queries (Souwmiya et al. 2015).

2.5 Antibiotic susceptibility of bacterial isolates

Antibiotic susceptibility of the bacterial isolates was tested using 8 different antibiotic discs including cefoxitin (30µg), clindamycin (2µg), doxycycline (30µg), erythromycin (15µg), levofloxacin (5µg), minocycline (30µg), tetracycline (30µg), as well as trimethoprim-sulfamethoxazole (12.5/23.75 µg). A single colony of the pure bacterial isolates was inoculated into 3 mL of nutrient broth (OXOID) and incubated under anaerobic conditions for 16-18 hours at 37°C. Approximately 100 µL of the culture was dispensed into 3 mL of sterile water, vortexed, and compared to a 0.5 McFarland standard. Fifty microliters of the culture with confirmed turbidity were lawned on Mueller-Hinton agar using a sterile wooden applicator and dried for about one minute. The antibiotic discs were placed on the surface of the agar, while a sterile empty disc immersed in sterile water that acts as the negative control was placed on the agar using sterile forceps and gently pressed. This procedure was performed in triplicates in a laminar airflow cabinet. The agar plates with the antibiotic discs were then incubated for 24 hours at 37°C under anaerobic conditions, and the antimicrobial activity of each disk was determined by measuring the diameter of the zone of inhibition. The results were interpreted as resistant, intermediate, or sensitive according to the Clinical and Laboratory Standards Institute (CLSI) guidelines (CLSI 2021).

2.6 Statistical analysis

The diameter of the zone of inhibition was analyzed for significant differences using the one-way ANOVA to compare the mean differences between groups influenced by one independent variable and to understand if there was any effect on the dependent variable or any significant difference from each other. Significance was accepted at $P \leq 0.05$.

3 Results

3.1 Anaerobic bacteria isolated from acne samples

Out of 50 sequenced isolates, 68% (n=34) were identified as *Staphylococcus epidermidis*, followed by *S. aureus* 8% (n=4) and *S. marcescens* 6% (n=3), with each isolate matching with sequences that had Query Cover of 100 percent and E-value of 0.0. The lower the E-value, the more significant the match. Furthermore, a 100% query cover indicates the target sequence in the database spans the whole query sequence (Figure 1).

3.2 Antimicrobial susceptibility of bacterial isolates

A significant proportion of bacterial isolates were susceptible to all eight tested antibiotics. However, 26% (n=13) of the tested bacterial species isolates were resistant to clindamycin, while resistance to erythromycin was detected in 36% (n=18) of bacterial isolates. Resistance to cefoxitin was detected in 6% (n=3) of isolates, with 2% (n=1) exhibiting intermediate susceptibility. Only 2% (n=1) of bacterial isolates were found to be resistant to sulfamethoxazole-trimethoprim as well as doxycycline, while resistance to levofloxacin was detected in 2% (n=1) of isolates. Out of the 50 isolates screened, 20% (n=10) of isolates exhibited resistance to tetracycline, and 4% (n=2) of bacterial isolates exhibited intermediate susceptibility to tetracycline. The susceptibility rates of the tested isolates are depicted in Figure 2.

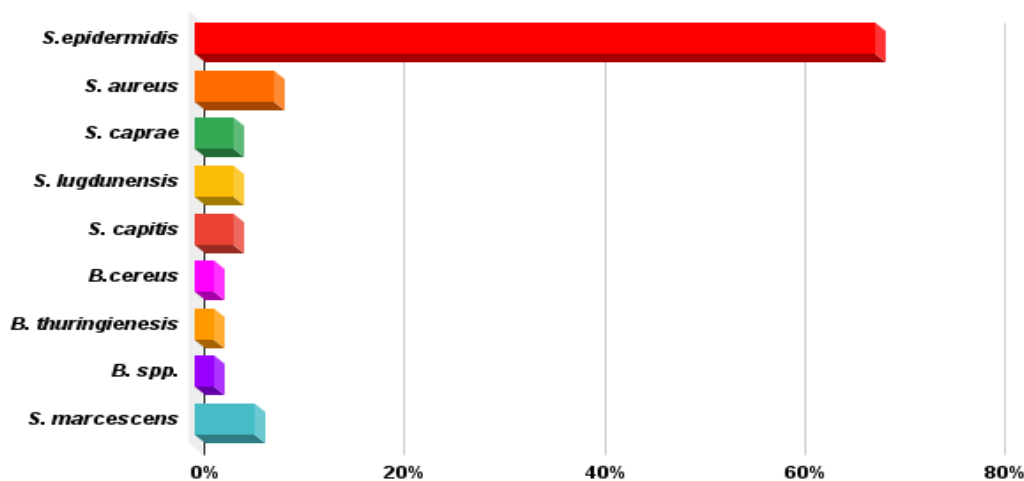


Figure 1 The proportion of anaerobic bacterial species isolated from acne samples based on the sequencing data

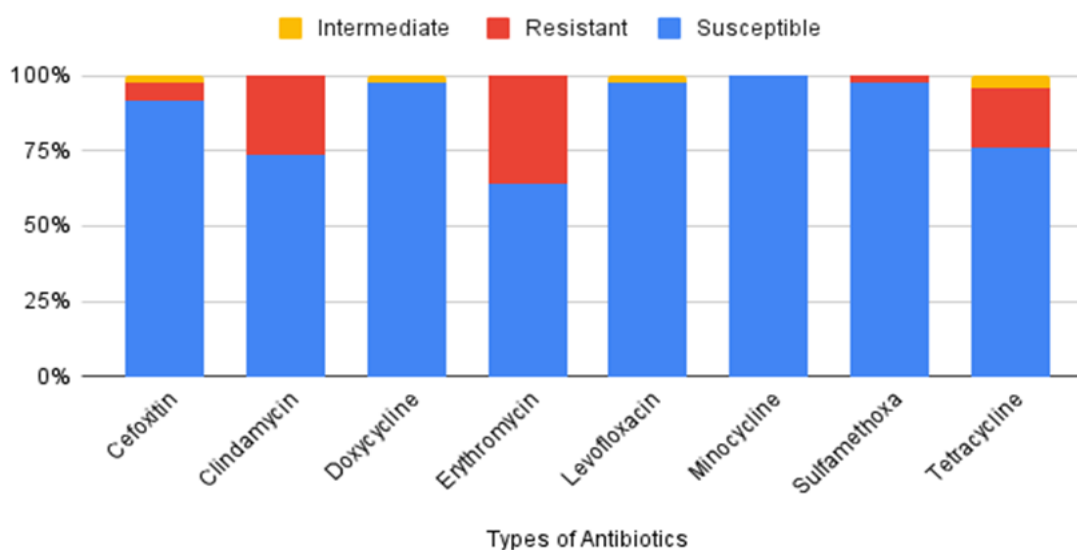


Figure 2 Antibiotic susceptibility rates of bacterial isolates against eight types of antibiotics

4 Discussion

The 16S rRNA gene sequencing showed that the anaerobic cultures of the acne samples were comprised predominantly of *Staphylococcus epidermidis*, followed by *S. aureus* and *Serratia marcescens*. This result is consistent with the findings reported by Alkhwaja et al. (2020) and Sitohang et al. (2019). Conversely, a study by Legiawati et al. (2023) reported that *C. acnes* was the most isolated pathogen from acne vulgaris, followed by *S. epidermidis*. However, a comparison cannot be made since *C. acnes* was not reported in this study. Due to the high isolation rate and growing understanding of the human skin microbiome, questions concerning the role of skin commensals, including *S. epidermidis*, in the physiopathology of acne have arisen. *S. epidermidis* has been observed to increase inflammatory acne. Furthermore, an imbalance of skin commensals in favour of *S. epidermidis* may aggravate sebaceous unit inflammation, although the specific pathway that triggers this inflammation has not yet been elucidated (Tabri 2018). Conversely, several studies have reported an antagonistic role played by *S. epidermidis* against *C. acnes*, in which *S. epidermidis* limits the *in vivo* proliferation of *C. acnes* by producing succinic acid, a fatty acid fermentation product that possesses antimicrobial activity (Claudel et al. 2019). The relative proportion of *S. aureus* isolated in this study was significantly lower than that of *S. epidermidis*, which is concurrent with the abovementioned studies. This is because there is no reported causal link between *S. aureus* and the development of acne vulgaris, but rather an indirect relationship whereby *S. aureus* can cause secondary infections of acne lesions in some patients (Totte et al. 2016).

In our study, 6% of swab samples were cultivated with a Gram-negative bacteria (*S. marcescens*), which is not a typical skin

commensal. Long-term antibiotic treatment alters the typical follicular microbial community, making the presence of Gram-negative bacteria more prevalent (Sun and Chang 2017). Gram-negative folliculitis should be suspected in acne vulgaris patients who have been on long-term antibiotics and have primarily inflammatory lesions, such as pustules, nodules, or papules (Tan et al. 2017).

The disk diffusion assay carried out revealed that all 8 tested antibiotics were effective against a significant majority of the tested bacterial strains, suggesting that the rate of resistance in this particular study was much lower than that of similar studies (Ruchiattan et al. 2023; Gamil et al. 2023). The greatest proportion of isolates exhibiting resistance were mainly against 2 antibiotics, i.e. clindamycin and erythromycin. Both the topical antibiotics clindamycin and erythromycin are the most prescribed antibiotics for *Acne vulgaris*. As such, resistance to these antibiotics is frequently observed in patients undergoing a long-term (approximately 6 to 8 weeks) of monotherapy using one of these antibiotics (Alkhwaja et al. 2020).

Alkhwaja et al. (2020) documented the incidence of cross-resistance to both clindamycin and erythromycin in both *S. epidermidis* and *S. aureus*. The presence of the *erm(X)* resistance gene, which confers resistance to the macrolide, Lincosamide, and Streptogramin B (MLS) group of antibiotics, is suspected to be the cause of cross-resistance between erythromycin and clindamycin. This explains why antibiotic resistance patterns in isolates from the same patient are similar, implying gene transfer between species.

Gram-positive bacteria develop resistance to macrolides through ribosomal RNA methylation, enzymatic inactivation of the antibiotic, and active reflux. Erythromycin ribosome methylases (*Erm*) are

enzymes that methylate rRNA and are encoded by the *erm* gene. In resistant bacteria, the *erm* proteins dimethylate the A2058 residue of 23S rRNA, located within the ribosome's V-domain. This prevents the antibiotic from binding, resulting in the macrolide losing its effectiveness and causing the bacteria to become resistant to the macrolide antibiotic (Munita and Arias 2016). In terms of enzymatic inactivation of macrolides, esterases and phosphotransferases are synthesized to inhibit antibiotics by interacting with them, preventing antibiotics from attaching to the bacteria's binding sites. Active efflux confers resistance to macrolides in bacteria by actively pumping out the antibiotics, reducing the antimicrobial's overall efficiency (Munita and Arias 2016).

In the patients of this current study, the resistance to the tetracyclines was lower than resistance to erythromycin and clindamycin. Further analysis revealed that tetracycline had the highest resistance among the three antibiotics in the tetracycline group, with a single isolate showing intermediate susceptibility to doxycycline and no resistance to minocycline. This lack of resistance to minocycline and reduced resistance rate to the tetracycline group compared to erythromycin and clindamycin appears to corroborate findings by Sutcliffe et al. (2020).

Many patients participating in this study have received treatment with benzoyl peroxide (BPO). Benzoyl peroxide, a commonly utilized acne treatment, is a potent non-antibiotic antibacterial agent with keratolytic, anti-inflammatory, and wound-healing qualities (Yang et al. 2020). A cross-sectional study by Sardana et al. (2016) comparing different routes of acne treatment, such as antibiotics and benzoyl peroxide, reported that the treatment group with benzoyl peroxide had the least number of resistant strains. Therefore, it could be postulated that benzoyl peroxide treatment resulted in a significant proportion of the tested isolates being susceptible to the antibiotics used in this study.

Conclusion

In this study, *S. epidermidis* was the most commonly isolated bacterium from the acne sample, followed by *S. aureus*. In contrast to previous research, most bacterial isolates were found to be sensitive to all eight antibiotics tested. This is an important result because numerous investigations of a similar nature have found a large proportion of resistant bacteria, which indicates that when physicians cautiously prescribe antibiotics and when patient compliance is satisfactory, antibiotic resistance can be minimized. The use of alternative, non-antibiotic acne treatment, such as benzoyl peroxide, may be another factor in the low resistance rates among isolates found in this study. On the other hand, bacterial resistance was mostly found against clindamycin and erythromycin. It is, therefore, crucial to practice appropriate prescription and use of antibiotics to prevent the emergence of antibiotic and multi-drug-resistant bacteria.

Acknowledgements

We would like to thank the Director General of Health Malaysia for his permission to publish this article. This study was funded by INTI Research Grant 2021: Seed Grant INTI-FHLS-11-02-2021.

Conflict of Interest

None of the authors have a conflict of interest to report. This paper has not been submitted for publication in any other journal.

References

- Alkhwaja, E., Hammadi, S., Abdelmalek, M., Mahasneh, N., Alkhwaja, B., & Abdelmalek, S. M. (2020). Antibiotic resistant *Cutibacterium acnes* among acne patients in Jordan: a cross sectional study. *BMC Dermatology*, 20(1), 17. doi: 10.1186/s12895-020-00108-9.
- Alnabati, N. A., Al-Hejin, A. M., Noor, S. O., Ahmed, M. M., Abu-Zeid, M., & Mleeh, N.T. (2021). The antibacterial activity of four Saudi medicinal plants against clinical isolates of *Propionibacterium acnes*. *Biotechnology and Biotechnological Equipment*, 35(1), 415–424. <https://doi.org/10.1080/13102818.2021.1885992>
- Claudel, J. P., Auffret, N., Leccia, M. T., Poli, F., Corvec, S., & Dréno, B. (2019). *Staphylococcus epidermidis*: A potential new player in the physiopathology of acne? *Dermatology*, 235(4), 287–294. <https://doi.org/10.1159/000499858>
- CLSI (2021). Performance Standards for Antimicrobial Susceptibility Testing. 31st ed. CLSI supplement M100. Wayne PA: Clinical Laboratory Standards Institute; 2021.
- Dimitrakopoulou, M. E., Stavrou, V., Kotsalou, C., & Vantarakis, A. (2020). Boiling extraction method VS commercial Kits for bacterial DNA isolation from food samples. *Journal of Food Science and Nutrition Research*, 3, 311-319.
- Gamil, H. D., Mustafa, S. A. G., Amer, R. M. M., & Khashaba, S. A. E. (2023). Implications of antimicrobial resistance during acne treatment: review article. *The Egyptian Journal of Hospital Medicine*, 9, 821-823.
- Legiawati, L., Halim, P. A., Fitriani, M., Hikmahrachim, H. G., & Lim, H. W. (2023) Microbiomes in Acne Vulgaris and Their Susceptibility to Antibiotics in Indonesia: A Systematic Review and Meta-Analysis. *Antibiotics*, 12(1),145. <https://doi.org/10.3390/antibiotics12010145>
- Mawardi, P., Ardiani, I., Primisawitri, P. P., & Nareswari, A. (2021). Dual role of *Cutibacterium acnes* in acne vulgaris

- pathophysiology. *Bali Medical Journal*, 10(2), 486. <https://doi.org/10.15562/bmj.v10i2.2358>.
- Munita, J. M., & Arias, C. A. (2016). Mechanisms of antibiotic resistance. *Microbiology Spectrum*, 4(2). <https://doi.org/10.1128/microbiolspec.vmbf-0016-2015>
- Pauzenberger, L., Heller, V., Ostermann, R.C., Laky, B., Heuberger, P. R. & Anderl, R. (2019). *Cutibacterium acnes* (formerly *Propionibacterium acnes*) contamination of the surgical field during shoulder arthroscopy. *Arthroscopy: The Journal of Arthroscopic & Related Surgery*, 35 (6), 1750–1757. <https://doi.org/10.1016/j.arthro.2019.01.024>.
- Ruchiatan, K., Rizqandaru, T., Satjamanggala, P. R., Tache, N., Cahyadi, A. I., et al. (2023). Characteristics of Biofilm-Forming Ability and Antibiotic Resistance of *Cutibacterium acnes* and *Staphylococcus epidermidis* from *Acne vulgaris* Patients. *Clinical Cosmetic Investigational Dermatology*, 16, 2457-2465. <https://doi.org/10.2147/CCID.S422486>
- Sardana, K., Gupta, T., Kumar, B., Gautam, H. K., & Garg, V. K. (2016). A cross-sectional pilot study of antibiotic resistance in *Propionibacterium acnes* strains in Indian acne patients using 16S-RNA polymerase chain reaction: A comparison among treatment modalities including antibiotics, benzoyl peroxide, and isotretinoin. *Indian Journal of Dermatology*, 61(1), 45. <https://doi.org/10.4103/0019-5154.174025>
- Shoaib, M., Muzammil, I., Hammad, M., Bhutta, Z., & Yaseen, I. A. (2020). Mini-Review on commonly used biochemical tests for identification of bacteria. *International Journal of Research Publications*, 54 (1). 10.47119/IJRP100541620201224.
- Sitohang, I.B.S., Fathan, H., Effendi, E., & Wahid, M. (2019). The susceptibility of pathogens associated with acne vulgaris to antibiotics. *Medical Journal of Indonesia*, 28, 21–27. <https://doi.org/10.13181/mji.v28i1.2735>.
- Sowmiya, M., Malathi, J., Swarnali, S., Priya, J. P., Therese, K. L., & Madhavan, H. N. (2015). A study on the characterization of *Propionibacterium acnes* isolated from ocular clinical specimens. *The Indian Journal of Medical Research*, 142 (4), 438. <https://doi.org/10.4103/0971-5916.169209>
- Sun, K.L., & Chang, J. M. (2017). Special types of folliculitis which should be differentiated from acne. *Dermato-Endocrinology*, 9(1), e1356519. <https://doi.org/10.1080/19381980.2017.1356519>
- Sutcliffe, J., McLaughlin, R., Webster, G., Read, A. F., Drlica, C., Elliott, R., & Stuart, I. (2020). Susceptibility of *Cutibacterium acnes* to topical minocycline foam. *Anaerobe*, 62, 02169. <https://doi.org/10.1016/j.anaerobe.2020.102169>.
- Tabri, F. (2018). The association between *Staphylococcus epidermidis* and palmitic acid level in patients with acne vulgaris. *Surgical and Cosmetic Dermatology*, 10(3). <https://doi.org/10.5935/scd1984-8773.20191121382>
- Tan, A.U., Schlosser, B. J., & Paller, A. S. (2017). A review of diagnosis and treatment of acne in adult female patients. *International Journal of Women's Dermatology*, 4(2), 56-71. doi: 10.1016/j.ijwd.2017.10.006.
- Totté, J. E., van der Feltz, W. T., Bode, L. G., van Belkum, A., van Zuuren, E. J., & Pasmans, S. G. (2016). A systematic review and meta-analysis on *Staphylococcus aureus* carriage in psoriasis, acne and rosacea. *European Journal of Clinical Microbiology & Infectious Diseases*, 35 (7), 1069–1077. <https://doi.org/10.1007/s10096-016-2647-3>
- Walsh, T. R., Efthimiou, J., & Dréno, B. (2016). Systematic review of antibiotic resistance in acne: An increasing topical and oral threat. *The Lancet Infectious Diseases*, 16(3). [https://doi.org/10.1016/s1473-3099\(15\)00527-7](https://doi.org/10.1016/s1473-3099(15)00527-7).
- Yang, Z., Zhang, Y., Lazić Mosler, E., et al. (2020). Topical benzoyl peroxide for acne. *Cochrane Database of Systematic Reviews*, 2020(3), CD011154. <https://doi.org/10.1002/14651858.cd011154.pub2>



Journal of Experimental Biology and Agricultural Sciences

<http://www.jebas.org>

ISSN No. 2320 – 8694

Cytotoxic Study of Zinc Oxide Nanoparticles on Cervical Cancer Cell Line

Harshyini Maheswaran¹, Sinouvassane Djearamane^{1,4*},
Anto Cordelia Tanislaus Antony Dhanapal², Wong Ling Shing³

¹Department of Biomedical Sciences, Faculty of Science, UniversitiTunku Abdul Rahman (UTAR), Kampar Campus, Jalan Universiti, Bandar Barat, 31900 Kampar, Perak, Malaysia

²Department of Chemical Science, Faculty of Science, UniversitiTunku Abdul Rahman (UTAR), Kampar Campus, Jalan Universiti, Bandar Barat, 31900 Kampar, Perak, Malaysia

³Faculty of Health and Life Sciences, INTI International University, Persiaran Perdana BBN, Putra Nilai, 71800 Nilai, Negeri Sembilan, Malaysia

⁴Biomedical Research Unit and Lab Animal Research Centre, Saveetha Dental College, Saveetha Institute of Medical and Technical Sciences, Saveetha University, Chennai 602 105, India

Received – June 05, 2023; Revision – August 01, 2023; Accepted – October 31, 2023

Available Online – November 30, 2023

DOI: [http://dx.doi.org/10.18006/2023.11\(5\).815.821](http://dx.doi.org/10.18006/2023.11(5).815.821)

KEYWORDS

Zinc oxide nanoparticles

Chemical synthesis

HeLa cell

FESEM

EDX

MTT assay

ABSTRACT

The advancement of nanomedicine drugs as an outcome of nanotechnology offers tremendous potential to enhance cancer-fighting tactics. Scientists have begun studying the role of NPs in immunotherapy, an area that is particularly beneficial in treating malignancies. Conventional treatment of cancer uses medications known as chemotherapy that frequently cause adverse effects on healthy tissues. Zinc is a vital micronutrient for the well-being of humans; therefore, nanomaterials such as zinc oxide nanoparticles (ZnO NPs) are progressively appealing as cutting-edge medical agents with implementations like anticancer properties. A bottom-up approach was utilized to chemically produce the ZnO NPs, which were characterized using Field Emission Scanning Electron Microscope (FESEM) and Energy Dispersive X-ray analysis (EDX). MTT assays have been carried out to study the cell viability percentage against multiple ZnO NPs concentrations and durations. The white ZnO NPs displayed a diverse morphology within the nanoscale range, featuring rod and spherical shapes. This synthesis was confirmed through EDX, which revealed distinct peaks corresponding to zinc and oxygen, affirming the formation of pure ZnO NPs. MTT assay data showed that ZnO NPs had a dose and time-dependent cytotoxicity against HeLa cells. This observation suggests that the ZnO NPs possess the potential to combat cancer and may hold promise for applications in biomedical research, particularly in the development of anticancer drugs.

* Corresponding author

E-mail: drsino31@gmail.com (Sinouvassane Djearamane)

Peer review under responsibility of Journal of Experimental Biology and Agricultural Sciences.

Production and Hosting by Horizon Publisher India [HPI]
(<http://www.horizonpublisherindia.in/>).
All rights reserved.

All the articles published by [Journal of Experimental Biology and Agricultural Sciences](#) are licensed under a [Creative Commons Attribution-NonCommercial 4.0 International License](#) Based on a work at www.jebas.org.



1 Introduction

Cancer is a condition of unrestricted, random cell division and invasiveness, which is caused by environmental variables, including radiation and pollutants exposure, unhealthy lifestyles like a poorly balanced diet, and stress, as well as inherited genetics (Anand et al. 2008). Cancer is most commonly triggered by mutations or changes in the expression patterns of protooncogenes, tumour suppressor genes, and DNA repair genes. The focus of present cancer treatment is to kill the cancerous cells with chemotherapeutic medicines, typically administered through chemotherapy or radiation therapy. Nevertheless, these options frequently lead to several adverse consequences, owing to the effect on healthy neighbouring tissues (Sztandera et al. 2019; Amjad et al. 2022).

Nanotechnology enables a novel approach to biomedical operations at the molecular level. Nanoparticles (NPs) with sizes ranging from 1 to 100 nm show distinct properties that vary significantly from fine particles or bulk materials (Moore and Chow 2021). NPs used in biomedical studies are extremely diversified in size, structure, morphology, chemical composition, hydrophobicity, electrostatic charge, surface chemistry, and other characteristics (Sahu et al. 2021). Nanomaterials are widely used in cosmetics, sunscreens, sporting goods, electronics, tyres, and other everyday items (Sim and Wong 2021). Furthermore, nanotechnologies have transformed medical advances, especially in imaging, diagnostic methods, and drug delivery. NPs can diagnose cancer because of the leaky characteristics of malignancy blood vessels that allow NPs to penetrate and accumulate in cancer cells due to their minuscule size (Gavas et al. 2021). Nanoxel, Eligard, and Onivyde are a few examples of FDA-approved nanomedicines (Sim and Wong 2021).

Zinc oxide nanoparticles (ZnO NPs) are among the top essential metal oxides applied in materials science on account of their noteworthy physical, chemical, and biological characteristics such as biocompatibility, environmental friendliness, relatively inexpensive, and non-toxicity (Maheswaran et al. 2021). Reports have shown that ZnO NPs also have antibacterial (Sirelkhathim et al. 2015), antifungal (Ahmadpour Kermani et al. 2021), antiviral (Kumar et al. 2018), wound healing (Metwally et al. 2022), and many other notable biopotencies. Furthermore, ZnO NPs notably impact cancer cells (Dobrucka et al. 2017; Rajeshkumar et al. 2018; Zhao et al. 2018; Motazedi et al. 2020). Zinc ion (Zn^{2+}), a soluble form of ZnO, is a trace element the human body requires and participates in enzymatic reactions throughout protein and nucleic acid production (Singh et al. 2021; Mandal et al. 2022). The Food and Drug Administration (FDA) lists zinc oxide as one of the harmless metal oxides that can be applied in the food industry (Shaba et al. 2021). Thus, the application of ZnO NPs seems to be non-toxic to normal tissues while being effective enough to act against malignant apoptosis sensitization (Wang et al. 2009; Hassan et al. 2017; Singh et al. 2021).

The chromogenic MTT (dimethylthiazol-diphenyltetrazolium bromide) assay developed by Mosmann (1983) is a redox chemical reaction extensively used as a cell metabolic activity assay. It quantifies metabolic activity because it is primarily based on tetrazolium ring cleavage in active mitochondria, and therefore, the action takes place merely in alive cells (Pintor et al. 2020). Consequently, it is frequently utilized to evaluate cell viability or drug cytotoxicity. Yellow tetrazolium MTT salt undergoes a redox reaction to become formazan by a plethora of intracellular oxidoreductase enzymes, prominently nicotinamide adenine dinucleotide (NADH) reductase (Luis et al. 2019).

In this study, we strived to investigate the cytotoxicity of chemically synthesized ZnO NPs at various concentrations (3.13, 6.25, 12.5, 25, 50 and 100 $\mu\text{g}/\text{mL}$) and durations (24 hrs, 48 hrs and 72 hrs) on cervical (HeLa) cell lines using MTT Assay.

2 Materials and Methods

2.1 Synthesis of ZnO NPs

To chemically synthesize ZnO NPs, 1 mol of sodium hydroxide (NaOH) was added dropwise into 0.5 mol of zinc nitrate ($Zn(NO_3)_2$). The solution was continuously stirred for two hours at 50 °C. After that, the white suspension was spun in a centrifuge at a speed of 3000 revolutions per minute (rpm) for 10 minutes. The sediment was rinsed using distilled water and centrifuged again. The resultant pellet was transferred into a crucible and calcinated at 400 °C for two hours.

2.2 Characterization of ZnO NPs

FESEM was employed to study the size in addition to the morphology of the ZnO NPs. EDX was implemented to characterize the chemical make-up of the ZnO NPs.

2.3 Cultivation of HeLa Cells

The human cervical cancer cell line (HeLa) was bought from the American Type Culture Collection (ATCC, USA). The cells were cultivated in a 25 mL flask with Dulbecco's Modified Eagle's Medium (DMEM), enriched with 10% fetal bovine serum (FBS), and incubated in a 37 °C incubator with 5% CO_2 . The cells were passaged into four flasks every week using Trypsin-EDTA.

2.4 Cytotoxicity Assessment

The cytotoxic impact of ZnO NPs on cancer cells was assessed using the MTT assay. Once the cells were about 70% confluent, they were trypsinized and seeded in 96-well plates. After 24 hours, the cells were treated with varying ZnO NPs concentration for 24, 48 and 72 hours. A volume of 20 μL of 5 mg/mL MTT solution was put into each well, and the plate was kept in the dark for 4 hours. The

supernatant was then aspirated, and 100 μ L of dimethyl sulfoxide (DMSO) was introduced to every well. At 550 nm, the absorbance was measured using a microplate reader. The following equation was used to quantify the percentage of cell viability using optical density (OD), and the graph of the percentage of cellular viability against ZnO NPs concentrations was plotted. Negative control and Cisplatin acted as the positive control were used in the experiment.

$$\text{Percentage of cellular viability (\%)} = \frac{\text{OD of treated cells}}{\text{OD of negative control}} \times 100 \quad (\text{Eq.1})$$

3 Results

3.1 Synthesis of ZnO NPs

Chemical ZnO NPs were effectively produced through the precipitation process. Zinc nitrate and sodium hydroxide were used as the precursors. Figure 1 (a) shows the white suspension formed after continuous stirring for two hours. Figures 1 (b) and 1 (c) depict the white pellet after washing with distilled water and the ZnO NPs powder after heat treatment at 400 $^{\circ}$ C, respectively.

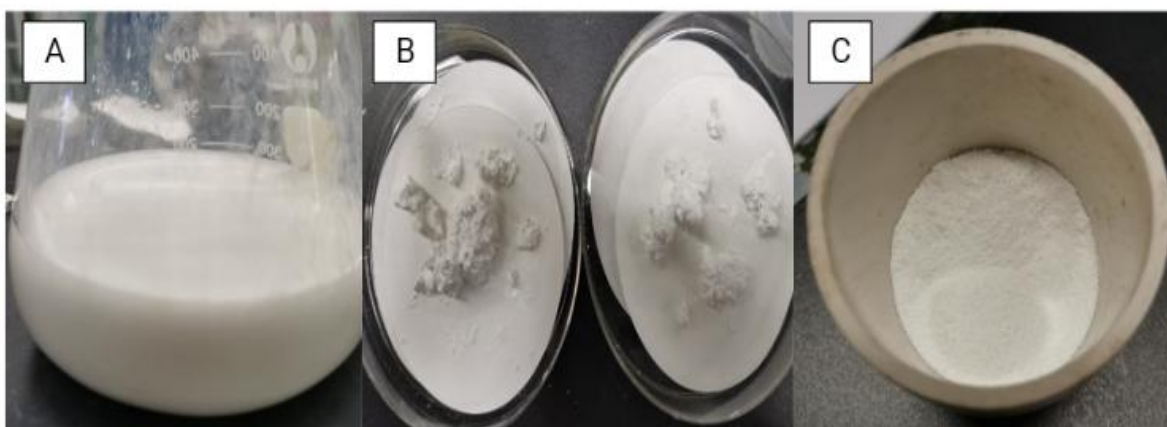


Figure 1 Process of chemical synthesis of ZnO NPs (a) white suspension of zinc hydroxide (Zn(OH)_2), (b) Zn(OH)_2 pellet after washing, (c) ZnO NPs powder after calcination.

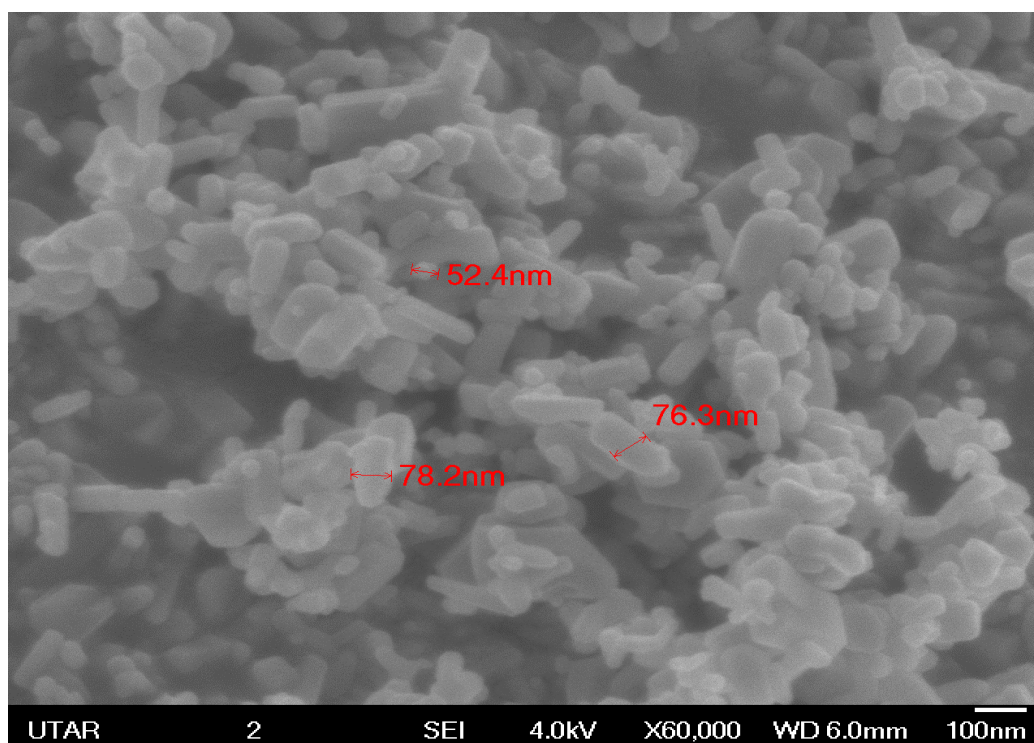


Figure 2 FESEM imaging of chemically synthesized ZnO NPs.

3.2 Characterization of ZnO NPs

3.2.1 Field Emission Scanning Electron Microscope (FESEM)

FESEM examination of the chemically synthesized ZnO NPs at a magnification of 60000x was carried out. Figure 2 revealed rod and spherical-shaped particles with smooth surfaces and some agglomeration. The size of the ZnO NPs was within the nano scale, ranging between 52.4 – 78.2 nm.

3.2.2 Energy dispersive X-ray (EDX)

EDX investigation of the synthesized ZnO NPs was performed to study the chemical components. Figure 3 illustrates peak absorbance corresponding to zinc and oxygen molecules in Spectrum 1,

affirming the synthesis of clean ZnO. The inset image shows the percentage of zinc, oxygen, and carbon in the ZnO NPs sample.

3.3 Cytotoxicity Assessment

HeLa cells were exposed to ZnO NPs at concentrations of 3.125, 6.25, 12.5, 25, 50 and 100 $\mu\text{g/mL}$ for 24, 48, and 72 hours and the cytotoxicity was evaluated through MTT assay. The cytotoxic consequence of ZnO NPs revealed that the growth inhibitory activity against HeLa cells was dose and time-dependent, as noted in Figure 4. HeLa cells were also treated with similar concentrations and durations of Cisplatin, the positive control. All the tested concentrations documented distinguishable elevated cytotoxicity effects (Figure 5).

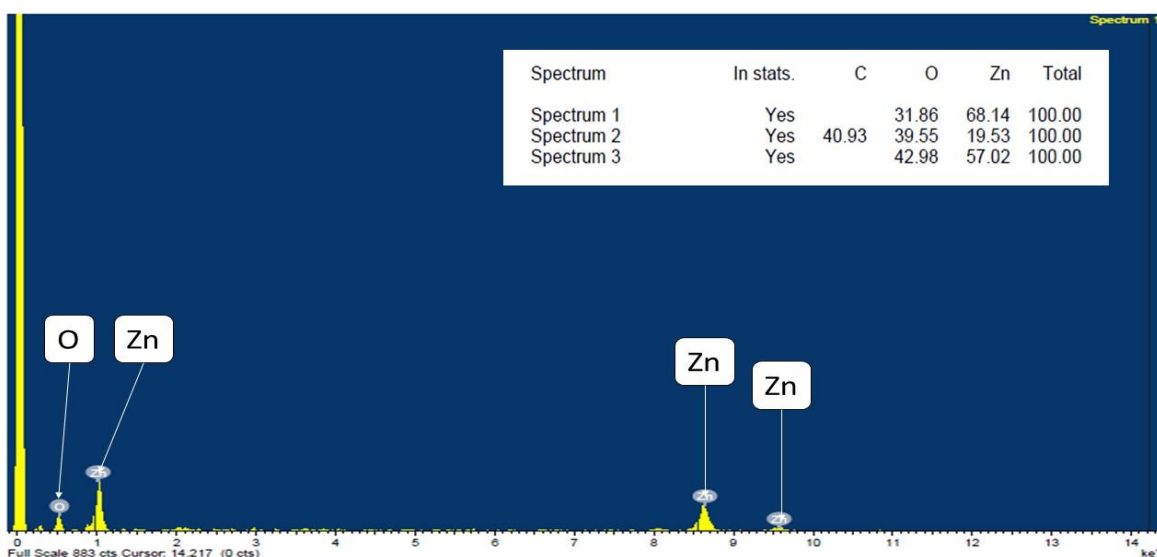


Figure 3 EDX of chemically synthesized ZnO NPs.

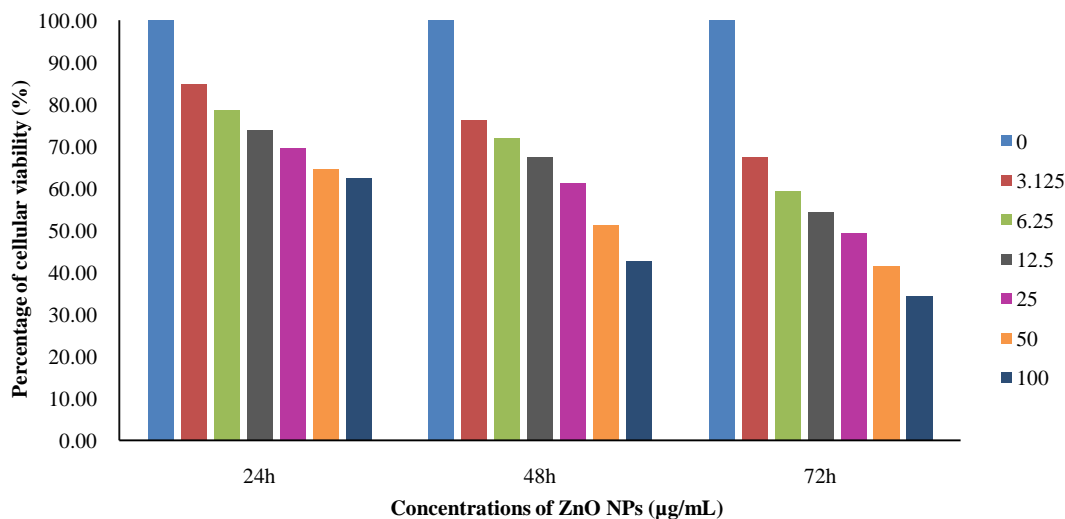


Figure 4 Percentages of cell viability on HeLa cancer cells upon treatment with ZnO NPs.

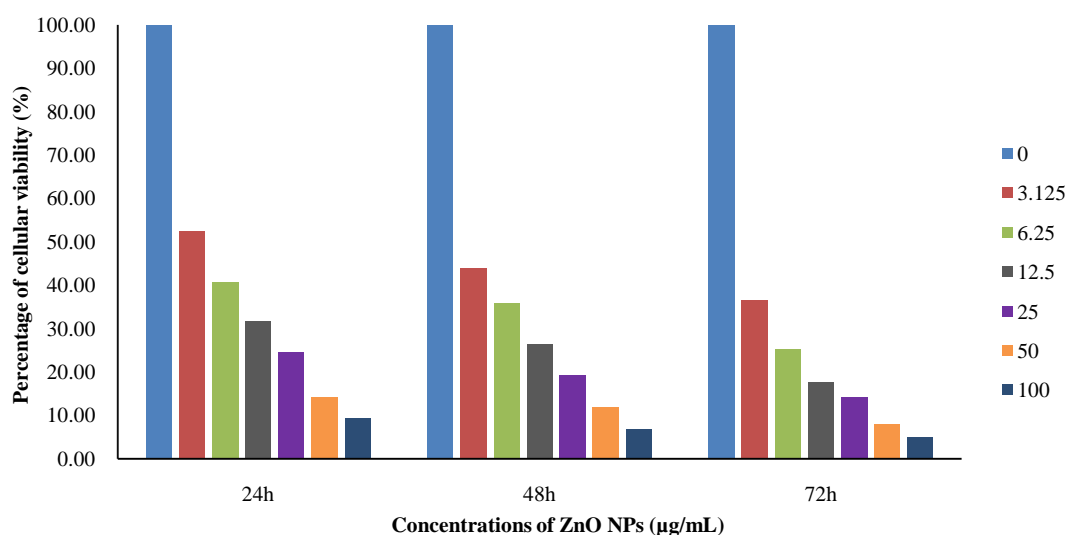


Figure 5 Percentages of cell viability on HeLa cancer cells upon treatment with Cisplatin.

4 Discussion

The chemical synthesis of ZnO NPs is depicted in Figure 1. Zinc nitrate was the precursor salt, and sodium hydroxide was the reducing agent. Once both the chemicals were mixed, a white suspension (Namasivayam et al. 2020) of $Zn(OH)_2$ formed, which was rinsed with distilled water to eliminate any residues from the synthesis (Norouzi Jobie et al. 2021). During calcination, the water evaporates; consequently, $Zn(OH)_2$ was transformed into ZnO (Biron et al. 2020).

The SEM micrograph of the chemically synthesized ZnO NPs showed a mixture of rod and spherical-shaped particles, as observed in Figure 2. The NPs have an estimated size range of 52.4 – 78.2 nm in diameter, proving that the ZnO NPs are in the nano range. It was also observed that there was some form of agglomeration between the ZnO NPs. This could be because the synthesis did not include capping agents to regulate the size of the ZnO NPs (Biron et al. 2020). The EDX spectrum of the synthesized ZnO NPs shown in Figure 3 visualized a singular peak of an oxygen molecule at 0.5 keV, and triple peaks of a zinc molecule were noted at 1.00, 8.65 and 9.60 keV. The elemental composition of ZnO NPs from the EDX spectrum inset indicated zinc and oxygen elements with a weight percentage of 68.14% and 31.86% of Spectrum 1, respectively. Similar EDX results were previously reported by Norouzi Jobie et al. (2021). Minimal carbon traces were noticed, which could be due to the contribution of carbon tape used during the EDX analysis (Taheraslani and Gardieniers 2019).

Viability assays such as MTT, a sensitive colourimetric assay, determine the cellular response to a toxicant. This study aimed to study the cytotoxic impact of ZnO NPs against HeLa cells at 24,

48 and 72 hrs, as evidenced in Figure 4. There was a notable decrease in cell viability at the highest concentration in 48 and 72 hrs, where the maximum cell death was 57.36% and 65.61%, respectively. IC_{50} of about 50 µg/mL and 25 µg/mL were recorded at 48 and 72 hrs. Although no IC_{50} was noted at 24 hrs, the cell viability decreased to 62.39% at 100 µg/mL. The data showed a predictable concentration and time-dependent cell viability loss of the HeLa cell line upon interaction with ZnO NPs. ZnO NPs showed considerable killing effects on the HeLa cell line. Figure 5 displays the percentage of cell viability on HeLa cancer cells upon treatment with the positive control, Cisplatin. The IC_{50} value of Cisplatin at 24 hrs was about 3.13 µg/mL; at 48 hrs and 72 hrs, it was lower than that. This indicated that Cisplatin is a good measure of positive control due to the cell mortality it brings about.

The cytotoxicity of the HeLa cell line against ZnO NPs increased with higher concentration and longer duration. The possible toxicity mechanism of ZnO NPs is that they generate ROS, which causes mitochondrial damage, lipid peroxidation and DNA damage. There is a possibility of membrane rupture and cytotoxicity when ZnO NPs enter the cell membrane (Ali et al. 2018). The action mechanism of ZnO NPs on cancerous cells could also most likely be based on the discharge of solubilized Zn^{2+} ions within the cells, which consequently destroyed the electron transport chain in the mitochondria by releasing a massive sum of ROS. This then causes mitochondrial dysfunction, protein activity imbalance, and the inevitable death of cancer cells by apoptosis signalling pathways (Khashan et al. 2020).

Conclusion

ZnO NPs were chemically synthesized using $Zn(NO_3)_2$ as the precursor. The synthesized ZnO NPs were analyzed using SEM

and EDX. SEM visualized that the ZnO NPs were a combination of rod and spherical-shaped particles with 52.4 – 78.2 nm in diameter. EDX analysis confirmed the yield of pure ZnO NPs. The cytotoxicity study of ZnO NPs on the HeLa cell line was studied using an MTT assay, which showed a typical cytotoxicity pattern. The study revealed a duration-dependent loss in the survival of the cells in tandem with increasing the dose of the ZnO NPs. Maximum cell death of 65.61% was observed at the highest concentration in 72 hrs on HeLa cells. This reveals that the synthesized ZnO NPs have cancer-killing potential and can be helpful in biomedical research for anticancer drug development.

Conflict of Interest

The authors have declared no conflicts of interest. All co-authors have read and reviewed the manuscript, and there are no financial conflicts to disclose.

References

- Ahmadpour Kermani, S., Salari, S., & Ghasemi Nejad Almani, P. (2021). Comparison of antifungal and cytotoxicity activities of titanium dioxide and zinc oxide nanoparticles with amphotericin B against different *Candida* species: In vitro evaluation. *Journal of clinical laboratory analysis*, 35(1), e23577. <https://doi.org/10.1002/jcla.23577>
- Ali, A., Phull, A.R., & Zia, M. (2018). Elemental zinc to zinc nanoparticles: Is ZnO NPs crucial for life? Synthesis, toxicological, and environmental concerns. *Nanotechnology Reviews*, 7(5), 413–441. <https://doi.org/10.1515/ntrev-2018-0067>
- Amjad, M. T., Chidharla, A., & Kasi, A. (2022). Cancer Chemotherapy. In *StatPearls*. StatPearls Publishing. <http://www.ncbi.nlm.nih.gov/books/NBK564367/>
- Anand, P., Kunnumakara, A. B., Sundaram, C., Harikumar, K. B., Tharakan, S. T., Lai, O. S., Sung, B., & Aggarwal, B. B. (2008). Cancer is a Preventable Disease that Requires Major Lifestyle Changes. *Pharmaceutical Research*, 25(9), 2097–2116. <https://doi.org/10.1007/s11095-008-9661-9>
- Biron, D., Santos, V., & Bergmann, C. (2020). Synthesis and Characterization of Zinc Oxide Obtained by Combining Zinc Nitrate with Sodium Hydroxide in Polyol Medium. *Materials Research*, 23, e20200080. <https://doi.org/10.1590/1980-5373-mr-2020-0080>
- Dobrucka, R., Dlugaszewska, J., & Kaczmarek, M. (2017). Cytotoxic and antimicrobial effects of biosynthesized ZnO nanoparticles using of *Chelidonium majus* extract. *Biomedical Microdevices*, 20(1), 5. <https://doi.org/10.1007/s10544-017-0233-9>
- Gavas, S., Quazi, S., & Karpiński, T. M. (2021). Nanoparticles for Cancer Therapy: Current Progress and Challenges. *Nanoscale Research Letters*, 16, 173. <https://doi.org/10.1186/s11671-021-03628-6>
- Hassan, H. F. H., Mansour, A. M., Abo-Youssef, A. M. H., Elsadek, B. E. M., & Messiha, B. A. S. (2017). Zinc oxide nanoparticles as a novel anticancer approach; in vitro and in vivo evidence. *Clinical and Experimental Pharmacology & Physiology*, 44(2), 235–243. <https://doi.org/10.1111/1440-1681.12681>
- Khashan, K. S., Sulaiman, G. M., Hussain, S. A., Marzoog, T. R., & Jabir, M. S. (2020). Synthesis, Characterization and Evaluation of Antibacterial, Anti-parasitic and Anticancer Activities of Aluminum-Doped Zinc Oxide Nanoparticles. *Journal of Inorganic and Organometallic Polymers and Materials*, 30(9), 3677–3693. <https://doi.org/10.1007/s10904-020-01522-9>
- Kumar, R., Sahoo, G., Pandey, K., Nayak, M. K., Topno, R., Rabidas, V., & Das, P. (2018). Virostatic potential of zinc oxide (ZnO) nanoparticles on capsid protein of cytoplasmic side of chikungunya virus. *International Journal of Infectious Diseases*, 73, 368. <https://doi.org/10.1016/j.ijid.2018.04.4247>
- Luis, C., Castaño-Guerrero, Y., Soares, R., Sales, G., & Fernandes, R. (2019). Avoiding the Interference of Doxorubicin with MTT Measurements on the MCF-7 Breast Cancer Cell Line. *Methods and Protocols*, 2(2), Article 2. <https://doi.org/10.3390/mps2020029>
- Maheswaran, H., Wong, L. S., Dhanapal, A. C. T. A., Narendhirakannan, R. T., Janakiraman, A. K., & Djearamane, S. (2021). Toxicity of Zinc Oxide Nanoparticles on Human Skin Dermal Cells. *Journal of Experimental Biology and Agricultural Sciences*, 9(Spl-1-GCSGD_2020), S95-S100. [https://doi.org/10.18006/2021.9\(Spl-1-GCSGD_2020\).S95.S100](https://doi.org/10.18006/2021.9(Spl-1-GCSGD_2020).S95.S100)
- Mandal, A. K., Katuwal, S., Tettey, F., Gupta, A., Bhattarai, S., et al. (2022). Current Research on Zinc Oxide Nanoparticles: Synthesis, Characterization, and Biomedical Applications. *Nanomaterials*, 12(17), Article 17. <https://doi.org/10.3390/nano12173066>
- Metwally, A. A., Abdel-Hady, A.N. A. A., Haridy, M. A. M., Ebnalwaled, K., Saied, A. A., & Soliman, A. S. (2022). Wound healing properties of green (using *Lawsonia inermis* leaf extract) and chemically synthesized ZnO nanoparticles in albino rats. *Environmental Science and Pollution Research*, 29(16), 23975–23987. <https://doi.org/10.1007/s11356-021-17670-5>
- Moore, J. A., & Chow, J. C. L. (2021). Recent progress and applications of gold nanotechnology in medical biophysics using artificial intelligence and mathematical modeling. *Nano Express*, 2(2), 022001. <https://doi.org/10.1088/2632-959X/abddd3>

- Mosmann, T. (1983). Rapid colorimetric assay for cellular growth and survival: Application to proliferation and cytotoxicity assays. *Journal of Immunological Methods*, 65(1–2), 55–63. [https://doi.org/10.1016/0022-1759\(83\)90303-4](https://doi.org/10.1016/0022-1759(83)90303-4)
- Motazedi, R., Rahaiee, S., & Zare, M. (2020). Efficient biogenesis of ZnO nanoparticles using extracellular extract of *Saccharomyces cerevisiae*: Evaluation of photocatalytic, cytotoxic and other biological activities. *Bioorganic Chemistry*, 101, 103998. <https://doi.org/10.1016/j.bioorg.2020.103998>
- Namasivayam, S. K. R., Shyamsundar, D., Prabanch, M. M., Bharani, R. A., & Avinash, G. P. (2020). Inhibitory potential of molecular mechanism of pathogenesis with special reference to biofilm inhibition by chemogenic zinc oxide nanoparticles. *Letters of Applied NanoBioScience*, 10, 1862–1870.
- Norouzi Jobie, F., Ranjbar, M., Hajizadeh Moghaddam, A., & Kiani, M. (2021). Green synthesis of zinc oxide nanoparticles using *Amygdalus scoparia* Spach stem bark extract and their applications as an alternative antimicrobial, anticancer, and anti-diabetic agent. *Advanced Powder Technology*, 32(6), 2043–2052. <https://doi.org/10.1016/j.appt.2021.04.014>
- Pintor, A. V. B., Queiroz, L. D., Barcelos, R., Primo, L. S. G., Maia, L. C., & Alves, G. G. (2020). MTT versus other cell viability assays to evaluate the biocompatibility of root canal filling materials: A systematic review. *International Endodontic Journal*, 53(10), 1348–1373. <https://doi.org/10.1111/iej.13353>
- Rajeshkumar, S., Kumar, S. V., Ramaiah, A., Agarwal, H., Lakshmi, T., & Roopan, S. M. (2018). Biosynthesis of zinc oxide nanoparticles using *Mangifera indica* leaves and evaluation of their antioxidant and cytotoxic properties in lung cancer (A549) cells. *Enzyme and Microbial Technology*, 117, 91–95. <https://doi.org/10.1016/j.enzmictec.2018.06.009>
- Sahu, T., Ratre, Y. K., Chauhan, S., Bhaskar, L. V. K. S., Nair, M. P., & Verma, H. K. (2021). Nanotechnology based drug delivery system: Current strategies and emerging therapeutic potential for medical science. *Journal of Drug Delivery Science and Technology*, 63, 102487. <https://doi.org/10.1016/j.jddst.2021.102487>
- Shaba, E. Y., Jacob, J. O., Tijani, J. O., & Suleiman, M. A. T. (2021). A critical review of synthesis parameters affecting the properties of zinc oxide nanoparticle and its application in wastewater treatment. *Applied Water Science*, 11(2), 48. <https://doi.org/10.1007/s13201-021-01370-z>
- Sim, S., & Wong, N. K. (2021). Nanotechnology and its use in imaging and drug delivery (Review). *Biomedical Reports*, 14(5), 1–9. <https://doi.org/10.3892/br.2021.1418>
- Singh, Th. A., Sharma, A., Tejwan, N., Ghosh, N., Das, J., & Sil, P. C. (2021). A state of the art review on the synthesis, antibacterial, antioxidant, antidiabetic and tissue regeneration activities of zinc oxide nanoparticles. *Advances in Colloid and Interface Science*, 295, 102495. <https://doi.org/10.1016/j.cis.2021.102495>
- Sirelkhatim, A., Mahmud, S., Seeni, A., Kaus, N. H. M., Ann, L. C., et al. (2015). Review on Zinc Oxide Nanoparticles: Antibacterial Activity and Toxicity Mechanism. *Nano-Micro Letters*, 7(3), 219–242. <https://doi.org/10.1007/s40820-015-0040-x>
- Sztandera, K., Gorzkiewicz, M., & Klajnert-Maculewicz, B. (2019). Gold Nanoparticles in Cancer Treatment. *Molecular Pharmaceutics*, 16(1), 1–23. <https://doi.org/10.1021/acs.molpharmaceut.8b00810>
- Taheraslani, M., & Gardeniers, H. (2019). High-Resolution SEM and EDX Characterization of Deposits Formed by CH₄+Ar DBD Plasma Processing in a Packed Bed Reactor. *Nanomaterials*, 9(4), 589. <https://doi.org/10.3390/nano9040589>
- Wang, H., Wingett, D., Engelhard, M. H., Feris, K., Reddy, K. M., et al. (2009). Fluorescent dye encapsulated ZnO particles with cell-specific toxicity for potential use in biomedical applications. *Journal of Materials Science: Materials in Medicine*, 20(1), 11–22. <https://doi.org/10.1007/s10856-008-3541-z>
- Zhao, C., Zhang, X., & Zheng, Y. (2018). Biosynthesis of polyphenols functionalized ZnO nanoparticles: Characterization and their effect on human pancreatic cancer cell line. *Journal of Photochemistry and Photobiology B: Biology*, 183, 142–146. <https://doi.org/10.1016/j.jphotobiol.2018.04.031>



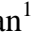










Journal of Experimental Biology and Agricultural Sciences

<http://www.jebas.org>

ISSN No. 2320 – 8694

Comparative Evaluation of Masson's Trichrome and Picrosirius Red Staining for Digital Collagen Quantification Using ImageJ in Rabbit Wound Healing Research

Khan Sharun^{1*} , S. Amitha Banu¹ , Merlin Mamachan¹ , Athira Subash² ,
Karikalan Mathesh³ , Rohit Kumar¹ , Obli Rajendran Vinodhkumar⁴ , Kuldeep Dhama² ,
Laith Abualigah^{5,6,7,8,9,10,11} , Abhijit M. Pawde¹ , Amarpal 

¹Division of Surgery, ICAR-Indian Veterinary Research Institute, Izatnagar, Bareilly, Uttar Pradesh, India

²Division of Pathology, ICAR-Indian Veterinary Research Institute, Izatnagar, Bareilly, Uttar Pradesh, India

³Centre for Wildlife Conservation, Management and Disease Surveillance, ICAR-Indian Veterinary Research Institute, Izatnagar, Bareilly, Uttar Pradesh, India.

⁴Division of Epidemiology, ICAR-Indian Veterinary Research Institute, Izatnagar, Bareilly, Uttar Pradesh, India

⁵Computer Science Department, Prince Hussein Bin Abdullah Faculty for Information Technology, Al al-Bayt University, Mafraq 25113, Jordan

⁶Hourani Center for Applied Scientific Research, Al-Ahliyya Amman University, Amman 19328, Jordan

⁷MEU Research Unit, Middle East University, Amman 11831, Jordan

⁸Department of Electrical and Computer Engineering, Lebanese American University, Byblos 13-5053, Lebanon

⁹School of Computer Sciences, Universiti Sains Malaysia, Pulau Pinang 11800, Malaysia

¹⁰School of Engineering and Technology, Sunway University Malaysia, Petaling Jaya 27500, Malaysia

¹¹Applied Science Research Center, Applied Science Private University, Amman 11931, Jordan

Received – October 10, 2023; Revision – November 17, 2023; Accepted – November 29, 2023

Available Online – November 30, 2023

DOI: [http://dx.doi.org/10.18006/2023.11\(5\).822.833](http://dx.doi.org/10.18006/2023.11(5).822.833)

KEYWORDS

Collagen content

Digital image analysis

Differential staining

ImageJ

Histopathology

ABSTRACT

The therapeutic potential of Pluronic F127 (PF127) hydrogel loaded with adipose-derived stromal vascular fraction (AdSVF), mesenchymal stem cells (AdMSC), and conditioned media (AdMSC-CM) for repairing full-thickness skin wounds was evaluated using a rabbit model. The rabbits were randomly divided into eight groups with six animals each and treatment was given as per the predetermined protocol (3 doses at one-week interval): Group A (Control), Group B (AdSVF), Group C (AdMSC), Group D (AdMSC-CM), Group E (PF127), Group F (AdSVF + PF127), Group G (AdMSC + PF127), and Group H (AdMSC-CM + PF127). Skin tissue samples were collected from the healing wounds on day 28 for staining and collagen quantification. Collagen density (Area %) was quantified using tissue sections stained with Masson's Trichrome (MT) and Picrosirius Red (PSR) stain using the Colour Deconvolution plugin of ImageJ and RGB stack method, respectively. These techniques function based on

* Corresponding author

E-mail: sharunkhansk@gmail.com, info@sharunkhan.com (Khan Sharun)

Peer review under responsibility of Journal of Experimental Biology and Agricultural Sciences.

Production and Hosting by Horizon Publisher India [HPI]
(<http://www.horizonpublisherindia.in/>).
All rights reserved.

All the articles published by [Journal of Experimental Biology and Agricultural Sciences](http://www.jebas.org) are licensed under a [Creative Commons Attribution-NonCommercial 4.0 International License](https://creativecommons.org/licenses/by/4.0/) Based on a work at www.jebas.org.



Wound healing

separating different colour channels in the stained tissue sections to isolate the collagen fibers and then quantifying them through thresholding and image analysis. Across the treatment groups, both staining methods generally showed a trend of increased collagen density compared to the control group. For most groups, PSR staining consistently indicated slightly lower collagen densities than MT staining. However, the overall trends were similar in both staining. The comparison between PSR and MT staining methods revealed that both techniques effectively assess collagen density in healing wounds. However, there were subtle differences in the absolute values obtained, with PSR staining tending to yield slightly lower collagen density measurements than MT. These differences can be attributed to the distinct mechanisms of these staining methods. Therefore, both staining methods can digitally quantify collagen density in wound healing research.

1 Introduction

Wound healing is a complex and dynamic process involving various cellular and molecular events to restore tissue integrity and functionality (Bist et al. 2021; Banu et al. 2023). Collagen, a major extracellular matrix (ECM) component, is pivotal in tissue repair, providing structural support and guiding cellular activities (Kular et al. 2014). In this study, PF127 hydrogel is loaded with adipose-derived stromal vascular fraction (AdSVF), mesenchymal stem cells (AdMSC), and conditioned media (AdMSC-CM). These components are chosen for their regenerative potential and ability to influence the wound-healing microenvironment. Accurate and reproducible quantification of collagen density is imperative for evaluating the success of wound healing interventions. Masson's Trichrome (MT) and Picrosirius Red (PSR) staining methods are selected for their well-established roles in visualizing and quantifying collagen fibers in tissue sections (Marcos-Garcés et al. 2017; Costa et al. 2019).

MT staining is a widely used histological technique to visualize collagen fibers in tissue sections (Van De Vlekkert et al. 2020). This staining method is precious because it can differentiate collagen from other tissue components, providing enhanced contrast and detailed information about collagen morphology and distribution. The principle behind MT staining lies in the differential affinity of tissue components for specific dyes (Chang and Kessler 2008). MT staining finds its applications in various realms of research and diagnostics. Researchers often rely on its ability to assess collagen density, with the intensity of the blue or green colouration acting as a quantitative indicator. Beyond quantification, the method detects fibrotic changes, making it a go-to tool for identifying pathological conditions like cardiac fibrosis, liver cirrhosis, and pulmonary fibrosis (Chang and Kessler 2008; Van De Vlekkert et al. 2020).

PSR staining is a widely used histological technique that provides excellent visualization of collagen fibers within tissue sections (Lattouf et al. 2014; López De Padilla et al. 2021). While its true power is often showcased under polarized light, PSR staining is also valuable when observed under regular brightfield microscopy (López De Padilla et al. 2021). This technique enhances the

contrast between collagen and surrounding tissues, offering detailed insights into collagen distribution, density, and morphology (Lattouf et al. 2014). The principle of PSR staining involves the interaction between the dye and collagen fibers. Picrosirius Red, derived from the synthetic dye Sirius Red F3BA, has a specific affinity for collagen (Sharma et al. 2015). When applied to tissue sections, PSR binds to collagen molecules, resulting in distinct colouration under brightfield microscopy (Lattouf et al. 2014; López De Padilla et al. 2021). Both methods offer distinct advantages, and their comparative evaluation in this study aims to elucidate their efficacy in the specific context of digital collagen quantification.

In wound healing research, accurately quantifying collagen density is essential for assessing the efficacy of therapeutic interventions. This study evaluates two widely used staining methods, MT and Picrosirius Red, for digitally quantifying collagen density in a rabbit model of full-thickness skin wounds. The rationale behind this investigation lies in the need for robust and reliable techniques to measure collagen levels precisely, aiding in the comprehensive understanding of wound healing responses to various treatments.

Understanding the comparative performance of these staining methods is critical for researchers and clinicians involved in wound healing studies. Reliable collagen quantification contributes to optimizing therapeutic strategies and enhances the translatability of preclinical findings to clinical applications (Marcos-Garcés et al. 2017). We hypothesize that both MT and PSR staining methods will effectively quantify collagen density in healing wounds but may yield subtle differences in absolute values due to their distinct mechanisms of action. The results of this comparative evaluation will guide researchers in selecting the most suitable staining method for their specific wound-healing research contexts.

2 Materials and Methods

2.1 Masson's Trichrome staining

The MT staining procedure was performed on paraffin-embedded tissue sections. These sections were initially dewaxed by

immersion in xylene until the paraffin was removed entirely. Subsequently, a series of descending alcohol concentrations (100%, 90%, 70% and 50% alcohol) were used for rehydration, followed by a rinse in distilled water. The nuclei of the tissue sections were stained with Weigert's iron haematoxylin for approximately 5-10 minutes, and the excess stain was removed by rinsing with tap water. Cytoplasm and muscle fibers were stained using Biebrich scarlet-acid fuchsin solution for 15-30 minutes, followed by another rinse in distilled water. The sections were treated with a phosphomolybdic-phosphotungstic acid solution to differentiate collagen and muscle fibres for 15 minutes. Collagen fibers were stained blue by immersing the sections in an aniline blue solution for 5-10 minutes, followed by a brief rinse in distilled water. After acid differentiation with 1% acetic acid solution, sections underwent gradual dehydration through ascending alcohol concentrations (70%, 80%, 90%, and 100% alcohol) and were cleared in xylene. Finally, a mounting medium (DPX) was applied to each section, covered with a glass coverslip, and allowed to dry. The stained tissue sections were then examined under a light microscope with appropriate filters for MT staining, facilitating the distinction of collagen fibers (blue) in histological analysis.

2.2 Collagen quantification using the Colour Deconvolution plugin in ImageJ software

Collagen density (Area %) was quantified using tissue sections stained using MT stain based on the protocol described by Chen et

al. (2017) with modifications. The principle behind quantifying collagen in skin stained with MT stain using the Colour Deconvolution plugin in ImageJ is based on the separation of different colour channels in the stained tissue sections to isolate the collagen fibers and then quantifying them through thresholding and image analysis (Ruifrok and Johnston 2001; Landini et al. 2021).

The first step involves installing the ImageJ software on a computer. To achieve this, the user downloads and installs the software opens it, and loads the digital image of the MT-stained skin section by navigating through "File" > "Open" and selecting the image file. Moving on to the second step, the user is provided with two methods for installing and setting up the colour deconvolution plugin. In Method 1, the Color Deconvolution plugin is downloaded from the ImageJ website, saved in the "plugins" folder within the ImageJ directory, and ImageJ is restarted to ensure plugin recognition. In Method 2, the user is guided to download the JAR file from a specified link, and in ImageJ, the plugin is installed by going to the "Plugins" menu, selecting "Install...." and following the prompts. The user may need to restart ImageJ to complete the installation.

Select the "Straight Line" tool from the ImageJ toolbar. This tool allows us to measure the length of the scale bar (Figure 1). By clicking at one end of the scale bar in the image and without releasing the mouse button, drag the line to the other end of the scale bar. Release the mouse button to draw a straight line along

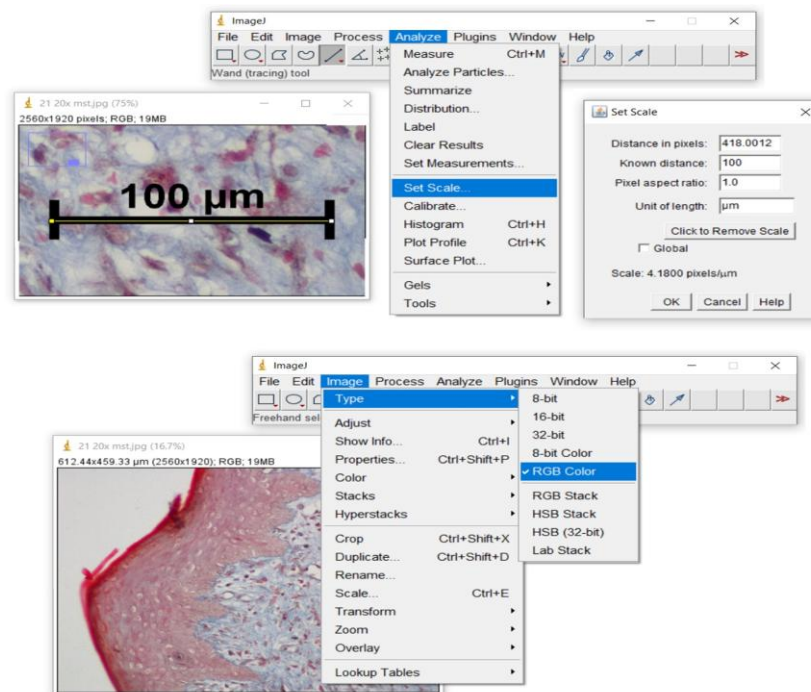


Figure 1 Steps for performing collagen quantification in ImageJ. The scale has to be calibrated to ensure accurate measurements.

Use the straight-line selection tool to draw a line along the scale bar and set the known measurement. The input images should be converted to RGB images before performing the analysis

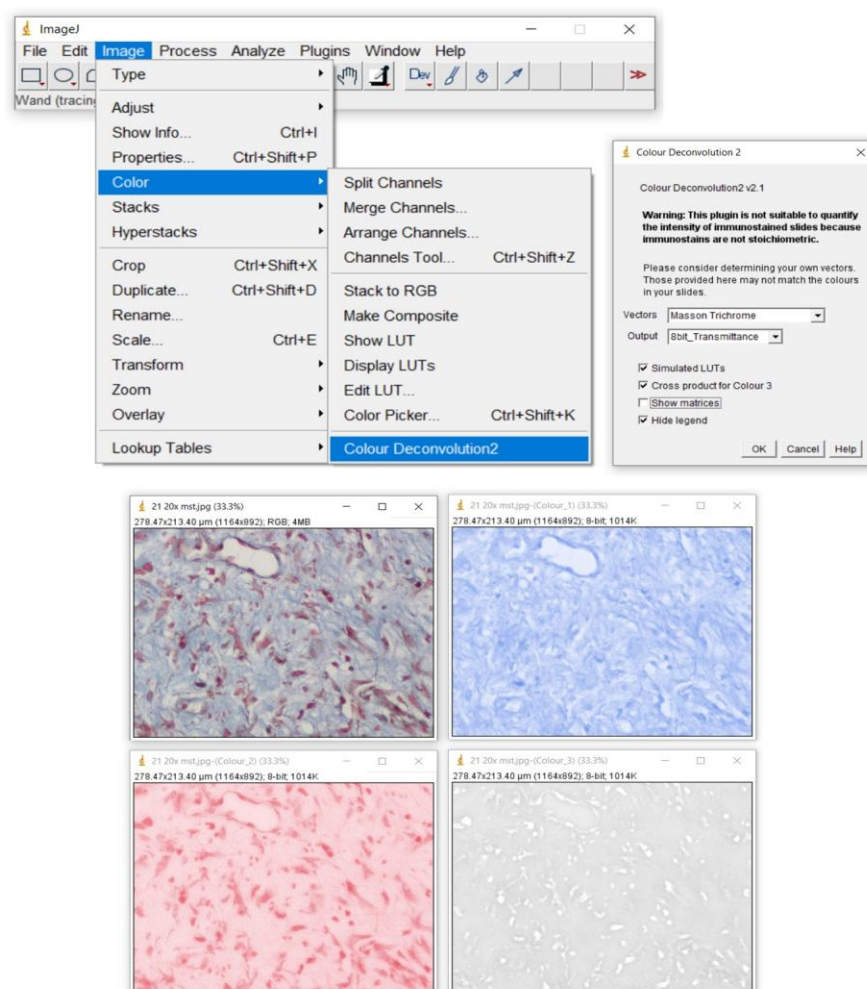


Figure 2 Steps for performing collagen quantification using image deconvolution technique in ImageJ. Choose the Masson's Trichrome stain vector in the Colour Deconvolution dialog box. This will create separate grayscale images corresponding to each stain (red, blue and green components)

the scale bar. In the ImageJ main menu, go to "Analyse." Select "Set Scale." This will open the "Set Scale" dialog box. In the "Set Scale" dialog box, Enter the known distance of the scale bar (in micrometres) in the "Known Distance" box. Set the unit of length (e.g., μm) in the "Unit of Length" box. Click "OK" to set the scale. Open the image to analyze. The input images were converted to RGB images by clicking on the "Image" menu (Figure 1), clicking on the "Type" box, and then "RGB Color." Click on "Image" > "Color" in the menu bar and select "Colour Deconvolution2." In the Colour Deconvolution dialog box, the Masson's Trichrome stain vector should be chosen (Figure 2) (Ruifrok and Johnston 2001; Landini et al. 2021).

Parameters were set as indicated in Figure 3. This was followed by clicking "OK" to perform the colour deconvolution. This will create separate grayscale images corresponding to each stain (red, blue and green components) and select the grayscale image

corresponding to the collagen stain (blue). Click on "Image" > "Adjust" > "Threshold" to open the Threshold dialog box (Figure 3). Adjust the threshold settings to segment the collagen fibers accurately. The settings mentioned above are appropriate to achieve the best results. Click "Apply" to apply the threshold to the image, making the collagen fibers appear as a black and white binary image. In the ImageJ main menu, click on "Analyze." From the dropdown menu, select "Set Measurements." This will open the "Set Measurements" dialog box. In the dialog box, make sure the following options are checked: "Area" to measure the area of selected regions, "Standard Deviation" to calculate the standard deviation of pixel values within the selected regions (Ruifrok and Johnston 2001; Landini et al. 2021), "Area Fraction" to determine the fraction of the total area covered by the selected regions, "Display Label": to display labels or names for the measured regions, and "Limit to Threshold" to limit measurements to areas within the threshold (Figure 4).

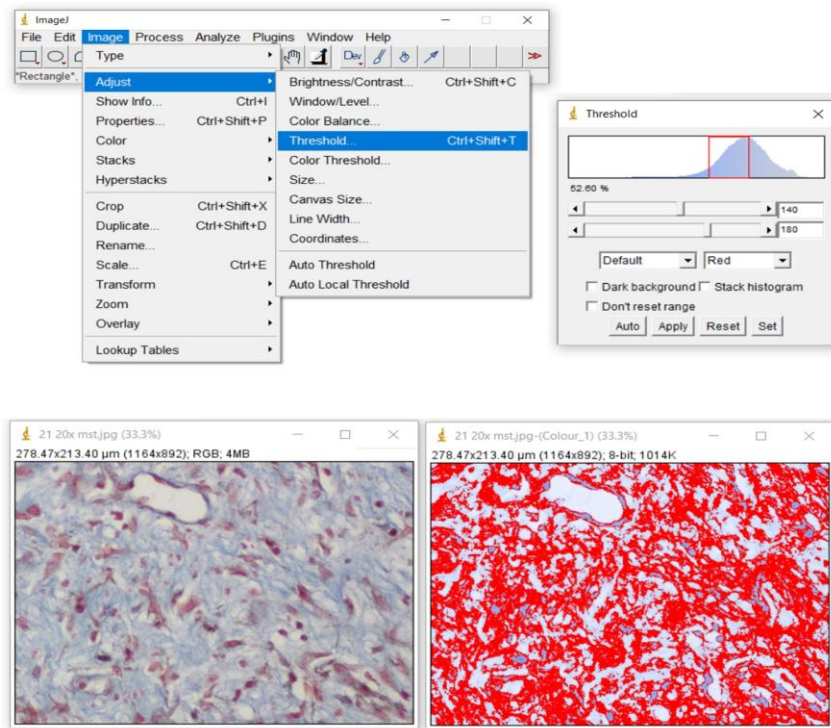


Figure 3 Steps for performing image thresholding in ImageJ. The grayscale image corresponding to the collagen stain (blue) will be selected. The threshold settings should be adjusted to segment the collagen fibers accurately

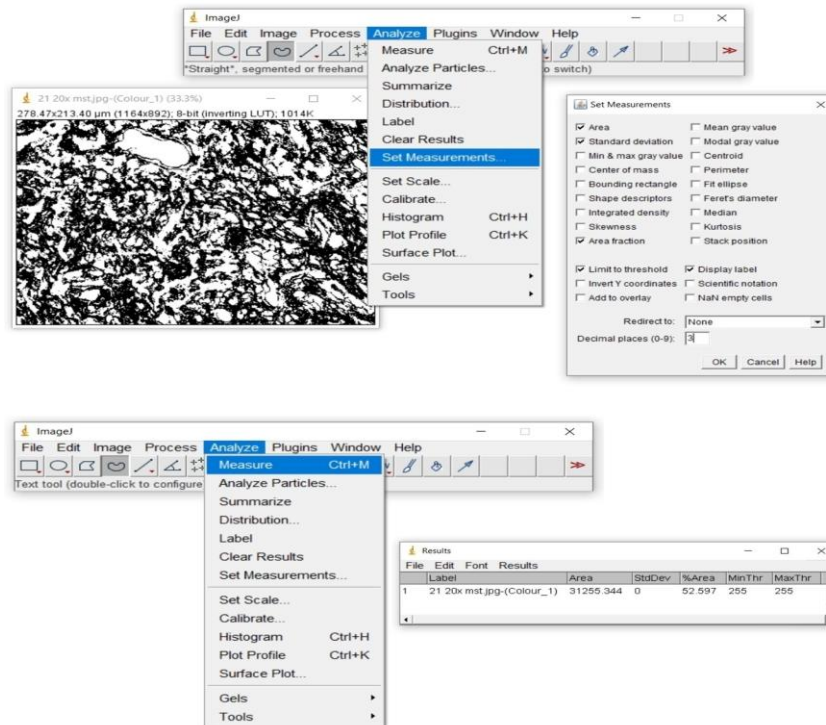


Figure 4 Steps for performing collagen quantification in ImageJ. Once the threshold is applied, the collagen fibers appear as a black and white binary image. Once the measurement parameters are set, ImageJ will calculate and measure the area, standard deviation, and area fraction of the regions of interest (ROIs) within the threshold

Go back to the ImageJ main menu and select "Analyze." From the dropdown menu, choose "Measure" (or "Ctrl + M" can be pressed on the keyboard). ImageJ will calculate and measure the area, standard deviation, and area fraction of the regions of interest (ROIs) within the threshold. The measurement results will be displayed in the "Results" window. To further analyze or quantify the ROIs, they can be manually selected and extracted by using tools such as the "ROI Manager" in ImageJ ("Analyze" > "Tools" > "ROI Manager"). Once the ROIs are selected, area-based analysis can be performed. The results table will show measurements of the collagen area in the selected image. To quantify collagen in multiple images, the steps for each image can be repeated (Ruifrok and Johnston, 2001; Landini et al. 2021). Export or save the measurement results for further analysis if needed. Import the measurement results into a spreadsheet program for data analysis and visualization.

2.3 Picosirius red staining for collagen estimation

PSR stain (Solution A) was prepared by mixing 0.5 g of Direct Red 80/Sirius red F3B (Sigma-Aldrich, Catalog # 365548) in 500 ml of saturated aqueous solution of picric acid. This solution was considered stable and can be stored for at least 3 years and used multiple times. Solution B is acidified water made by mixing 5 ml of glacial acetic acid in 1 litre of distilled water. The tissue sections were deparaffinized by incubating them in xylene (two changes) and then rehydrated by passing them through a graded ethanol series (100%, 90%, 70%, 50% and distilled water). The nuclei were stained using Weigert's iron haematoxylin (8 min) and the

slides for 10 minutes in running tap water. The sections were stained in PSR (Solution A) for one hour. It has to be noted that longer staining time with PSR did not improve the staining quality, but shorter staining times were discouraged, even if the colours appeared satisfactory.

After staining, the sections were washed in two changes of acidified water (Solution B). Most of the water was removed from the slides either by vigorous shaking or, in the case of a few slides, by blotting with damp filter paper. The sections were then dehydrated in three changes of 100% ethanol. Finally, the sections were cleared in xylene and mounted using a mounting medium and coverslip. Once the slides were prepared, the collagen fibers were visualized using a light microscope.

2.4 Collagen quantification in picosirius stained sections

Open the image of the picosirius stained tissue section in ImageJ. Measure the scale bar in the image using the straight-line selection tool. Create a line selection along the length of the scale bar. Go to "Analyze" in the menu bar and select "Set Scale." In the "Set Scale" dialog box, Ensure that the "Distance in Pixels" field is automatically populated with the length of the line selection. Enter the known distance (in μm) in the "Known Distance" field. Set the "Unit of Length" to " μm " (micrometres). Click "OK" to apply the scale to the image. In the menu bar, go to "Image" and select "Type," then choose "RGB Stack" to split the image into its red, green, and blue channels (Figure 5). After splitting, go to "Image" and select "Stacks," then choose "Make Montage" to view all three

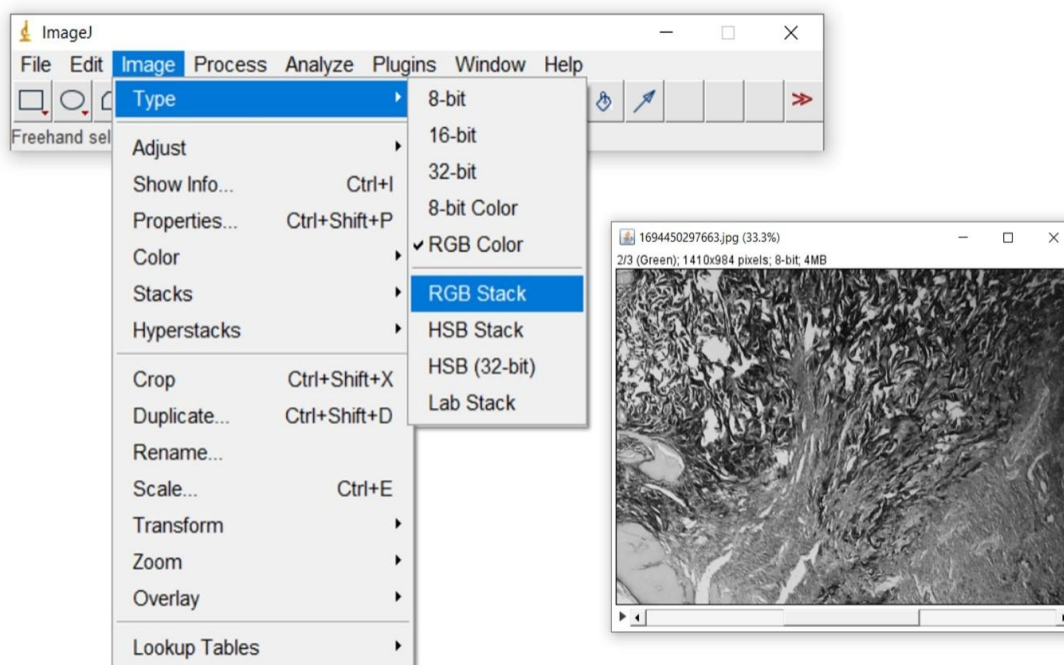


Figure 5 Steps for performing collagen quantification using RGB stacking technique in ImageJ

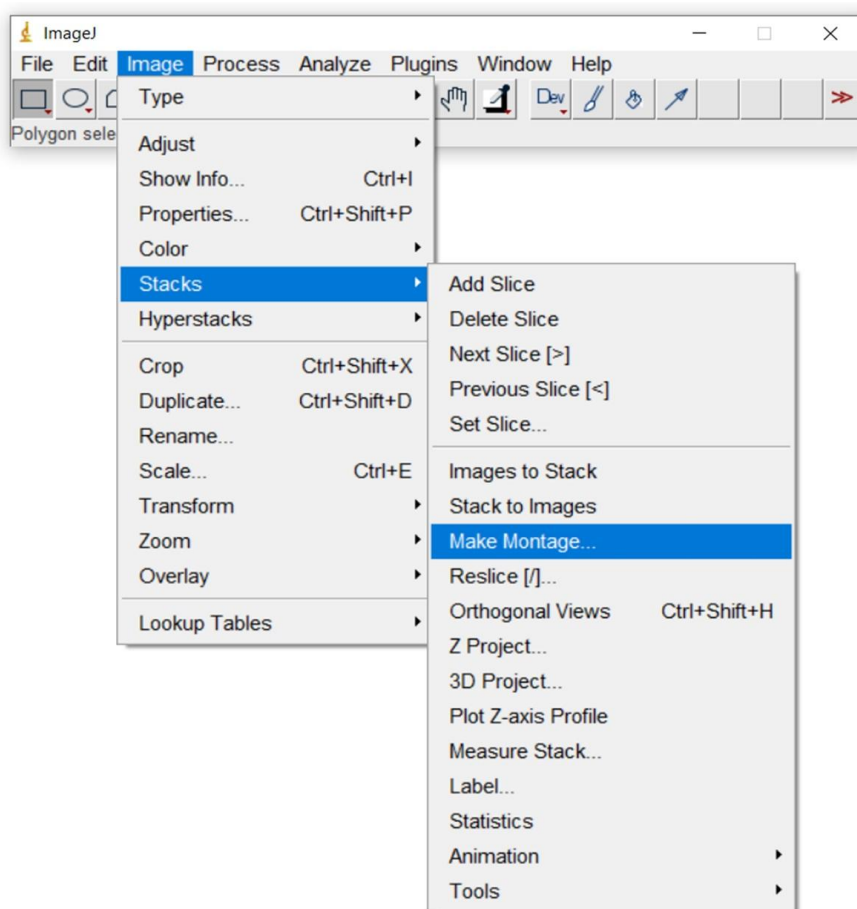


Figure 6 Steps for performing collagen quantification using RGB stacking technique in ImageJ. This will split the image into its red, green, and blue channels. A montage was done to view all three channels simultaneously

channels simultaneously (Figure 6) (Ruifrok and Johnston 2001; Landini et al. 2021). Select the RGB stack, making sure the green channel is chosen. While the Green channel is selected, go to "Image," then select "Adjust" and choose "Threshold." The "Threshold" tool will open, and the green channel will be thresholded automatically.

However, the threshold for accurate collagen detection was manually adjusted. Move the lower slider to the right until the red-stained collagen is highlighted in red while the background is

mostly black. Once the threshold is set correctly, click "Apply" in the "Threshold" tool. Open the "Analyze" menu and select "Set Measurements." In the "Set Measurements" dialog box, check the following options: "Area," "Area Fraction," "Limit to Threshold," and "Display Label." Close the "Set Measurements" dialog. To measure the thresholded collagen area, go to "Analyze" and choose "Measure." The area and percent area of the thresholded collagen will be displayed in the "Results" window (Figure 7) (Ruifrok and Johnston 2001; Landini et al. 2021).

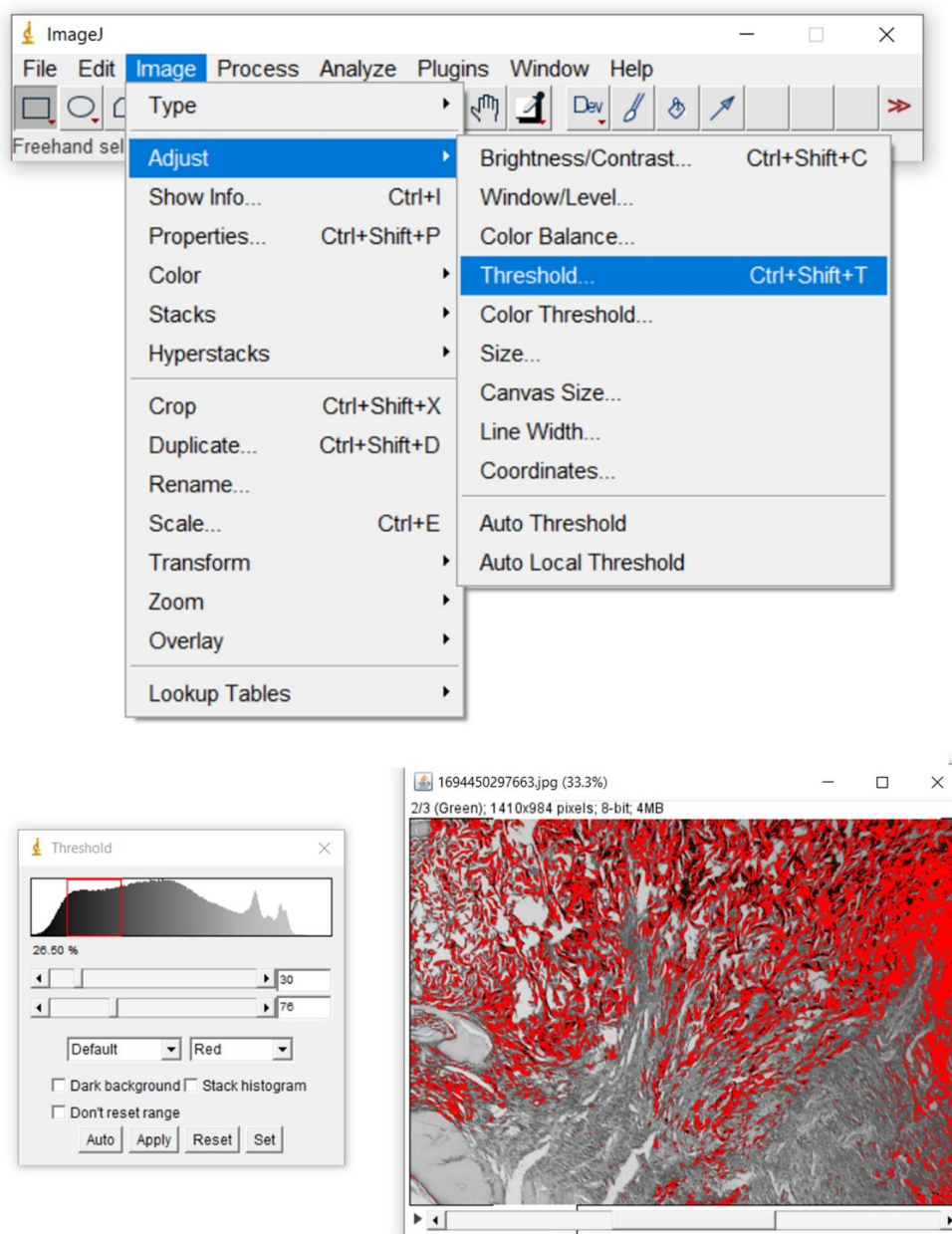


Figure 7 Steps for performing collagen quantification using RGB stacking technique in ImageJ.
The threshold settings should be adjusted to segment the collagen fibers accurately

3 Results

3.1 Masson's Trichrome versus Picrosirius Red Staining

In MT staining, collagen fibers are stained blue. By staining collagen blue, this technique allows for the visualization and assessment of collagen distribution and content in tissue samples (Figure 8). Blue-stained collagen fibers are often seen as tissues' structural framework or scaffold. Muscle fibers, cytoplasm, and keratinized structures (such as keratinized skin cells) are stained

red or pink in MT staining. This staining is achieved using Biebrich scarlet-acid fuchsin solution. The dark black colouration of the nuclei results from the staining with Weigert's iron haematoxylin.

In PSR staining, collagen appeared red against a pale-yellow background under brightfield microscopy (Figure 8). The nuclei ideally appeared black, although they might often appear grey or brown due to the extended exposure to picrosirius red, which caused some degree of de-staining of the nuclei.

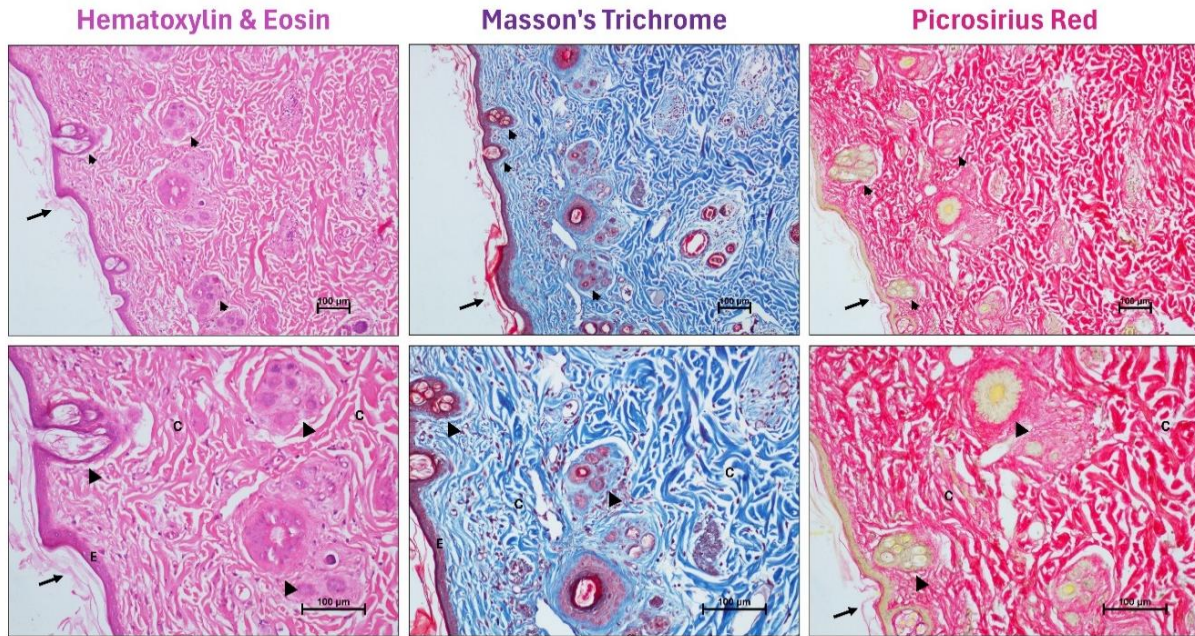


Figure 8 Photomicrographs of healthy rabbit skin from dorsum showing normal histological structures (Top panels - x100 and Lower panels - x200). The stained section of normal rabbit skin shows a well-organized structure with intact epithelium, hair follicles, and a loose connective tissue dermis. Note: keratin layer (black arrow), epidermis (E), collagen fibers (C), hair follicles (black arrowhead)

Masson's Trichrome Vs Picrosirius Red

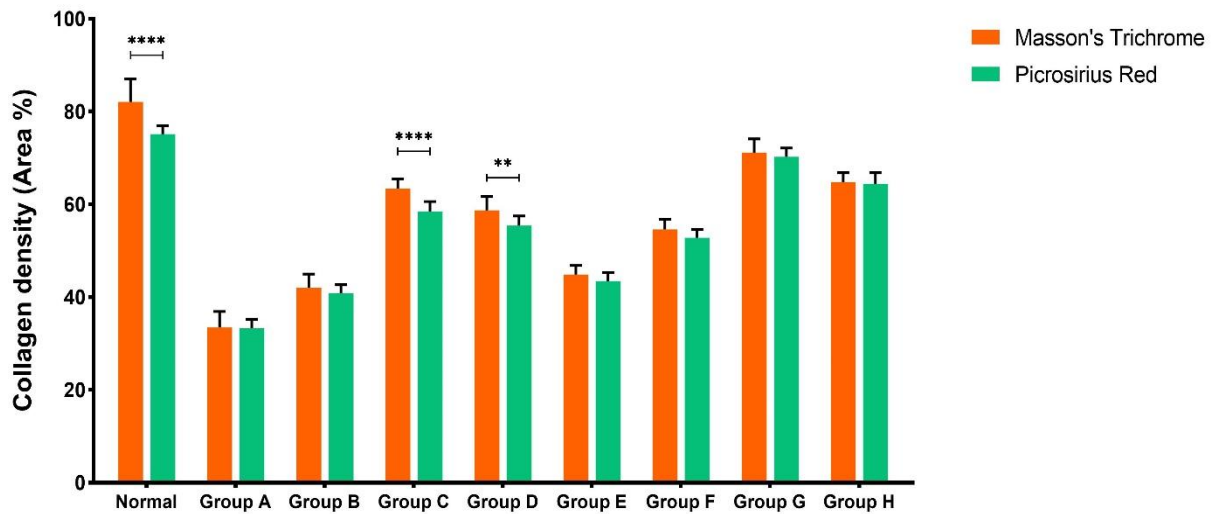


Figure 9 Comparative analysis of collagen density (Area %) values generated from MT and PSR stained sections using colour deconvolution and RGB stack methods. Note: ** - $p < 0.01$ and **** - $p < 0.0001$

3.2 Comparison of collagen density in Masson's Trichrome and Picrosirius Red stained sections

We compared the collagen density values obtained using two different staining methods, PSR and MT (Figure 9). This provides insights into how these techniques measure collagen

content and organization in the healing wounds of the studied groups. The baseline collagen density in healthy skin, measured with PSR staining, was $75.15 \pm 1.78\%$. MT staining, on the other hand, indicated a slightly higher baseline collagen density of $82.08 \pm 4.95\%$. Across the treatment groups, both staining methods generally showed a trend of increased collagen density

compared to the control group. For most groups, PSR staining consistently indicated slightly lower collagen densities than MT staining. However, the overall trends were similar.

The comparison between PSR and MT staining methods revealed that both techniques are effective in assessing collagen density in healing wounds. However, there were subtle differences in the absolute values obtained, with PSR tending to yield slightly lower collagen density measurements than MT. These differences can be attributed to the distinct mechanisms of these staining methods. PSR specifically stains collagen fibers and provides an enhanced visualization of collagen organization, making it suitable for assessing collagen fiber quality and maturity.

4 Discussion

The histological assessment conducted by trained pathologists utilizing semi-quantitative scoring techniques has traditionally been employed for evaluating collagen fiber density. Nevertheless, the subjective nature of this histologic evaluation is susceptible to inter-observer bias, leading to diminished accuracy and reproducibility due to inherent methodological constraints (Lee et al. 2001). Previous studies have focused on assessing collagen fibers by categorizing them based on the different scoring systems. Regrettably, this system was limited to demonstrating qualitative improvements and couldn't provide quantitative data (Meyer et al. 2017). In contrast, the methodology used in this study facilitates the direct comparison of collagen fiber density using continuous values and rigorous statistical analysis, allowing for a quantitative assessment of the therapeutic effects. MT stain is a histological staining method that uses multiple dyes to distinguish various tissue components. The stain typically consists of Weigert's Haematoxylin (stains nuclei dark purple or black), Aniline blue (stains collagen fibers blue), and Biebrich scarlet-acid fuchsin (stains cytoplasm other cellular components red).

MT techniques effectively provide intense staining for collagen fibers in connective tissue. This technique is best for collagen fibres' quantitative visualization and analysis capabilities. However, they fall short in selectively staining specific structures, such as the basal membrane (Constantine and Mowry 1968). This lack of selectivity poses challenges in accurately differentiating structures, especially in the presence of thin collagen fibers that may exhibit different colours within the same tissue section. MT staining is hindered by a background stained red by the dye, complicating the distinction between true colours observed (Street et al. 2014).

PSR staining is a more straightforward and highly effective method for examining collagen arrangement. This technique offers results superior to routine staining techniques (Juengsomjit et al.

2022). This technique involves Sirius red reacting with basic groups in collagen molecules through its sulfonic acid groups, thereby effectively staining the collagens (Junqueira et al. 1979). Unlike trichrome staining, PSR staining has been widely regarded as the benchmark for detecting and quantitatively estimating collagen in histological sections of both normal and abnormal tissues (Segnani et al. 2015).

A study evaluated a porcine model for pathomorphological age assessment of surgically excised skin wounds. The results were assessed through special staining techniques involving MT and picrosirius red. MT and PSR stains confirmed newly formed collagen and effectively evaluated increased collagen deposition (Barington et al. 2018). Both these stainings have addable advantages in predicting the variation in levels of myofibroblast and collagen in wound healing (Owens et al. 2010).

The principle begins with colour deconvolution, which separates these individual stains into distinct grayscale channels. The Colour Deconvolution plugin in ImageJ takes advantage of the fact that each stain has a characteristic colour spectrum (Ruifrok and Johnston 2001; Landini et al. 2021). Using mathematical algorithms, the plugin separates the RGB (Red-Green-Blue) colour channels of the stained image into grayscale images corresponding to each stain. In this case, the blue collagen stain is isolated. After separating the collagen stain into a grayscale image, the next step involves setting a suitable threshold (Chen et al. 2017). Thresholding converts the grayscale image into a binary image, where the collagen fibers appear black against a white background. This is achieved by specifying intensity values above which pixels are considered part of the collagen (black) and below which they are not (white) (Chen et al. 2017). The choice of thresholding values depends on the image's staining intensity and background noise. After measuring the collagen area in one or more images, analysis was done to derive quantitative information (total collagen area) (Chen et al. 2017; Elshazly et al. 2023).

Conclusion

Picrosirius Red staining consistently indicated slightly lower collagen densities than Masson's Trichrome staining. However, the overall trends were similar in both staining. The comparison between Picrosirius Red and Masson's Trichrome staining methods revealed that both techniques effectively assess collagen density in healing wounds. However, there were subtle differences in the absolute values obtained, with Picrosirius Red staining tending to yield slightly lower collagen density measurements than Masson's Trichrome. These differences can be attributed to the distinct mechanisms of these staining methods. Therefore, based on our findings, both staining methods can digitally quantify collagen density in wound healing research.

Acknowledgements

The authors thank the Director, ICAR-Indian Veterinary Research Institute, Izatnagar, Bareilly, India, and the All-India Network Program on Diagnostic Imaging and Management of Surgical Conditions in Animals (AINP-DIMSCA) for providing the necessary research facilities to carry out this work.

Funding

The authors declare that no funds, grants, or other support were received during the preparation of this manuscript.

Data availability

Datasets supporting the conclusions of this article are included within the manuscript.

Declarations

Competing interests

All authors declare that no commercial or financial relationships exist that could, in any way, lead to a potential conflict of interest.

Ethics approval and consent to participate

All experimental protocols used in the study were approved by the Institutional Animal Ethics Committee (IAEC), ICAR-Indian Veterinary Research Institute, vide order No. 26-1/2022-23/JD(R) under protocol no. IAEC/07.07.2022/S31.

References

Banu, S. A., Pawde, A. M., Sharun, K., Kalaiselvan, E., Shivaramu, S., et al. (2023). Evaluation of bone marrow-derived mesenchymal stem cells with eggshell membrane for full-thickness wound healing in a rabbit model. *Cell and tissue banking*, 10.1007/s10561-023-10105-0.

Barington, K., Dich-Jørgensen, K., & Jensen, H. E. (2018). A porcine model for pathomorphological age assessment of surgically excised skin wounds. *Acta veterinaria Scandinavica*, 60(1), 33.

Bist, D., Pawde, A. M., Amarpal, Kinjavdekar, P., Mukherjee, R., et al. (2021). Evaluation of canine bone marrow-derived mesenchymal stem cells for experimental full-thickness cutaneous wounds in a diabetic rat model. *Expert opinion on biological therapy*, 21(12), 1655–1664.

Chang, J. Y., & Kessler, H. P. (2008). Masson trichrome stain helps differentiate myofibroma from smooth muscle lesions in the head and neck region. *Journal of the Formosan Medical Association*, 107(10), 767–773.

Chen, Y., Yu, Q., & Xu, C. B. (2017). A convenient method for quantifying collagen fibers in atherosclerotic lesions by ImageJ software. *International Journal of Clinical and Experimental Medicine*, 10(10): 14904-14910.

Constantine, V. S., & Mowry, W. (1968). Selective staining of human dermal collagen. *The Journal of Investigative Dermatology*, 50(5), 414-18.

Costa, G. M., Araujo, S. L., Xavier Júnior, F. A. F., Morais, G. B. D., Silveira, J. A. D. M., Viana, D. D. A., & Evangelista, J. S. A. M. (2019). Picrosirius red and Massons Trichrome staining techniques as tools for detection of collagen fibers in the skin of dogs with endocrine dermatopathologies. *Ciência Animal Brasileira*. e-55398.

Elshazly, N., Saad, M. M., El Backly, R. M., Hamdy, A., Patrino, M., et al. (2023). Nanoscale borosilicate bioactive glass for regenerative therapy of full-thickness skin defects in rabbit animal model. *Frontiers in Bioengineering and Biotechnology*, 11, 1036125.

Juengsomjit, R., Meesakul, O., Arayapisit, T., Larbcharoensub, N., & Janebodin, K. (2022). Polarized Microscopic Analysis of Picrosirius Red Stained Salivary Gland Pathologies: An Observational Study. *European journal of dentistry*, 16(4), 930–937.

Junqueira, L.C., Bignolas, G., & Brentani, R.R. (1979). Picrosirius staining plus polarization microscopy, a specific method for collagen detection in tissue sections. *Journal of Histochemistry & Cytochemistry*, 11(04):447–455.

Kular, J. K., Basu, S., & Sharma, R. I. (2014). The extracellular matrix: Structure, composition, age-related differences, tools for analysis and applications for tissue engineering. *Journal of tissue engineering*, 5, 2041731414557112.

Landini, G., Martinelli, G., & Piccinini, F. (2021). Colour deconvolution: stain unmixing in histological imaging. *Bioinformatics*, 37(10), 1485-1487.

Lattouf, R., Younes, R., Lutomski, D., Naaman, N., Godeau, G., Senni, K., & Changotade, S. (2014). Picrosirius red staining: a useful tool to appraise collagen networks in normal and pathological tissues. *The journal of histochemistry and cytochemistry*, 62(10), 751–758.

Lee, E. S., Kim, J. H., Im, S., Lee, K. B., Sohn, S., & Kang, W. H. (2001). Application of computerized image analysis in pigmentary skin diseases. *International Journal of Dermatology*, 40(1), 45-49.

- López De Padilla, C. M., Coenen, M. J., Tovar, A., De la Vega, R. E., Evans, C. H., & Müller, S. A. (2021). Picrosirius Red Staining: Revisiting Its Application to the Qualitative and Quantitative Assessment of Collagen Type I and Type III in Tendon. *The journal of histochemistry and cytochemistry*, *69*(10), 633–643.
- Marcos-Garcés, V., Harvat, M., Molina Aguilar, P., Ferrández Izquierdo, A., & Ruiz-Saurí, A. (2017). Comparative measurement of collagen bundle orientation by Fourier analysis and semiquantitative evaluation: reliability and agreement in Masson's trichrome, Picrosirius red and confocal microscopy techniques. *Journal of microscopy*, *267*(2), 130–142.
- Meyer, P. F., de Oliveira, P., Silva, F. K. B. A., da Costa, A. C. S., Pereira, C. R. A., Casenave, S., Valentim Silva, R. M., et al. (2017). Radiofrequency treatment induces fibroblast growth factor 2 expression and subsequently promotes neocollagenesis and neoangiogenesis in the skin tissue. *Lasers in Medical Science*, *32*(8): 1727-1736.
- Owens, P., Engelking, E., Han, G., Haeger, S. M., & Wang, X. J. (2010). Epidermal Smad4 deletion results in aberrant wound healing. *The American journal of pathology*, *176*(1), 122-133.
- Ruifrok, A. C., & Johnston, D. A. (2001). Quantification of histochemical staining by color deconvolution. *Analytical and quantitative cytology and histology*. *23*(4):291-9.
- Segnani, C., Ippolito, C., Antonioli, L., Pellegrini, C., Blandizzi, C., Dolfi, A., & Bernardini, N. (2015). Histochemical Detection of Collagen Fibers by Sirius Red/Fast Green Is More Sensitive than van Gieson or Sirius Red Alone in Normal and Inflamed Rat Colon. *PLoS one*, *10*(12), e0144630.
- Sharma, R., Rehani, S., Mehendiratta, M., Kardam, P., Kumra, M., et al. (2015). Architectural Analysis of Picrosirius Red Stained Collagen in Oral Epithelial Dysplasia and Oral Squamous Cell Carcinoma using Polarization Microscopy. *Journal of clinical and diagnostic research*, *9*(12), EC13–EC16.
- Street, J. M., Souza, A. C., Alvarez-Prats, A., Horino, T., Hu, X., Yuen, P. S., & Star, R. A. (2014). Automated quantification of renal fibrosis with Sirius Red and polarization contrast microscopy. *Physiological reports*, *2*(7), e12088.
- Van De Vlekkert, D., Machado, E., & d'Azzo, A. (2020). Analysis of Generalized Fibrosis in Mouse Tissue Sections with Masson's Trichrome Staining. *Bio-protocol*, *10*(10), e3629.



Journal of Experimental Biology and Agricultural Sciences

<http://www.jebas.org>

ISSN No. 2320 – 8694

Ecological desalination of anchovy residues and their mixture with soybean meal for the production of poultry feed: Optimization of waste through response surface methodology (RSM)

Ilham BOUMENDIL^{1*} , Mhammed SISOUANE² , Youness EL HAIMER³ ,
Nabil BOUNOUAR², Jihane KHAMLICH¹, Asmae BAGGAR¹ , Amal SAFTI¹ 

¹Laboratory Biochemistry Environment and Agri-food, Department of Biology, Faculty of Science and Technics Mohammedia, Hassan II University Casablanca, Morocco.

²Laboratory of Water and Environnement(LEE), Faculty of Sciences, Chouaib Doukkali University, PO Box 20, El Jadida, M-24000, Morocco.

³Laboratory of Coordination and Analytical Chemistry (LCCA), Faculty of Sciences, Chouaib Doukkali University, PO Box 20, El Jadida, M-24000, Morocco.

Received – June 13, 2023; Revision – October 06, 2023; Accepted – November 25, 2023

Available Online – November 30, 2023

DOI: [http://dx.doi.org/10.18006/2023.11\(5\).834.844](http://dx.doi.org/10.18006/2023.11(5).834.844)

KEYWORDS

Salted anchovy bones

Poultry feed

Soybean meal

Response surface methodology

ABSTRACT

Salted anchovy bones are a non-recyclable waste product containing high salt levels. However, they also contain valuable minerals such as calcium, phosphorus, potassium, magnesium, and nitrogen. This study aimed to find a cost-effective method to desalinate anchovy bones while preserving their nutritional value and repurposing them as a raw material for poultry feed. Through various tests, we were able to reduce the salt content of the anchovy bones from 15.4% to 4.7% using a 50/50 percent mixture of tap water and from 15.4% to 3.7% using a mixture of tap water and soybean meal in a 30/70 percent ratio. Combining soybean meal with desalted anchovy bones resulted in a nutritional composition comparable to that found in poultry feed, reducing salt content. The response surface method (RSM) was employed to determine the optimal proportions of desalted anchovy bones (70-90%) and soybean meal (10-30%) and to study the variables affecting the concentrations of NaCl, Ca, P, Ash, and TNM. The study revealed the influence of desalted anchovy bone and soybean meal percentages on these concentrations. This study demonstrates that the method used provides an ideal approach for understanding the interactions between input parameters (% DAR, % SM) and output parameters (NaCl, Ca, P, Ash, and TNM) and shows promising results for the desalination of anchovy bones using a soybean meal cake as well as the feasibility of creating poultry feed.

* Corresponding author

E-mail: ilhamboumendil@gmail.com (Ilham BOUMENDIL)

Peer review under responsibility of Journal of Experimental Biology and Agricultural Sciences.

Production and Hosting by Horizon Publisher India [HPI]
(<http://www.horizonpublisherindia.in/>).
All rights reserved.

All the articles published by [Journal of Experimental Biology and Agricultural Sciences](#) are licensed under a [Creative Commons Attribution-NonCommercial 4.0 International License](#) Based on a work at www.jebas.org.



1 Introduction

The European anchovy (*Engraulis encrasicolus*) is a highly significant small pelagic fish in terms of biomass and commercial interest (Fernández-Corredor et al. 2021), and it represents one of the most important fisheries in the Mediterranean region (Paone et al. 2021). The production of anchovy fillets generates substantial biological waste in the form of bones (Paone et al. 2021). Maritime countries eat primarily fish (Nurulnadia et al. 2021). Moreover, salting anchovies results in a large volume of residues containing a high NaCl content, which is typically discarded (Marchetti et al. 2021). These discards are considered wasteful regarding fishery resources, representing a significant portion of the overall marine harvest (Washington and Ababouch 2011, Ababouch et al. 2009). Fish bones comprise approximately 70% inorganic and 30% organic matter by weight (Kizilkaya et al. 2010). The majority of the inorganic fraction is composed of hydroxyapatite (HAP), which is a form of calcium phosphate with the chemical formula $\text{Ca}_{10}(\text{PO}_4)_6(\text{OH})_2$ (Kizilkaya et al. 2010). Salt waste poses a significant challenge to the recycling of fishery products (Boumendil et al. 2020). Unfortunately, information regarding salted fishmeal is scarce (Hasan et al. 2019). Given its properties, the biological waste from canned fish, specifically the bones, can serve as a starting point for poultry feed production after being rinsed with drinking water to reduce its high NaCl content. Plant by-products are considered nutrient-rich sources and inexpensive functional substances with diverse potential applications (Taarji et al. 2018). Soy sauce is an excellent alternative to replace NaCl without compromising the nutritional value of the feed (Kremer et al. 2009). However, soybean meal is highly sought-after in the animal feed sector due to its protein richness. Therefore, in this study, the desalted waste derived from anchovy bones will be valorized by incorporating soybean meal as a co-substrate. The primary objective of this study is to develop an environmentally friendly desalination process that preserves the nutritional value of anchovy bones. The secondary aim is to enhance the value of these bones in the animal feed sector. To achieve these goals, the response surface method (RSM) will be employed to determine the optimal ratios of desalted anchovy bone waste (70-90%) and

soybean meal (10-30%) for desalination anchovy bones and preparing poultry feed.

2 Materials and Methods

2.1 Raw materials

In this study, salted anchovy (*Engraulis encrasicolus*) bones were collected in August 2022 from an industrial plant in Morocco. They were then transported in a cooling box at approximately 4°C.

2.2 Preparation of Anchovy Bones

Under laboratory conditions, the salted anchovy bones were separated from the meat and dried at 60°C until a constant weight was achieved. The dried bones were ground by a blender and sieved to a size of 800 µm for further processing.

2.3 Removal of Salt Content

A solid-liquid extraction method was employed to remove the salt content from the anchovy bones. The bones were immersed in potable water in a ratio of 50% bones to 50% water (m/v). The extraction process was conducted at 25°C with magnetic stirring at 300 rpm for 24 hours. After the extraction, the mixture was filtered, and the resulting solution was stored in a refrigerator until its final use.

2.4 Physicochemical analysis of anchovy bones and soybean meal

The results of each desalination test represent the average of three repetitions. The NaCl salt content in anchovy bones was determined using the titrimetric method (Ababouch et al. 2009). The ash content was obtained by incinerating the sample for 12 hours at a temperature of 550°C (Köprücü and Özdemir 2005). The resulting ash was dried at 105°C until a constant mass (AOAC 1990). The fat content was determined at 100°C according to the procedure described in (AOAC 2005). The total nitrogen content was determined using the Kjeldahl (Horwitz and International 2000). The crude cellulose fraction was determined by the AOAC



Figure 1 The raw materials used in this study: (a) salted anchovy bones, (b) desalted anchovy bones and (c) soybean meal

method (AOAC and Horwitz 1975). The Ca, Mg, K, and P ions concentrations were measured following the protocols described in AOAC and Horwitz (1975).

2.5 Experimental Design

To analyze the collected data and determine the correlation between the dependent and independent variables, regression analysis with Response Surface Methodology (RSM) was employed using Design-Expert software version 13.0.14.0. The objective was to investigate the response (Yi) of specific constant factors, i.e., Salt (%), Ca (g/kg), P (g/kg), ash (%), and TNM (%). A mathematical equation representing each response surface (Yi) was used. The main purpose of RSM is to optimize operating conditions that meet specific requirements (Myers et al. 2016).

The polynomial equation (1), shown at the bottom of the diagram, describes the response Y:

$$Y = f(y) = \beta_0 + \beta_1X_1 + \beta_2X_2 + \beta_{12}X_1X_2 + \beta_{11}X_1^2 + \beta_{22}X_2^2 + \varepsilon \quad (1)$$

In equation (1), Yi represents the predicted response corresponding to the independent variables Xi (i = 1, 2), β_0 is the constant term, β_{ij} (i = 1, 2 and j = 1, 2) represents the interaction terms between variables and quadratic terms, where i and j are the coefficients of the linear terms, and ε represents the residual error.

The significance and fit of each finding in the developed model were carefully examined. Non-significant terms were removed using the same program, and an intervention surface plot was generated. The response surface method (RSM) was utilized to optimize the method parameters for modifying the nutrient composition of the manufactured poultry feed. The independent variables analyzed were the amounts of desalted anchovies and soybean meal. The goal was to maximize the yield (Y) of salts, phosphorus (g/Kg), TNM%, Ash%, and Ca (g/Kg). The central Composite Design (CCD) is a useful technique in statistical design that allows the investigation of component impacts on responses and optimization studies. By employing this technique, a quadratic surface can be fitted, enabling the analysis of parameter relationships while reducing the number of required tests. A CCD-based batch experiment was conducted to evaluate the effect of desalted anchovy and soybean meal proportions on poultry feed synthesis. The design space was constructed in the initial tests, and

the factors were encoded at ± 1 for the factorial points and 0 for the center point. As shown in Table 1, these codes indicate the range of variation for each factor. This study aimed to develop a method for natural desalination by combining soybean meal and desalted anchovies to create an optimal poultry feed.

3 Results and Discussion

3.1 Nutrient composition of raw materials

Unused salted fishmeal, particularly in the case of salted fish, causes significant losses to the canning industries. Desalting has been investigated as a solution to this problem. It involves the solid-liquid extraction of various components, such as Na⁺ and Cl⁻ ions, and soluble proteins from the salted product into the desalting water. Research has shown that replacing salt with soy sauce is an effective method for reducing the sodium content. Consequently, the concept of desalting fishmeal using potable water and soybean meal and creating future “poultry products” was developed. The chemical composition of soybean meal (SM), desalted anchovy residue (DAR), and salted anchovy residue (SAR) produced is presented in Table 2. The salted anchovy residues were successfully rinsed to remove a significant amount of salts (from 15.4% to 4.7%) without significantly altering the other chemical characteristics of the anchovy residues.

The results presented in Table 1 are based on a comprehensive examination of the experimental parameters and independent variables. The results obtained from the various formulations tested during the experiment are shown in Table 2. The study aimed to develop a regression model that accurately represents the relationships between the dependent and independent variables. To achieve this goal, the researchers employed Response Surface Methodology (RSM) and conducted preliminary tests to optimize the process. Table 3 was used for a precise and reliable evaluation of the variable responses before constructing the RSM mathematical model and determining the ideal experimental conditions to achieve the desired response values. The study focused on analyzing the effects of desalted anchovy proportions (X1), soybean meal proportions (X2), and their interactions on the levels of salt (%), Ca (g/Kg), P (g/Kg), Ash (%), and TNM (%) at two distinct levels.

The data presented in Table 3 were obtained from empirical assessments, as described in Table 4, and served as the basis for

Table 1 Factor levels of independent variables for poultry feed synthesis.

Independent variables	Variables coded	Unit	Range and level of actual and coded values		
			-1	0	1
Desalted Anchovies Residues (DAR) (%)	X1	%	70	80	90
Soybean Meal (SM) (%)	X2	%	10	20	30

Table 2 Chemical composition of anchovy bones and soybean meal

Settings	Samples		
	SAR	DAR	SM
%Salt	15.4	4.70	0.4
Dry matter %	94.83	96.18	90.40
Ash%	16.09	13.98	7.50
Ca (g/Kg)	34.80	27.15	4.2
Mg (g/Kg)	3.50	3.02	3.0
K (g/Kg)	3.80	3.10	22.1
P(g/Kg)	17.4	14.2	6.8
TNM %	34.12	29.73	38.08
MG%	7.12	5.83	3.31
CB%	0.00	0.00	6.39

SAR: salted anchovies residues, DAR: desalted anchovies residues, and SM: soybean meal.

Table 3 Real value with responses of independent factors

Factors			Responses			
DAR (%)	SM (%)	Salt (%)	Ca (g/Kg)	P (g/Kg)	Ash (%)	TNM (%)
70	10	3.33	19.425	10.62	10.536	24.619
70	20	3.37	19.845	11.3	11.286	28.427
70	30	3.41	20.265	11.98	12.036	32.235
80	10	3.8	22.14	12.04	11.934	27.592
80	20	3.84	22.56	12.62	12.84	31.34
80	20	3.94	22.5	12.72	12.684	31.4
80	20	3.89	22.6	12.82	12.64	31.44
80	20	3.78	22.66	12.66	12.74	31.49
80	30	3.88	22.98	13.4	13.434	35.208
90	10	4.27	24.855	13.46	13.332	30.565
90	20	4.31	25.275	14.14	14.082	34.373
90	30	4.35	25.695	14.82	14.832	38.181

SAR: salted anchovies residues, DAR: desalted anchovies Residues, SM: soybean meal

the models created in this study. These models established the relationship between the independent variables and the five response variables are salt (%), Ca (g/Kg), P (g/Kg), Ash (%), and TNM (%), using a second-order polynomial equation. Desalted anchovy and soybean meal amounts were denoted as X1 and X2, respectively. The two-factor interaction coefficients (X1X2) and the second-order terms (X1² and X2²) represented the quadratic impact and the interaction between two factors, respectively. The coefficients (X1 and X2) with only one factor represented the separate effects of each component. According to Filli et al.

(2010), favourable regression terms indicated synergistic effects, while negative values indicated antagonistic effects.

3.2 Analysis of variance (ANOVA)

Analysis of variance (ANOVA) was used to analyze the principal composite design, dividing the information into four distinct categories, i.e. sequential P-value, unadjusted P-value, adjusted R-squared value, and predicted R-squared value. The P-value summary of the ANOVA study (Table 3) showed a link with the

Table 4 Assessment of the second-order polynomial equation derived for the five responses

Response variables	Second-order polynomial models	Regression coefficient	
		R ²	Radj ²
SALT %	$-0.75+0.065*\text{DAR}+0.0085*\text{SM}+5.86\text{E}-13*\text{DAR} * \text{SM}-1.112\text{E}-4\text{DAR}^2-1.12\text{E}-4*\text{SM}^2$	0.9893	0.9804
TNM%	$-0.58+0.311*\text{DAR}+0.3843*\text{SM}+2.93\text{E}-12\text{DAR} * \text{SM}- 8.7\text{E}-5*\text{DAR}^2-8.7\text{E}-5*\text{SM}^2$	0.9999	0.9998
Ash%	$-1.39+0.083\text{SM}+ 3.58\text{E}-12*\text{DAR} * \text{SM}-2.1\text{E}-4*\text{DAR}^2-2.1\text{E}-4*\text{SM}^2$	0.9984	0.9971
Ca(g/Kg)	$-0.66+0.288\text{DAR}*\text{DAR}+0.046*\text{SM}+6.2145\text{E}-17\text{DAR}*\text{SM}-0.1\text{E}-3*\text{DAR}^2-0.1\text{E}-3*\text{SM}^2$	0.9997	0.9994
P(g/Kg)	$0.50+0.13\text{DAR}*\text{DAR}+0.065*\text{SM} +4.15637\text{E}-17 * \text{DAR}*\text{SM}+7.5\text{E}-5*\text{DAR}^2 -7.5\text{E}-5*\text{SM}^2$	0.9985	0.9972

*TNM: Total Nitrogen Material; *DAR: Desalted Anchovies Residues; *SM: Soybean Meal; *R²: coefficient of determination* Radj: Adjusted R².

proposed quadratic model. Any words with a P-value equal to or higher than 0.05 are now considered significant phrases according to the 95% criterion used.

ANOVA F-value tests were employed to assess the significance of each model type. In addition, a goodness-of-fit test was conducted to evaluate the appropriateness of the models. This test determines the suitability of the provided model by using it as the numerator in an F-test to examine the null hypothesis. The lack of fit was identified by comparing the variance around the model with the inherent variation within the repeated data. This test, as per the approach of Bhatti et al. (2011), has been employed for estimating model diversity. It was subsequently argued that the least significant quadratic model may not be suitable.

The results indicate that the linear and quadratic terms were the main variables influencing the performance of the parameter under

study. The number of terms in the model's R-squared was used to assess its ability to explain variability around the mean. However, Taran and Aghaie (2015) found that the adjusted R-squared tends to decrease as the number of terms increases, suggesting that adding more terms does not necessarily improve the model's value. The statistical program used in this analysis also tested regression models and assessed the significance of model-specific coefficients without considering a goodness-of-fit test. The significance of each coefficient was determined using the P-value, highlighting the importance of understanding the inherent interactions among the tested components (Shrivastava et al. 2008). As stated, a higher F-test result and a lower P-value indicate a greater significance level for the corresponding coefficient. The coefficient of variation (CV), obtained by dividing the estimate's standard deviation by the mean value of the observed response, was employed to assess the replicability and reproducibility of the models (Shrivastava et al. 2008). The calculations yielded CV values of 0.14% for TNM,

Table 5 Analysis of variance (ANOVA) for the full quadratic model

Source	Sum of Squares	df	Mean Square	F-value	p-value	
TNM Model	140.05	5	28.01	13685.44	< 0.0001	Significant
X ₁ -DAR	53.03	1	53.03	25913.34	< 0.0001	
X ₂ -SM	87.01	1	87.01	42513.56	< 0.0001	
X ₁ X ₂	0.0000	1	0.0000	0.0000	1.0000	
X ₁ ²	0.0002	1	0.0002	0.0998	0.7628	
X ₂ ²	0.0002	1	0.0002	0.0998	0.7628	
Residual	0.0123	6	0.0020			
Lack of Fit	0.0002	3	0.0001	0.0169	0.9964	Not significant
Pure Error	0.0121	3	0.0040			
Cor Total	140.05	11				
Std. Dev.	0.0452	R ²		0.9999		
Mean	31.41	Adjusted R ²		0.9998		
CV %	0.1440	Predicted R ²		0.9999		
		Adeq Precision		423.9649		

Source	Sum of Squares	df	Mean Square	F-value	p-value	
Salt Model	1.34	5	0.2672	111.24	< 0.0001	Significant
X ₁ -DAR	1.33	1	1.33	551.77	< 0.0001	
X ₂ -SM	0.0096	1	0.0096	4.00	0.0925	
X ₁ X ₂	0.0000	1	0.0000	0.0000	1.0000	
X ₁ ²	0.0003	1	0.0003	0.1405	0.7207	
X ₂ ²	0.0003	1	0.0003	0.1405	0.7207	
Residual	0.0144	6	0.0024			
Lack of Fit	0.0003	3	0.0001	0.0240	0.9940	Not significant
Pure Error	0.0141	3	0.0047			
Cor Total	1.35	11				
Std. Dev.	0.0490	R ²	0.9893			
Mean	3.85	Adjusted R ²	0.9804			
CV %	1.27	Predicted R ²	0.9817			
		Adeq Precision	29.4321			
Ash Model	15.10	5	3.02	770.40	< 0.0001	Significant
X ₁ -DAR	11.73	1	11.73	2990.42	< 0.0001	
X ₂ -SM	3.37	1	3.37	860.68	< 0.0001	
X ₁ X ₂	0.0000	1	0.0000	0.0000	1.0000	
X ₁ ²	0.0012	1	0.0012	0.2999	0.6037	
X ₂ ²	0.0012	1	0.0012	0.2999	0.6037	
Residual	0.0235	6	0.0039			
Lack of Fit	0.0012	3	0.0004	0.0526	0.9813	not significant
Pure Error	0.0224	3	0.0075			
Cor Total	15.13	11				
Std. Dev.	0.0626	R ²	0.9984			
Mean	12.70	Adjusted R ²	0.9971			
CV %	0.4932	Predicted R ²	0.9971			
		Adeq Precision	97.0203			
Ca Model	45.29	5	9.06	3919.03	< 0.0001	Significant
X ₁ -DAR	44.23	1	44.23	19136.83	< 0.0001	
X ₂ -SM	1.06	1	1.06	457.96	< 0.0001	
X ₁ X ₂	0.0000	1	0.0000	0.0000	1.0000	
X ₁ ²	0.0003	1	0.0003	0.1154	0.7457	
X ₂ ²	0.0003	1	0.0003	0.1154	0.7457	
Residual	0.0139	6	0.0023			
Lack of Fit	0.0003	3	0.0001	0.0196	0.9955	not significant

Source	Sum of Squares	df	Mean Square	F-value	p-value	
Pure Error	0.0136	3	0.0045			
Cor Total	45.30	11				
Std. Dev.	0.0481	R ²	0.9997			
Mean	22.57	Adjusted R ²	0.9994			
CV %	0.2130	Predicted R ²	0.9995			
		Adeq Precision	184.4472			
P Model	14.87	5	2.97	781.09	< 0.0001	Significant
X ₁ -DAR	12.10	1	12.10	3176.82	< 0.0001	
X ₂ -SM	2.77	1	2.77	728.51	< 0.0001	
X ₁ X ₂	0.0000	1	0.0000	0.0000	1.0000	
X ₁ ²	0.0001	1	0.0001	0.0394	0.8492	
X ₂ ²	0.0001	1	0.0001	0.0394	0.8492	
Residual	0.0229	6	0.0038			
Lack of Fit	0.0001	3	0.0000	0.0066	0.9991	not significant
Pure Error	0.0227	3	0.0076			
Cor Total	14.90	11				
Std. Dev.	0.0617	R ²	0.9985			
Mean	12.72	Adjusted R ²	0.9972			
CV %	0.4853	Predicted R ²	0.9975			
		Adeq Precision	96.2491			

Table 6 Responses of synthetic poultry feeds to predicted values.

Run Order	SALT		Ca		P		TNM		Ash	
	Actual Value	Predicted Value	Actual Value	Predicted Value	Actual Value	Predicted Value	Actual Value	Predicted Value	Actual Value	Predicted Value
1	3.84	3.86	22.56	22.58	12.62	12.71	31.34	31.41	12.84	12.72
2	3.37	3.38	19.84	19.85	11.30	11.30	28.43	28.43	11.29	11.30
3	3.41	3.41	20.27	20.26	11.98	11.98	32.23	32.23	12.04	12.03
4	3.80	3.81	22.14	22.15	12.04	12.04	27.59	27.60	11.93	11.95
5	4.35	4.35	25.70	25.69	14.82	14.82	38.18	38.18	14.83	14.83
6	3.88	3.89	22.98	22.99	13.40	13.40	35.21	35.21	13.43	13.45
7	4.31	4.32	25.27	25.28	14.14	14.14	34.37	34.38	14.08	14.10
8	4.27	4.27	24.86	24.85	13.46	13.46	30.57	30.56	13.33	13.33
9	3.33	3.33	19.43	19.42	10.62	10.62	24.62	24.62	10.54	10.53
10	3.94	3.86	22.50	22.58	12.72	12.71	31.40	31.41	12.68	12.72
11	3.89	3.86	22.60	22.58	12.82	12.71	31.44	31.41	12.64	12.72
12	3.78	3.86	22.66	22.58	12.66	12.71	31.49	31.41	12.74	12.72

1.27% for salt, 0.49% for ash, 0.21 g/Kg for Ca, and 0.49 g/Kg for P, indicating that the model had reasonable reproducibility. The independent variables were used to generate projected values for the model, and a comparison with the experimental outcomes

revealed a strong correlation between the actual experimental response and the predicted response (Table 6). These results demonstrate the effectiveness of the approach for synthesizing poultry feed.

3.3 Checking Model Suitability

The models constructed using RSM must provide an accurate approximation to ensure a reliable assessment of the actual environment (Table 4). Filli et al. (2010) suggested that the verification procedure primarily employs the graphical and numerical approaches. The graphical approach considers the type of residuals representing the discrepancy between observed and

predicted values within the model, while the numerical method assesses the coefficient of determination (R^2) and adjusted R^2 ($Radj^2$).

When assessing the appropriateness of a model, the residuals of least-squares adjustments play a crucial role (Myers et al. 2004). The distribution of predicted values versus actual experimental values for SALT, Ca, P, TNM, and Ash is presented in Figure 2 (a,

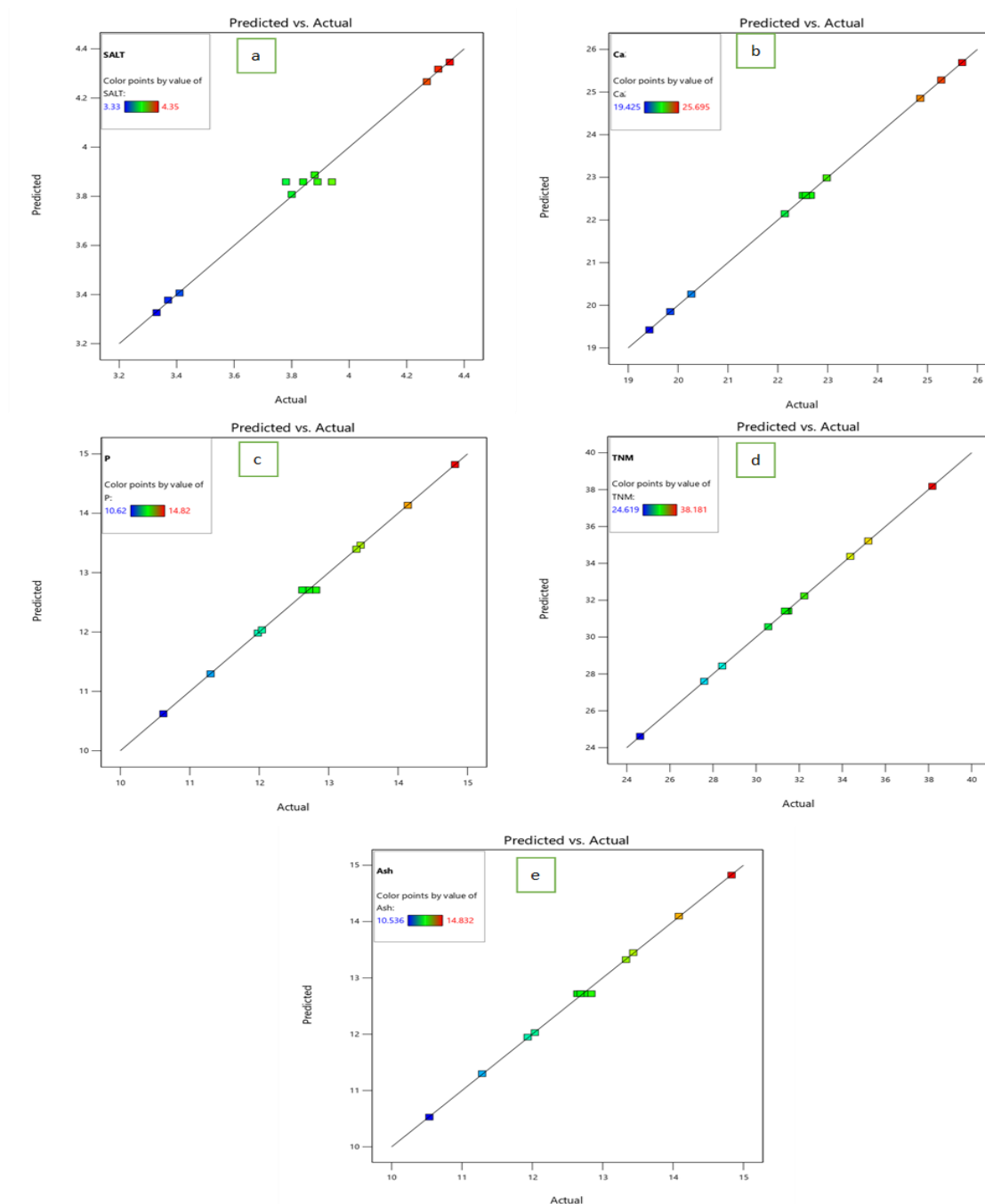


Figure 2 a, b, c, d and e displayed different graphs depicting predicted values versus experimental values for SALT, Ca, P, TNM, and Ash

b, c, d, and e). Regression coefficients of 98.93%, 99.97%, 99.85%, 99.99%, and 99.84% are determined by comparing each observed value with the predicted values obtained from the models, confirming that the regression model accurately describes the experimental data. The presence of evenly distributed points in the plots, forming a linear pattern, further supports the validity of the models. This alignment of points validates the assumption of typicality made in the study. In this context, 'n' represents the number of experimental trials, while 'p' denotes the number of predictors in the model, excluding the constant term. According to

Koocheki et al. (2009), an ideal R^2 should exceed 80%, while Chauhan and Gupta (2004) suggested an R^2 more significant than 78% is acceptable. The models in this study exhibit R^2 values ranging from 99.84% to 99.99% and R^2_{adj} values ranging from 98.04% to 99.98%, with both R^2 and R^2_{adj} values approaching 1 (Lee and Wang 1997; Zaibunnisa et al. 2009). These values are obtained by combining the two independent components mathematically. The significance of R^2 approaching unity is highlighted by the widely accepted notion that a higher R^2 indicates a better fit of the model to the experimental data. The

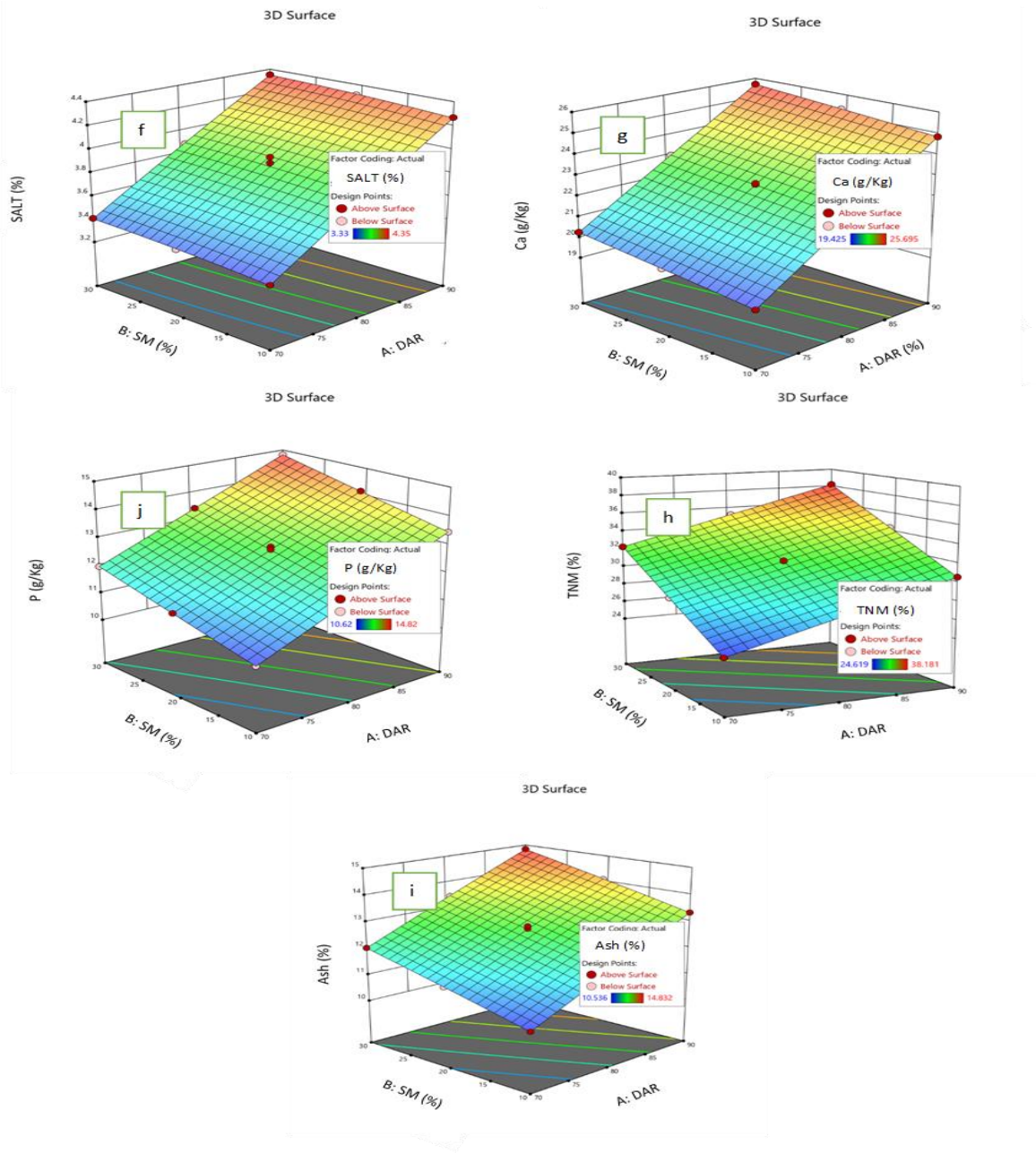


Figure 3 The interaction 3D of % SM and % DAR (f, g, h, i and j)

idea that adding additional components to a model continuously improves R^2 , regardless of their statistical significance, is no longer considered novel. Therefore, Koocheki et al. (2009) suggested that an R^2_{adj} exceeding 90% is a more acceptable criterion for determining model suitability, as a high R^2 does not always guarantee an adequate model. The higher R^2 values obtained in this experiment suggest the absence of non-essential terms in the model. In conclusion, the overall analysis from Figure 2 suggests that the distribution of poultry feed appears random and visually pleasing. This indicates that the model consistently captures the variability across all response values (Y). Thus, it is reasonable to infer that the model accurately represents the formulation of an organic anchovy residue and soybean meal-based poultry feed additive. The visual appearance of the plots in Figure 2 further supports this conclusion.

3.4 Interactive factors and effects on the addition of soybean meal for desalination

The response surface plots generated by the models visually represent the complex relationship between the independent and dependent variables. These three-dimensional graphs illustrate the intricate connections. The dataset was analyzed using the linear, quadratic, and interaction terms specified in Table 4 to create these visualizations. Liu et al. (2009) explained that each contour line on the graph represents a specific elevation above the plane, indicating the overlapping levels of the independent variables. The 3D response surfaces were constructed by carefully examining the variations in the two variables and observing how each response changed across the experimental range. Table 5 demonstrates a statistically significant interaction between % SM and % DAR, as indicated by the P-values ($P = 1.0000$ for MTN, salt, ash, and Ca). Notably, a higher % DAR led to higher TNM and ash percentages, while higher SM and DAR led to higher P and Ca percentages. Conversely, the percentage of salt decreases from 4.35% to 3.33% with soybean meal. This behaviour is illustrated in Figure 3, with preliminary validation shown in Table 3. The results were largely consistent with the predictions made by the model. The remarkable agreement between the confirmed results and the projected or anticipated yields of Ca, P, TNM, Ash, and salt, as shown in Table 6, ensures the accuracy of the models. Additionally, the reasonably high R^2 values (99.97% for Ca, 99.85% for P, 99.99% for TNM, 99.84% for Ash, and 98.93% for salt) demonstrate a strong resemblance between the lightly evaluated experimental values and the anticipated or projected values reported in Table 6. This further supports the accuracy and reliability of the suggested model.

3.5 Process optimization and validation of the waste associations

The model developed for process parameters underwent simplification using the response optimization program integrated into Design-Expert version 13.0.14.0. This software provides

optimal solutions regardless of the combinations of input variables. The highly interactive optimization approach considers the trade-offs across various independent components and responses (Agu et al. 2015). The response surface method (RSM) has proven effective in illustrating the relationship between response variables, particularly the percentage yield, and the variables involved in the desalination process. The reactions of interest include Salt, TNM, Ash, P, and Ca, while the process parameters encompass DAR and SM. The response optimizer effectively utilizes the generated models to generate the best outcomes for both the response variables and the independent factors.

Conclusion

The response surface method (RSM) was employed to determine the optimal parameters for the desalination of organic waste treatment and the synthesis of poultry feed. A second-degree polynomial model was utilized, and this approach proved effective in defining and predicting process responses to variations in input variables within the experimental range. The validity of the models was confirmed by fitting factor estimates to the model equations and obtaining consistent results. The optimization process, which included the amount of soybean meal and the main minerals TNM, Ash, Ca, P, and salt, allowed for the identification of the optimal conditions for desalting anchovy bones. The characteristics of soybean meal, in particular, highlight its commercial feasibility as a product for the desalination anchovy bones and its potential use as a future poultry feed.

References

- Ababouch, L., El Marrakchi, A., & Division, F. A. A. E. A. P. (2009). *Élaboration des semiconserves d'anchois: aspects économiques, techniques et hygiéniques*, Rome, FAO Fisheries and Aquaculture Technical Papers.
- Agu, C., Menkiti, M., Kadurumba, C., & Menkiti, N. (2015). Process parameter optimization for transformer oil extraction from *Terminalia catappa* seed using response surface methodology. *Journal of the Chinese Advanced Materials Society*, 3, 328-344.
- AOAC (1990). AOAC: official methods of analysis (Volume 1). *Contaminants, Agricultural chemicals*. Washington, DC, USA: Authority of the united states of america.
- AOAC (2005). *Of ficial Methods of Anal y sis*, GAITHERSBURG, MARY LAND 20877-2417, USA, AOAC INTERNATIONAL.
- AOAC & Horwitz, W. (1975). *Official methods of analysis*, Association of Official Analytical Chemists Washington, DC.
- Bhatti, M. S., Kapoor, D., Kalia, R. K., Reddy, A. S., & Thukral, A. K. (2011). RSM and ANN modeling for electrocoagulation of

- copper from simulated wastewater: Multi objective optimization using genetic algorithm approach. *Desalination*, 274, 74-80.
- Boumendil, I., Baggar, A., Yassif, F.Z., Fechtali, T., & Safi, A. (2020). Physicochemical Parameters of Moroccan Fish Salted Waste Desalting of Natural Process. In: Ezziyyani, M. (eds) *Advanced Intelligent Systems for Sustainable Development (AI2SD'2019)*. AI2SD 2019. *Advances in Intelligent Systems and Computing*, vol 1104. Springer, Cham. https://doi.org/10.1007/978-3-030-36671-1_46.
- Chauhan, B. & Gupta, R. (2004). Application of statistical experimental design for optimization of alkaline protease production from *Bacillus* sp. RGR-14. *Process Biochemistry*, 39, 2115-2122.
- Fernández-Corredor, E., Albo-Puigserver, M., Pennino, M. G., Bellido, J. M. & Coll, M. (2021). Influence of environmental factors on different life stages of European anchovy (*Engraulis encrasicolus*) and European sardine (*Sardina pilchardus*) from the Mediterranean Sea: A literature review. *Regional Studies in Marine Science*, 41, 101606.
- Filli, K., Nkama, I., Abubakar, U., & Jideani, V. A. (2010). Influence of of extrusion variables on some functional properties of extruded millet-soybean for the manufacture of 'fura': A Nigerian traditional food. *African Journal of Food Science*, 4, 342-352.
- Hasan, B., Putra, I., Suharman, I., Iriani, D., & Muchlisin, Z. A. (2019). Growth performance and carcass quality of river catfish *Hemibagrus nemurus* fed salted trash fish meal. *The Egyptian Journal of Aquatic Research*, 45, 259-264.
- Horwitz, W., & International, A. (2000). *Official Methods of Analysis of AOAC International*, AOAC International.
- Kizilkaya, B., Tekinay, A. A., & Dilgin, Y. (2010). Adsorption and removal of Cu (II) ions from aqueous solution using pretreated fish bones. *Desalination*, 264, 37-47.
- Koocheki, A., Taherian, A. R., Razavi, S. M., & Bostan, A. (2009). Response surface methodology for optimization of extraction yield, viscosity, hue and emulsion stability of mucilage extracted from *Lepidium perfoliatum* seeds. *Food Hydrocolloids*, 23, 2369-2379.
- Köprücü, K., & Özdemir, Y. (2005). Apparent digestibility of selected feed ingredients for Nile tilapia (*Oreochromis niloticus*). *Aquaculture*, 250, 308-316.
- Kremer, S., Mojet, J., & Shimojo, R. (2009). Salt reduction in foods using naturally brewed soy sauce. *Journal of Food Science*, 74, S255-S262.
- Lee, C., & Wang, W. (1997). *Biological statistics*. Science Press, Beijing.
- Liu, S., Yang, F., Zhang, C., Ji, H., Hong, P., & Deng, C. (2009). Optimization of process parameters for supercritical carbon dioxide extraction of Passiflora seed oil by response surface methodology. *The Journal of Supercritical Fluids*, 48, 9-14.
- Marchetti, M. D., Lugo, R. J. J., Massa, A. E., & Czerner, M. (2021). Valorization of residues from anchovy (*Engraulis anchoita*) salting-ripening process: Impact of desalting procedures in retention of biologically-active compounds. *LWT*, 150, 111896.
- Myers, R. H., Montgomery, D. C., & Anderson-Cook, C. M. (2016). *Response surface methodology: process and product optimization using designed experiments*, John Wiley & Sons.
- Myers, R. H., Montgomery, D. C., Vining, G. G., Borror, C. M., & Kowalski, S. M. (2004). Response surface methodology: a retrospective and literature survey. *Journal of quality technology*, 36, 53-77.
- Nurulnadia, M. Y., Nik-Nurasyikin, N. M. A., Ling, K. H., Zahid, B. M., Adiana, G., & Nurlemsha, B. I. (2021). Metal concentrations in fresh and salt-dried anchovy, *Encrasicolina devisi*, and estimation of target hazard quotient for consumers in Kuala Terengganu. *Regional Studies in Marine Science*, 41, 101595.
- Paone, E., Fazzino, F., Pizzone, D. M., Scurria, A., Pagliaro, M., Ciriminna, R., & Calabrò, P. S. (2021). Towards the anchovy biorefinery: Biogas production from anchovy processing waste after fish oil extraction with biobased limonene. *Sustainability*, 13, 2428.
- Shrivastava, A., Bajaj, I., Saudagar, P., & Singhal, R. (2008). Media Optimization for the Production of γ -Linolenic Acid by *Cunninghamella echinulata* var. *elegans* MTCC 552 Using Response Surface Methodology. *International Journal of Food Engineering*, 4(2), <https://doi.org/10.2202/1556-3758.1178>.
- Taarji, N., Da Silva, C. A. R., Khalid, N., Gadhi, C., Hafidi, A., Kobayashi, I., Neves, M. A., Isoda, H., & Nakajima, M. (2018). Formulation and stabilization of oil-in-water nanoemulsions using a saponins-rich extract from argan oil press-cake. *Food Chemistry*, 246, 457-463.
- Taran, M. & Aghaie, E. (2015). Designing and optimization of separation process of iron impurities from kaolin by oxalic acid in bench-scale stirred-tank reactor. *Applied Clay Science*, 107, 109-116.
- Washington, S., & Ababouch, L. (2011). *Private standards and certification in fisheries and aquaculture*, Food and Agriculture Organization of the United Nations Rome, 2011.
- Zaibunnisa, A., Norashikin, S., Mamot, S., & Osman, H. (2009). An experimental design approach for the extraction of volatile compounds from turmeric leaves (*Curcuma domestica*) using pressurized liquid extraction (PLE). *LWT-Food Science and Technology*, 42, 233-238.



Journal of Experimental Biology and Agricultural Sciences

<http://www.jebas.org>

ISSN No. 2320 – 8694

Efficient Solar-Powered IoT Drip Irrigation for Tomato Yield and Quality: An Evaluation of the Effects of Irrigation and Fertilizer Frequency

Sanya Kaunkid¹ , Apinan Aurasopon^{2*} 

¹Department of Engineering and Technology, Faculty of Science and Technology Nakhon PathomRajabhat University, Nakhon Pathom, Thailand, 73000

²Faculty of Engineering, Mahasarakham University, Mahasakham, Thailand, 44150

Received – June 30, 2023; Revision – October 30, 2023; Accepted – November 18, 2023

Available Online – November 30, 2023

DOI: [http://dx.doi.org/10.18006/2023.11\(5\).845.853](http://dx.doi.org/10.18006/2023.11(5).845.853)

KEYWORDS

Drip irrigation system

Fertilization

Time based irrigation

IoT

Tomato yield

ABSTRACT

The optimal management of irrigation and fertilization is crucial for maximizing the yield and quality of tomatoes grown in greenhouses. To address this challenge, this study aimed to develop and implement a solar-powered Internet of Things (IoT) based drip irrigation system for tomato cultivation in plastic roof net houses. Additionally, the study evaluated the effects of water and fertilizer frequency on tomato yield and quality. The experiment was designed with 2 irrigation frequencies (1 time in a day and 1 time in 2 days) and 3 fertilizer frequencies (1 time in 2, 4, and 6 days), with 4 replicates of the tomato variety CH154. The results showed that the solar-powered IoT-based drip irrigation system was efficient, precise in water and fertilizer control, and inexpensive to install and maintain. This allows for real-time monitoring of water flow rate, flow sensor status, treatment status, and electrical parameters on the Node-Red dashboard. Irrigation frequency had a significant impact ($p < 0.05$) on fruit number, weight, and length per plant, with 1-day irrigation resulting in a higher yield than 2-day irrigation. No significant interaction effect was found between irrigation and fertilizer frequency on tomato yield or quality. In conclusion, the solar-powered IoT-based drip irrigation system demonstrated precise control over water and fertilizer, proving its efficiency and cost-effectiveness. Real-time monitoring capabilities and the observed impact of irrigation frequency underscore its potential for enhancing tomato cultivation in greenhouses, offering a valuable contribution to sustainable and technology-driven agricultural practices.

* Corresponding author

E-mail: apinan.a@msu.ac.th (Apinan Aurasopon)

Peer review under responsibility of Journal of Experimental Biology and Agricultural Sciences.

Production and Hosting by Horizon Publisher India [HPI]
(<http://www.horizonpublisherindia.in/>).
All rights reserved.

All the articles published by [Journal of Experimental Biology and Agricultural Sciences](#) are licensed under a [Creative Commons Attribution-NonCommercial 4.0 International License](#) Based on a work at www.jebas.org.



1 Introduction

Tomato (*Solanum lycopersicum L.*) is one of the most essential vegetables in the human diet due to its specific nutritional value, such as lycopene, phenolics, and vitamin C, and is the world's third-largest vegetable crop after potato and sweet potato (Mohammad et al. 2013). Tomato plants flourish on well-drained, fertile, slightly acidic loam soils with a pH range of 6.2 to 6.8. The tomato plant will not grow well in very acidic soils (pH less than 5.6), alkaline (pH greater than 7.5), or insufficiently supplied (Jones 2008). Furthermore, tomato plants are susceptible to many diseases and pests, and the available water and nutrients directly affect how well they grow (Salokhe et al. 2005).

Most farmers are encouraged to grow tomatoes in greenhouses instead of open fields when cultivating tomatoes. This is because greenhouse tomatoes are better in fruit size, TSS content, ascorbic acid, and acid content than open-field tomatoes (Juárez-Maldonado et al. 2014). Producing crops in a greenhouse offers several advantages, including i) Crops do not need chemicals, ii) Greenhouses provide an excellent environment for growing crops, iii) Greenhouses help avoid damage from getting rid of pests like weeds, insects, plant diseases, and so on (Salokhe et al. 2005). In addition, the most important benefit of farming in greenhouses is that it is possible to keep production up all year.

Drip irrigation in greenhouse farming is one of the solutions to environmental and resource issues that provides the best yield and highest quality products for agricultural crops. This is accomplished using minimal water inputs and high fertilizer efficiency (Salokhe et al. 2005). This technique provides an efficient irrigation system by giving plants the appropriate nutrients to minimize nutrient leaching (Elasbah et al. 2019). Some studies state that applying the appropriate amount of water is essential to improve water usage efficiency and production. Inadequate irrigation frequency, on the other hand, can result in a crop water deficit and a decrease in yield due to a lack of water and nutrients (Nut et al. 2019; Wang and Xing 2017).

As previously stated, a lack of suitable irrigation and fertilization frequency on tomatoes is one of the challenges to achieving both a maximum yield and a high quality. It can be seen that smart irrigation systems have significantly advanced, and it could be applied to such a system with precise irrigation and fertilization rates to analyze the effect of the amount of irrigation in combination with the fertilizer supply. Consequently, this study aims to develop and implement a solar-powered drip irrigation system that works with the Internet of Things to grow tomatoes in plastic roof net houses and to evaluate the effects of water and fertilizer frequency on tomato yield and quality.

According to the available research, there has been a lot of technological development to support drip irrigation. Smart irrigation systems mostly use solar power and IoT technologies to minimize water usage and energy costs. In the case of the smart irrigation system, which is powered by solar energy, demand-side energy management is a crucial method for avoiding serious supply shortages and improving energy efficiency. Before they are built and put in place, solar cell systems must be evaluated to see if the electricity made by each solar cell is enough to power the whole system during the day and if the electricity can be stored in an electric battery. Off-grid solar systems are often utilized for smart irrigation, and they may be found in areas with no electricity or where there is limited available energy (Madeti and Singh 2017; Rahman et al. 2018; Bouzguenda et al. 2019).

Aside from the use of solar energy, Internet of Things (IoT) technology has recently become widely used in the smart irrigation system. IoT-based smart irrigation systems have become increasingly common and competitive because they may result in more efficient and optimum water usage and significant waste reduction. Several innovations in the automated irrigation system have been proposed, with micro-processor devices to collect data from sensing systems. These are Arduino (Bouzguenda et al. 2019; Mahfuz and Al-Mayeed 2020; Pawar and Vittal 2019), Node MCU (Nawandar and Satpute 2019; Liwal et al. 2020), Raspberry Pi, wireless sensor network (WSN), and so on (Deveci et al. 2015; Al-Ali et al. 2019). Many additional developed models have been realized using low-cost sensors and actuators and communicating through GSM, Bluetooth, and LoRa (Kabalci et al. 2016; Stark et al. 2020). Some studies are conducted remotely through the Internet and utilize web-based or mobile applications to monitor data in real-time (Joy and Manivannan 2016; Wu and Lin 2019; Nițulescu and Korodi 2020).

2 Material and Methods

2.1 Power system design

The system architecture is designed for a solar-powered drip irrigation system based on the Internet of Things, as shown in Figure 1. The primary elements that make up the system under consideration are as follows:

2.1.1 Solar power system

The solar power system is composed of several components such as photovoltaic modules that convert solar energy to electricity and supply power to the water pump; electrical batteries that store the electricity generated by the PV modules and supply it to the water pump at the rate required for irrigation; a charge controller or charge regulator that regulates the rate at which electric current is applied or drawn from the electrical batteries; and an inverter for DC/AC conversion.

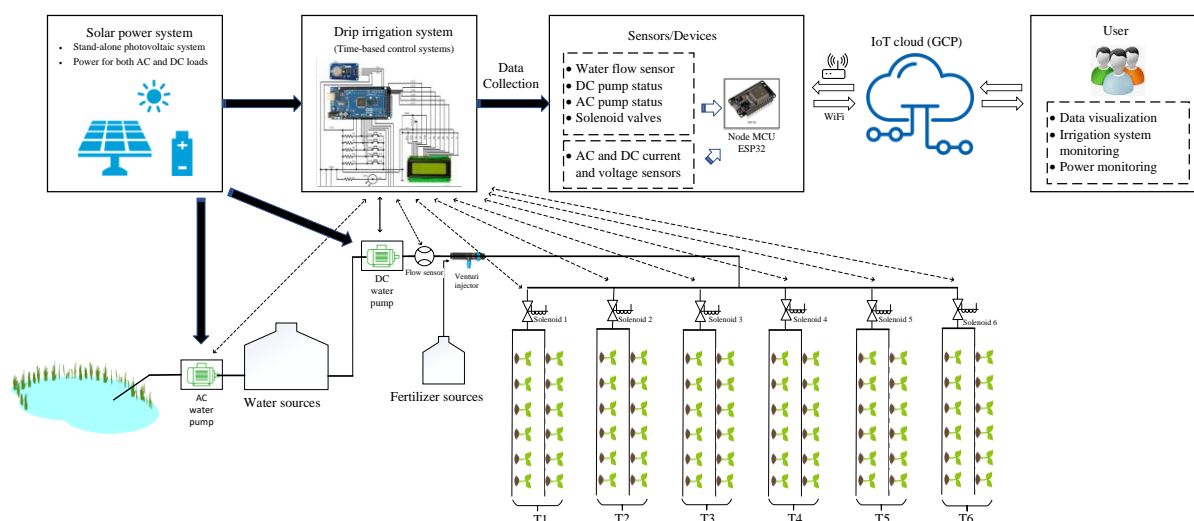


Figure 1 Overall system architecture

2.1.2 Energy requirement assessment

When using solar cells in stand-alone systems, the size of the solar panel, battery, charger, and inverter must be calculated to meet the requirements of electrical appliances such as water pumps and light bulbs. Calculating the energy demand is the most important task for optimal irrigation, as it considers the electricity source, working power, time for each item, and daily energy usage for each component. The energy demand for the solar PV system is presented in Table 1. The table in the bottom row presents the corrected daily capacity, with a correction factor of 25 percent.

2.1.3 Battery selection

To calculate the capacity of a 12V battery needed to supply 133.75 watts of power, we can use the following formula (Bouzguenda et al. 2019)

$$\text{Battery capacity} = \frac{\text{Daily Energy}}{\text{Battery Voltage}} \quad (1)$$

However, there are 20% energy losses while charging and discharging, and the estimated battery size is 13.94 Ah. In addition, the battery must have a minimum discharge depth for better operational life (DOD). In this analysis, a DOD of 50% is assumed, and as seen in the following equation, the battery

capacity is thus at least 27.88 Ah. Therefore, the most suitable battery current on the market is 30 Ah (Bouzguenda et al. 2019).

$$\text{Size of solar panel} = \frac{\text{Total battery capacity}}{\text{Charging time}} \quad (2)$$

2.1.4 Size of the solar panel

During the day, the battery can be entirely charged by solar panels. The peak sunlight in Thailand remains 4.54 hours a day. The size of a solar panel is determined by the total battery capacity divided by the charging time (equation 2). So, the size of the solar panel calculation is 36.85 W. This analysis's main power source was a 40 W polycrystalline solar panel.

2.2 IoT design system

2.2.1 IoT-based drip irrigation system

The architecture will provide time-based control systems to manage and control the drip irrigation system. The operation utilizes a processing board, the Arduino Mega 2560, and the DS1307 serial real-time clock (RTC) for timekeeping. At program start-up, the software will read the configuration value from the SD card, which will keep the default settings of time and water requirements in each tomato growth phase. This was performed by

Table 1 Daily irrigation system energy required

Device	Number of items	Voltage (V)	Current (mA)	Power (mW)	Operating time (hour)	Energy (Wh)
DC water pump	1	12	6,000	72,000	1	72
AC water pump	1	220	160	35,000	1	35
Daily energy (Wh)				107		
Adjusted daily energy (Wh)				133.75		

comparing the scheduling time and RTC to control relays for switching the DC water pump. The pump's control is managed by using a water flow sensor to obtain the desired quantity of water. The amount of water and fertilizer applied to each tomato treatment was managed by solenoid valves attached to the different treatments. During drip irrigation, the data from various sensors and devices, including water flow, DC and AC pump status, and solenoid valve status, is transmitted to the Node MCU ESP32 to be collected before being transmitted to the IoT cloud. This board was chosen because it is a low-energy consumption microcontroller with built-in Wi-Fi, dual-mode Bluetooth and low power consumption.

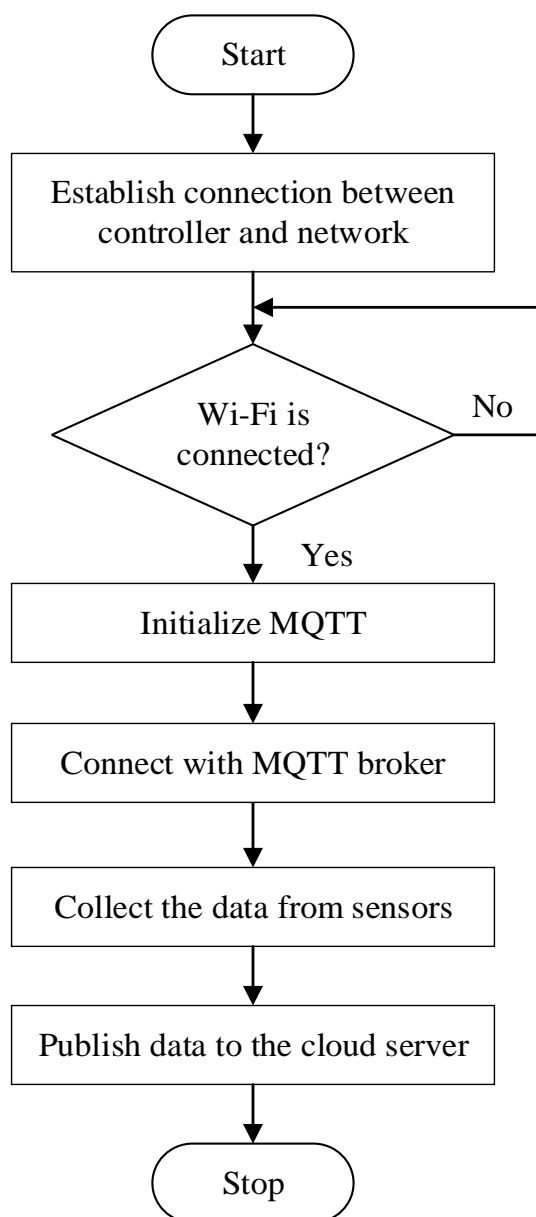


Figure 2 ESP32 programming flowchart

To monitor the electrical power usage, ESP32 is determined to be the system's micro-controller, collecting and processing data from current and voltage sensors and transmitting processed data to the cloud and servers via the Wi-Fi network. The application involves two mean sensors that sense four physical signals: AC current and voltage sensors (PZEM-004) and DC current and voltage sensors (PZEM-016). This smart energy sensor senses current and voltage, which provides overall energy consumption and reads in digital form. AC Digital power meter module PZEM-004T can handle voltage readings of up to 260 VAC and power up to 100A, despite power output at 3.3 or 5 volts. DC digital power meters and USB to 485 are available with PZEM-017 for high-sided electricity up to 300 volts and up to 300 A, with power 3.3 or 5 V. ESP32 is used to process electrical voltage and current values in real time to create DC and AC node sensors.

As part of communication between the data from sensors/devices and cloud service applications, the ESP32 collects and communicates real-time data via a Wi-Fi network. The collected data can be transferred to the cloud server via the Message Queuing Telemetry Transport (MQTT) protocol, an energy-efficient protocol that uses a low-energy application layer. Figure 2 shows the ESP32 programming flowchart as given below.

- Initialize the system and connect the controller and network via Wi-Fi Access Point.
- Check for the connectivity of Wi-Fi. If so, go to the next level. Alternatively, maintain the Wi-Fi link.
- Initialize the MQTT, connect to the broker, and subscribe to the topic.
- Collect the data from the measurement sensor.
- Publish the data to the cloud server.

2.2.2 Google Cloud Platform

The monitoring system used the Google Cloud Platform (GCP) to view the real-time sensor values. The core capability of Google Compute Engine is to create an instant and install Ubuntu 16.04 LTS operating system on this virtual machine. MQTT protocols, Node-RED, InfluxDB, and Grafana, are implemented for monitoring in the server section of the solution, as shown in Figure 3. The MQTT broker (Mosquito) serves as the main centre location in this application, and all data is sent to the broker through publish-subscribe communication.

2.3 Experimental setup

The experiment was conducted at the Creating Innovation for Sustainable Development Research Centre (CISD-RC), Nakhorn Pathom Rajabhat University, Thailand (Latitude: 13°51'41.6" N;

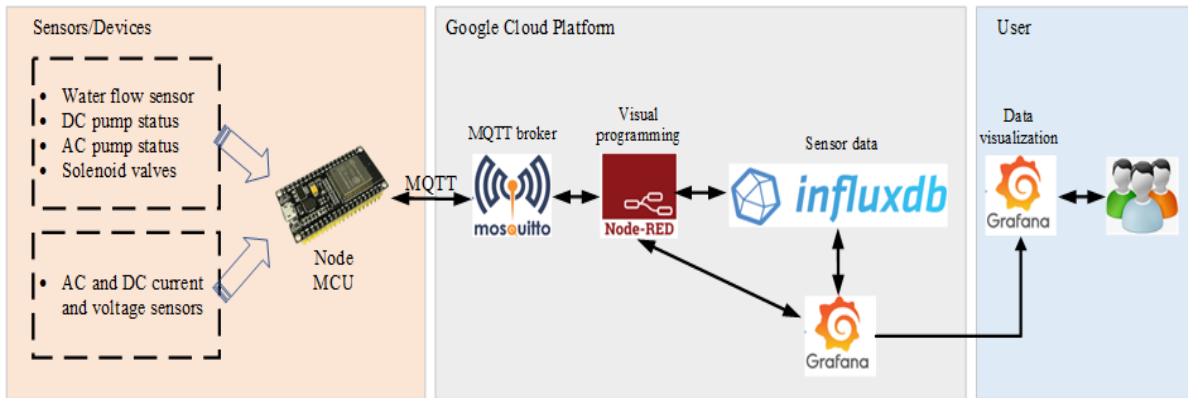


Figure 3 Monitoring system

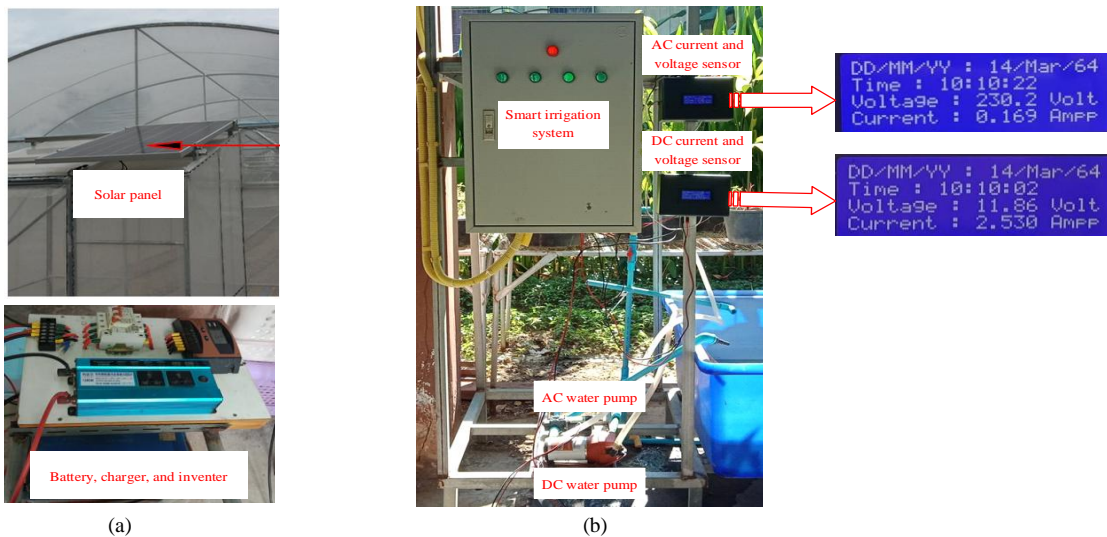


Figure 4 (a) Solar power system and (b) Smart drip irrigation system

Longitude: 99°59'49.6"E) during the growing season of 2019 and 2020. The tested variety was "CH154", developed from cherry tomatoes with a small fruit size, not more than 15 grams, and a sweet flavour. It is ready to harvest 70-75 days after germination.

The factorial experiments on tomato production were designed as 2x3 with 4 replicates in Completely Randomized Design (CRD) to evaluate the effects of irrigation and fertilizer frequency of cherry tomatoes (CH154 variety). Treatments consisted of two irrigation frequencies (1 time in 1 and 2 days) and three fertilizer frequencies (1 time in 2, 4, and 6 days)

We put seeds from the CH154 variety in seed-starting trays to grow cherry tomatoes. Plantain seedlings grow on coconut husks. Daily deep watering is recommended. After the seedlings had developed for 30 days, 576 seedlings were transplanted to each plot. The trees were planted in a greenhouse in a 12-inch round pot using planting material made up of a mixture of coconut husks and chopped coconut husks in a ratio of 1:1.

Experimental models on water consumption were applied based on Penman-Monteith models to evaluate the water requirements in each tomato growth phase: Initial, development, middle, and late stage. Salokhe et al. (2005) examined how much water a drip irrigation system needs in tropical areas. Regarding fertilization, the Jensen and Malter (1995) formula is used; it is a popular formula for growing tomatoes with high growth and yield (Jensen and Malter 1995).

Although a greenhouse with a permanent structure provides a chance to achieve maximum output and high-quality tomatoes, the cost of producing tomatoes in greenhouses is higher. Therefore, to reduce the construction expense, this research utilized a simple net house with a plastic roof for the field experiment. In a system implementation, a prototype of drip irrigation systems was assembled in a control cabinet and installed in the plastic roof net-house condition size of 12x20 m, as shown in Figure 4. The drip irrigation system was set up with high-pressure micro diaphragm water pumps. This pump used water and fertilizer from the water

and fertilizer tank to get to the field, and solenoid valves controlled it. Each treatment was separated into two rows utilizing 20 mm low-density polyethylene pipe (LDPE). Each row comprises 12 inches of round pots on both sides of the pipe. Set a distance of 40 cm between the pots, which can accommodate 48 pots per side, totalling 96 per row on both sides. Use a 3 mm drip pin to connect to a micro-PVC (MT/PVC) pipe to deliver water to each pot. The control system consists of a 1000-liter water tank and a 200-liter fertilizer tank connected to an AC 220 V pump that pumps water into the water tank. The system utilizes a DC 12V diaphragm pump with a flow rate of 7 liters/min for irrigation and a water flow sensor with a working range of 1–30 liters to monitor and control the amount of water and fertilizer for each treatment.

2.4 Statistical analysis

In data collection, weekly trends in vegetative development parameters were identified, and plant samples were collected using a CRD design to determine the crop yield and quality of tomatoes under different treatments. The statistical analysis was processed by one-way analysis of variance (ANOVA) using the SPSS computer software package to estimate the main effects of different sources of variation and their interactions. Treatment

means were compared at a 5% level of probability using the least significant difference (LSD) method.

3 Results

3.1 Data collecting for solar-powered IoT-based Drip Irrigation System

To verify the accuracy of voltage and current sensors, the experiment was carried out at Nakhorn Pathom Rajabhat University, Thailand (Latitude: 13°51'41.6" N; Longitude: 99°59'49.6"E) during December 11–12, 2020. The sensors detected four physical signals and were compared to traditional measuring equipment, including AC voltage and current sensors and DC voltage and current sensors. The results are summarized in Table 2. AC voltage and current sensors showed errors of 0.130 and 0.101 percent, respectively, while DC voltage and current sensors had errors of 0.297 and 5.173 percent.

To monitor the drip irrigation system, collected data, which includes the water flow rate of DC and AC pumps, flow sensor status, and treatment status, is transmitted to the IoT cloud and shown in real-time on the Node-RED dashboard (Figure 5)

Table 2 AC and DC voltage and current percent error

Experiment and trial		AC voltage		AC current		DC voltage		DC current	
Date	Time	Measured (V)	Standar (V)	Measured (A)	Standard (V)	Measured (V)	Standard (V)	Measured (A)	Standard (A)
12/11/2020	10:30 am	229.10	229.10	229.30	0.74	11.75	11.80	3.93	3.71
12/11/2020	04:30 pm	228.50	228.50	228.90	0.74	11.71	11.74	3.79	3.60
12/12/2020	10:30 am	229.20	229.20	229.50	0.74	11.73	11.76	3.82	3.68
12/12/2020	04:30 pm	229.10	229.10	229.40	0.74	11.75	11.78	3.91	3.70
Mean		228.98	229.28	228.98	229.28	11.74	11.77	3.86	3.67
% Error		0.130		0.101		0.297		5.173	



Figure 5 Caption of drip irrigation monitoring system

Table 3 Effect of irrigation, fertilization, and their interaction on tomato yield and quality

Treatments	Number of fruit/plant (number)	Fruit weight/plant(g)	Fruit weight (g)	Fruit width (mm)	Fruit length (mm)	TSS (°Brix)
Irrigation (days)						
1 (I ₁)	295.83 ^a	2333 ^a	9.38 ^a	.2120 ^a	34.11 ^a	8.66 ^a
2 (I ₂)	270.33 ^b	1833 ^b	8.67 ^b	.2152 ^a	31.37 ^b	8.30 ^a
F-test	6.33	8.44	5.62	1.73	10.33	2.26
p-value	0.02*	0.011*	0.03*	0.20	0.01**	0.15
Fertilizer (days)						
2 (F ₂)	273.16 ^b	1875 ^b	9.56 ^a	21.29 ^a	33.24 ^a	8.83 ^a
4 (F ₄)	286.22 ^a	2125 ^{ab}	8.66 ^b	21.03 ^a	32.86 ^a	8.40 ^a
6 (F ₆)	289.88 ^a	2250 ^a	8.84 ^{ab}	21.76 ^a	32.13 ^a	8.22 ^a
F-test	1.00	1.64	3.42	3.07	0.58	2.30
p-value	0.39	0.23	0.06	0.08	0.57	0.13
Irrigation*Fertilizer						
I ₁ F ₂	270.81 ^b	2000 ^{ab}	10.31 ^a	21.10 ^{ab}	34.85 ^{ab}	9.14 ^a
I ₁ F ₄	298.94 ^{ab}	2500 ^a	8.94 ^b	20.97 ^b	35.22 ^a	8.60 ^{ab}
I ₁ F ₆	317.75 ^a	2500 ^a	8.88 ^b	21.54 ^{ab}	32.28 ^b	8.26 ^{ab}
I ₂ F ₂	275.50 ^b	1750 ^b	8.81 ^b	21.49 ^{ab}	31.63 ^c	8.53 ^{ab}
I ₂ F ₄	273.50 ^b	1750 ^b	8.38 ^b	21.10 ^{ab}	30.51 ^c	8.20 ^b
I ₂ F ₆	262.00 ^b	2000 ^{ab}	8.81 ^b	21.98 ^a	31.99 ^{bc}	8.18 ^b
LSD (p<0.05)	NS	NS	NS	NS	NS	NS

3.2 Effects of irrigation and fertilizer frequency on tomato yield and quality

The results of the effects of irrigation and fertilizer frequency on cherry tomatoes (CH154 variety) are given in Table 3. The findings indicate that irrigation frequencies (1 time in 1 and 2 days) and three fertilizer frequencies (1 time in 2, 4, and 6 days) did not affect tomato yield and quality. Under the "Irrigation (days)" section in Table 3, the p-values for the F-test are provided. The p-values for the parameters like "Number of fruit/plant," "Fruit weight/plant," and others are less than 0.05, indicating statistical significance. On the other hand, under the "Fertilizer (days)" section, the p-values for F-test are often higher than 0.05, suggesting that the fertilizer frequencies did not significantly impact these parameters. So, while tomato yield and quality are discussed collectively, the document highlights that the irrigation frequencies significantly influenced these factors, whereas the fertilizer frequencies did not show a significant effect based on the statistical analysis. However, when looking at the detailed experimental results in Table 3, it becomes apparent that while irrigation frequencies did show significance for certain parameters (number of fruits per plant, fruit weight per plant, fruit weight, and

fruit length), the fertilizer frequencies did not have a significant effect on yield or quality.

4 Discussions

The advancements in drip irrigation technology are highlighted, focusing on integrating solar energy and IoT technology. Solar-powered smart irrigation systems' effectiveness and energy efficiency are evaluated, especially for off-grid areas. IoT in smart irrigation systems has become widespread due to its ability to optimize water usage and reduce waste. Adopting drip irrigation in greenhouses is promoted for efficient water and fertilizer usage, leading to higher crop yields and better quality. Integrating solar energy and IoT technology in smart irrigation systems is also emphasized to enhance efficiency and reduce waste.

An experiment was conducted to evaluate the effects of irrigation and fertilizer frequency on the yield and quality of cherry tomatoes (CH154 variety) grown in plastic roof net-houses greenhouses. The experiment used a 2x3 factorial design with 4 replicates and was conducted in a CRD design. The results showed that the frequency of irrigation (1 time in 1 day and 2 days) significantly affected the

number of fruits per plant, fruit weight per plant, fruit weight, and fruit length. Among the tested treatments, the 1-day irrigation treatment gave a higher yield and quality than the 2-day irrigation. However, the frequency of fertilizer (1 time in 2, 4, and 6 days) did not significantly affect yield or quality. The findings of this research were in agreement with those obtained by Wang and Xing (2017), who discovered that irrigation was more sensitive to fruit yield than fertilization. Besides, in a study concerning the cultivation of melons, Sensoy et al. (2007) found that the treatment that provided the highest irrigation compensation resulted in the highest melon yield (Sensoy et al. 2007). Further studies can be conducted to optimize the system and evaluate its impact on other crops and in different growing conditions (He et al. 2021; Zhang et al. 2022; Zhu et al. 2022). The study provides a foundation for future work in developing sustainable and efficient agricultural technologies.

Conclusions

The results of this study were as follows: (i) Solar-powered IoT-based drip irrigation systems can work with a precise irrigation time. All collected data, which includes the water flow rate of DC and AC pumps, flow sensor status, treatment status, and electrical parameters, can be shown in real-time on the Node-Red dashboard. It was recommended that the system was relatively inexpensive to install and maintain precise in its control of the water and fertilizer to the greenhouse tomato, (ii) For the effects of irrigation and fertilizer frequency on the CH154 variety of cherry tomato, both irrigation frequencies (1 time in 1 and 2 days) and three fertilizer frequencies (1 time in 2, 4, and 6 days) had no interaction effect on tomato yield and quality. The irrigation frequencies are significantly different ($p < 0.05$) for number of fruits per plant, fruit weight per plant, fruit weight, and fruit length. The frequency of 1-day irrigation gave a higher yield (number of fruits/plant and fruit weight/plant) than 2-day irrigation treatment.

Acknowledgement

This Research was Financially Supported by the Faculty of Engineering, Mahasarakham University (Grant year 2021).

References

- Al-Ali, A.R., Al Nabulsi, A., Mukhopadhyay, S., Awal, M. S., Fernandes, S., & Ailabouni, K. (2019). IoT-solar energy powered smart farm irrigation system. *Journal of Electronic Science and Technology*, *17*(4), 100017. DOI: <https://doi.org/10.1016/j.jnlest.2020.100017>
- Bouzguenda, M., Rajamohamed, S., Shwehdi, M. H., & Aldalbahi, A. (2019). Solar powered smart irrigation system based on low cost wireless network: A senior design project experience. *The International Journal of Electrical Engineering & Education*, *002072091986041*. <https://doi.org/10.1177/0020720919860414>
- Deveci, O., Onkol, M., Unver, H. O., & Ozturk, Z. (2015). Design and development of a low-cost solar powered drip irrigation system using Systems Modeling Language. *Journal of Cleaner Production*, *102*, 529–544. <https://doi.org/10.1016/j.jclepro.2015.04.124>
- Elasbah, R., Selim, T., Mirdan, A., & Berndtsson, R. (2019). Modeling of Fertilizer Transport for Various Fertigation Scenarios under Drip Irrigation. *Water*, *11*(5), 893. <https://doi.org/10.3390/w11050893>
- He, Z., Li, M., Cai, Z., Zhao, R., Hong, T., Yang, Z., & Zhang, Z. (2021). Optimal irrigation and fertilizer amounts based on multi-level fuzzy comprehensive evaluation of yield, growth and fruit quality on cherry tomato. *Agricultural Water Management*, *243*, 106360. <https://doi.org/10.1016/j.agwat.2020.106360>
- Jensen, M. H., & Malter, A. J. (1995). *Protected agriculture: A global review*. World Bank Publications, Washington DC.
- Jones, J. B. (2008). *Tomato plant culture: In the field, greenhouse, and home garden* (2nd ed). CRC Press.
- Joy, A., & Manivannan, D. (2016). Smart Energy Management and Scheduling using Internet of Things. *Indian Journal of Science and Technology*, *9*(48), 1-6. <https://doi.org/10.17485/ijst/2016/v9i48/108001>
- Juárez-Maldonado, A., Benavides-Mendoza, A., de-Alba-Romenus, K., & Morales-Diaz, A.B. (2014). Estimation of the water requirements of greenhouse tomato crop using multiple regression models. *Emirates Journal of Food and Agriculture*, *26*(10):885-897. DOI:10.9755/ejfa.v26i10.18270
- Kabalci, Y., Kabalci, E., Canbaz, R., & Calpbincici, A. (2016). Design and implementation of a solar plant and irrigation system with remote monitoring and remote control infrastructures. *Solar Energy*, *139*, 506–517. <https://doi.org/10.1016/j.solener.2016.10.026>
- Liwal, K. K., Vohra, M., Sheikh, H., Al-Khatib, O., Abdul Aziz, N., & Copiaco, C. (2020). Implementation of a sustainable and scalable vertical micro-farm. *Journal of Applied Horticulture*, *22*(1), 3–7. <https://doi.org/10.37855/jah.2020.v22i01.01>
- Madeti, S. R., & Singh, S. N. (2017). Monitoring system for photovoltaic plants: A review. *Renewable and Sustainable Energy Reviews*, *67*, 1180–1207. <https://doi.org/10.1016/j.rser.2016.09.088>
- Mahfuz, N., & Al-Mayeed, S. Md. (2020). Smart Monitoring and Controlling System for Aquaculture of Bangladesh to Enhance

- Robust Operation. *2020 IEEE Region 10 Symposium (TENSYP)*, 1128–1133. <https://doi.org/10.1109/TENSYP50017.2020.9230748>
- Mohammad, F. S., Al-Ghobari, H. M., & ElMarazky, M.S.A. (2013). Adoption of an intelligent irrigation scheduling technique and its effect on water use efficiency for tomato crops in arid regions. *Australian Journal of Crop Science*, 7(3):305-313
- Nawandar, N. K., & Satpute, V. R. (2019). IoT based low cost and intelligent module for smart irrigation system. *Computers and Electronics in Agriculture*, 162, 979–990. <https://doi.org/10.1016/j.compag.2019.05.027>
- Nițulescu, I.V., & Korodi, A. (2020). Supervisory Control and Data Acquisition Approach in Node-RED: Application and Discussions. *IoT*, 1(1), 76–91. <https://doi.org/10.3390/iot1010005>
- Nut, N., Phou, K., Mihara, M., Nuth, S., & Sor, S. (2019). Erd Effects of Drip Irrigation Frequency on Growth and Yield of Melon (*Cucumis melo L.*) under Net-house's Conditions. *International Journal of Environmental and Rural Development*, 10 (1), 146-152.
- Pawar, P., & Vittal K. P. (2019). Design and development of advanced smart energy management system integrated with IoT framework in smart grid environment. *Journal of Energy Storage*, 25, 100846. <https://doi.org/10.1016/j.est.2019.100846>
- Rahman, M. M., Selvaraj, J., Rahim, N. A., & Hasanuzzaman, M. (2018). Global modern monitoring systems for PV based power generation: A review. *Renewable and Sustainable Energy Reviews*, 82, 4142–4158. <https://doi.org/10.1016/j.rser.2017.10.111>
- Salokhe, V. M., Babel, M. S., & Tantau, H. J. (2005). Water requirement of drip irrigated tomatoes grown in greenhouse in tropical environment. *Agricultural Water Management*, 71 (3), 225-242.
- Sensoy, S., Ertek, A., Gedik, I., & Kucukyumuk, C. (2007). Irrigation frequency and amount affect yield and quality of field-grown melon (*Cucumis melo L.*). *Agricultural Water Management*, 88(1–3), 269–274. <https://doi.org/10.1016/j.agwat.2006.10.015>
- Stark, E., Kučera, E., Haffner, O., Drahoš, P., & Leskovský, R. (2020). Using Augmented Reality and Internet of Things for Control and Monitoring of Mechatronic Devices. *Electronics*, 9(8), 1272. <https://doi.org/10.3390/electronics9081272>
- Wang, X., & Xing, Y. (2017). Evaluation of the effects of irrigation and fertilization on tomato fruit yield and quality: a principal component analysis. *Scientific reports*, 7(1), 350. <https://doi.org/10.1038/s41598-017-00373-8>.
- Wu, C.K., & Lin, H.C. (2019). Development of Remote Sensing Data Collection and Management Platform via Internet. *Sensors and Materials*, 31(9), 2703. <https://doi.org/10.18494/SAM.2019.2320>
- Zhang, M., Xiao, N., Li, Y., Li, Y., Zhang, D., Xu, Z., & Zhang, Z. (2022). Growth and Fruit Yields of Greenhouse Tomato under the Integrated Water and Fertilizer by Moisture Irrigation. *Agronomy*, 12(7), 1630. <https://doi.org/10.3390/agronomy12071630>
- Zhu, K., Zhao, Y., Ma, Y., Zhang, Q., Kang, Z., & Hu, X. (2022). Drip irrigation strategy for tomatoes grown in greenhouse on the basis of fuzzy Borda and K-means analysis method. *Agricultural Water Management*, 267, 107598. <https://doi.org/10.1016/j.agwat.2022.107598>



Journal of Experimental Biology and Agricultural Sciences

<http://www.jebas.org>

ISSN No. 2320 – 8694

Application of olive mill waste-based biochar for improving wheat response to salt stress

Hanan M. Abou-Zeid^{1*} , Hesham M. Aly² 

¹Botany and Microbiology Department, Faculty of Science, Alexandria University, Egypt

²Forestry and Timber Trees Department, Horticulture Research Institute, Agricultural Research Center, Antoniadis Botanical Garden, Alexandria, Egypt

Received – June 17, 2023; Revision – November 07, 2023; Accepted – November 23, 2023

Available Online – November 30, 2023

DOI: [http://dx.doi.org/10.18006/2023.11\(5\).854.865](http://dx.doi.org/10.18006/2023.11(5).854.865)

KEYWORDS

Antioxidant enzymes

Biochar

Growth

Photosynthesis

Salinity

ABSTRACT

The production of olive mill solid waste (OMSW) raises concerns due to its toxicity and negative environmental impact. However, by utilizing pyrolysis, OMSW can be converted into biochar, a carbon-rich material that detoxifies the waste and preserves its nutrient content. The OMSW-based biochar possesses alkaline properties (pH 9.6), low electrical conductivity (EC), high cation exchange capacity (CEC), a porous surface morphology, various surface functional groups, and high mineral content. This study assessed the influence of two concentrations (5% and 10%) of OMSW-based biochar on wheat plants' growth biomarkers and physiological characteristics subjected to salt stress conditions (150 mM NaCl). Findings of the study revealed that salt stress had deleterious effects on various parameters, including shoot height, fresh and dry weights of shoots and roots, relative water content (RWC%), membrane stability index (MSI%), photosynthetic pigments, and photosynthetic parameters such as the coefficient of the effective quantum yield of photochemical energy conversion of PSII (Φ PSII), photochemical quenching (qP), and photochemical efficiency of PSII (F_o , F_m , F_v/F_o , and F_v/F_m). Furthermore, the levels of lipid peroxidation (MDA), hydrogen peroxide (H_2O_2), superoxide dismutase (SOD), and peroxidase (POD) activities significantly increased in stressed plants. On the other hand, applying both concentrations of OMSW-based biochar effectively improved the overall performance of wheat plants, irrespective of the presence of salinity. OMSW-based biochar is a promising strategy for promoting wheat growth in salt-stressed soil by improving various growth parameters and mitigating plant oxidative stress.

* Corresponding author

E-mail: hananmahmoud93@yahoo.com (Hanan M. Abou-Zeid)

Peer review under responsibility of Journal of Experimental Biology and Agricultural Sciences.

Production and Hosting by Horizon Publisher India [HPI]
(<http://www.horizonpublisherindia.in/>).
All rights reserved.

All the articles published by [Journal of Experimental Biology and Agricultural Sciences](#) are licensed under a [Creative Commons Attribution-NonCommercial 4.0 International License](#) Based on a work at www.jebas.org.



1 Introduction

Abiotic stresses are a threat to the food security of the globe, causing a reduction of 50% in crop production (Sofy et al. 2020). Salt stress is the most brutal environmental factor that can cause harsh effects on many crops. Wheat is considered one of the imperative food crops whose production faces stiff competition due to salt stress. Salinity disturbs plant physiological characteristics such as enzymatic activities, photosynthesis, membrane integrity, hormonal balance, and the uptake of water and nutrients. It induces oxidative stress that increases the reactive oxygen species (ROS) levels, damaging membrane lipids, proteins, and nucleic acids. Plants developed different mechanisms for alleviating its effects via anatomical, physiological, and metabolic changes (Abou-Zeid et al. 2020; Soliman et al. 2023).

The olive oil industry produces huge amounts of polluted by-products, such as solid waste (OMSW) and wastewater. OMSW is a complex mixture comprising residual fractions of pulp, seeds, and olive skins. It is characterized by high levels of polyphenols and heavy metals, which contribute to its phytotoxicity and resistance to degradation (Leon-Camacho et al. 2003). The valorization of OMSW has emerged as a significant research area for environmental protection through effective waste management strategies (Batuecas et al. 2019). Pyrolysis of solid waste has been recently applied for OMSW-based biochar production, offering a sustainable waste management approach (Aly 2016). Numerous studies have accounted for biochar's potential role in soil carbon sequestration, contributing to climate change mitigation (Han et al. 2020; Haddad et al. 2021).

Biochar, a carbon-rich solid material, has emerged as an environmentally friendly approach to mitigate the detrimental effects of salinity on plants. It is produced through pyrolysis from large biomass of agricultural residues and wastes, industrial organic wastes, and organic municipal solid wastes (Rodriguez et al. 2021). Generally, it is alkaline with high cation-exchange capacity; it is often used in agricultural systems to improve soil's physiochemical properties, such as water holding capacity, pH, and electrical conductivity (Sun et al. 2021). Organic carbon from biochar enhances the mineral composition in soil and contributes to crops grown under harsh environments (Hannan et al. 2021). Applying biochar plays an essential role in the activity of the soil-biological factors and can modify plants' physiological metabolism. The utilization of OMSW-based biochar has been found to affect leaf carbon assimilation and photosynthesis positively. It exhibits a high adsorption potential, which helps minimize plants' uptake of Na^+ ions. Additionally, OMSW-based biochar increases the content of K^+ ions in the xylem while reducing the Na^+/K^+ ratio. This leads to an improvement in the activities of antioxidant enzymes, thus reducing oxidative stress and enhancing the plants' resistance to salt stress (Akhtar et al.

2015; Iqbal et al. 2021; Soliman et al. 2023). However, high levels of biochar can contribute to an increase in soil salinity, as Thomas et al. (2013) reported. This study aimed to convert OMSW into biochar and evaluate the impact of incorporating OMSW-based biochar into the soil on wheat plants' growth biomarkers and physiological characteristics under both saline and non-saline conditions.

2 Materials and methods

2.1 Biochar production

OMSW was collected from an olive mill press in the Borg El-Arab region, Alexandria, Egypt, and olive pruning was air-dried before use. The biochar was produced through a slow pyrolysis process; the samples were prepared by placing them in crucibles with tightly sealed lids. Pyrolysis, an operation carried out under oxygen-limited conditions, was conducted in two stages. In the first stage, the pyrolysis temperature was gradually raised to 300 °C at a heating rate of 10 °C per minute using a muffle furnace; this temperature was maintained for 60 min. In the second stage, the biochar was allowed to cool overnight to room temperature; then, the pyrolysis temperature was raised to 500 °C at a heating rate of 10 °C min⁻¹ and held for 60 min. The OMSW-based biochar was allowed to cool to room temperature, then ground sieved through a ~2 mm mesh, and stored for subsequent analyses and treatments (Hassan et al. 2022).

2.2 Characterization of soil and biochar

The morphology and surface elemental analysis of the OMSW-based biochar was examined using an Energy Dispersive X-ray (EDX) spectrometer-Link ISIS analyzer integrated with a Scanning Electron Microscope (SEM). Fourier Transform Infrared (FTIR) spectroscopy was analyzed using a Perkin-Elmer Spectrum 1000 instrument to investigate the functional groups present. The soil and OMSW-based biochar were mixed with deionized water at a ratio of 1:5 and stirred for 24 hours. Subsequently, the mixture was centrifuged at 5000g for 10 min, and the resulting supernatant was used to analyze electrical conductivity (EC) and pH, following the method described by Novak et al. (2009). Soil and biochar organic matter were measured according to Sikora and Moore-Kucera (2014). After the ammonium acetate extraction method, the cation exchange capacity was detected for soil and OMSW-based biochar (Melo et al. 2013).

2.3 Plant material and growth conditions

Triticum aestivum L. (cv. Sakha 61) were acquired from the Agricultural Research Center, Giza, Egypt. The seeds were subjected to surface sterilization by immersing them in a 1% sodium hypochlorite solution for 30 seconds. Subsequently, the sterilized seeds were planted in pots with dimensions of 12 cm

(diameter) and 17 cm (length) filled with a soil mixture of clay and sand in a ratio of 1:2 (W/W). The soil mixture was amended with biochar at 0%, 5%, and 10% concentrations. Plants were irrigated with distilled water at two-day intervals. The plants were subjected to alternate-day application of NaCl (150 mM) starting 10 days after sowing, with a solution at a concentration of 150 mM. The experiment employed a completely randomized block design, with each treatment replicated four times under natural environmental conditions. After 18 days, plants with similar growth characteristics were harvested, thoroughly washed, gently dried and separated into shoots and roots. These plant parts were preserved for subsequent growth measurements and chemical analyses.

2.4 Estimation of growth biomarkers and photosynthetic pigments

Shoot height and the fresh weight (FW) of shoots and roots were determined. Dry weight (DW) was considered in shoots and roots that oven-dried at 70 °C for a duration of 72h. The quantification of photosynthetic pigments was performed using the method described by Moran (1982). The calculation of carotenoid content was carried out following the Wellburn procedure (1994).

2.5 Measurement of photosynthesis parameters

The chlorophyll fluorescence parameters were determined using the method described by Genty et al. (1989) and Van Kooten and Snel (1990). A chlorophyll fluorimeter OS-30P pulse modulated by Opti-sciences (Hudson, USA) was used, prior to the measurements, the leaf samples were subjected to a dark adaptation period of 30 min. The measurements were carried out using actinic light with an intensity of 400 mmol m⁻² s⁻¹ and a saturating pulse light of 8000 mmol m⁻² s⁻¹. The parameters that were measured include the coefficient of the effective quantum yield of photochemical energy conversion of PSII (ΦPSII), the photochemical quenching (qP), and the photochemical efficiency of PSII (F_o, F_m, F_v/F_o, and F_v/F_m).

2.6 Estimation of leaf relative water content (RWC%)

Leaf RWC% was assessed following the method described by Turner (1981). It was calculated using the formula: RWC (%) = (FW - DW) / (TW - DW) x 100, where FW represents the fresh weight of leaf discs, TW denotes the turgid weight measured after their immersing in water at room temperature for 24 h, and DW represents the weight of the oven-dry leaf discs at 80 °C for 4 hours.

2.7 Determination of membrane stability index (MSI%)

Leaf discs weighing 0.1 g were utilized for the measurement of MSI%. The leaf discs were submerged in two test tubes containing

10 ml of double distilled water. One tube (C₁) was maintained at 40 °C for 30 minutes, while the other (C₂) was placed in a boiling water bath at 100 °C for 15 minutes. The electrical conductivity of the solutions in both tubes was measured using a conductivity meter, as described by Deshmukh et al. (1991). MSI% = [1 - (C₁/C₂)] x 100.

2.8 Estimation of malondialdehyde and hydrogen peroxide content

Malondialdehyde (MDA) content was detected following the method of Wang et al. (2009) and calculated using the following formula:

$$\text{MDA } (\mu\text{mol g}^{-1} \text{ FW}) = [6.45(\text{OD}_{532} - \text{OD}_{600}) - 0.56(\text{OD}_{450}) \times 1000] / \text{wt.}$$

Hydrogen peroxide (H₂O₂) was estimated according to Velikova and Loreto (2005) method.

2.9 Extraction and determination of antioxidant enzymes activities

Fresh (1g) shoots and roots were extracted in 50 mM phosphate buffer containing 0.5 mM EDTA (pH 7.5), centrifuged at 10,000g (4 °C) for 10 min, the supernatant was kept for protein content determination (Hartree 1972), and assays of some enzymes activities. Superoxide dismutase (SOD, EC 1.15.1.1) activity was assayed following Giannopolitis and Ries (1977) method. Peroxidase (POD, 1.11.1.7) activity was estimated as described by Noreen and Ashraf (2009) via the record of the changes in absorbance at 470 nm every 20s in the reaction solution. The catalase activity (CAT, 1.11.1.6) was assessed according to Zhang et al. (2005) method following the decomposition of H₂O₂ at 240 nm.

2.10 Statistical analysis

Data were subjected to one-way analysis of variance (ANOVA) using the statistical software package SPSS (version 20). Duncan's multiple-range test was applied to identify means of significant differences. Statistical significance was defined at a level of P ≤ 0.05.

3 Results

3.1 Characteristics of biochar

The physicochemical characteristics of OMSW-based biochar produced by slow pyrolysis are depicted in Table 1. There was a high variability of organic matter, EC, pH and CEC; the mean values for the OMSW-based biochar were higher than those recorded in the soil. Several peak intensities were detected in the FTIR spectra corresponding to the OMSW-based biochar, indicating the presence of several functional groups (Figure 1). For example, the peak at 754.976 cm⁻¹ showed the aromatics, 1°, 2° amines, and bend alkenes function groups; the peak at 1566.769 cm⁻¹ was

Table 1 Basic properties of the studied soil and of OMSW-based biochar

Parameter	Soil	Biochar
Organic matter (%)	74.45	94.7
Electrical conductivity (dS m ⁻¹)	0.24	0.86
pH	6.68	9.61
Cation exchange capacity (cmol kg ⁻¹)	18.88	35.85

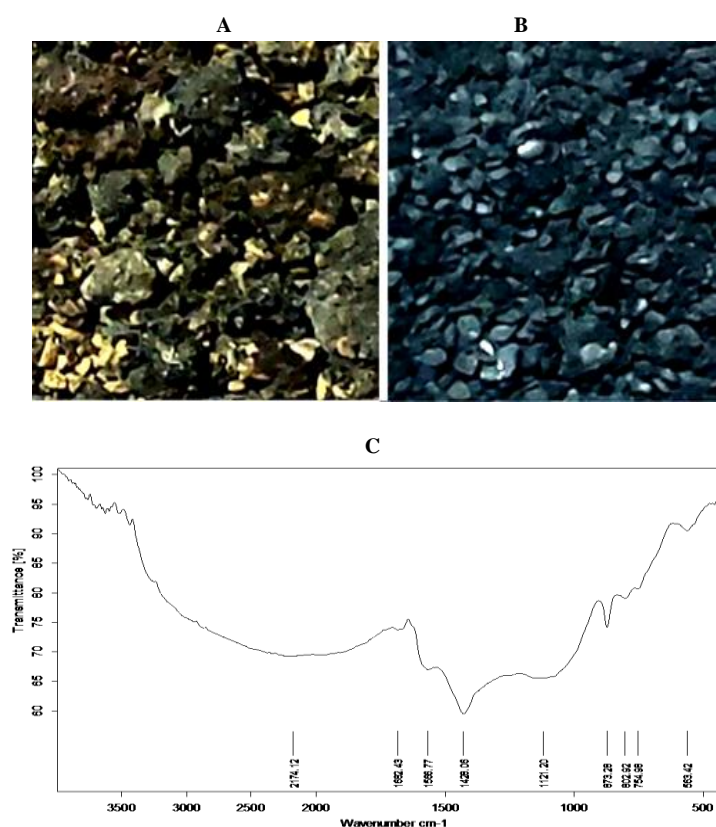


Figure 1 OMSW (A), OMSW-based biochar (B), and (C) the FTIR spectra of OMSW-based biochar

Table 2 FTIR-spectroscopy absorption peaks and their associated functional groups of OMSW-based biochar. Data was adopted from reference (Nandiyanto et al. 2019)

Wave number (cm ⁻¹)	Functional group/ Assignments
2174.124	-C≡C- stretch, C≡N stretch (alkynes, nitriles)
1682.427	-C=C-stretch, C=O stretch (alkenes, carbonyls)
1566.769	N-H bend (1° amines)
1428.057	C-C stretch (in ring- aromatics)
1121.199	C-O stretch, C-N stretch (alcohols, carboxylic acids, esters, ethers, aliphatic amines)
873.282, 802.9145	C-H "oop", N-H wag, =C-H (aromatics, 1°, 2° amines, bend alkenes)
754.976	C-H "oop", C-Cl stretch, =C-H (aromatics, alkyl halides, bend alkenes)
563.424	C-Br stretch, C-Cl stretch (halides)

attributed to N-H deformations of 1° amines group, while the peak intensity at 1121.199 cm^{-1} showed the presence of a C–O stretch and C–N stretch chemical bond that may indicate the presence of aliphatic amines, carboxylic acids, alcohols, esters and ethers (Table 2 and Figure 1). Element percentages

were measured using the energy dispersive spectroscopic (EDX) analysis of OMSW-based biochar; the average percent of carbon was 66.70 ± 0.29 , and the presence of macro- and micro-nutrients was detected, as mentioned in Table 3 and Figure 2.

Table 3 The elemental composition of OMSW-based biochar by EDX analysis

Element	Mass%	Atom%
C	66.70 ± 0.29	75.15 ± 0.29
N	0.90 ± 0.03	0.77 ± 0.06
O	20.30 ± 0.48	17.05 ± 0.38
Na	0.46 ± 0.05	0.96 ± 0.04
Mg	1.53 ± 0.06	0.95 ± 0.06
Al	0.42 ± 0.04	0.21 ± 0.02
Si	0.74 ± 0.04	0.36 ± 0.02
P	2.65 ± 0.13	1.39 ± 0.07
S	0.15 ± 0.02	0.06 ± 0.01
Cl	0.22 ± 0.02	0.09 ± 0.01
K	2.21 ± 0.08	1.17 ± 0.03
Ca	3.15 ± 0.09	1.46 ± 0.03
Fe	0.37 ± 0.03	0.29 ± 0.04
Zn	0.20 ± 0.07	0.09 ± 0.04

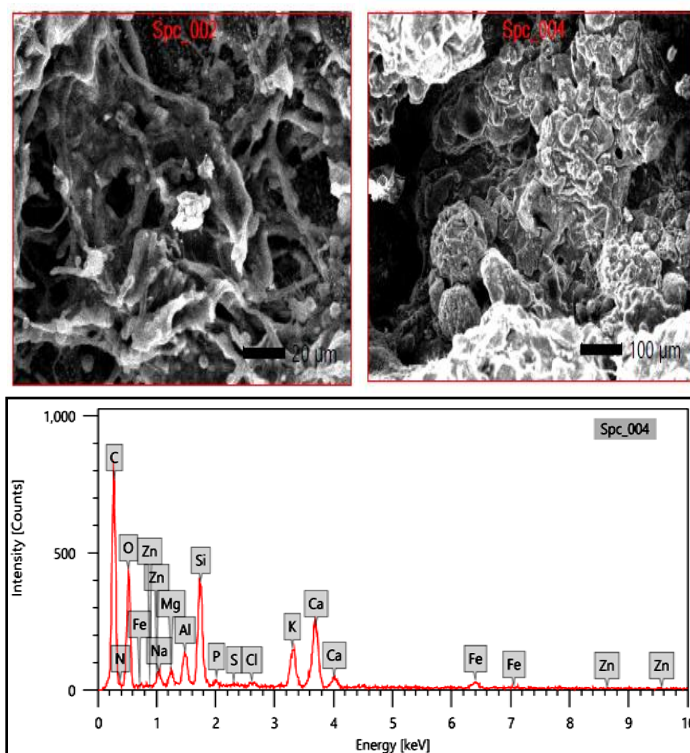


Figure 2 The energy dispersive spectroscopic (EDX) analysis of OMSW-based biochar

3.2 Growth biomarkers, photosynthetic pigments, and photosynthetic parameters

Figure 3 illustrates a significant reduction in growth biomarkers of wheat seedlings treated with 150 mM NaCl. The shoot height was reduced by approximately 37% compared to the control (Figure 3A). Similarly, the FW of shoots and roots showed reductions of about 54% and 61%, respectively, while the DW showed reductions of 49% for shoots and 60% for roots, all relative to their respective controls (Figure 3C and 3D). However, biochar provoked an increase in the aforementioned growth characteristics compared to the controls. Particularly, the DW of roots treated with 5% and 10% biochar showed an increase of approximately 25% and 38%, respectively, while the DW of shoots did not exhibit significant changes compared to their controls. Furthermore, biochar amendments at both 5% and 10% concentrations enhanced the growth characteristics of wheat seedlings under non-saline treatments (Figure 3). Salinity caused a reduction of approximately 28% in leaf RWC% compared to the control, which was effectively mitigated by biochar application (Figure 3B). Both concentrations of OMSW-based biochar (5% and 10%) resulted in a 10% increase in RWC under non-saline conditions compared to the control.

Using OMSW-based biochar significantly increased the content of leaf photosynthetic pigments in wheat plants grown under optimal conditions (Figure 4). However, irrigation with salt water (150

mM) led to a significant reduction of approximately 50% for Chl a, 31% for Chl b, and 45% for carotenoids, compared to the controls. OMSW-based biochar alleviated this negative effect on photosynthetic pigments under normal and saline conditions. Notably, the combined impact of 10% biochar and 150 mM NaCl resulted in a substantial increase in Chl a, Chl b, and Carotenoids contents, with approximately 36%, 34%, and 49% higher levels, respectively, compared to the control group. However, applying 5% biochar in the presence of salt didn't significantly affect Chl b and Carotenoid. Under salt-free conditions, applying OMSW-based biochar led to an increase in Chl a, Chl b, and Carotenoid contents, mainly when used at a concentration of 10%; the increase values reached about 52%, 45%, and 30%, respectively, compared to the control (Figure 4).

Salinity stress in this study resulted in alterations of the leaves-photosynthetic parameters (Φ PSII, qP and Fv/Fm). They were significantly reduced by 46%, 40%, and 11%, respectively, compared to the unstressed plants (Figure 4). The application of OMSW-based biochar showed higher values for these photosynthetic parameters, with increases of approximately 12%, 32%, and 2% for 5% OMSW-based biochar and 28%, 38%, and 3% for 10% OMSW-based biochar, respectively, with respect of the controls. The amelioration of the decline was more pronounced in plants treated with 10% OMSW-based biochar under salinity stress conditions.

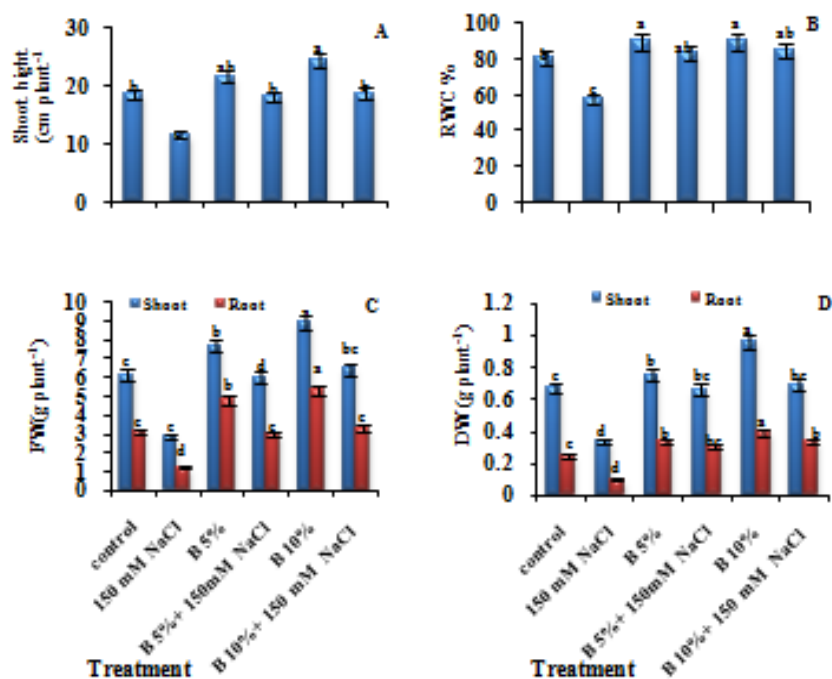


Figure 3 Effects of the interaction between salinity and OMSW-based biochar on growth biomarkers of 18-day-old wheat seedlings. A: shoot length, B: leaf relative water content (RWC), C: fresh weight and D: dry weight. Values are means \pm SE (n = 4), bars followed by different letters indicate significant difference at $p \leq 0.05$ (Duncan's multiple range test)

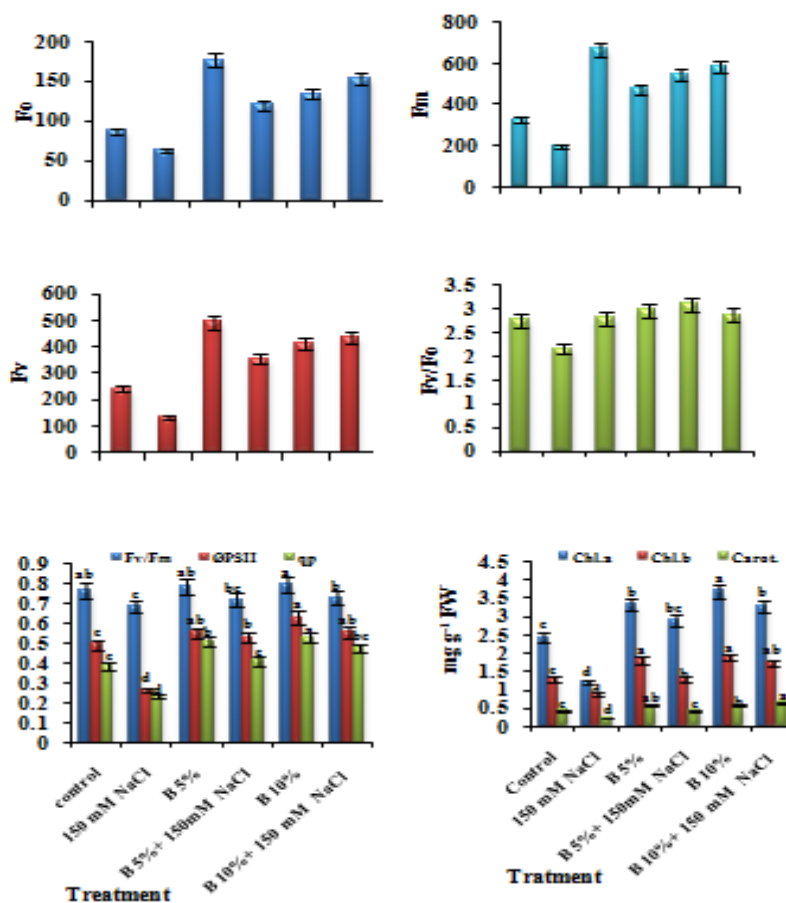


Figure 4 Effects of the interaction between salinity and OMSW-based biochar on photosynthetic efficiency and photosynthetic pigments of 18-day-old wheat leaves. Values are means \pm SE ($n=4$), bars followed by different letters indicate significant difference at $p \leq 0.05$ (Duncan's multiple range test)

3.3 Membrane stability index, malondialdehyde and hydrogen peroxide content

Figure 5A depicts the cell membrane stability index (MSI%), representing the percentage of membrane injury and damage. Notably, a significant decrease in MSI% was observed in response to 150 mM NaCl, reaching about 29%, indicating membrane destabilization, compared to plants grown under normal conditions ($p \leq 0.05$). However, applying OMSW-based biochar at concentrations of 5% and 10% increased MSI% by 7% and 9%, respectively, for plants grown without salinity. Similarly, under salt stress conditions, the presence of 10% OMSW-based biochar led to a 6% increase in MSI%. The results in Figures 5B and 5C indicated that MDA and H_2O_2 content significantly increased in the 150 mM NaCl-stressed plants. There was a considerable increase of 52% in MDA content in shoots and 35% in roots, while the corresponding values for H_2O_2 were 43% and 45% under salinity stress compared to normal conditions. A significant interaction effect of salinity and OMSW-based biochar was observed on MDA

and H_2O_2 . Under saline conditions, their content was significantly reduced by 15% and 11% in shoots and by 10% and 4% in roots with the application of 10% biochar compared to their controls.

In this experiment, salt stress led to a significant increase in the activity of SOD up to 39% and 32% in shoots and roots, respectively; the analogous values for POD were 43% and 33% compared to the controls (Figure 5E and 5F). The supplementation of 10% OMSW-based biochar effectively decreased SOD and POD activity in salt-stressed wheat plants, reaching approximately 32% and 16% for SOD and 8% and 24% for POD in shoots and roots, respectively. Conversely, the activity of CAT was significantly decreased under 150 mM salt stress, with reductions of 16% in shoots and 17% in roots compared to the controls. Otherwise, the impact of OMSW-biochar improved CAT activity by 32% and 14% in shoots and roots, respectively, under non-saline conditions at the 10% OMSW-based biochar concentration. Under saline conditions, the corresponding values were 24% and 8%, respectively.

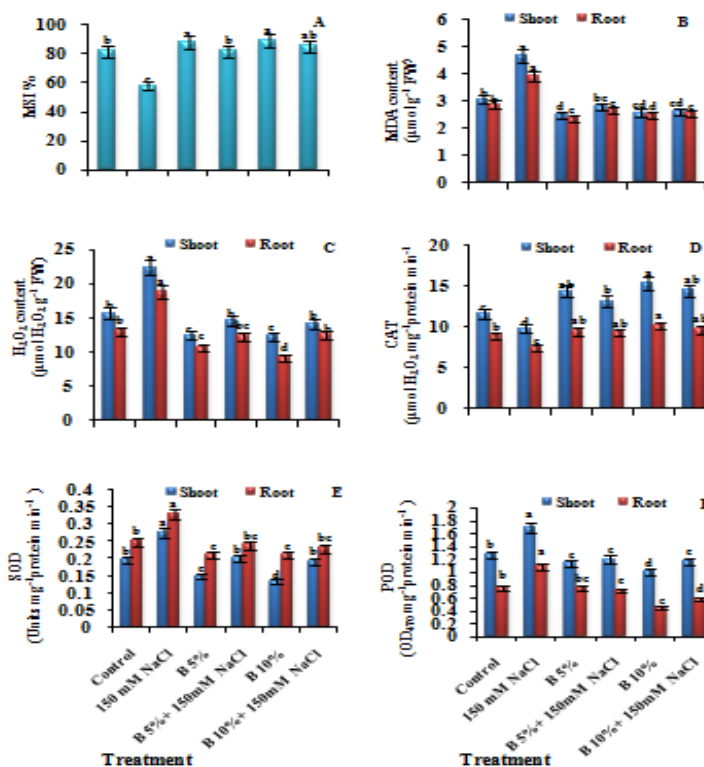


Figure 5 Effects of the interaction between salinity and OMSW-based biochar on A: membrane stability index (MSI%), B: malondialdehyde content (MDA), C: hydrogen peroxide content (H_2O_2), D: catalase activity, E: superoxide dismutase (SOD) activity and F: peroxidase (POD) activity of 18-day-old wheat seedlings. Values are means \pm SE (n= 4), bars followed by different letters indicate significant difference at $p \leq 0.05$ (Duncan's multiple range test)

4 Discussion

Salt stress is a severe abiotic threat that restricts crop plant productivity and is negatively associated with reduced soil organic matter and C:N ratio. It also alters the soil microbial community by decreasing biomass and activity (Yan et al. 2015). Consistent with previous studies by Abou-Zeid et al. (2021) and Ekinci et al. (2022), the findings confirm the negative effects of 150 mM salt stress on wheat plants' growth and physiological characteristics. A significant reduction in growth biomarkers might be referred to the decrease in water availability that induced anomalous alterations in osmotic stress, nutritional imbalance, Na^+ toxicity, and variations in photosynthesis (Abou-Zeid et al. 2020). The results demonstrated decreased photosynthetic pigments and photosynthetic parameters ($\Phi PSII$, qP and Fv/Fm) under 150 mM salt stress (Figure 4). The osmotic effect of salt stress due to the accumulation of Na^+ and Cl^- ions may lead to stomatal closure. At the same time, the disrupted activity of PSII could be attributed to disturbances in the ionic composition within the stroma caused by the influx of both ions, potentially resulting in alterations in the thylakoid structure (Ekinci et al. 2022). These effects may be associated with the inhibitory impact of salt on synthesis enzymes, the elevation of chlorophyllase activity, which is imitative of the

damage of the photosynthetic apparatus, as well as the reduction in mineral availability required for chlorophyll biosynthesis (Sahin et al. 2018).

Furthermore, the damage to plant tissues consequently leads to excessive release of ROS, which causes lipid peroxidation, as MDA indicates, disrupting the MSI% (Yan et al. 2018). Numerous studies depicted that increased antioxidant enzyme activities are virtually associated with the salt tolerance of crops (Talaat and Shawky 2014; Azeem et al. 2023). In the current work, 150 mM salinity stress enhanced the activity of SOD and POD, which are involved in scavenging ROS and contribute to plant tolerance (Figure 5). In accordance with the current study, Kahrizi et al. (2012) reported that the induction of SOD, POD is the popular salt sensitivity mechanism for ROS production. Conversely, CAT activity is reduced, which is called the salt effect on the enzyme system (Farouk and AL-Huqail 2022).

The current work aimed to investigate the potential application of OMSW-based biochar in alleviating salinity stress on wheat plants. Biochar is a carbon-rich material produced from organic matter, it exhibits stability in soil, and it has been shown to improve its physicochemical and biological properties, such as physical

structure, water holding capacity, and biological activity, ultimately creating favourable conditions for enhanced plant growth even under salt stress (Kapoor et al. 2022).

According to the present results, both OMSW-based biochar concentrations (5% and 10%) improved wheat plant growth, regardless of salinity stress. Li et al. (2022) previously reported that biochar amendment can reduce the entry of Na^+ ions into plant cells and ease the negative effects of salinity stress. This beneficial effect can be attributed to its porous structure and the high specific surface area. In this study, the pyrolysis temperature used to produce OMSW-based biochar resulted in a high nutrient content and increased nutrient bioavailability. Additionally, OMSW-based biochar exhibited a high pH value (9.61), which is important for soil pH neutralization and facilitates the accessibility of phosphorus and micronutrients in the soil (Rawat et al. 2019). Furthermore, the high cation exchange capacity of OMSW-based biochar designates its ability to retain and release nutrients, thereby increasing the availability of plant roots' mineral absorption (Haider et al. 2022).

Corroborating our results with Farouk and AL-Huqail (2022) and Ekinici et al. (2022) findings have reported a reduction in oxidative biomarkers sustaining water relations, boosting redox homeostasis, and antioxidant aptitude, as well as regulating antioxidant enzyme activity and element content in the plant reflect on the affirmative effects of biochar application in mitigating the impact of salinity on borage and cabbage plants. EDX analysis proved that the direct wheat growth improvement of OMSW-based biochar appliance under normal or stressful conditions associated with increasing nutrients such as N, K, Ca, Mg, and Fe could be significant in reducing Na^+ via the increase of other elements in soil under salinity or because of the high potential of biochar for adsorption of Na^+ (Table 3 and Figure 2). Our results follow those of Ibrahim et al. (2020) and El-Gamal et al. (2021).

Applying OMSW-based biochar at concentrations of 5% and 10% significantly increased photosynthetic pigments in wheat plants under normal growth conditions and under 150 mM salt stress. The maximal mitigation of salinity arbitrated decline was detected in the photosynthetic parameters above the salt-stressed ones in plants treated with OMSW-based biochar. This might be due to OMSW-based biochar increased leaves-nitrogen level, enhanced photosynthetic rate by increasing the chlorophylls biosynthesis, oxidation of water at PSII, and Calvin cycle enzymes-activities besides the increase in the CO_2 absorption on account of the stomatal conductance and the nutrient uptake (Akhtar et al. 2015). Consistent with these findings, biochar application under saline conditions has been reported to improve plant growth and photosynthesis in maize and potato plants (Khan et al. 2022; Mahmoud et al. 2022). Biochar protects membrane stability, enhances water uptake, maintains nutrient balance, and reduces the

production of ROS through the enhancement of antioxidant activities; consequently, it significantly improves the plant's tolerance to salt stress (Ndiate et al. 2022; Wu et al. 2023). Results of the current work showed an improvement in MSI% along with a reduction in MDA and H_2O_2 content (Figure 5B and 5C), as well as the activity of SOD, POD, and CAT in wheat plants treated with OMSW-based biochar under normal and saline irrigation. This observation is in accordance with previous studies by Zhang et al. (2020) and Cong et al. (2023) on soybean and maize plants, respectively. Contrarily, the findings of Ufkay et al. (2021) indicate that a heightened application rate of biochar may exacerbate the detrimental impacts of salinity on soil. This exacerbation is attributed to the cumulative levels of soil EC, which can cause a transition from beneficial to detrimental conditions for plant growth.

Conclusion

The application of OMSW-based biochar in soil subjected to 150 mM salt stress demonstrated beneficial effects on wheat plant growth by mitigating the adverse impacts of salinity. The effectiveness of biochar was strongly influenced by its properties, including CEC, EC, porosity, functional groups, mineral content, and application rates. Salinity stress reduced growth, RWC%, MSI%, photosynthetic pigments, and photosynthetic parameters (ΦPSII , qP, and Fv/Fm). Salinity induces oxidative stress, as evidenced by increased MDA, H_2O_2 , and antioxidant enzyme activity levels. However, these detrimental effects were alleviated by supplementing OMSW-based biochar at 5% and 10% concentrations. The study's findings highlight the positive interactions between salinity stress and biochar, which positively influence wheat plants' growth biomarkers and physiological characteristics. The application of OMSW-based biochar holds significant potential for enhancing plant growth in salt-stressed soil.

Conflict of Interest

The authors disclose that they have no conflicts of interest to declare.

References

- Abou-Zeid, H.M., Ismail, G.S.M., & Abdel-Latif, S.A. (2020). Influence of seed priming with ZnO nanoparticles on the salt-induced damages in wheat (*Triticum aestivum* L.) plants. *Journal of Plant Nutrition*, 44(5), 629–643. <https://doi.org/10.1080/01904167.2020.1849288>
- Abou-Zeid, H.M., Saber, N., Abdelrahim, B.I., & Ismail, G.S.M. (2021). Nitrogen biofertilizer alleviates the inhibitory effect of cadmium on physiology and nitrogen assimilation in maize plants.

- International Journal of Agriculture and Biology*, 25, 98–108. doi: 10.17957/IJAB/15.1643
- Akhtar, S.S., Andersen, M.N., & Liu, F. (2015). Residual effects of biochar on improving growth, physiology and yield of wheat under salt stress. *Agriculture Water Management*, 158, 61–68. <https://doi.org/10.1016/j.agwat.2015.04.010>
- Aly, H.M. (2016). Biochar and its importance in adsorption of antibiotic and heavy metals from aqueous solutions. *Ecological Question*, 24, 75–78. <http://dx.doi.org/10.12775/EQ.2016.014>
- Azeem, M., Pirjan, K., Qasim, M., Mahmood, A., Javed, T., et al. (2023). Salinity stress improves antioxidant potential by modulating physio-biochemical responses in *Moringa oleifera* Lam. *Scientific Reports*, 13(1), 1–17. <https://doi.org/10.1038/s41598-023-29954-6>
- Batuecas, E., Tommasi, T., Battista, F., Negro, V., Sonetti, G., et al. (2019). Life cycle assessment of waste disposal from olive oil production: anaerobic digestion and conventional disposal on soil. *Journal of Environmental Management*, 237, 94–102. <https://doi.org/10.1016/j.jenvman.2019.02.021>
- Cong, M., Hu, Y., Sun, X., Yan, H., Yu, G., et al. (2023) Long-term effects of biochar application on the growth and physiological characteristics of maize. *Frontiers in Plant Science*, 14, 1172425. doi: 10.3389/fpls.2023.1172425
- Deshmukh, P.S., Sairam, R.K., & Shukla, D.S. (1991). Measurement of ion leakage as a screening technique for drought resistance in wheat genotypes. *Indian Journal of Plant Physiology*, 34, 89–91
- Ekinci, M., Turan, M., & Yildirim, E. (2022). Biochar mitigates salt stress by regulating nutrient uptake and antioxidant activity, alleviating the oxidative stress and abscisic acid content in cabbage seedlings. *Turkish Journal of Agriculture and Forestry*, 3, 28–37. <https://doi.org/10.3906/tar-2104-81>
- El-Gamal, S.M.A., Serag, El-Din, W.M., Farouk, S., & Mokhtar, N.A.Y.O. (2021). Integrated effects of biochar and potassium silicate on borage plant under different irrigation regimes in sandy soil. *Journal of Horticultural Science and Ornamental Plants*, 13, 60–76. doi: 10.5829/idosi.jhsop.2021.60.76
- Farouk, S., & AL-Huqail, A.A. (2022). Sustainable biochar and/or melatonin improve salinity tolerance in borage plants by modulating osmotic adjustment, antioxidants, and ion homeostasis. *Plants*, 11, 765. <https://doi.org/10.3390/plants11060765>
- Genty, B., Briantais, J.M., & Baker, N.R. (1989). The relationship between quantum yield of photosynthetic electron transport and quenching of chlorophyll fluorescence. *Biochimica Biophysica Acta*, 990 (1), 87–92
- Giannopolitis, C.N., & Ries, S.K. (1977). Superoxide dismutase: II. Purification and quantitative relationship with water-soluble protein in seedlings. *Plant Physiology*, 59(2), 315–318
- Haddad, K., Jeguirim, M., Jellali, S., Thevenin, N., Ruidavets, L., & Limousy, L. (2021). Biochar production from cypress sawdust and olive mill wastewater: agronomic approach. *Science of The Total Environment*, 752, 141713. <https://doi.org/10.1016/j.scitotenv.2020.141713>
- Haider, F. U., Wang, X., Farooq, M., Hussain, S., Cheema, S. A., et al. (2022). Biochar application for the remediation of trace metals in contaminated soils: implications for stress tolerance and crop production. *Ecotoxicology Environmental Safety*, 230, 113165. doi: 10.1016/j.ecoenv.2022.113165
- Han, L., Sun, K., Yang, Y., Xia, X., Li, F., Yang, Z., & Xing, B. (2020). Biochar's stability and effect on the content, composition and turnover of soil organic carbon. *Geoderma*, 364, 114184. <https://doi.org/10.1016/j.geoderma.2020.114184>
- Hannan, F., Islam, F., Huang, Q., Farooq, M.A., Ayyaz, A., et al. (2021). Interactive effects of biochar and mussel shell activated concoctions on immobilization of nickel and their amelioration on the growth of rapeseed in contaminated aged soil. *Chemosphere*, 282, 130897. <https://doi.org/10.1016/j.chemosphere.2021.130897>
- Hartree, E.F. (1972). Determination of protein: a modification of the Lowry method that gives a linear photometric response. *Analytical Biochemistry*, 48, 422–427
- Hassan, N.A., Aly, H.M., Wahba, T.F., & Shaker, N. (2022). Laboratory evaluation of four types of biochar to manage some stored product insects. *The International Journal of Tropical Insect Science*, 42, 2959–2968. <https://doi.org/10.1007/s42690-022-00824-4>
- Ibrahim, M.E.H., Ali, A.Y.A., Zhou, G., Elsiddig, A.M.I., Zhu, G., Nimir, N.E.A., & Ahmad, I. (2020) Biochar application affects forage sorghum under salinity stress. *Chilean Journal of Agricultural Research*, 80, 317–325
- Iqbal, J., Shah, N.S., Sayed, M., Niazi, N.K., Imran, M., et al. (2021). Nano-zerovalent manganese/biochar composite for the adsorptive and oxidative removal of Congo-red dye from aqueous solutions. *Journal of Hazard Materials*, 403, 123854. <https://doi.org/10.1016/j.jhazmat.2020.123854>
- Kahrizi, S., Sedghi, M., & Sofalian, O. (2012). Effect of salt stress on proline and activity of antioxidant enzymes in ten durum wheat cultivars *Annals of Biological Research*, 3, 3870–3874

- Kapoor, A., Sharma, R., Kumar, A., & Sepehya, S. (2022). Biochar as a means to improve soil fertility and crop productivity: a review. *Journal of Plant Nutrition*, *45*, 1–9. doi:10.1080/01904167.2022.2027980
- Khan, I., Luan, C., Qi, W., Wang, X., Yu, B., et al. (2022). The residual impact of straw mulch and biochar amendments on grain quality and amino acid contents of rainfed maize crop. *Journal of Plant Nutrition*, *46*, 1283–1295. doi: 10.1080/01904167.2022.2056483
- Leon-Camacho, M., Viera-Alcaide, I., & Ruiz-Mendez, M.V. (2003). Elimination of polycyclic aromatic hydrocarbons by bleaching of olive pomace oil. *The European Journal of Lipid Science and Technology*, *105* (1), 512–525. <https://doi.org/10.1002/ejlt.200390010>
- Li, Z., Zhu, L., Zhao, F., Li, J., Zhang, X., et al. (2022). Plant salinity stress response and nano-enabled plant salt tolerance. *Frontiers in Plant Science*, *13*, 843994. doi: 10.3389/fpls.2022.843994
- Mahmoud, A. W. M., Samy, M. M., Sany, H., Eid, R. R., Rashad, H. M., & Abdeldaym, E. A. (2022). Nanopotassium, nanosilicon, and biochar applications improve potato salt tolerance by modulating photosynthesis, water status, and biochemical constituents. *Sustainability*, *14*, 723. doi: 10.3390/su14020723
- Melo, L.C., Coscione, A.R., Abreu, C.A., Puga, A.P., & Camargo, O.A. (2013). Influence of pyrolysis temperature on cadmium and zinc sorption capacity of sugar cane straw-derived biochar. *BioResources*, *8*, 4992–5004. doi:10.15376/biores.8.4.4992-5004
- Moran, R. (1982). Formulae for determination of chlorophyllous pigments extracted with N,N-dimethyl formamide. *Plant Physiology*, *69* (6), 1376–81. doi: 10.1104/pp.69.6.1376.
- Nandiyanto, A.B.D., Oktiani, R., & Ragadhita, R. (2019). How to read and interpret FTIR spectroscopy of organic material. *Journal of Science and Technology*, *4* (1), 97–118. <http://ejournal.upi.edu/index.php/ijost/>
- Ndiate, N. I., Zaman, Q. U., Francis, I. N., Dada, O. A., Rehman, A., et al. (2022). Soil amendment with arbuscular mycorrhizal fungi and biochar improves salinity tolerance, growth, and lipid metabolism of common wheat (*Triticum aestivum* L.). *Sustainability*, *14*, 3210. doi: 10.3390/su14063210
- Noreen, Z., & Ashraf, M. (2009). Changes in antioxidant enzymes and some key metabolites in some genetically diverse cultivars of radish (*Raphanus sativus* L.). *Environmental and Experimental Botany*, *67*(2), 395–402
- Novak, J., Lima, I., & Xing, B. (2009). Characterization of designer biochar produced at different temperatures and their effects on a loamy sand. *Annals of Environmental Science*, *3* (843), 195–206
- Rawat, J., Saxena, J., & Sanwal, P. (2019). Biochar: A sustainable approach for improving plant growth and soil properties. In V. Abrol, & P. Sharma (Eds.), *Biochar-an imperative amendment for soil and the environment*. *IntechOpen*, <https://doi.org/10.5772/intechopen.82151>
- Rodriguez, J.A., Lustosa Filho, J.F., Melo, L.C.A., de Assis, I.R., & Oliveira, T.S. (2021). Co-pyrolysis of agricultural and industrial wastes changes the composition and stability of biochars and can improve their agricultural and environmental benefits. *Journal of Analytical and Applied Pyrolysis*, *155*, 105036
- Sahin, U., Ekinci, M., Ors, S., Turan, M., Yildiz, S., & Yildirim, E. (2018). Effects of individual and combined effects of salinity and drought on physiological, nutritional and biochemical properties of cabbage (*Brassica oleracea* var. capitata). *Scientia Horticulturae*, *240*, 196–204.
- Sikora, L.J., & Moore-Kucera, J. (2014) Soil test methods from the southeastern United States. Athens, GA: University of Georgia, College of Agriculture Experiment Stations 180. Retrieved from <http://www.clemson.edu/agrvlb/sera6/MethodsManualFinalSERA6.pdf>
- Sofy, M.R., Elhindi, K.M, Farouk, S., & Alotaibi, M.A. (2020). Zinc and paclobutrazol mediated regulation of growth, upregulating antioxidant aptitude and plant productivity of pea plants under salinity. *Plants*, *9*, 1197
- Soliman, M. H., Alnusairi, G.S.H., Khan, A.A., Alnusaire, T.S., Fakhr, M.A., et al. (2023). Biochar and selenium nanoparticles induce water transporter genes for sustaining carbon assimilation and grain production in salt-stressed wheat. *Journal of Plant Growth Regulations*, *42*, 1522–1543 <https://doi.org/10.1007/s00344-022-10636-y>
- Sun, Y., Xiong, X., He, M., Xu, Z., Hou, D., et al. (2021). Roles of biochar-derived dissolved organic matter in soil amendment and environmental remediation: A critical review. *Chemical Engineering Journal*, *424*, 130387. <https://doi.org/10.1016/j.cej.2021.130387>
- Talaat, N.B., & Shawky, B.T. (2014). Protective effects of arbuscular mycorrhizal fungi on wheat (*Triticum aestivum* L.) plants exposed to salinity. *Environmental and Experimental Botany*, *98*(1), 20–31

- Thomas, S.C., Frye, S., Gale, N., Garmon, M., Launchbury, R., et al. (2013). Biochar mitigates negative effects of salt additions on two herbaceous plant species. *Journal of Environmental Management*, 129, 62–68.
- Turner N.C. (1981). Techniques and experimental approaches for the measurement of plant water status. *Plant and Soil*, 58, 339–366
- Ufkay, K., Toptas, A., Yanik, J., & Aktas, L. (2021). Does biochar alleviate salt stress impact on growth of salt-sensitive crop common bean. *Communications in Soil Science and Plant Analysis*, 52 (5), 456-469. doi: 10.1080/00103624.2020.1862146
- Van Kooten, O., & Snel, J.F.H. (1990). The use of chlorophyll fluorescence nomenclature in plant stress physiology. *Photosynthesis Research*, 25 (3), 147–50. doi: 10.1007/BF00033156
- Velikova, V., & Loreto, F. (2005). On the relationship between isoprene emission and thermo tolerance in *Phragmites australis* leaves exposed to high temperatures and during the recovery from a heat stress. *Plant Cell and Environment*, 28, 318–327
- Wang, C., Zhang, S.H., Wang, P.F., Hou, J., Zhang, W.J., Li, W., & Lin, Z.P. (2009). The effect of excess Zn on mineral nutrition and antioxidative response in rapeseed seedlings. *Chemosphere*, 75, 1468–1476
- Wellburn, A.R. (1994). The spectral determination of chlorophylls a and b, as well as total carotenoids, using various solvents with spectrophotometers of different resolution. *Journal of Plant Physiology*, 144 (3), 307–13
- Wu, Y., Wang, X., Zhang, L., Zheng, Y., Liu, X., & Zhang, Y. (2023). The critical role of biochar to mitigate the adverse impacts of drought and salinity stress in plants. *Frontiers in Plant Science*, 14, 1163451. doi: 10.3389/fpls.2023.1163451
- Yan, N., Marschner, P., Cao, W.H., Zuo, C.Q., & Qin, W. (2015). Influence of salinity and water content on soil microorganisms. *International Soil and Water Conservation Research*, 3, 316–323. <https://doi.org/10.1016/j.iswer.2015.11.003>
- Yan, Y., Pan, C., Du, Y., Li, D., & Liu, W. (2018). Exogenous salicylic acid regulates reactive oxygen species metabolism and ascorbate– glutathione cycle in *Nitraria tangutorum* Bobr. under salinity stress. *Physiology and Molecular Biology of Plants*, 24 (4), 577–589
- Zhang, H., Jiang, Y., He, Z. & Ma, M. (2005). Cadmium accumulation and oxidative burst in garlic (*Allium sativum*). *Journal of Plant Physiology*, 162(9) 977–984
- Zhang, Y., Ding, J., Wang, H., Su, L., & Zhao, C. (2020). Biochar addition alleviates the negative effects of drought and salinity stress on soybean productivity and water use efficiency. *BMC Plant Biology*, 20, 288 <https://doi.org/10.1186/s12870-020-02493-2>



Journal of Experimental Biology and Agricultural Sciences

<http://www.jebas.org>

ISSN No. 2320 – 8694

Work Place Self-Management by Academic Cum Clinical Physiotherapist – A Case Study

Vinodhkumar Ramalingam^{1*}, Mythri Jain¹, Prathap Suganthirababu¹,
Jagatheesan Alagesan¹ Pradeep Balakrishnan², Prathibha Duraimurugan¹,
Balarathna¹, Mohammed Hussain¹, Wong Ling Shing^{3*}

¹Saveetha College of Physiotherapy, Saveetha Institute of Medical and Technical Sciences, Chennai, India

²School of Health Sciences, KPJ University College, Kota Seriemas, Nilai, Negeri Sembilan, Malaysia

³Faculty of health and life sciences, INTI international University, Nilai, Negeri Sembilan, Malaysia

Received – June 05, 2023; Revision – August 10, 2023; Accepted – October 06, 2023

Available Online – November 30, 2023

DOI: [http://dx.doi.org/10.18006/2023.11\(5\).866.870](http://dx.doi.org/10.18006/2023.11(5).866.870)

KEYWORDS

Physiotherapist

Work-related musculoskeletal disorders

Rapid entire body assessment

Visual analogue scale

Exercise

Healthy lifestyle

ABSTRACT

One of the main issues in industrialized nations is work-related musculoskeletal disorders (WMSD), which are linked to demanding and repetitive work environments. Repetitive actions and work without leisure can lead to musculoskeletal problems. To prevent this occurrence, promoting healthy lifestyle self-care management is essential. The main objective of this case study was to assess the risk of work-related musculoskeletal disorders in professional physiotherapist and their workplace self-management. Case Description: a case of a 39-year-old male assistant professor cum clinical practitioner with 12 years of experience in the profession, who engages in using the computer for 6 hours a day for his academic and clinical documentation purposes, was assessed in the workstation. He complains of neck and shoulder pain after engaging in front of the computer for more than one hour, which he manages during the routine practice. He manages his pain by doing simple exercises like chin tuck-in and shoulder bracing by taking a short break every hour while working on a computer. Musculoskeletal-related pain was analyzed using the VAS score (visual analogue scale), and the level of the risks was analyzed using the rapid entire body assessment (REBA) scale. The case study showed that professional physiotherapists have a high risk of MSDs due to their engagement in multiple tasks and less attention to body posture. Regular exercise in the workstation and ergonomic workplace awareness would prevent the occurrence of work-related MSD.

* Corresponding author

E-mail: vinodhkumar.scpt@saveetha.com (Vinodhkumar Ramalingam);
lingshing.wong@newinti.edu.my (Wong Ling Shing)

Peer review under responsibility of Journal of Experimental Biology and Agricultural Sciences.

Production and Hosting by Horizon Publisher India [HPI]
(<http://www.horizonpublisherindia.in/>).
All rights reserved.

All the articles published by [Journal of Experimental Biology and Agricultural Sciences](#) are licensed under a [Creative Commons Attribution-NonCommercial 4.0 International License](#) Based on a work at www.jebas.org.



1 Introduction

Physiotherapists are primary healthcare specialists who assess and manage patients of all ages with various conditions, health-related issues, illnesses, or traumas that restrict their ability to mobilize and perform activities of daily living. One of the main issues in industrialized nations is work-related musculoskeletal disorders (WMSDs), which are linked to demanding and repetitive work environments. According to Sekkay et al. (2018) WMSDs are those that are deemed to be caused by the workplace environment and individual performance. By recognizing and realizing the effects of "work-related" musculoskeletal conditions, the World Health Organization (WHO) has described WMSDs as multifactorial, meaning that many risk factors contribute to and exacerbate these illnesses (Sauter et al. 1993). The prevalence of WMSDs among Indian physiotherapists was 89% in males and 96% in females (Iqbal and Alghadir 2015). Likewise, a recent study in 2022 among physiotherapists in Malaysia reported the prevalence of WMSDs was highest in the neck (52.6%), followed by other body segments (YI et al. 2022). In addition to this, the prevalence of WMSDs among physiotherapists in Uttar Pradesh, India, was 82%, with low back and neck pain reported among physiotherapists due to high job demands (Nagar and Nouman 2022). Furthermore, the study reported that lower back and neck pain is more common among dentists, physiotherapists, and surgeons (Suganthirababu et al. 2023). Additionally, a study in 2016 found that persistent muscle contraction and jobs requiring repetitive motion are the common causes of WMSD, and 92% of the dentists in Bhopal, India, experienced pain and discomfort in at least one part of the body region (Batham and Yasobant 2016).

WMSDs have become a global public health issue due to the increased frequency of these injuries, which are caused by the existence of risk factors. Clinically, work-related soft tissue damage is known by a variety of titles, such as WMSDs, repetitive strain injuries (RSI), repetitive motion injuries (RMI), and diseases brought on by cumulative trauma (Nunes 2009). Work-related musculoskeletal disorders (WMSD) can affect the lower back, lower limbs, and upper limb extremities and are caused or exacerbated by work. Impaired body structures such as muscles, joints, tendons, ligaments, nerves, and bones constitute WMSDs and the localized blood circulation system, primarily brought on or exacerbated by the work itself (Okunribido et al. 2011). Aside from physically demanding jobs, the ageing of the workforce also contributes to the prevalence of WMSD because the likelihood of developing a WMSD is more closely linked to the disparity between job demands and the worker's physical capabilities (a decline in work capacity with age). In the medical field, musculoskeletal problems have long been diagnosed (Mahajan et al. 2023).

On the other hand, repetitive actions and work without leisure among healthcare professionals can lead to musculoskeletal problems. To prevent this occurrence, self-care management is essential among healthcare professionals, especially professional physiotherapists. Self-care management between the demanding work cultures will help in the unwinding of the stress that is faced by academic cum clinical physiotherapists. Academic physiotherapists those who are involved in high use of screens affecting the neck and shoulder posture, whereas for the role of a clinician, the workplace revolves around activities related to patients' aid, requiring the greatest amount of physical strength and techniques of loading and unloading of the force on the pylon were discussed (Prall and Ross 2019).

The first person to recognize the WMSD condition was the Italian doctor Bernardino Ramazzini in the eighteenth century. He recognized a link between some musculoskeletal problems and jobs because of the adoption of uncomfortable postures and the execution of abrupt and erratic motions (Campo et al. 2008). It is well established that there is a strong link between WMSD and the workplace, particularly concerning the physical risk factors of specific vocations, such as uncomfortable postures, high repetition, excessive force, static labour, cold, or vibration. Increasing workload and stress are contributing factors, and it increasingly appears that additional psychological elements also play a role in developing those conditions (Nunes and Bush 2012). The risks of MSD during formwork techniques were evaluated using the Rapid Entire Body Assessment (REBA) approach. The REBA method was used to assess WMSD and assigned a single score based on the posture evaluation and factors related to load, coupling, and activity to each body region to evaluate the posture chosen (e.g., the most awkward posture, the most prevalent posture, and the posture with the most force exerted) (Hignett and McAtamney 2000). The prevalence rate is high since physiotherapists' work involves repeated movements and sustained postures (Iqbal and Alghadir 2015; Batham and Yasobant 2016). Despite this prevalence rate, self-care or management in the workplace among physiotherapists needs more attention and has not been addressed in past research. Considering this, the primary goal of the present study was to identify WMSDs among professional physiotherapists and understand workplace self-management.

2 Case description

A 39-year-old male assistant professor cum clinical practitioner with 12 years of experience in the profession, engages in using computers for 6 hours a day for academic and clinical documentation purposes, was assessed at the workstation. His pain was analyzed using a VAS score (visual analogue scale), and the risk of developing MSD was measured using the rapid entire body

Table 1 Participants demographic details

Name	Mr. R	
Gender	Male	
Age	39	
Dominant hand	Right	
Occupation	Working as an Assistant Professor and practising as a clinical therapist	
Work duration	10-12 hours daily	
Workstation assessment for MSD	Pain	Hert's neck and shoulder with VAS score 3/10
	REBA	6 (Moderate risk category)

assessment (REBA) scale. He complained of neck and shoulder pain with a VAS score of 3/10 after sitting in front of the computer for more than one hour, which he managed during the routine practice. He sometimes works for about 12 hours a day without taking a break. He doesn't have any history of mental stress. He follows a typical diet and does not drink alcohol or smoke. Due to his busy work schedule, he does not participate in any sports or other physical activities for fun.

By assessing the work-related risk using the REBA scale, we found that he had a REBA score of 6, which is in the moderate-risk category (Table 1).

3 Results

The postures of the upper limbs (arm, forearm, wrist), trunk, neck and lower limbs (thigh, leg and foot) postures were evaluated using the REBA method; the most prevalent posture, the posture maintained for the longest period during the working cycle, the posture requiring the most physical effort, and the posture that produces the most discomfort. The REBA score represents the level of MSD risk for the job task being evaluated. The minimum REBA score was 1, and the maximum REBA score was 15.

Additionally, he had back and neck problems for the past two years and feels more worn out at the end of the shift. He is entirely aware of the value of ergonomics in the workplace, but he doesn't follow it because of the stress brought on by his workload and his need for medical attention. To prevent uncomfortable pain in the workplace, he does some exercises like chin tucks (Figure 1) for forward neck posture and shoulder bracing (Figure 2) to avoid rounded shoulders, occipital and scalene stretch (Figure 3) for 10 times and 3 repetitions and 2 sets twice a day.



Figure 1 Chin tucks exercise



Figure 2 Shoulder bracing exercise



Figure 3 Occipital and scalene stretch

4 Discussion

The study uses the VAS and REBA scales to assess the risk of a work-related musculoskeletal disorder (WMSDs) in a professional physiotherapist and their workplace self-management. Based on the worksite assessment, the participant's REBA score was 6, in the moderate-risk category; however, the pain intensity was mild, with a VAS score of 3/10. Professional physiotherapists are generally knowledgeable about workplace ergonomics and understand how to manage risk factors and other complications. But few, due to their hectic commitment to the work, will be excused from following the worksite ergonomic or posture care guidelines. This is related to the fact that experienced healthcare professionals learned to modify their work posture to avoid WMSDs or that physiotherapists with WMSDs may change careers or leave physiotherapy entirely (Salik and Özcan, 2004; Maheshwari et al. 2015). Furthermore, physiotherapists with more work experience are more likely to develop musculoskeletal problems because they typically spend 45 to 60 minutes per patient during a single session (Jacquier-Bret and Gorce 2023). The repositioning and mobilization of joints and soft tissues, as well as bent or twisted body positions while transferring patients, have all been found to enhance the risk of WRMDs in physiotherapists (Gorce and Jacquier-Bret 2023). The importance of ergonomics, a healthy work environment, injury prevention, counselling, etc., must be emphasized during physiotherapy to use body force efficiently and effectively without unintentionally loading any particular body part. This will reduce the prevalence of WMSDs and increase productivity (Campo et al. 2008). On the other hand, ergonomic research has shown that using chairs with adjustable height, armrests, and supports is an effective intervention for reducing musculoskeletal pain (Rempel et al. 2006). It is important for a physiotherapist to study self-management, as it is the only way to prevent work-related musculoskeletal disorders and work ergonomically to maintain productivity. However, this case study reports the workstation assessment of a single person, which is limited to generalizing the problems assessed. The authors recommend that future studies include more participants working more than 10 hours daily.

Conclusion

The results of this study can conclude that professional physiotherapists practising self-care exercise at the workplace would reduce susceptibility to work-related musculoskeletal problems. Despite being aware of the significance of ergonomics, adhering to it adequately by the health care professional will prevent the occurrence of work-related musculoskeletal disorders in physiotherapists and promote a healthy lifestyle.

Acknowledgements

Thank the participant for giving up his valuable time to participate in this case study.

References

- Batham, C., & Yasobant, S. (2016). A risk assessment study on work-related musculoskeletal disorders among dentists in Bhopal, India. *Indian Journal of Dental Research*, 27(3), 236.
- Campo, M., Weiser, S., Koenig, K. L., & Nordin, M. (2008). Work-related musculoskeletal disorders in physical therapists: a prospective cohort study with 1-year follow-up. *Physical Therapy*, 88(5), 608–619.
- Gorce, P., & Jacquier-Bret, J. (2023). Global prevalence of musculoskeletal disorders among physiotherapists: a systematic review and meta-analysis. *BMC Musculoskeletal Disorders*, 24(1), 265.
- Hignett, S., & McAtamney, L. (2000). Rapid entire body assessment (REBA). *Applied Ergonomics*, 31(2), 201–205.
- Iqbal, Z., & Alghadir, A. (2015). Prevalence of work-related musculoskeletal disorders among physical therapists. *Medycyna pracy*, 66(4), 459–469. <https://doi.org/10.13075/mp.5893.00142>.
- Jacquier-Bret, J., & Gorce, P. (2023). Prevalence of Body Area Work-Related Musculoskeletal Disorders among Healthcare Professionals: A Systematic Review. *International Journal of Environmental Research and Public Health*, 20(1), 841.
- Mahajan, D., Gupta, M. K., Mantri, N., Joshi, N. K., Gnanasekar, S., et al. (2023). Musculoskeletal disorders among doctors and nursing officers: an occupational hazard of overstrained healthcare delivery system in western Rajasthan, India. *BMC Musculoskeletal Disorders*, 24(1), 1-10.
- Maheshwari, P., Soni, R., & Parkash, N. (2015). Work related musculoskeletal disorders: a survey of physiotherapists in tricity. *International Journal of Physiotherapy*, 2(6), 1091–1096.
- Nagar, R., & Nouman, D. (2022). The prevalence of shoulder pain in physiotherapist due to long day practice. *International Journal of Multidisciplinary Educational Research*, 11(8), 20-23.
- Nunes, I. L. (2009). FAST ERGO_X—a tool for ergonomic auditing and work-related musculoskeletal disorders prevention. *Work*, 34(2), 133–148.
- Nunes, I. L., & Bush, P. M. (2012). Work-related musculoskeletal disorders assessment and prevention. *Ergonomics-A Systems Approach*, 1, 30.
- Okunribido, O. O., Wynn, T., & Lewis, D. (2011). Are older workers at greater risk of musculoskeletal disorders in the

- workplace than young workers?—A literature review. *Occupational Ergonomics*, 10(1–2), 53–68.
- Prall, J., & Ross, M. (2019). The management of work-related musculoskeletal injuries in an occupational health setting: the role of the physical therapist. *Journal of Exercise Rehabilitation*, 15(2), 193.
- Rempel, D. M., Krause, N., Goldberg, R., Benner, D., Hudes, M., & Goldner, G. U. (2006). A randomized controlled trial evaluating the effects of two workstation interventions on upper body pain and incident musculoskeletal disorders among computer operators. *Occupational and Environmental Medicine*, 63(5), 300–306.
- Salik, Y., & Özcan, A. (2004). Work-related musculoskeletal disorders: a survey of physical therapists in Izmir-Turkey. *BMC Musculoskeletal Disorders*, 5, 1–7.
- Sauter, S., Hales, T., Bernard, B., Fine, L., Petersen, M., Putz-Anderson, V., Schleiffer, L., & Ochs, T. (1993). Summary of two NIOSH field studies of musculoskeletal disorders and VDT work among telecommunications and newspaper workers. *LUCZAK H., CAKIR A., CAKIR G.-Work with Display Units*, 92, 229–234.
- Sekkay, F., Imbeau, D., Chinniah, Y., Dubé, P.A., de Marcellis-Warin, N., Beauregard, N., & Trépanier, M. (2018). Risk factors associated with self-reported musculoskeletal pain among short and long distance industrial gas delivery truck drivers. *Applied Ergonomics*, 72, 69–87.
- Suganthirababu, P., Parveen, A., Mohan Krishna, P., Sivaram, B., Kumaresan, A., et al. (2023). Prevalence of work-related musculoskeletal disorders among health care professionals: A systematic review. *Work (Reading, Mass.)*, 74(2), 455–467. <https://doi.org/10.3233/WOR-211041>.
- YI, Y., Pillai, S., & Vinodhkumar Ramalingam, O. (2022). Prevalence of work related musculoskeletal disorders (WRMSD) and the associated risk factors among malaysian physiotherapists: A cross sectional study. *Journal of Physical Education and Sport*, 22(32), 239.